Distribution Agreement

In presenting this thesis or dissertation as a partial fulfillment of the requirements for an advanced degree from Emory University, I hereby grant to Emory University and its agents the non-exclusive license to archive, make accessible, and display my thesis or dissertation in whole or in part in all forms of media, now or hereafter known, including display on the world wide web. I understand that I may select some access restrictions as part of the online submission of this thesis or dissertation. I retain all ownership rights to the copyright of the thesis or dissertation. I also retain the right to use in future works (such as articles or books) all or part of this thesis or dissertation.

Signature:

_____ _____

Elizabeth Magnotti Date

Self-assembly of porous α-helical nanosheets

By

Elizabeth Magnotti
Doctor of Philosophy

Chemistry

_____

Dr. Vincent P. Conticello
Advisor

_____

Dr. David Lynn
Committee Member

_____

Dr. Khalid Salaita
Committee Member

Accepted:

_____

Lisa A. Tedesco, Ph.D.
Dean of the James T. Laney School of Graduate Studies

_____

Date

Self-assembly of porous a-helical nanosheets

By

Elizabeth Magnotti

B.S., University of Virginia

Advisor: Vincent P. Conticello, Ph.D.

An abstract of
A dissertation submitted to the Faculty of the James T. Laney School of Graduate Studies of Emory University in partial fulfillment of the requirements for the degree of

Doctor of Philosophy
in Chemistry
2016

Self-assembly of porous a-helical nanosheets

By

Elizabeth Magnotti

B.S., University of Virginia

Advisor: Vincent P. Conticello, Ph.D.

A dissertation submitted to the Faculty of the James T. Laney School of Graduate Studies of Emory University in partial fulfillment of the requirements for the degree of

Doctor of Philosophy
in Chemistry
2016

Abstract

Self-assembly of porous α-helical nanosheets

By Elizabeth Magnotti

Two-dimensional materials, or nanosheets, such as graphene, which is 300 times stronger than steel and the best conductor of electricity, are enticing for applications in electronics, filtration, and energy storage. Proteins, which undergo hierarchical self-assembly into highly ordered structures, as a result of the amino acid sequence, are promising substrates for additional two-dimensional materials. Collagen mimetic peptides and peptoids, or N-substituted polyglycines, have been utilized to create two-dimensional materials, which can template the growth of inorganic materials and can be utilized as substrates for enzymatic reactions. The introduction of pores within biological nanosheets, could grant these materials additional roles in molecular encapsulation and charge transfer. In the following dissertation, α-helical peptides were utilized to create the first example of porous biological nanosheets. A three-fold α-helical design allowed for the generation of highly ordered nanosheets, whose phenotypes may be rationally modulated by manipulating the amino acid sequence. The results of these studies provide an alternate model for the design of interacting α-helices and provide a strategy for the design of porous structures.

Acknowledgments

I would like to extend my deepest gratitude to my advisor for the past five years, Dr. Vincent Conticello. Dr. Conticello is an extraordinary scientist, due to his devotion to science, his attention to detail, and creativity. Dr. Conticello sets high standards for all aspects of being a scientist, from doing systematic experiments to creating top-notch figures for journal articles. The high standards that Dr. Conticello has set for my research have been instrumental to my research success. Furthermore, Dr. Conticello has dedicated countless hours to my intellectual growth, taking the time to answer my plethora of emails and coming to Emory on the weekends to help me prepare for my 2nd year qualifying exam. In addition to helping me to attain my research goals, Dr. Conticello has allowed me to pursue other interests, such as teaching and mentoring, both of which have granted me a desire to stay in academia. Dr. Conticello has also shown me that research is truly global and how to establish productive collaborations. I am very thankful that he allowed me to study mass spectrometry in Italy. Finally, Dr. Conticello's great sense of humor and compassion have made me truly enjoy my time at Emory. I will be very proud that my name will be linked to Dr. Conticello's in the research realm.

In addition to my advisor, I would like to thank my committee members Dr. David Lynn and Dr. Khalid Salaita, who have been positive influences in my graduate school career. Dr. David Lynn gave me the opportunity to teach a biochemistry course to nursing students, which has motivated me to pursue a career path as a professor. Furthermore, Dr. David Lynn has given me a whole new perspective on science, teaching me how to use metaphors like "human water molecules" to explain

invisible chemical forces at outreach events. Dr. Lynn also has been instrumental in helping me to communicate science and is one of the most creative people I have ever met. Dr. Khalid Salaita has spent many hours advising me on both science and careers. The complex questions that Dr. Salaita has asked at each of my talks have inspired me to think about research problems from multiple angles. Additionally, Dr. Salaita allowed me to observe a post-doctoral fellow interviewee for his own lab. This experience was extremely helpful for my own post-doctoral fellowship interview. Both Dr. Lynn and Dr. Salaita have immensely supplemented my graduate school experience, and I have really appreciated and benefited from their wonderful mentoring.

In addition to my PhD committee, several individuals at Emory have contributed to my success in graduate school. Thank you to the newly minted PhD graduates, Dr. Chunfu Xu and Dr. Tao Jiang, who patiently trained me in most biophysical experimental techniques and still advise me. I am also grateful for the current members of the Conticello laboratory, Charlie Modlin, Becky Bartlett, Spencer Hughes, and Shengyuan Wang, who have provided feedback on all of my research presentations. The undergraduates and high school students, Lillian Hough, Allison Harker, and Rachel Cooper, that I have trained have taught me how to serve as a good mentor and truly have lit up my laboratory. I would also like to thank the lab of Dr. David Lynn for being wonderful colleagues, in particular Rolando Rengifo who assisted me with one of my final experiments. I am very indebted to Dr. Anil Mehta, who has served as both a collaborator and mentor. He is one of the most patient people I have ever met and has been a great resource for

both solid-state NMR and the graduate school experience. I would also like to thank Dr. Erin Schuler and Dr. Kevin Yehl for advising me on experiments and techniques.

I would also like to extend my gratitude to many collaborators who have contributed to the research projects described in my dissertation. Dr. Xiaobing Zuo from Argonne National Laboratory provided assistance with small angle x-ray scattering experiments and interpretation and has been an invaluable resource. Dr. Joseph Wall of Brookhaven National Laboratory performed the scanning transmission electron microscopy imaging experiments. Dr. Elizabeth Wright and her graduate student Rebecca Dillard performed cryo-electron microscopy imaging experiments and assisted with preliminary cryo-EM reconstruction experiments. Arshad Karumbamkandathil and Qiongyi Shang of Dr. Tim Lian's laboratory have graciously allowed me to use their atomic force microscope to collect height measurements for my nanosheets. Dr. Fred Strobel has assisted with mass spectrometry analysis. The Emory University Microscopy Core staff, including Hong Yi, Art McCanna, and Jeannette Taylor, have trained me on electron microscopy and patiently assisted me with complex imaging problems.

Finally, I would like to thank my family members for supporting everything I do and encouraging me always, even when I am discouraged. I am also very grateful for my golden retriever Shelby who always makes me smile. I would also like to thank my best friends in Atlanta, Leah Connors and Ellen Litkowski, who have made Atlanta home. I am also extremely grateful to my undergraduate research mentor Dr. Charles Grisham, who encouraged me to go to graduate school. Without the help of the individuals described above, this dissertation would not be possible.

List of Figures

Chapter 1 Two-Dimensional Peptide and Protein Self Assembly

1.1 Introduction

The construction of structurally defined nanoscale assemblies from collections of molecules represents a significant challenge for the development of advanced materials. Biological substrates, such as proteins and nucleic acids, represent attractive candidates for the creation of nanomaterials. Peptides and proteins comprise defined sequences of amino acids, in which the formation of higher-order structures can be encoded through the progression of structural hierarchy. Thus, the primary structure of peptides and proteins may be manipulated to define structure and introduce function in the resultant nanomaterials. Biological assemblies have often been classified on the basis of dimensionality. One-dimensional nanomaterials, e.g., nanofibrils, nanoribbons, and nanotubes, commonly occur in nature as cytoskeletal elements or as components of organelles and have been created through rational design. Examples of one-dimensional materials found in nature, include actin microfilaments and collagen fibers [1-3]. In addition, synthetic one-dimensional assemblies have been created using rational design from a variety of structural motifs including α-helical coiled-coils [4-16], β-strands [17-26], β-hairpins [27-30], and collagen triple helices [31-40]. Three-dimensional nanomaterials, i.e., peptide and protein crystals, can be produced systematically. From 1975 to 2015, the Protein Data Bank has grown to over 100,000 supramolecular crystals.

However, the *de novo* design of protein crystals still represents a significant challenge, although progress has been made in recent years [41].

Two-dimensional peptide and protein assemblies occur relatively infrequently in native biological systems, at least in comparison to one-dimensional assemblies. Bacterial and archaeal S-layers represent the best studied examples of two-dimensional protein based assemblies. Significant research effort has been directed toward modification of the S-layer systems for applications in two-dimensional nanoarchitectonics. Recent research suggests that organized two-dimensional assemblies may be more common than originally anticipated. Chemoreceptors form multi-component two-dimensional arrays in *E. coli* that display a highly cooperative response in ligand binding events [42]. Moreover, bactofilins, a class of bacterial cytoskeletal protein [43], and certain sterile alpha motif domains, a class of eukaryotic scaffolding proteins [44-46], can self-assemble into structurally ordered two-dimensional arrays. Some evidence suggests that the formation of these two-dimensional assemblies may be critical for their native biological function. A greater understanding of the principles that govern the formation and the underlying structure of these natural two-dimensional assemblies may provide insight into design of functional synthetic two-dimensional nanomaterials [47].

Nanoarchitectonics involves the development of methods to control the organization of molecules in supramolecular structures for device fabrication. This approach underlies an emerging field in advanced materials creation and represents an excellent conceptual platform upon which to design two-dimensional materials [47,48]. Two-dimensional nanoarchitectonics techniques have been used in the design of organic and inorganic materials, and these principles may be extended, in principle, to biological

materials [49]. This chapter focuses on developments in the field of two-dimensional peptide and protein assemblies, and, where applicable, the nanoarchitectonic principles associated with the design of these materials. For the purposes of this chapter, a two-dimensional assembly is defined as a structure in which the lateral size in the *x*-*y* dimensions is larger than the thickness/height in the *z*-dimension (((*x*≈*y*)/*z* ≥ 10), as was suggested in previous reviews [49]. This chapter begins with a discussion of surface layers, a biological example of a proteinaceous two-dimensional assembly and two-dimensional layered structures that have been adventitiously discovered in the crystal structures of native and synthetic peptides. These results highlight the functional possibilities for the design of two-dimensional assemblies[41,50-63]. The discussion continues with a description of stable two-dimensional assemblies derived from synthetic peptides and proteins. While nanosheet formation has in many instances occurred serendipitously, rational design methods have recently been employed to create two-dimensional protein assemblies of defined structure [36,37,64-88].

1.2 Biological surface layers (S-layers)

Surface layers (or S-layers) represent the most common biological example of a two-dimensional assembly. Surface layers make up the outermost cell envelope component of many organisms and account for ten percent of cellular proteins in *Archaea* and *Bacteria*. S-layers cover cell surfaces during all stages of growth and cell division. In *Archaea*, S-layers represent the only wall component outside the plasma membrane. In contrast, S-layers in bacteria adhere to either the peptidoglycan component of the cell wall (Gram positive bacteria) or to the lipopolysaccharide outer membrane (Gram negative bacteria) component. S-layers are identified by freeze-etching of intact cells.

Most surface layers are composed of a single protein or glycoprotein molecule, which spontaneously self-assembles into ordered two-dimensional arrays, covering the entire surface of an organism. The S-layers require approximately 500,000 copies of the component protein to cover the entire surface of an average size rod-shaped prokaryotic cell, which necessitates a rapid rate of synthesis of the surface layer protein (circa 400 copies per second)[55,60,62,63].

Electron crystallography, scanning probe microscopy, and x-ray and neutron scattering have been employed to obtain information about the two-dimensional spatial arrangement of S-layer proteins. S-layers exhibit varied lattice types, including oblique (p1, p2), square (p4), and hexagonal (p3, p6) (Figure 1.1). Typical unit cells range from three to 30 nm in dimension[63]. Surface layers of bacteria display thicknesses of five to 20 nm thick whereas S-layers of archaea have thicknesses up to 70 nm. S-layers frequently contain structurally uniform pores ranging from two to eight nm in size [63]. S-layer proteins have an outer face, which is charge neutral, and an inner face, which is often either net negatively or positively charged [62]. As a result, functional groups on the surfaces of the S-layers are well aligned, and many experimenters have appended molecules or nanoparticles onto the S-layer surfaces [62].

Although S-layer proteins exhibit limited primary structure homology, they share common functional domains, which are responsible for cell-wall binding and self-assembly. The position of the cell-wall binding domain varies with bacterial species. In the bacterial species *Bacillacea*, the *N*-terminal domain is responsible for cell-wall binding. S-layer proteins from *Bacillaceae* contain three S-layer homology (SLH) motifs, which interact with secondary cell wall polymers (SCWPs) that are charged with

pyruvate. In *P. alvei*, the SLH motifs have a dual-recognition function, recognizing both SCWPs and peptidoglycan. S-layer proteins which lack SLH motifs are anchored to different types of SCWPs through either their *N*- or *C*- termini. In order to elucidate the S-layer protein domains responsible for self-assembly, truncated mutants of the S-layer protein SbpA from *Lysinibacillus bacillus CCM2177* have been generated. Truncation of SbpA resulted in either a non-native S-layer lattice symmetry or a complete inability of SbpA to self assemble [63].

S-layer proteins are between 40 kDa and 170 kDa in size. Many bacterial S-layer proteins are weakly acidic with isoelectric points between 4 and 6. Some archaeal S-layer proteins have higher isoelectric points (pI ≈ 8 – 10). In bacteria, 40-60 % of the S-layer amino acid sequence is hydrophobic, suggesting that hydrophobic interactions help to stabilize S-layer self-assembly. Additionally, negatively charged carboxylates and positively charged amino groups are found in close proximity to each other on the surface of the S-layer, suggesting that ionic interactions also may stabilize S-layer self-assembly. Some S-layers are stabilized by the addition of divalent cations, such as Ca^{2+}, which interact with acidic residues on the S-layer surface[59]. S-layer proteins can be extracted from the cell wall using hydrogen-bond disrupting agents, such as urea or guanidinium hydrochloride. Isolated S-layer proteins can reassemble in solution upon dialysis of the disrupting agents into either flat sheets or open-ended cylinders (Figure 1.1) [50]. Interestingly, surface-layer morphology on the cell wall is dependent only on characteristics of the individual surface-layer protein rather than the surface. Surface layer proteins of one organism can attach to another organism and form a lattice of the same pattern. Surface layer proteins can also reassemble at interfaces, including the air-

water interface, at planar lipid films, and on solid surfaces [63].

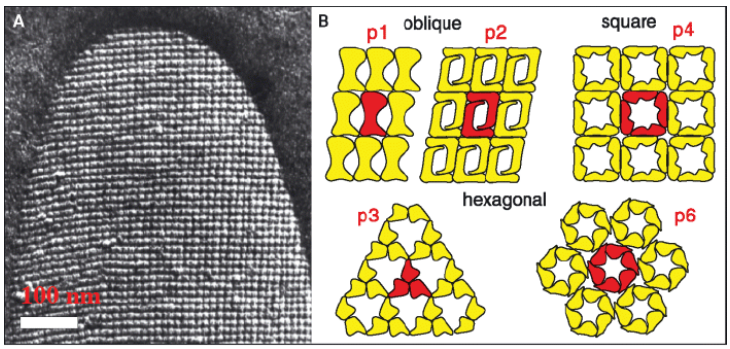

C

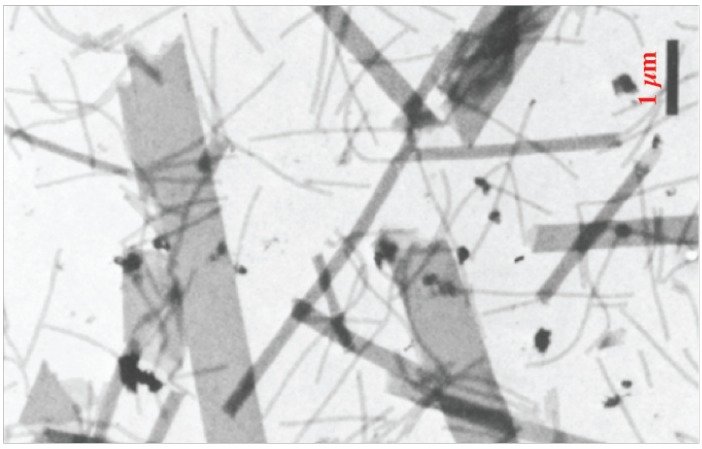

Figure 1.1 Bacterial surface layers a. an electron micrograph of a freeze etched and Pt/C shadowed preparation of an organism displaying a square (p4 lattice) b. Potential lattice types for S-layers c. Self-assembled nanotubes and nanosheets from the S-layer of Bacillus stearothermophilus NRS2004/3a generated in the presence of low concentrations of CaCl2 [50, 55]

In the cellular environment, S-layers adopt a variety of functional roles. S-layer proteins can serve as molecular sieves; pores within S-layer lattices allow for the passage of molecules with molecular weights up to 30 kDa. S-layer proteins can serve as binding sites for exoenzymes, such as high molecular mass amylase. In cyanobacteria, S-layer proteins play a unique ecological role, serving as templates for fine-grain mineralization and bioremediation[63]. The wide variety of functions and intricate structural features of S-layer proteins highlights the potential of two-dimensional assemblies as advanced

materials. The functional complexity of native S-layer assemblies provides insight for the potential roles that can be developed for synthetic two-dimensional assemblies as nanoarchitectonic platforms.

1.3 Crystal Structures

Two-dimensional layered structures have been observed in crystallographic

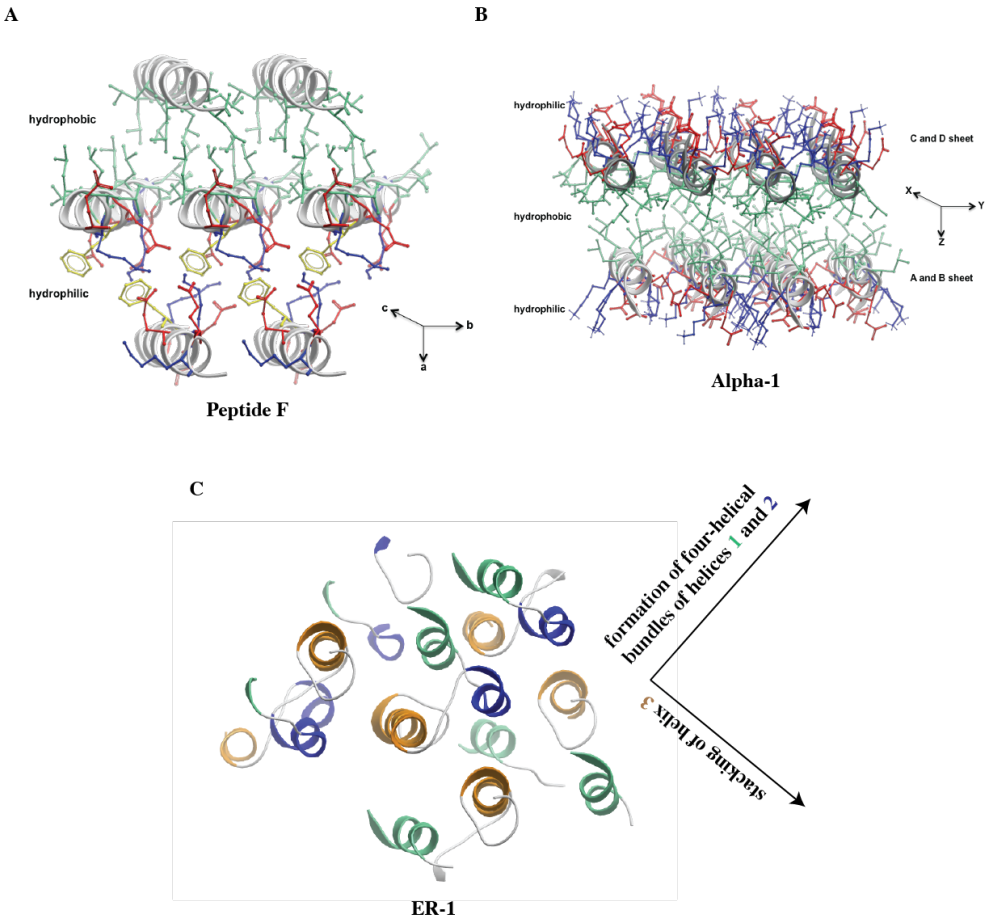

Figure 1.2 Crystal structures containing two-dimensional layers a. two-dimensional layer formed by Peptide F (PDB ID: 1PEF) [51] b. Bilayer formed by peptide Alpha-1 (PDB ID: 1BYZ) [61] c. Packing of ER-1 into 2D layer; three helix bundle indicated by helices within triangle (PDB ID: 2ERL) [57-58]; Figures generated using Molsoft's ICM Browser Pro; hydrophobic amino acid, acidic residues, and basic residues colored green, red, and blue, respectively

structural determinations of peptides and proteins [41,51-53,57,58,61]. These structural analyses afford information on the intermolecular interactions between subunits within a layer, which reveal design principles that may be employed to create two-dimensional assemblies through rational design. For example, the amphiphilic helical peptide **F** was shown to form a novel, multilayered structure (Figure 1.2a) [51]. Peptide **F** was soluble in apolar, organic solvents and retained its helicity in solution. The crystal structure of **F** revealed rows of close-packed, parallel helices. Salt bridges between the carboxyl terminus and a lysine residue on an adjacent helix, and a hydrogen bond between a glutamine residue and the amino terminus caused growth along the b crystallographic axis. Rows of parallel helices stabilized by polar interactions packed antiparallel to each other along the a axis such that the interfaces between **F** alternated between hydrophobic and hydrophilic, forming a two-dimensional plane. The packing of the **F** helices followed the 3-4 "ridges-into-grooves" convention [69]. The three-dimensional crystal was formed when planes of sheets stacked along the crystallographic c-axis.

In another case, the crystal structure of the amphiphilic peptide **Alpha-1** at neutral pH revealed an interesting two-dimensional arrangement of α-helices (Figure 1.2b) [61]. Four helical molecules, assigned names of **A**, **B**, **C**, and **D**, pack into the P1 crystal space group. In the X dimension, which is oriented parallel to the helical axis, columns are formed through stacking of **Alpha-1** helices; head to tail stacking is stabilized through a hydrogen bond between a bridging water molecule and the *N*-terminal acetyl group. In the Y-dimension, which is oriented perpendicular to the helical axis, the side chains of antiparallel helices **A** and **B** interacted through tight ridges-into-grooves interdigitation. Helices **A** and **B** were not in register in the X-dimension. One copy of helix **A** interacted

with two copies of helix **B**. Stacking of helices in the X-dimension and ridges-into-grooves interactions between helices in the Y-dimension resulted in two-dimensional sheet formation in the X-Y plane. Helices **C** and **D** interacted similarly to generate a second sheet parallel to that formed by helices **A** and **B**. Due to peptide **Alpha-1**'s amphiphilicity, each helix contained a hydrophobic face made up of leucine residues and a charged face composed of lysines and glutamates. Therefore, in the z-dimension, sheets composed of **A** and **B** alternated with sheets composed of **C** and **D**, such that the hydrophobic face of each sheet is buried and the charged faces form a zipper between structurally adjacent sheets of helices. A similar bilayer sheet arrangement was observed in the centro-symmetric crystal structure of a 1:1 mixture of D- and L-Alpha-1 peptides [54].

Balaram and co-workers have demonstrated that packing of columns of helices into sheets is a common feature within the crystal structures of short, synthetic helical peptides; permitting both parallel and antiparallel orientations between structurally adjacent sheets of helices [53]. Helices in adjacent sheets can be oriented either in exact registration, that is, one in which the termini of helices are aligned between adjacent sheets, or can be displaced out of register. Columnar packing has also been observed in the crystal structures of coiled-coil assemblies, which can in certain cases result in the formation of sheets of helices [41,52]. Computational methods were employed to design a trimeric coiled-coil sequence that assembled into stacked layers of defined symmetry within the crystalline state [41]. Finally, the three-helical bundle protein Er-1, a pheromone from the eukaryotic organism *Euplotes raikovi*, crystallizes in a densely packed layered structure that may underlie its biological role as a signaling molecule

during cell mating [57,58]. A two-dimensional sheet of Er-1 is formed when helix A and B from two molecules interact to form a four-helical bundle along the x-axis and when helix C stacks antiparallel along the y-axis (Figure 1.2c). Despite the ubiquity of layered packing in the crystal structures of short helical peptides and proteins, this phenomenon has yet to be effectively translated into the fabrication of persistent nanosheet structures in solution. This observation may arise from the fact that, especially in the case of short peptides, the intermolecular interactions are weak and incapable of supporting the formation of shape-persistent assemblies that are thermodynamically stable in solution under ambient conditions.

1.4 β-sheet peptide based 2D assemblies

Short β-sheet peptides have been employed as substrates for the creation of two-dimensional assemblies. These two-dimensional structures often coexist with one-

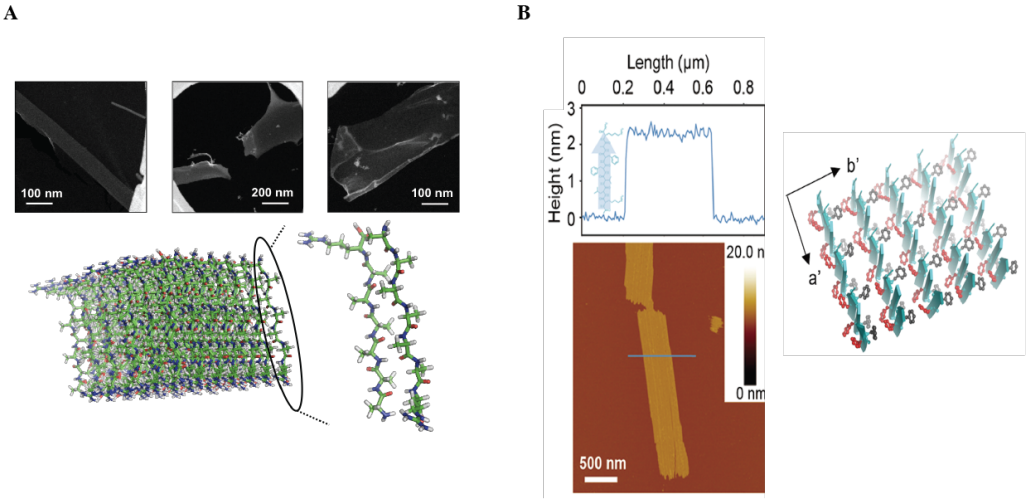

Figure 1.3 Two-dimensional structures formed by β-sheet structures a. Scanning transmission electron microscopy images of A_6R revealing a single thickness ribbon, irregular and broken sheet, and folded over sheet (from left to right) and model for two-dimensional layer formation (left, bottom) [70] b. AFM image of KLVFFAL nanosheets (left) and model for sheet formation (right) [72]

dimensional nanotubes or fibrils. Hamley *et al*. investigated the assembly of the short amyloidogenic peptide AAKLVFF, which can form nanotubes, fibrils, and two-dimensional stiff tapes depending on the solvent composition. Peptide AAKLVFF formed fibrils in aqueous solution, whereas in pure methanol, AAKLVFF formed nanotubes. In methanol:water mixtures, (70:30 weight ratio, respectively), AAKLVFF formed polydisperse stiff tapes [68]. The morphologies of the respective assemblies has been attributed to variations in hydrogen-bonding under different solvent compositions [67,68]. In the presence of aqueous solutions of 100 to 300 mM sodium chloride, AAKLVFF formed tapes, which can associate laterally into thicker tapes [66]. When β-alanine (2-aminopropionic acid), in which the amino group is bound to the β-carbon, is substituted into the peptide sequence in place of α-alanine, flexible fibrils are observed in solution [66]. Salt addition to βAβAKLVFF enhances twisting of the flexible fibrils. At low salt concentrations (100 mM NaCl), twisted tapes are observed, and at higher concentrations (250 mM NaCl), some nanotubes are observed [26]. The twisting of fibrils may be attributed to charge screening effects on the edge of the peptide fibrils. Under acidic conditions without salt, the peptide exhibited a net positive charge. Salt addition decreased the electrostatic repulsion between fibrils allowing for twisting and in the case of higher salt concentrations closing of the twisted fibrils into nanotubes [66]. Numerous studies of fibrillogenic β-sheet peptides have indicated significant polymorphism, in which different self-assembled forms, including fibrils, coiled ribbons, and tubes, in a manner that depended on the solution conditions under which the peptides were assembled [89]. Therefore, it is possible that many β-sheet peptides could also

sample conformations that would result in the formation of persistent nanosheet structures in solution.

The self-assembly of the amphiphilic peptide A_6R provides an illustration of this complex phase behavior that can be observed for dynamic oligopeptide systems. Peptide A_6R formed ultrathin (circa 3 nm in thickness) nanosheets and nanotubes in solution in a manner that depended on its concentration (Figure 1.3a) [70]. At low concentrations, thin nanosheets were observed as the predominant species in solution, but coexisted with tape-like structures. Some nanosheets also exhibited folding at the edges. In contrast, at higher concentrations, cryo-TEM measurements indicated that nanotubes were the dominant species. A model for the different modes of assembly was proposed in which curvature of the nanosheets resulted from the difficulty associated with packing the bulky arginine side-chain into an anti-parallel dimer. At low concentrations of peptide, electrostatic interactions between the arginine side chain and C-terminal carboxylates, stabilized the packing of the peptides into planar sheets. Interestingly, the peptides within the sheets did not display a persistent backbone conformation. However, at high peptide concentrations, the hydrogen bonding network derived from β-sheet formation induced curvature in the nanosheets, which resulted in nanotube formation [70].

Recently, Dai et al. reported the formation of nanosheets that adopted a β-sheet conformation in the self-assembled state [72]. These peptides were derived from mutants of the amyloidogenic Aβ(16-22) peptide sequence, KLVFFAE, in which the K16 or E22 were replaced with other charged residues. The most thoroughly characterized peptide system, KLVFFAK, derives from the E22K mutant associated with the Italian familial form of the Aβ sequence. This peptide self-assembles into persistent nanosheets from

acidic phosphate buffer (pH 2.0). Note that this behavior differs significantly from the wild-type KLVFFAE peptide, which under similar conditions coils into ribbons that close to form nanotubes of uniform dimension [90]. The KLVFFAK nanosheets are composed of antiparallel β-sheet fibrils in which the peptide backbone is perpendicular to the surface of the sheet on the basis of AFM height measurements (Figure 1.3b). FT-IR spectroscopy and X-ray fiber diffraction measurements confirm the anti-parallel orientation of peptides in a cross-β fibril structure. Self-assembly of the nanosheet in the lateral directions occurs through a combination of hydrogen bonding along the fibril axis and commensurate stacking of the β-sheets as a result of the packing of hydrophobic side chains. Despite the potential for twisting of the β-sheet due to the chirality of the peptide backbone, KLVFFAK maintains a flat sheet-like morphology over an extended area. Two hydrophobic surfaces, designated "A" and "B", could be distinguished on the basis of peptide sequence, which occur on opposite sides of the β-sheets. Mutagenesis studies suggested that self-association of β-sheets was mediated through "face to back" packing in which an "A" interface selectively interacts with a "B" interface. The presence of salt concentrations up to 0.5 M NaCl cause an increase in nanosheet lateral dimensions due to charge screening of the repulsive interactions between positively charged lysine side chains which are found on the nanosheet surfaces. Nanosheet assemblies derived from KLVFFAK were able to mediate HIV infection and retroviral gene transfer into the HEK293T cell line. The efficacy of transfection could be correlated with the nanosheet architecture, in which the positively charged surfaces of the assembly could effectively bind to the negatively charged surface of the membrane-enveloped retrovirus.

1.5 Collagen-based nanosheets

In the past five years, collagen-mimetic peptides have also been used as building blocks for the design of two-dimensional materials. Native collagen forms a left-handed triple helix with a polyproline-II secondary structure. Its sequence is made up of tripeptide repeats Xaa-Yaa-Gly, where Xaa is typically proline and Yaa is the unnatural amino acid (4*R*)-hydroxyproline; the core of the triple helix is made up of glycine molecules whereas proline and (4*R*)-hydroxyproline face the outside of the triple helix. Collagen-mimetic peptides (CMPs) are typically 40 amino acids or less in length and have been shown, in certain circumstances, to recapitulate the properties of native

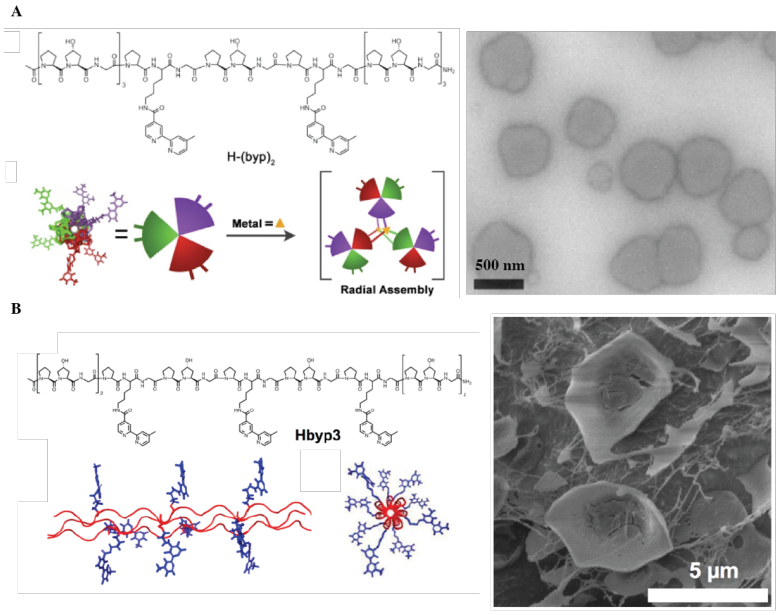

Figure 1.4 Metal stabilized collagen assemblies a. sequence of H-(byp)$_2$ and model for its self assembly; electron micrograph represents a peptide disc formed in the presence of metal ions [83] b. Sequence and model for assembly of Hbyp3 and cryo-SEM image of curved discs formed by Hbyp3 [36]

collagen [37]. CMPs can be easily synthesized using solid-phase peptide synthesis methods. Several techniques have been shown to promote formation of two-dimensional assemblies from collagen-mimetic peptides, including metal-ion coordination [83],

introduction of aromatic amino acids [83,36], a mixture of right-handed and left-handed triple helices [87], hydrophobic interactions [79], and ionic interactions [74-76].

The first example in the literature of a two-dimensional assembly generated from collagen-mimetic peptides involved the use of metal-ion coordination to stabilize peptide discs [83]. A nine triplet collagen mimetic peptide **H-(byp)$_2$** of sequence (Pro-Hyp-Gly)$_9$ was synthesized by solid-phase peptide synthesis. At the fourth and sixth triplet, bipyridine ligands were conjugated to lysines that replaced the canonical (4*R*)-hydroxyproline amino acids, which would otherwise occupy the Yaa positions of the triad repeats (Figure 1.4a). In the absence of metal ions, dynamic light scattering measurements indicated that **H-(byp)$_2$** formed assemblies with two distinct size-distributions; the distribution with a hydrodynamic radius of 3 nm corresponded to **H-(byp)$_2$** monomeric triple-helices whereas the distribution with a hydrodynamic radius of 75 nm corresponded to aggregates of **H-(byp)$_2$**. After the addition of Fe(II) to **H-(byp)$_2$**, the distribution corresponding to monomeric collagen triple helices was lost, and a distribution with a larger hydrodynamic radius of 300 nm was observed. Transmission electron microscopy imaging revealed that in the absence of metal **H-(byp)$_2$** formed ill-defined aggregates. In contrast, images of **H-(byp)$_2$** with the addition of Fe(II) formed round-dislike assemblies with diameters between 50 to 500 nm (Figure 1.4a). Atomic force microscopy (AFM) measurements showed that the assemblies had thicknesses of 10 nm close to the theoretical length of **H-(byp)$_2$**. This measurement is consistent with the authors' proposed model for metal-promoted radial assembly (Figure 1.4a). The bipyridine ligands of three adjacent triple helices formed two metal-ion coordination

sites; the addition of Fe(II) promoted radial assembly of triple helices and creation of peptide discs [83].

To extend upon this work, Chmielewski, *et al.,* modified the design of **H-(byp)$_2$** to incorporate an additional bipyridine ligand with the goal of inducing disc assembly in the absence of metal ions [36]. The resultant sequence of **Hbyp3** contained three bipyridine ligands per peptide, or nine bipyridine ligands per triple helix (Figure 1.4b). Strong aromatic interactions between **Hbyp3** triple helices promoted radial growth of peptide discs. Dynamic light scattering experiments revealed large assemblies with diameters of 1100 nm. TEM revealed similar disc structure morphologies to those of **H-(byp)$_2$** in the presence of Fe(II) but with larger diameters between 0.5 and 1.5 μm. Cryo-SEM imaging revealed that the surface of these assemblies is curved, and the thickness of the curved discs was between 12 and 16 nm. Small-angle x-ray scattering measurements supported a model in which collagen triple helices pack into a cuboidal arrangement with interdigitating bipyridine ligands. This work shows that the addition of the additional aromatic group can promote the formation of stable peptide discs in the absence of metal-ions (Figure 1.4b).

Based on this model, the edges of the curved discs had free bipyridine ligands that were available for metal ion coordination. The addition of Fe(II) to a solution of curved discs resulted in the formation of rounded structures with diameters between 1.5 and 3.0 μm. TEM and AFM analysis of these objects suggested the presence of collapsed spheres. Cryo-SEM showed that the spheres were hollow with wall thicknesses between 15 and 18 nm, and SAXS measurements supported a cubic arrangement of triple helices of **Hbyp3**. After the addition of EDTA to preformed hollow spheres, disc-like structures

were observed. Collectively, this data supported a model in which hollow sphere formation is a result of metal ion coordination to the bipyridine moieties on the ends of the **Hbyp3** discs [36]. Moreover, these data demonstrated that 2D peptide assemblies could be elaborated into more complex 3D objects through introduction of additional non-covalent interactions.

Shape complementarity can also be used to guide the formation of two-dimensional assemblies [87]. Natural proteins prefer to utilize homochiral molecular recognition, as they exclusively comprise sequences of *L*-amino acids. However, as described above for the crystal structure of *D,L*-Alpha-1, the formation of stable heterochiral complexes can be observed using synthetic peptides [87]. Richardson, et al., have suggested that heterochiral packing of helices would allow for the maximal number of ridges-into-grooves packing interactions between adjacent pairs of helices [69]. To test the influence of this shape complementarity on self-assembly, collagen-mimetic peptides were used as substrates. In the collagen-mimetic peptide **(Pro-Pro-Gly)$_{10}$**, proline side chains form the ridges and grooves of the triple helix. The cyclic aliphatic side chain of proline prevents the contribution of ionic interactions, hydrogen bonding, and side-chain flexibility to the packing of helices. Thus, the shape of the helix interface should determine molecular packing.

The two collagen-mimetic peptides, **[(P$_L$P$_L$G)$_{10}$]$_3$** and **[(P$_D$P$_D$G)$_{10}$]$_3$** were used to investigate the effect of helical handedness on self-assembly. Computational models of **[(P$_L$P$_L$G)$_{10}$]$_3$** and **[(P$_D$P$_D$G)$_{10}$]$_3$** showed that the two peptides exhibit the same thermal stability and solubility but opposite helical handedness. The **[(P$_L$P$_L$G)$_{10}$]$_3$** peptide forms a continuous left-handed ridge while **[(P$_D$P$_D$G)$_{10}$]$_3$** forms a right-handed ridge. Short-range

van der Waals interactions were calculated for two like-handed and opposite-handed structures. The calculations predicted that the triple helical grooves of opposite handedness would interdigitate and interact more tightly than those between like-handed triple helices (Figure 1.5a). TEM analysis showed that a 1:1 molar mixture of $\mathbf{[(P_LP_LG)_{10}]_3}$ and $\mathbf{[(P_DP_DG)_{10}]_3}$ resulted in the formation of well-ordered micrometer sized nanosheets (Figure 1.5a). AFM measurements indicated that the thickness of the nanosheets was about 10 nm, close to the length of the collagen mimetic peptides. Depletion of one enantiometer reduces the yield of nanosheets, which suggests that nanosheets may only form when left-handed ridges can interdigitate with right-handed ones. This work shows that, in a minimal system, shape complementarity can be used to

promote the formation of two-dimensional assemblies.

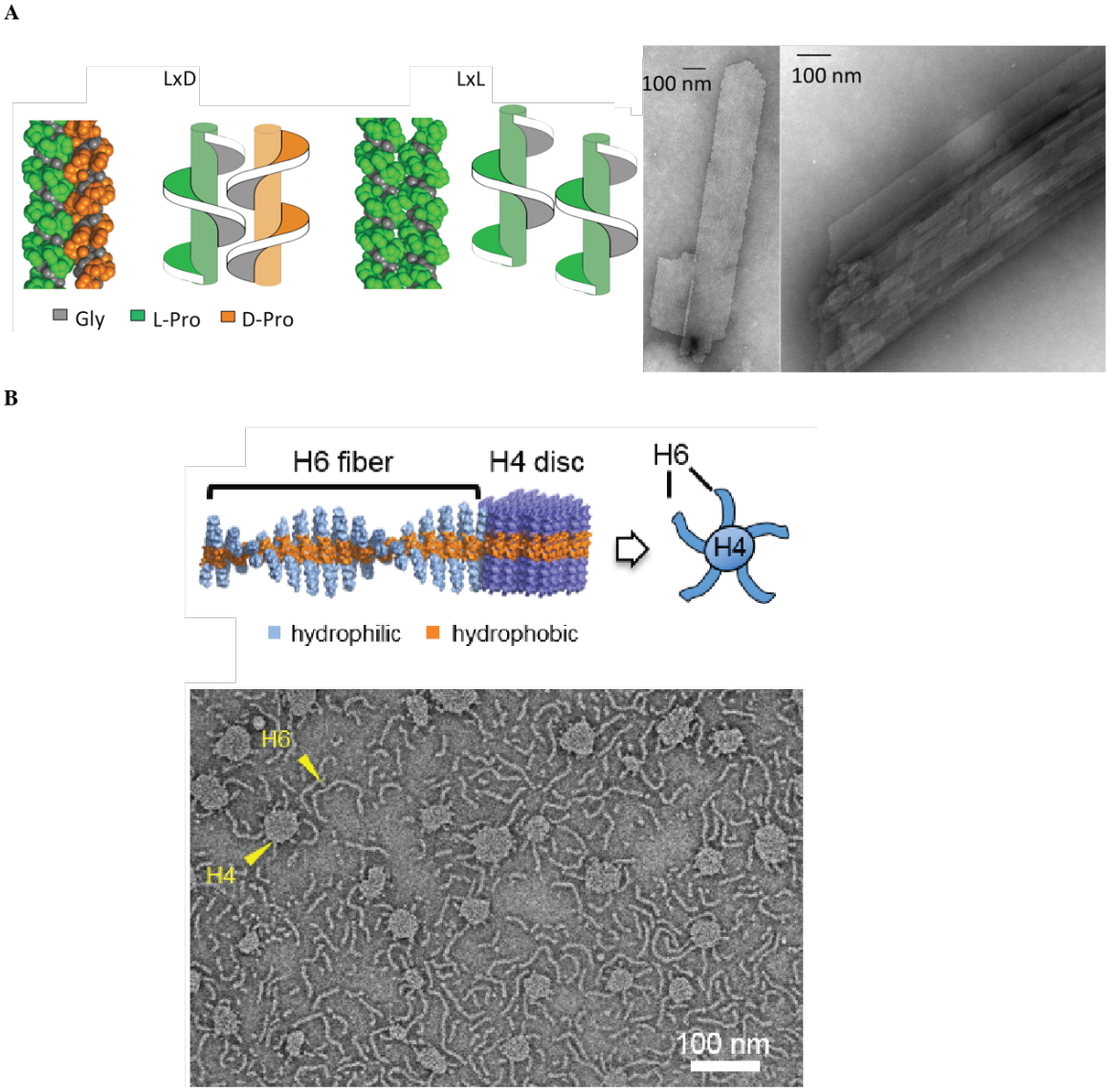

Figure 1.5 Collagen nanosheets stabilized by shape complementarity and the hydrophobic effect [87] **a.** nanosheets formed through heterochiral assembly of **$[(P_LP_LG)_{10}]_3$** and **$[(P_DP_DG)_{10}]_3$** **b.** Nanostars formed by peptides **H4** and **H6** [79]

Further work by Nanda *et al*. investigated the effect of hydrophobic residues on CMP self-assembly [79]. In natural collagen, leucine and isoleucine most frequently occupy the Xaa position and Yaa position respectively. The peptide **H4** was designed to interrogate the effect of incorporation of these residues at the respective Xaa and Yaa

positions within a pppphhpppp sequence pattern, in which *p* and *h* denote Pro-Hyp-Gly and Leu-Ile-Gly triplets, respectively. Computer simulations of **H4** predicted that this sequence pattern would form disc-like structures, and TEM imaging revealed that at pH

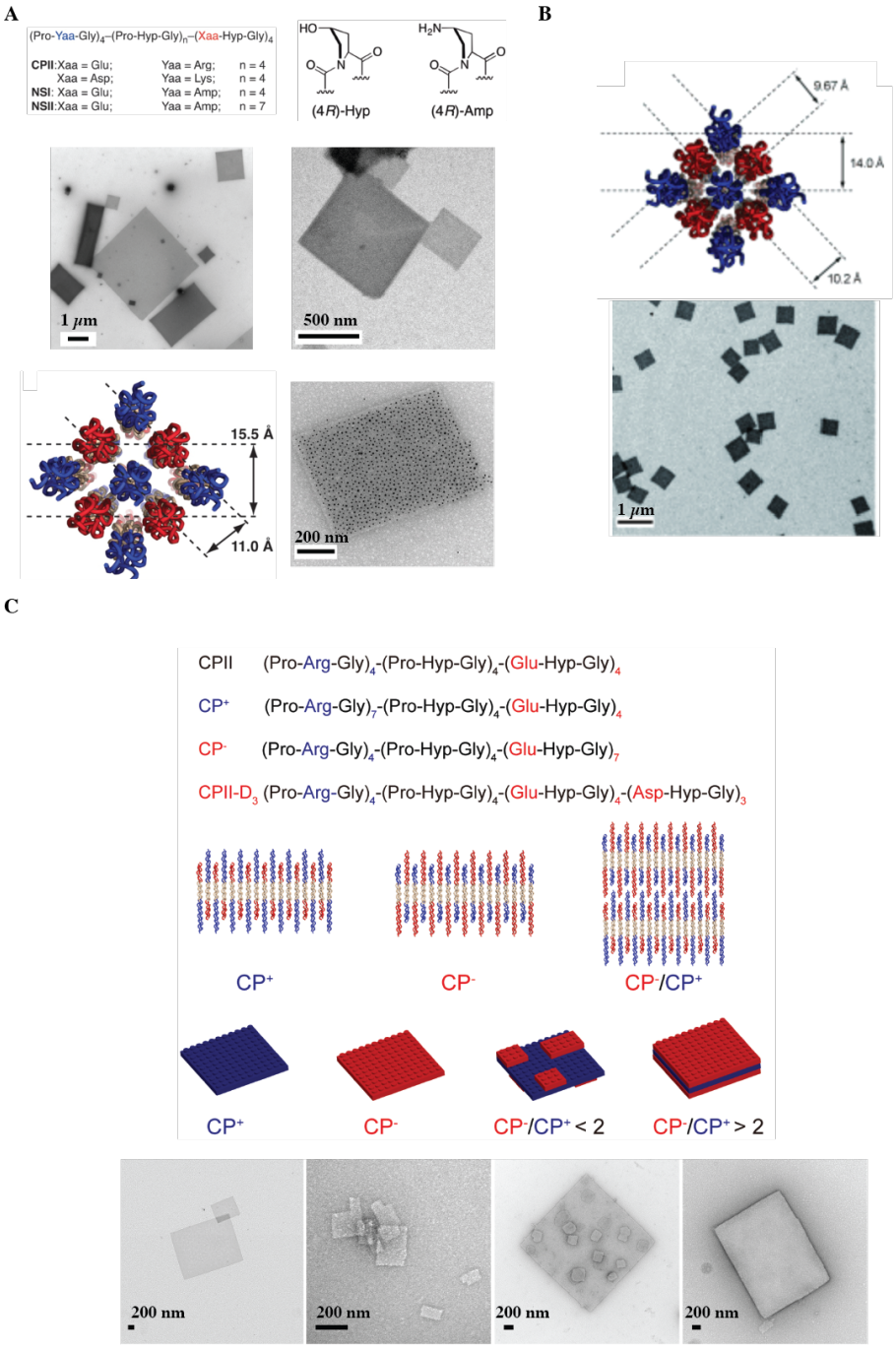

Figure 1.6 Collagen nanosheets stabilized by electrostatic interactions a. sequences of nanosheets formed by NSI and NSII; TEM image of NSI (middle left) and NSII

nanosheets in the absence (middle right) and presence of cationic gold nanoparticles (bottom right); Structural model of NSII nanosheets (bottom left) b. Structural model and TEM image of NSIII nanosheets c. sequences of asymmetrically charged symmetry variants and models for nanosheets formed by a mixture of CP^+ and CP^-; TEM images of CP^+ nanosheets, CP^- nanosheets, mixed nanosheets resulting from a CP^-/CP^+ mixtures from a concentration ratio of 1:5, mature nanosheets formed from a CP^-/CP^+ mixture at a concentration ratio of 2:1

7.4, peptide **H4** assembled into nanodiscs, which frequently extended end-on from the hydrophobic carbon coated copper EM grid (Fig X.9). The nanodiscs were 10 nm thick, equivalent to the length of the CMP, suggesting that the triple helices were oriented perpendicular to the surface of the nanodiscs. The nanodiscs had a range of diameters from 50 nm to 1.0 μm and appeared to be very flexible. Peptides **H2** and **H3**, which contained decreased number of hydrophobic amino acids relative to peptide **H4** assembled into disc-like structures similar to **H4**. Peptide **H3**, which contains three hydrophobic amino acids, was generated by replacement of leucine with proline in the first hydrophobic triplet of **H4**. Peptide **H2** was generated through by replacement of isoleucine with hydroxyproline in the first hydrophobic triplet of **H3**. An increase in the content of hydrophobic triads from two to three hydrophobic triplets led to the sequence pattern *ppphhhpppp*, in which six hydrophobic Leu or Ile amino acids were incorporated to afford peptide **H6**. Interestingly, rather than nanodisks, peptide **H6** forms nanofibers of several microns in length after thermal annealing. One hypothesis the authors had for this unexpected nanofiber formation was misfolding of **H6** into amyloid fibrils due to increasing hydrophobicity. However, **H6** did not bind Congo Red, a common probe for amyloidosis, and the characteristic twisted cross-β structure of amyloid fibers was not observed by TEM. An alternative structural model for **H6** is a helical tape in which triple helices pack at an angle. In this model, the hydrophobic ends of **H6** would be exposed.

Mutagenesis of the first leucine of peptide **H6** to proline afforded peptide **H5**, which is intermediate in hydrophobicity between **H4** and **H6**. TEM revealed that **H5** forms both fibers characteristic of **H6** and nanodiscs characteristic of **H4**. A mixture of peptides **H4** and **H6** results in the formation of peptide nanostars (Figure 1.5b). Peptide nanostars are stabilized through hydrophobic interactions between the edges of **H4** discs and the ends of **H6** fibers (Figure 1.5b). These results indicate that hydrophobic contacts can mediate formation of stable nanostructures in the structural context of the collagen triple helix. Moreover, the relative hydrophobic content can alter the balance between one-dimensional and two-dimensional assemblies through the nature of intermolecular interactions between protomers.

Electrostatic interactions between oppositely charged residues can also be employed to direct the self-assembly of collagen-mimetic peptides into two-dimensional nanostructures. Conticello *et al*. used the previously characterized CMP **CPII** as a basis for the design of peptides **NSI**, **NSII**, and **NSIII** [75,37]. **CPII** formed oriented axial fibrils through electrostatic interactions between triple helices [37]. **CPII** has three domains $(Pro\text{-}Arg\text{-}Gly)_4$- $(Pro\text{-}Hyp\text{-}Gly)_4$-$(Glu\text{-}Hyp\text{-}Gly)_4$. The central hydrophobic block of **CPII** stabilized the triple helical conformation whereas the charged blocks facilitated the linear oligomerization of triple helices within fibrils into a staggered orientation similar to native collagen. Although **CPII** was designed to form fibrils, surprisingly, under most conditions in solution, two-dimensional structures could be observed. Two sequence variants of **CPII**, **NSI** and **NSII**, were designed to bias the creation of layered two-dimensional assemblies through selective interactions between triple helices (Figure 1.6a). The variant **NSI** had the unnatural amino acid (2S,4R)-4-

aminoproline (Amp) in place of arginine in the positively charged block. The stereoelectronic properties of Amp are similar to those of (2S,4R)-4-hydroxyproline in that the pyrrolidine ring adopts a Cγ-exo ring pucker conformation. The variant **NSII** exhibited the same domains as **NSI** with a hydrophobic block lengthened to seven triplets. Since **NSII** deviated from the symmetric triblock architecture of **CPII,** it should be precluded from the formation of fibrils and should favor the formation of sheets. Both peptides formed characteristic triple helical structures by CD; **NSI** had a melting transition of temperature of 32°C while **NSII** exhibited a higher melting transition of 60°C as a consequence of the presence of the additional copies of the stabilizing (Pro-Hyp-Gly) triad in the central block. TEM imaging confirmed the formation of supramolecular structures of **NSI** and **NSII** in solution (Fig X.10). **NSI** and **NSII** both assembled into two-dimensional nanoscale sheets with sharp, well-defined edges. AFM measurements of single layer sheets of **NSI** and **NSII** afforded thicknesses near the length of the respective peptides. In neutral buffered aqueous solution, **NSI** usually formed multilayer sheets, whereas **NSII** typically formed sheets of one or two layers in thickness. The thicker **NSI** nanosheets were more robust to biophysical measurements and characterized further using scanning transmission electron microscopy (STEM) and small angle x-ray scattering (SAXS). Mass per area measurements of **NSI** supported a tetragonal arrangement of triple helices within nanosheets. SAXS and electron diffraction measurements supported the formation of two-dimensional assemblies in solution with a high degree of internal order.

These two-dimensional collagen assemblies can be employed as scaffolds for the presentation of chemical functionality at the surface of the nanosheet. The structural

model for the nanosheet indicates the presence of the N- and C-termini of the peptides at the surface of the assemblies. The **NSII** nanosheets were chosen for use as substrates due to greater thermal stability. Cationic gold nanoparticles (10 nm core diameter functionalized with (11-mercaptoundecyl)-N,N,N-trimethylammonium bromide) were incubated with **NSII** nanosheets. The positively charged ammonium ions attached to the gold nanoparticles interact selectively with the negatively charged carboxylates at the C-termini of the peptides. TEM images revealed that the gold nanoparticles spread out evenly on the surface of the **NSII** nanosheets (Figure 1.6a). To promote a more specific interaction of gold nanoparticles with the surface of the nanosheets, a variant of **NSII**, **NSII***, was synthesized in which the N-terminus was capped with the D-biotin-15-amido-4,7,10,13-tetraoxapentadecyl group (biotin-dPEG$_4$). **NSII*** assembled into nanosheets with similar morphology to **NSII**. The **NSII*** nanosheets bind selectively to streptavidin-tagged gold nanoparticles, whereas the parent **NSI** peptide does not exhibit any binding to streptavidin-tagged gold nanoparticles. The biotin-streptavidin interactions can also be used to immobilize **NSII*** nanosheets on glass surfaces with retention of the nanosheets' morphology [75].

Further work by Conticello *et al*. resulted in the production of nanosheets, which are homogenous both in sheet thickness and lateral dimensions [76]. A sequence variant of **NSI**, **NSIII**, was designed in which the (2S,4R)-4-aminoproline (Amp) residue was replaced with (2S,4S)-4-aminoproline (amp). Amp and amp display opposite preferences for ring puckers of the pyrrolidine side-chain. Amp prefers the Cγ-exo ring pucker, while amp adopts the Cγ-endo ring pucker. Crystallographic analysis indicates that the Xaa and Yaa positions prefer different ring puckers, Cγ-endo and Cγ-exo, respectively. Therefore,

amp was encoded in the Xaa position and, to compensate for this adjustment, the glutamic acid residues were moved to the Yaa position of the **NSIII** sequence. The **NSIII** peptide formed a stable triple helix in solution and assembled into structurally homogenous nanosheets, which exhibited single layer thicknesses, equivalent to the theoretical length of the peptide, and a mean diagonal distance of 679 nm (Figure 1.6b). In contrast to **NSI** nanosheets, the **NSIII** nanosheets exhibited a tetragonal lattice, which is slightly distorted into a pseudotetragonal packing arrangement.

More recently, Conticello *et al*. demonstrated control of the z-dimension or sheet-stacking dimension of collagen-mimetic peptides through the use of asymmetrically charged peptide variants [74]. The peptides **CP^{+}** and **CP^{-}** are based on the **CPII** peptide described previously and contain all natural amino acids, making them promising for future applications. In contrast to **CPII**, **CP^{+}** and **CP^{-}** have extended positively and negatively charged blocks, respectively (Figure 1.6c). **CP^{+}** and **CP^{-}** both formed nanosheets in solution with positive charge localized on the surface of **CP^{+}** and negative charge located on the surface of **CP^{-}**. In contrast to **CP^{+}**, which formed sheets within hours even at dilute peptide concentrations (< 0.2 mg/mL), **CP^{-}** formed nanosheets over a period of months at high peptide concentrations (> 5 mg/mL). The addition of calcium to **CP^{-}** accelerated the rate of self-assembly of **CP^{-}** through coordination of glutamic acid residues on adjacent triple helices. Zeta potential measurements, charged nanoparticle binding assays, electrostatic force microscopy (EFM) were performed on the nanosheet assemblies to determine the charge states of the nanosheet surfaces. These measurements supported the author's model for nanosheet assembly in which positive charge occurs on the surface of **CP^{+}** nanosheets, whereas negative charge occurs on the surface of **CP^{-}**

nanosheets. AFM measurements reveal that the **CP$^+$** and **CP$^-$** peptides formed single layer nanosheets due to the high charge density on the individual nanosheets. Since nanosheets derived from **CP$^+$** and **CP$^-$** have oppositely charged surfaces, interaction may occur to form multi-layer sheets of defined composition. When **CP$^-$** is added to preformed **CP$^+$** nanosheets at a concentration ratio of less than 2:1 (**CP$^-$**: **CP$^+$**), layered structures are observed in which small sheets have grown on the surface of the **CP$^+$** nanosheets (Figure 1.6c). At concentrations greater than 2:1 (**CP$^-$**: **CP$^+$**), the small nanosheets on the surface fuse into a single continuous layer extending over the entire surface of both sides of the **CP$^+$** nanosheet. Atomic force microscopy measurements revealed that these nanosheets are three layers thick, and EFM measurements revealed that these nanosheets have negatively charged surfaces. Electron diffraction measurements of the single-layer and multilayer nanosheets revealed that the 2D lattices were tetragonal. Most importantly, the lattice spacings of the single layer and multiple-layer sheets coincided almost exactly. Therefore, the **CP$^+$** nanosheets can nucleate triple-layer formation and transfer structural information to the nascent nanosheet. Rational design of collagen-mimetic peptides has been used successfully to control several aspects of two-dimensional self-assembly. The sequence motif and ease of self-assembly makes collagen-mimetic peptides promising candidates for the development of functional two-dimensional biomaterials.

1.6 Peptoid Nanosheets

Peptoids, or *N*-substituted glycines, represent a bioinspired building block for two-dimensional materials. In contrast to amino acids, peptoid monomers are achiral and side chains are attached to the amide nitrogen instead of to the α-carbon. Peptoids

represent attractive building blocks for two-dimensional materials because their achirality and lack of hydrogen bond donor allow for simplicity of design. Sequence-specific peptoids are easily synthesized using the solid-phase submonomer method of synthesis [80].

Since peptoids are similar to proteins in primary structure, the rules that govern protein folding can be co-opted to direct rational design of peptoids. In proteins, sequence pattern oftentimes is indicative of secondary structure, and the driving force of folding into tertiary structures is the hydrophobic effect.

A minimalist set of peptoid monomers was used to test the effect of sequence pattern on self-assembly [80]. *N*-(2-phenethyl) glycine (Npe) was used as a nonpolar monomer, and *N*-(2-aminoethyl) glycine (Nae) and *N*-(2-carboxyethyl) glycine (Nce)

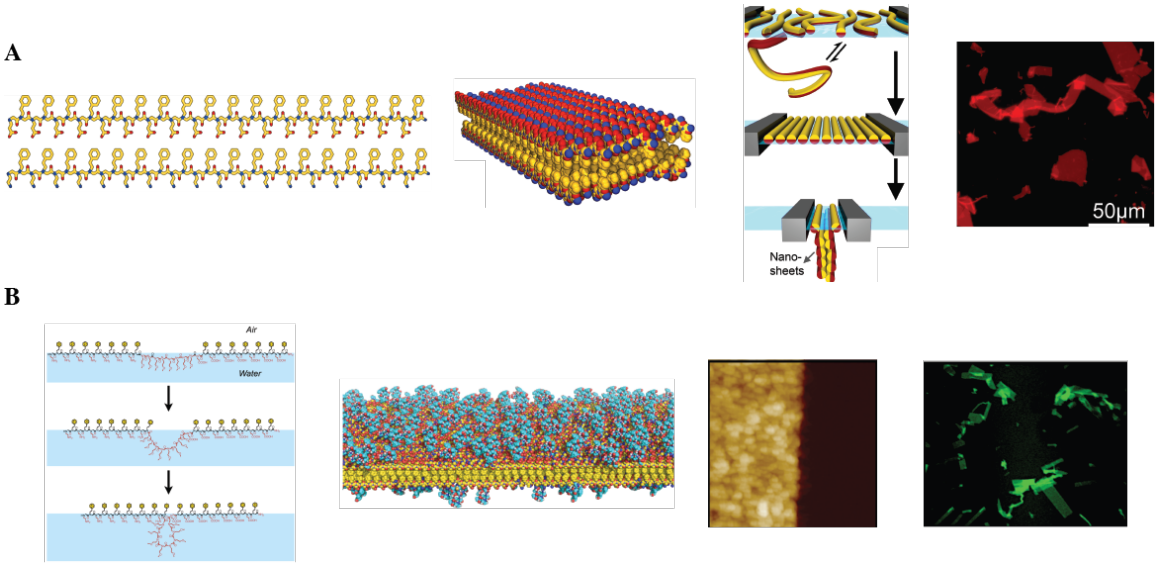

Figure 1.7 Peptoid nanosheets a. Chemical structure of peptoids $(Nae\text{-}Npe)_{18}$ and $(Nce\text{-}Npe)_{12}$, peptoid chain organization within peptoid nanosheets, schematic mechanism for peptoid nanosheet self-assembly through surface compression, and peptoid nanosheets labeled with Nile Red dye (left to right) b. Mechanism of loop formation through compression at air-water interface, structural model for loops on the surface of peptoid nanosheets, AFM image of gold-decorated peptoid nanosheet, immunofluorescence detection of phosphorylated peptoid nanosheets (left to right)[80, 85, 81]

were used as positively and negatively charged building blocks, respectively. Pairs of complementary sequences with two-fold [$(Nae\text{-}Npe)_{18}$ and $(Nce\text{-}Npe)_{18}$], three-fold, [$(Nae\text{-}Npe\text{-}Npe)_{12}$ and $(Nce\text{-}Npe\text{-}Npe)_{12}$], and four-fold [$(Nae\text{-}Npe\text{-}Npe\text{-}Npe)_{9}$ and $(Nce\text{-}Npe\text{-}Npe\text{-}Npe)_{9}$] symmetry were synthesized. Neither the three-fold or four-fold pairs formed well-defined assemblies. However, a 1:1 molar mixture of the two-fold symmetric peptides formed two-dimensional nanostructures (Figure 1.7a). The lengths of the edges of the nanosheets were tens to hundreds of micrometers. Scanning electron microscopy (SEM) revealed that the two opposite sides of the sheets had straight edges whereas the other two sides had rough edges. These images were consistent with a structural model in which the peptoids are aligned in one direction with the sharp edge. Atomic force microscopy measurements revealed that the nanosheets were very flat with thicknesses around 2.7 nm. X-ray diffraction and aberration corrected transmission electron microscopy (TEAM) were used to analyze the molecular structure of the sheets. X-ray diffraction measurements in solution showed that the nanosheets were not stacked but free-floating. TEAM imaging allowed for direct observation of the peptoid chains. The peptoids are ordered along the direction of the sharp edge of the nanosheet. The peptoids are fully extended in an all-*trans* conformation such that charged and hydrophobic side chains are on opposite sides of the peptoid backbone [80].

A range of conditions was investigated to determine the optimal parameters for self-assembly of the nanosheets. Nanosheets formed within a wide pH range between pH 2 and 13 with an optimal pH around 8-9. The nanosheets were observed to be stable in the presence of organic solvents (up to 50 % acetonitrile). To determine whether ionic

interactions or hydrophobic interactions contributed to sheet formation, a series of peptoids were created in which either the ionic groups or hydrophobic groups were replaced with N-(2-methoxyethyl)glycine (Nme). A series of variant peptoids, (Nce-Nme)$_{18}$, (Nae-Nme)$_{18}$, and (Nme-Npe)$_{18}$, were investigated. None of these peptoid variants produced nanosheets, which indicated that both ionic and hydrophobic interactions were required to stabilize the nanosheets. Based on these results, a model for a peptoid bilayer was proposed in which the Npe residues of two peptoid chains face each other to minimize the exposure of this hydrophobic group to aqueous solution. The positively and negatively charged side chains at the water contacting surfaces of the nanosheets interact through electrostatic attraction between complementary charges. The peptoid chains may not be perfectly in register, leaving protruding sticky ends, which allow for growth in two dimensions. The peptoid sheets can be used as scaffolds to display biologically active peptides. The streptavidin biotin binding peptide ligand cyclo-[CHPQFC] was connected to the *N*-terminus of the peptoid [Nae-Npe]$_{18}$ through a hydrophilic linker. A mixture of this modified peptide with the original [Nce-Npe]$_{18}$ resulted in the normal production of nanosheets. The introduction of fluorescently labeled streptavidin (Cy3-streptavidin) resulted in fluorescent nanosheets, demonstrating the technological potential of peptoid nanosheets [80].

Zuckermann and co-workers have investigated the mechanism of formation of these peptoid sheets in aqueous solution [85,86]. Preferential self-assembly occurred under conditions in which the peptoid solution was shaken but not when stirred. Stirring induces significant shear forces, whereas shaking induces shear forces, mixing, and interfacial expansion and contraction. These results suggested that generation of

preparative amounts of nanosheets requires control of intermediates that form at the air-water interface. Self-assembly of nanosheets relied on formation, compression, and collapse of a peptoid monolayer at the air-water interface (Figure 1.7a). The self-assembled peptoid monolayer at the air-water interface was in equilibrium with free peptoid monomers in solution. In the compression step, the surface pressure is increased, which aligned the peptoid chains and promoted close packing. Further compression caused collapse of the monolayer into solution. Nanosheets were formed when two monolayers combined into a bilayer, burying hydrophobic residues [85,86]. Zuckermann *et al*. also investigated the formation of peptoid nanosheets at the oil-water interface [84]. The identity of the nonpolar oil layer determined whether nanosheets could be produced. Short chain aliphatic solvents like pentane, hexane, and heptane all allowed for nanosheet formation while longer alkane molecules such as hexadecane and mineral oil prevented sheet formation. The higher viscosity of longer alkane molecules prevented collapse of the surface monolayer into a bilayer. The aromaticity of benzene and toluene also prevented nanosheet formation due to extensive pi-pi interactions between the solvents and Npe residues [84].

The interfacial mechanism of assembly for peptoid nanosheets can be utilized to introduce a peptide loop on the surface of the sheets (Figure 1.7b) [81]. To determine the potential for loop formation, a single peptoid chain of sequence $(\text{Nae-Npe})_{13}$-$(\text{Nme})_{x}$-$(\text{Nce-Npe})_{13}$ was synthesized. Compression at the air-water interface forced the block of Nme residues to form a loop, thereby maximizing interactions between peptoid chains in the monolayer. Peptoids that comprised sequences in which the number of Nme monomers (x) corresponded to four, eight, or twelve residues formed nanosheets in

solution, which confirmed the hypothesis that self-assembly at the air-water interface can be utilized for loop formation. Zuckermann and co-workers have also demonstrated that peptide loops can replace the Nme block of the nanosheets. One peptoid molecule contained a consensus phosphorylation sequence for casein kinase II (CK2a) within the loop region. Nanosheets containing this protein recognition block formed nanosheets with thicknesses greater than the thicknesses of nanosheets without loop regions, suggesting that the loops were on the surface of the nanosheets. The nanosheets were incubated with CK2a, a kinase, which phosphorylates the serine of the consensus sequence. A FITC-labeled monoclonal antibody was employed to detect the phosphorylated nanosheets through immunofluorescence imaging (Figure 1.7b) [81]. The Nme block of the nanosheets can also be replaced with an inorganic material recognition peptide. Incubation of these modified nanosheets with tetrachloroaurate anion, $[AuCl_4]^-$, resulted in nanosheets with thin metallic gold films on the surface of the assemblies (Figure 1.7b). These results demonstrate that a knowledge of the nanosheet structure combined with insight into the mechanism of nanosheet formation afford the opportunity to design functional nanosheets.

1.7 Peptide Assembly: Boundary Constrained 2D Assembly

Short synthetic peptides can also form two-dimensional assemblies at the air-water interface. The amino acid tyrosine frequently occurs within the self-associating

sequences of amyloidogenic proteins such as β_2-microglobulin, transthyretin, and the

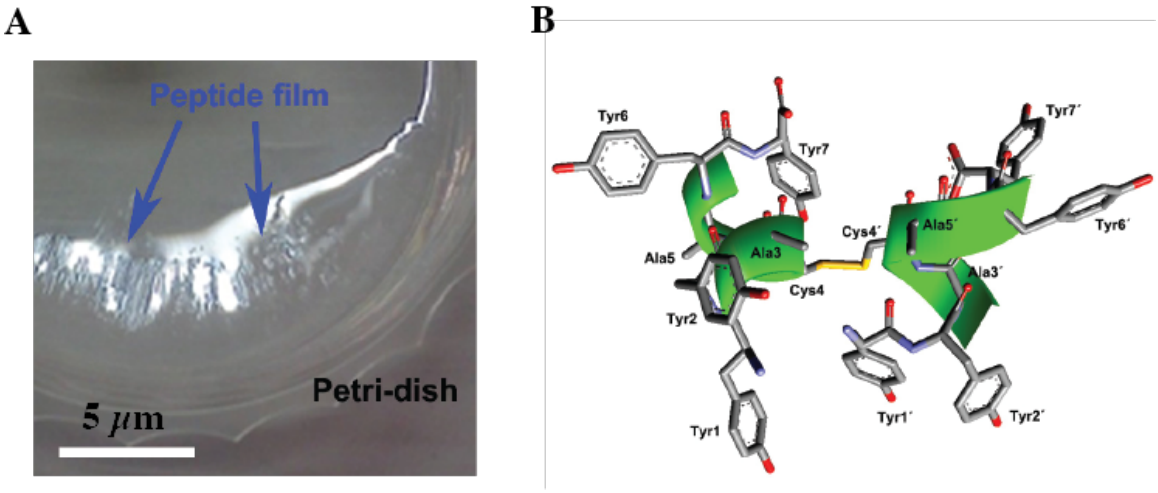

Figure 1.8 Boundary constrained 2D assembly a. Formation of a peptide film on a water droplet b. model for YYACAYY dimer stabilized by a disulfide bond

SUP35 prion. The tyrosine side-chain displays an amphiphilic character due to the phenol substituent. Therefore, folding of tyrosine-rich sequences can result in the formation of stabilizing hydrophobic contacts from interactions between the aromatic rings, while the hydroxyl groups maintain polar interactions at the aqueous interface. The incorporation of multiple tyrosine residues was employed as a design element for the construction of short peptides (5-7 amino acids) that could self-assemble at the air-water interface. Jang, *et al*., designed seventeen oligopeptides containing tyrosine residues at different levels of incorporation and within different sequence contexts [73]. These peptides self-assembled to form supramolecular structures of different morphology, including nanofibrils and nanosheets. Notably, several of the peptides could induce the formation of faceted surfaces on water droplets that contained dissolved monomeric peptide. The mechanism of facet formation was studied in detail for the peptide YYACAYY. Oxidation of the cysteine residue of YYACAYY afforded the disulfide-bonded dimer, which was a prerequisite for the formation of faceted droplets.

A kinetic analysis of the YYACAYY peptide indicated that the highest rate of facet formation occurred at a pH that was closest to the isoelectric point of the peptide (~ 5.5). Detailed structural analysis indicated that facet formation resulted from deposition of a peptide film at the air-water interface (Figure 1.8a). The films could be transferred to a silicon substrate or a carbon grid for AFM and TEM analysis. TEM analysis provided evidence for the presence of 2D assemblies, which grew in the lateral *x-y* dimensions. AFM analysis revealed that the films were flat and consisted of multiple, stacked nanosheets with a height of 1.4 nm, which was confirmed using X-ray diffraction analysis of the films. The sheet thickness of 1.4 nm was postulated to result from packing of a disulfide-bonded YYACAYY dimer in the plane of the nanosheet (Figure 1.8b). The dimer is essential to facet formation, and, when treated with the reducing agent dithiothreitol, the films were observed to break down. Conversely, when the YYACAYY peptide was incubated in the presence of the oxidizing agent, DMSO, the resultant dimer formation enhanced the kinetics of film formation. Circular dichroism spectra and nuclear magnetic resonance spectroscopy indicate that the dimer adopts an α-helical secondary structure whereas the monomer remains unfolded. A model for facet formation involves initial solubilization of the YYACAYY peptide as a monomer, followed by an orientation of the monomer at the air-water interface in which the hydrophobic tyrosine side chains point toward the air, tight lateral interactions between tyrosine side chains, and finally dimerization induced by the oxygen-rich environment at the interface [73].

The nanosheets derived from facet formation at the interface can be used as to mimic enzymatic catalysis. *In situ* generated tyrosyl radicals represent important intermediates that can serve as conduits for electron transfer in biological redox

processes. Electrolytic oxidation of the tyrosyl residues in the YYACAYY peptide films provided a mechanism to facilitate oxidation of pyrrole to the conductive polymer polypyrrole. As a further demonstration, treatment of the YYACAYY peptide films with copper(II) chloride resulted in a supramolecular complex that could mimic the selective redox properties of metallo-enzymes. The metallated film could oxidatively polymerize pyrrole into polypyrrole. In contrast, solutions of copper(I) or copper(II) cations in the presence of monomeric tyrosine were not active for pyrrole oxidation. Thus, the self-assembly of the structured thin films proved critical to the development of emergent reactivity [73].

1.8 Protein assemblies: metal-stabilized cytochrome c 1D, 2D, and 3D assemblies

Tezcan, *et al*., shows that metal-ion coordination may be used to stabilize 1D, 2D, and 3D assemblies of mutant derivatives of the protein cytochrome (cyt) cb 562 [64]. Using the computational design program Rosetta, a variant of (cyt) cb 562 was produced called **RIDC3 [91]**. The variant protein contains polar residues on its surface, which allow for highly specific interactions between protein molecules. **RIDC3** contains low-affinity and high-affinity zinc-binding sites. The high-affinity binding site comprises His73 and His77 from one monomer and His63 from the other monomer, while the *N*-terminal alanine and Glu39 comprise the low-affinity binding site. Zinc coordination vectors in the high-affinity site are perpendicular to each other, and the authors postulate that these orthogonal zinc coordination vectors may promote assembly in two dimensions [64]. Zinc binding stabilizes a C_2-symmetric dimer. In addition to the zinc binding sites, small hydrophobic amino acids line the dimeric interface, which enhanced the stability of

the dimer.

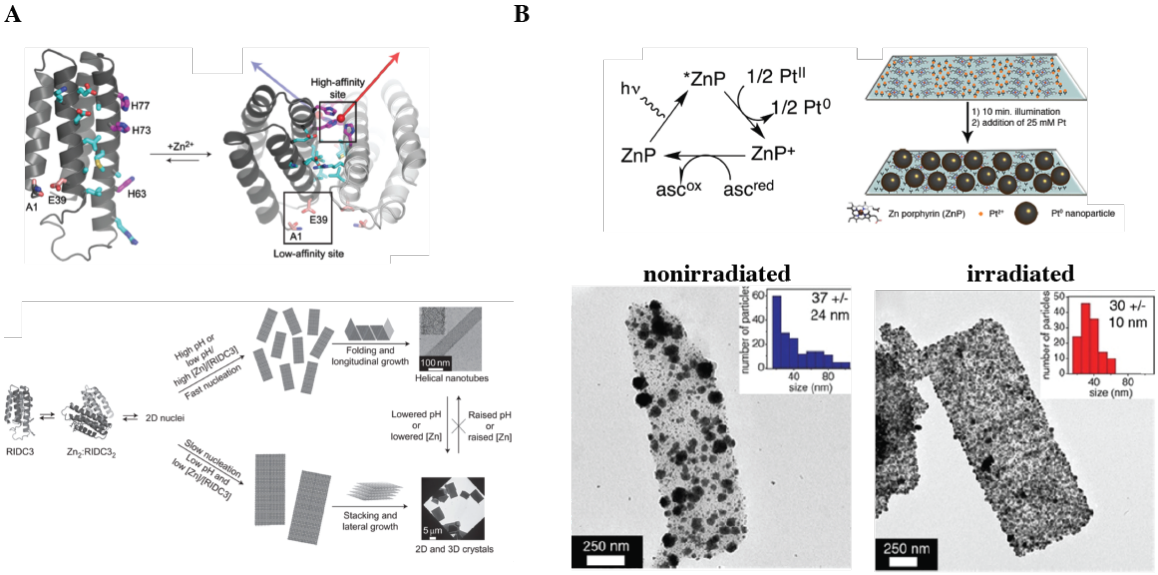

Figure 1.9 Metal-stabilized cytochrome assemblies (a) Conversion of RIDC3 monomer into C2-symmetric dimer through addition of zinc; high affinity and low affinity zinc coordination sites where high affinity coordination vectors are orthogonal to each other; assembly mechanism (bottom) depicts formation of helical nanotubes through folding and longitudinal growth of 2D sheets; 2D crystal formation at low pH and ratios of Zn: RIDC3; 3D crystal formation through stacking of 2D sheets (b) Photocatalytic cycle for reduction of Pt^{2+} to Pt^{0} by ZnP on the surface of RIDC3; Scheme for redox-mediated growth of platinum nanoparticles on the ZnP-RIDC3 arrays (top right); TEM images of nonirradiated (bottom left) and irradiated ZnP-RIDC3 arrays (bottom right) showing a nonuniform distribution of PtNPs and uniform coverage of the RIDC3 surface with PtNPs, respectively; Reprinted with permission from [64, 65]

In solution, Tezcan et al. observed assemblies of **RIDC3**, whose morphology was dependent on both the concentration of zinc and the pH of the solution. At high pH or at high concentrations of zinc, the high-affinity zinc-binding sites are fully deprotonated, and nucleation is rapid, resulting in 1D helical nanotube formation. At pH 5.5, where the high-affinity zinc-binding sites are partially protonated, nucleation is slow, and large 2D sheets are formed. In order to determine the structural basis of self-assembly, 3D arrays of **RIDC3** were grown for X-ray diffraction analysis. Based on the fact that 2D

assemblies preferentially form at slow nucleation rates and 1D assemblies preferentially form at higher nucleation rates, the authors hypothesized that 3D assemblies would form at even slower nucleation rates than 2D assemblies. Large 3D assemblies formed in an aqueous buffered solution containing 2-(bis-(2-hydroxyethyl)-amino)-2-hydroxymethylpropane-1,3-diol (bis-Tris). At pH 5.5, the high-affinity zinc binding sites are partially protonated and therefore zinc coordination is in competition with protonation of the histidine residues. Furthermore, the bis-Tris buffer can also coordinate zinc, lowering the available concentration of zinc in the solution, and allowing three-dimensional growth of **RIDC3** under slow nucleation conditions [64].

X-ray diffraction measurements of the **RIDC3** crystals reveal that the three dimensional arrays are produced through stacking of two-dimensional **RIDC3** sheets. Three different zinc coordination environments are involved in stabilizing the two-dimensional assemblies along the c and b crystallographic axes. The perpendicular zinc coordination vectors from the high affinity zinc-coordination sites stabilize two-dimensional growth in the b-c layer. Along the c-axis, RIDC3 dimers connect through interaction between Zn1 in a high-affinity site and Glu81. Along the b-axis, RIDC3 dimers connect head to tail through Zn2 in a high-affinity site and Glu49. A third zinc ion, Zn3, is bound to a low-affinity site interacts with a second Glu49 allowing the formation of a 2D array (Figure 1.9a).

Interestingly, the 1D nanotubes observed at high pH or high zinc concentration can also result from the nanosheets when curvature is induced along the two-dimensional lattice. In contrast to the 2D nanosheets, the Zn3 interface must bend and twist to transform the nanosheets into nanotubes. The research of Tezcan, *et al*., highlights the

importance of understanding the structure of two-dimensional assemblies, since they represent intermediates between one-dimensional and three-dimensional structures. Manipulation of the interfacial interactions between protomers can be employed as a mechanism to control the morphology of the resultant assemblies. Furthermore, it demonstrates the utility of computational methods to the rational design of supramolecular assemblies, including nanotubes and nanosheets.

In nanomaterial creation, it is necessary that the designed nanomaterials form well-defined structures with potential function for use in materials applications, i.e., as nanoarchitectonic scaffolds. In recent work, Tezcan, *et al.,* demonstrated the exceptional stability of the **RIDC3** 1D nanotubes and 2D arrays and showed that these supramolecular structures can be used as templates for the growth of platinum nanoparticles [65]. The 1D nanotubes and 2D **RIDC3** assemblies can be prepared in large quantities through careful control of their environments. At pH 5.5, the addition of 100 equivalents of Zn^{2+} results in immediate formation of 1D nanotubes while the addition of 10 molar excess Zn^{2+} results in 2D-arrays. While the parent 2D lattice (single protein sheet) contains 1.5 Zn^{2+} moieties/ monomer, the 1D nanotubes and 2D arrays contain higher amounts of associated zinc, which suggested that zinc coordinates to surface aspartic acid and glutamic acid residues. Furthermore, the thickness of flattened 1D nanotubes is close to the thickness of two-single layered sheets whereas the 2D-arrays are made up of between 5 and 20 layers of nanosheets. These metal-stabilized architectures are stable under conditions of temperature and solvent composition that denature the uncomplexed soluble protein subunits. The 1D and 2D assemblies are stable at temperatures up to 80 °C. Under these conditions, the 1D nanotubes converted

quantitatively to 2D-arrays after five hours, possibly due to higher thermal stability of the 2D-arrays compared to the nanotubes. Both 1D and 2D assemblies are stable in polar organic solvents, such as DMF and methanol.

Since the parent protein of **RIDC3**, cyt cb_{562}, uses its iron-porphyrin cofactor to participate in electron transfer reactions, the protein **RIDC3** was also hypothesized to be redox-active. The redox-active properties of **RIDC3** can be used to facilitate the growth of platinum nanoparticles on the assemblies through coordination of platinum to surface aspartic acid and glutamic acid residues. When one-dimensional and two-dimensional RIDC3 assemblies are incubated with platinum (Pt^{2+}) overnight at room temperature and subsequently reduced with ascorbate, TEM images reveal that the surfaces of the 1D nanotubes and 2D arrays have attached dendritic platinum nanoparticles (Pt^{o}). Since the thermostability of the two-dimensional arrays improved with overnight incubation of Pt^{2+}, the assemblies were incubated with Pt^{2+} at 99°C. Subsequent TEM images revealed single platinum nanoparticles on the surface of the assemblies (Figure 1.9b). In contrast, in the absence of one-dimensional or two-dimensional **RIDC3** templates, large amorphous platinum aggregates were formed.

In an attempt to gain better control of platinum nanoparticle formation and determine the role of the iron-porphyrin cofactor in nanoparticle growth, the iron porphyrin cofactor of **RIDC3** was replaced with a zinc porphyrin cofactor. The zinc-porphyrin cofactor is redox-inactive in its ground state, but exhibits strong reductant/oxidant properties upon excitation with UV-visible light. The **ZnP-RIDC3** protein assembled into the same two-dimensional arrays as its **FeP-RIDC3** parent protein. When **ZnP-RIDC3** is irradiated and incubated with platinum, platinum

nanoparticles with a tight size distribution are observed immediately. In contrast, when **ZnP-RIDC3** is incubated with platinum but not exposed to light, there is a two-hour lag phase preceding nanoparticle growth, and the nanoparticles have a broad size distribution. For the parent **FeP-RIDC3** assemblies, light exposure did not affect the growth of platinum nanoparticles, however the growth kinetics were significantly faster than the non-irradiated **ZnP-RIDC3** assemblies. These results suggest that the iron-porphyrin cofactor of RIDC3 acts as a redox conduit between ascorbate and Pt^{2+} ions. Furthermore, since the excited state of **ZnP-RIDC3** is a better reductant than **Fe-RIDC3**, the excited state generates platinum nanoparticles on the surface of the **RIDC3** assemblies more efficiently [65]. The work of Tezcan et al. provides another example of the use of metal-ion coordination to control two-dimensional self-assembly.

1.9 Protein Assemblies: Protein Fusion Strategies

Fusion of two distinct protein subunits that are independently capable of forming discrete oligomers has become a useful strategy for the creation of supramolecular protein assemblies [92-95], including highly ordered two-dimensional sheets. Sinclair, *et al*, reported a class of fusion proteins that they designated "crysalins", which were capable of self-assembly into one- or two-dimensional protein lattices through formation of multi-subunit protein assemblies. These assemblies were designed such that the subunits incorporate rotational symmetry axes of equal order [88]. The protein subunits were chosen such that their *N*- and *C*-termini were located near the rotational symmetry axis and, therefore, were accessible for fusion (Figure 1.10a). The most successful example of this approach involved fusion of the Streptag I peptide to the *C*-terminus of the fourfold symmetric protein aminolevulinic acid dehydrogenase (ALAD) through a

linker. The addition of streptavidin resulted in the formation of 2D lattices with crystalline order to a resolution of at least 18 Å on the basis of TEM image analysis (Figure 1.10a). Similarly, fusion of ALAD to a heteromeric pair of coiled-coil peptides (Lac21E and Lac21K) resulted in the formation of an ordered two-dimensional protein lattice upon mixing of the charge-complementary fusion peptides [88,96].

1.10 Protein Assemblies: Computational Design of 2D Assemblies

Baker, *et al*., reported the production of a proteinaceous two-dimensional array with internal pores through computational design [78]. These researchers hypothesized that a protein with C_3, C_4, or C_6 rotational symmetry would enable easy tiling of a two-dimensional protein pattern. Additionally, a protein with smooth surfaces would be

advantageous for the construction of nanosheets for applications as scaffolds. Proteins of

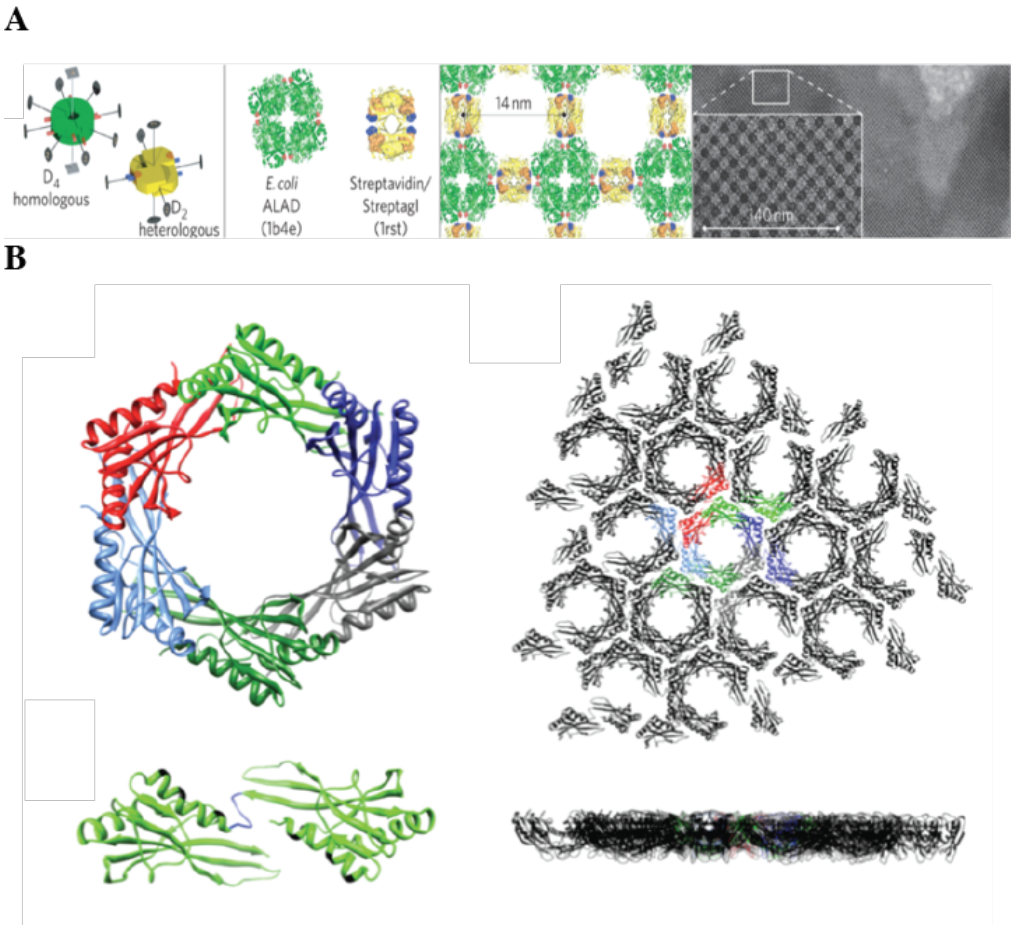

Figure 1.10 Protein assemblies formed using protein fusion and computational design strategies (a) Rotational symmetry axes of *Escherichia coli* ALAD (green) and streptavidin (yellow), structure of *Escherichia coli* ALAD (green) and streptavidin/Streptag I complex (yellow), formation of a two-dimensional lattice of ALAD/Streptag I and streptavidin with 14 nm between adjacent protomers, TEM image of 2D lattice containing ALAD/Streptag I and Streptavidin (b) Ribbon structure of wild type STM4215, ribbon structure of TTM dimer linked by a flexible linker, top view of expected hexagonal tiling pattern of TTM dimers which are shown in different colors, side view of expected hexagonal tiling pattern of TTM dimers

this type would permit the introduction of binding peptides into the flexible loops, which would be presented on the surfaces of the corresponding nanosheet. Furthermore, a protein with termini oriented such that the *N*-terminus of one oligomer can be fused to the *C*-terminus of another oligomer through a linker would enable the creation of a well-

ordered two-dimensional lattice. The Protein Data Bank was evaluated to find a protein with these characteristics, and Rosetta's symmetric docking was run on models meeting these criteria. The protein STM4215 from *S. typhimurium* was utilized for 2D array generation, because it met the aforementioned criteria (Figure 1.10b). Although the function of STM4215 is unknown, the crystal structure of STM4215 revealed that the protein is a homohexamer that defines a central pore of three nanometers in diameter. Each subunit in the homohexamer coordinates a Ca^{2+} ion through three reduced cysteines. The 19 C-terminal amino acids of STM4215 were not resolved and thus flexible. Therefore, these amino acids were eliminated, producing the protomer "**T**". Using the Rosetta software suite, interfacial mutations were made to eliminate steric hindrance and charge repulsion and therefore optimize tight packing between hexamers. This monomer was called **TM**. Further, Baker et al. introduced a hexaglycine linker, which could be used to join two "TM" monomers in a head to tail fashion. The hexaglycine linker allowed connections between homohexamers into a two-dimensional array, while precluding linkage between two subunits of the same hexamer. The resultant dimer was called **TTM**.

Since STM4215 contained the attached ligand calcium (II), calcium (II) was added to a solution of **TTM**. Calcium addition triggered nanosheet formation in solution. Fluorescence microscopy images revealed polydisperse particles between 1 and 10 μm and occasional large thin nanosheets that were greater than 100 μm in length. Native proteins rarely form structures with long-range order within this size regime. Therefore, computational design represents a very promising for the construction of protein-based

two-dimensional nanoarchitectonics, particularly in cases in which the tiling of protomers can match the symmetry of permissible plane groups [97].

1.11 Conclusions and outlook

As discussed above, significant progress has been achieved over the last decade in the construction of structurally defined two-dimensional assemblies derived from peptides, proteins, and structurally related foldamers. A variety of non-covalent interactions have been introduced into peptide and protein sequences in order to promote nanosheet formation. The most promising approaches have focused on the incorporation of electrostatically complementary interactions and metal ion coordination. Often, these directed interactions are supplemented with packing of hydrophobic side chains at interfaces between protomers. Computational approaches permit optimization of the hydrophobic packing interactions with consequent stabilization of the interfaces. Moreover, orthogonal functionality can be introduced into the assemblies through chemical modification or the incorporation of prosthetic groups. These modifications promote novel modes of chemical reactivity, which should enhance the potential for fabrication of complex multi-functional nano-materials (i.e., the nanoarchitectonic approach). These hybrid materials may find uses in tissue engineering or in electronics applications, in which the robustness and structural specificity of the peptide/protein may be useful to create complex functional interfaces.

In the following chapters, a new method is utilized to develop α-helix based two-dimensional assemblies. In order to make these nanosheets appropriate for nanoarchitectonics, the internal structure and forces, which stabilize these nanosheets are investigated.

1.12 References Uncategorized References

1. Egelman EH, Francis N, DeRosier DJ (1982) F-actin is a helix with a random variable twist. Nature 298 (5870):131-135
2. Galkin VE, Orlova A, Vos MR, Schroder GF, Egelman EH (2015) Near-atomic resolution for one state of F-actin. Structure 23 (1):173-182. doi:10.1016/j.str.2014.11.006
3. Prockop DJ, Fertala A (1998) The collagen fibril: the almost crystalline structure. J Struct Biol 122 (1-2):111-118. doi:10.1006/jsbi.1998.3976
4. Anzini P, Xu C, Hughes S, Magnotti E, Jiang T, Hemmingsen L, Demeler B, Conticello VP (2013) Controlling self-assembly of a peptide-based material via metal-ion induced registry shift. J Am Chem Soc 135 (28):10278-10281. doi:10.1021/ja404677c
5. Dong H, Paramonov SE, Hartgerink JD (2008) Self-assembly of alpha-helical coiled coil nanofibers. J Am Chem Soc 130 (41):13691-13695. doi:10.1021/ja8037323
6. Dublin SN, Conticello VP (2008) Design of a selective metal ion switch for self-assembly of peptide-based fibrils. J Am Chem Soc 130 (1):49-51. doi:10.1021/ja0775016
7. Kojima S, Kuriki Y, Yoshida T, Yazaki K, Miura K-i (1997) Fibril Formation by an Amphipathic .ALPHA.-Helix-Forming Polypeptide Produced by Gene Engineering. Proceedings of the Japan Academy 73 (1):7-11. doi:10.2183/pjab.73.7
8. Ogihara NL, Ghirlanda G, Bryson JW, Gingery M, DeGrado WF, Eisenberg D (2001) Design of three-dimensional domain-swapped dimers and fibrous oligomers. Proc Natl Acad Sci U S A 98 (4):1404-1409. doi:10.1073/pnas.98.4.1404
9. Pandya MJ, Spooner GM, Sunde M, Thorpe JR, Rodger A, Woolfson DN (2000) Sticky-end assembly of a designed peptide fiber provides insight into protein fibrillogenesis. Biochemistry 39 (30):8728-8734
10. Papapostolou D, Smith AM, Atkins ED, Oliver SJ, Ryadnov MG, Serpell LC, Woolfson DN (2007) Engineering nanoscale order into a designed protein fiber. Proc Natl Acad Sci U S A 104 (26):10853-10858. doi:10.1073/pnas.0700801104
11. Potekhin SA, Melnik TN, Popov V, Lanina NF, Vazina AA, Rigler P, Verdini AS, Corradin G, Kajava AV (2001) De novo design of fibrils made of short alpha-helical coiled coil peptides. Chem Biol 8 (11):1025-1032
12. Ryadnov MG, Woolfson DN (2003) Introducing branches into a self-assembling peptide fiber. Angew Chem Int Ed Engl 42 (26):3021-3023. doi:10.1002/anie.200351418
13. Ryadnov MG, Woolfson DN (2003) Engineering the morphology of a self-assembling protein fibre. Nat Mater 2 (5):329-332. doi:10.1038/nmat885
14. Wagner DE, Phillips CL, Ali WM, Nybakken GE, Crawford ED, Schwab AD, Smith WF, Fairman R (2005) Toward the development of peptide nanofilaments and nanoropes as smart materials. Proc Natl Acad Sci U S A 102 (36):12656-12661. doi:10.1073/pnas.0505871102
15. Zimenkov Y, Conticello VP, Guo L, Thiyagarajan P (2004) Rational design of a nanoscale helical scaffold derived from self-assembly of a dimeric coiled coil motif. Tetrahedron 60 (34):7237-7246. doi:http://dx.doi.org/10.1016/j.tet.2004.06.068
16. Zimenkov Y, Dublin SN, Ni R, Tu RS, Breedveld V, Apkarian RP, Conticello VP (2006) Rational design of a reversible pH-responsive switch for peptide self-assembly. J Am Chem Soc 128 (21):6770-6771. doi:10.1021/ja0605974

17. Aggeli A, Bell M, Boden N, Keen JN, Knowles PF, McLeish TC, Pitkeathly M, Radford SE (1997) Responsive gels formed by the spontaneous self-assembly of peptides into polymeric beta-sheet tapes. Nature 386 (6622):259-262. doi:10.1038/386259a0
18. Aggeli A, Bell M, Carrick LM, Fishwick CW, Harding R, Mawer PJ, Radford SE, Strong AE, Boden N (2003) pH as a trigger of peptide beta-sheet self-assembly and reversible switching between nematic and isotropic phases. J Am Chem Soc 125 (32):9619-9628. doi:10.1021/ja021047i
19. Aggeli A, Nyrkova IA, Bell M, Harding R, Carrick L, McLeish TC, Semenov AN, Boden N (2001) Hierarchical self-assembly of chiral rod-like molecules as a model for peptide beta -sheet tapes, ribbons, fibrils, and fibers. Proc Natl Acad Sci U S A 98 (21):11857-11862. doi:10.1073/pnas.191250198
20. Bowerman CJ, Liyanage W, Federation AJ, Nilsson BL (2011) Tuning beta-sheet peptide self-assembly and hydrogelation behavior by modification of sequence hydrophobicity and aromaticity. Biomacromolecules 12 (7):2735-2745. doi:10.1021/bm200510k
21. Dong H, Paramonov SE, Aulisa L, Bakota EL, Hartgerink JD (2007) Self-assembly of multidomain peptides: balancing molecular frustration controls conformation and nanostructure. J Am Chem Soc 129 (41):12468-12472. doi:10.1021/ja072536r
22. Janek K, Behlke J, Zipper J, Fabian H, Georgalis Y, Beyermann M, Bienert M, Krause E (1999) Water-soluble beta-sheet models which self-assemble into fibrillar structures. Biochemistry 38 (26):8246-8252. doi:10.1021/bi990510+
23. Marini DM, Hwang W, Lauffenburger DA, Zhang S, Kamm RD (2002) Left-Handed Helical Ribbon Intermediates in the Self-Assembly of a β -Sheet Peptide. Nano Letters 2 (4):295-299. doi:10.1021/nl015697g
24. Matsumura S, Uemura S, Mihara H (2004) Fabrication of nanofibers with uniform morphology by self-assembly of designed peptides. Chemistry 10 (11):2789-2794. doi:10.1002/chem.200305735
25. Zhang S, Holmes T, Lockshin C, Rich A (1993) Spontaneous assembly of a self-complementary oligopeptide to form a stable macroscopic membrane. Proc Natl Acad Sci U S A 90 (8):3334-3338
26. Swanekamp RJ, DiMaio JT, Bowerman CJ, Nilsson BL (2012) Coassembly of enantiomeric amphipathic peptides into amyloid-inspired rippled beta-sheet fibrils. J Am Chem Soc 134 (12):5556-5559. doi:10.1021/ja301642c
27. Nagarkar RP, Hule RA, Pochan DJ, Schneider JP (2008) De novo design of strand-swapped beta-hairpin hydrogels. J Am Chem Soc 130 (13):4466-4474. doi:10.1021/ja710295t
28. Pochan DJ, Schneider JP, Kretsinger J, Ozbas B, Rajagopal K, Haines L (2003) Thermally reversible hydrogels via intramolecular folding and consequent self-assembly of a de novo designed peptide. J Am Chem Soc 125 (39):11802-11803. doi:10.1021/ja0353154
29. Schneider JP, Pochan DJ, Ozbas B, Rajagopal K, Pakstis L, Kretsinger J (2002) Responsive hydrogels from the intramolecular folding and self-assembly of a designed peptide. J Am Chem Soc 124 (50):15030-15037
30. Choo DW, Schneider JP, Graciani NR, Kelly JW (1996) Nucleated Antiparallel β -Sheet That Folds and Undergoes Self-Assembly: A Template Promoted Folding Strategy

toward Controlled Molecular Architectures. Macromolecules 29 (1):355-366. doi:10.1021/ma950703e
31. Cejas MA, Kinney WA, Chen C, Leo GC, Tounge BA, Vinter JG, Joshi PP, Maryanoff BE (2007) Collagen-related peptides: self-assembly of short, single strands into a functional biomaterial of micrometer scale. J Am Chem Soc 129 (8):2202-2203. doi:10.1021/ja066986f
32. Cejas MA, Kinney WA, Chen C, Vinter JG, Almond HR, Jr., Balss KM, Maryanoff CA, Schmidt U, Breslav M, Mahan A, Lacy E, Maryanoff BE (2008) Thrombogenic collagen-mimetic peptides: Self-assembly of triple helix-based fibrils driven by hydrophobic interactions. Proc Natl Acad Sci U S A 105 (25):8513-8518. doi:10.1073/pnas.0800291105
33. Kar K, Ibrar S, Nanda V, Getz TM, Kunapuli SP, Brodsky B (2009) Aromatic interactions promote self-association of collagen triple-helical peptides to higher-order structures. Biochemistry 48 (33):7959-7968. doi:10.1021/bi900496m
34. Koide T, Homma DL, Asada S, Kitagawa K (2005) Self-complementary peptides for the formation of collagen-like triple helical supramolecules. Bioorg Med Chem Lett 15 (23):5230-5233. doi:10.1016/j.bmcl.2005.08.041
35. O'Leary LE, Fallas JA, Hartgerink JD (2011) Positive and negative design leads to compositional control in AAB collagen heterotrimers. J Am Chem Soc 133 (14):5432-5443. doi:10.1021/ja111239r
36. Przybyla DE, Perez CMR, Gleaton J, Nandwana V, Chmielewski J (2013) Hierarchical Assembly of Collagen Peptide Triple Helices into Curved Disks and Metal Ion-Promoted Hollow Spheres. J Am Chem Soc 135 (9):3418-3422. doi:DOI 10.1021/ja307651e
37. Rele S, Song YH, Apkarian RP, Qu Z, Conticello VP, Chaikof EL (2007) D-periodic collagen-mimetic microfibers. J Am Chem Soc 129 (47):14780-14787. doi:DOI 10.1021/ja0758990
38. Xu F, Li J, Jain V, Tu RS, Huang Q, Nanda V (2012) Compositional Control of Higher Order Assembly Using Synthetic Collagen Peptides. J Am Chem Soc 134 (1):47-50. doi:10.1021/ja2077894
39. Yamazaki CM, Asada S, Kitagawa K, Koide T (2008) Artificial collagen gels via self-assembly of de novo designed peptides. Biopolymers 90 (6):816-823. doi:10.1002/bip.21100
40. Kotch FW, Raines RT (2006) Self-assembly of synthetic collagen triple helices. Proc Natl Acad Sci U S A 103 (9):3028-3033. doi:10.1073/pnas.0508783103
41. Lanci CJ, MacDermaid CM, Kang SG, Acharya R, North B, Yang X, Qiu XJ, DeGrado WF, Saven JG (2012) Computational design of a protein crystal. Proc Natl Acad Sci U S A 109 (19):7304-7309. doi:10.1073/pnas.1112595109
42. Briegel A, Wong ML, Hodges HL, Oikonomou CM, Piasta KN, Harris MJ, Fowler DJ, Thompson LK, Falke JJ, Kiessling LL, Jensen GJ (2014) New insights into bacterial chemoreceptor array structure and assembly from electron cryotomography. Biochemistry 53 (10):1575-1585. doi:10.1021/bi5000614
43. Vasa S, Lin L, Shi C, Habenstein B, Riedel D, Kuhn J, Thanbichler M, Lange A (2015) beta-Helical architecture of cytoskeletal bactofilin filaments revealed by solid-state NMR. Proc Natl Acad Sci U S A 112 (2):E127-136. doi:10.1073/pnas.1418450112

44. Gundelfinger ED, Boeckers TM, Baron MK, Bowie JU (2006) A role for zinc in postsynaptic density asSAMbly and plasticity? Trends Biochem Sci 31 (7):366-373. doi:10.1016/j.tibs.2006.05.007
45. Knight MJ, Joubert MK, Plotkowski ML, Kropat J, Gingery M, Sakane F, Merchant SS, Bowie JU (2010) Zinc binding drives sheet formation by the SAM domain of diacylglycerol kinase delta. Biochemistry 49 (44):9667-9676. doi:10.1021/bi101261x
46. Baron MK, Boeckers TM, Vaida B, Faham S, Gingery M, Sawaya MR, Salyer D, Gundelfinger ED, Bowie JU (2006) An architectural framework that may lie at the core of the postsynaptic density. Science 311 (5760):531-535. doi:10.1126/science.1118995
47. Ariga K, Ji QM, Hill JP, Bando Y, Aono M (2012) Forming nanomaterials as layered functional structures toward materials nanoarchitectonics. Npg Asia Mater 4. doi:ARTN e17
DOI 10.1038/am.2012.30
48. Avinash MB, Govindaraju T (2014) Nanoarchitectonics of biomolecular assemblies for functional applications. Nanoscale 6 (22):13348-13369. doi:DOI 10.1039/c4nr04340e
49. Govindaraju T, Avinash MB (2012) Two-dimensional nanoarchitectonics: organic and hybrid materials. Nanoscale 4 (20):6102-6117. doi:DOI 10.1039/c2nr31167d
50. Messner P, Pum D, Sleytr UB (1986) Characterization of the ultrastructure and the self-assembly of the surface layer of Bacillus stearothermophilus strain NRS 2004/3a. J Ultrastruct Mol Struct Res 97 (1-3):73-88
51. Taylor KS, Lou MZ, Chin TM, Yang NC, Garavito RM (1996) A novel, multilayer structure of a helical peptide. Protein Sci 5 (3):414-421
52. Ogihara NL, Weiss MS, Degrado WF, Eisenberg D (1997) The crystal structure of the designed trimeric coiled coil coil-VaLd: implications for engineering crystals and supramolecular assemblies. Protein Sci 6 (1):80-88. doi:10.1002/pro.5560060109
53. Vasudev PG, Shamala N, Balaram P (2008) Nucleation, growth, and form in crystals of peptide helices. J Phys Chem B 112 (4):1308-1314. doi:10.1021/jp077231d
54. Patterson WR, Anderson DH, DeGrado WF, Cascio D, Eisenberg D (1999) Centrosymmetric bilayers in the 0.75 A resolution structure of a designed alpha-helical peptide, D,L-Alpha-1. Protein Sci 8 (7):1410-1422. doi:10.1110/ps.8.7.1410
55. Sleytr UB, Egelseer EM, Ilk N, Pum D, Schuster B (2007) S-Layers as a basic building block in a molecular construction kit. Febs J 274 (2):323-334. doi:10.1111/j.1742-4658.2006.05606.x
56. Sleytr UB, Huber C, Ilk N, Pum D, Schuster B, Egelseer EM (2007) S-layers as a tool kit for nanobiotechnological applications. FEMS Microbiol Lett 267 (2):131-144
57. Weiss MS, Anderson DH, Raffioni S, Bradshaw RA, Ortenzi C, Luporini P, Eisenberg D (1995) A cooperative model for receptor recognition and cell adhesion: evidence from the molecular packing in the 1.6-A crystal structure of the pheromone Er-1 from the ciliated protozoan Euplotes raikovi. Proc Natl Acad Sci U S A 92 (22):10172-10176
58. Anderson DH, Weiss MS, Eisenberg D (1996) A challenging case for protein crystal structure determination: the mating pheromone Er-1 from Euplotes raikovi. Acta Crystallogr D Biol Crystallogr 52 (Pt 3):469-480. doi:10.1107/S0907444995014235
59. Baranova E, Fronzes R, Garcia-Pino A, Van Gerven N, Papapostolou D, Pehau-Arnaudet G, Pardon E, Steyaert J, Howorka S, Remaut H (2012) SbsB structure and

lattice reconstruction unveil Ca2+ triggered S-layer assembly. Nature 487 (7405):119-122. doi:10.1038/nature11155
60. Pum D, Weinhandl M, Hodl C, Sleytr UB (1993) Large-Scale Recrystallization of the S-Layer of Bacillus-Coagulans E38-66 at the Air-Water-Interface and on Lipid Films. J Bacteriol 175 (9):2762-2766
61. Prive GG, Anderson DH, Wesson L, Cascio D, Eisenberg D (1999) Packed protein bilayers in the 0.90 angstrom resolution structure of a designed alpha helical bundle. Protein Sci 8 (7):1400-1409
62. Pum D, Toca-Herrera JL, Sleytr UB (2013) S-Layer Protein Self-Assembly. Int J Mol Sci 14 (2):2484-2501. doi:DOI 10.3390/ijms14022484
63. Sleytr UB, Schuster B, Egelseer EM, Pum D (2014) S-layers: principles and applications. Fems Microbiol Rev 38 (5):823-864. doi:Doi 10.1111/1574-6976.12063
64. Brodin JD, Ambroggio XI, Tang CY, Parent KN, Baker TS, Tezcan FA (2012) Metal-directed, chemically tunable assembly of one-, two- and three-dimensional crystalline protein arrays. Nat Chem 4 (5):375-382. doi:Doi 10.1038/Nchem.1290
65. Brodin JD, Carr JR, Sontz PA, Tezcan FA (2014) Exceptionally stable, redox-active supramolecular protein assemblies with emergent properties. P Natl Acad Sci USA 111 (8):2897-2902. doi:DOI 10.1073/pnas.1319866111
66. Castelletto V, Hamley IW, Cenker C, Olsson U (2010) Influence of Salt on the Self-Assembly of Two Model Amyloid Heptapeptides. J Phys Chem B 114 (23):8002-8008. doi:DOI 10.1021/jp102744g
67. Castelletto V, Hamley IW, Harris PJF (2008) Self-assembly in aqueous solution of a modified amyloid beta peptide fragment. Biophys Chem 138 (1-2):29-35. doi:DOI 10.1016/j.bpc.2008.08.007
68. Castelletto V, Hamley IW, Harris PJF, Olsson U, Spencer N (2009) Influence of the Solvent on the Self-Assembly of a Modified Amyloid Beta Peptide Fragment. I. Morphological Investigation. J Phys Chem B 113 (29):9978-9987. doi:DOI 10.1021/jp902860a
69. Chothia C, Levitt M, Richardson D (1981) Helix to helix packing in proteins. J Mol Biol 145 (1):215-250
70. Hamley IW, Dehsorkhi A, Castelletto V (2013) Self-assembled arginine-coated peptide nanosheets in water. Chem Commun 49 (18):1850-1852. doi:DOI 10.1039/c3cc39057h
71. Hamley IW, Dehsorkhi A, Castelletto V, Furzeland S, Atkins D, Seitsonen J, Ruokolainen J (2013) Reversible helical unwinding transition of a self-assembling peptide amphiphile. Soft Matter 9 (39):9290-9293. doi:DOI 10.1039/c3sm51725j
72. Dai B, Li D, Xi W, Luo F, Zhang X, Zou M, Cao M, Hu J, Wang W, Wei G, Zhang Y, Liu C (2015) Tunable assembly of amyloid-forming peptides into nanosheets as a retrovirus carrier. Proc Natl Acad Sci U S A 112 (10):2996-3001. doi:10.1073/pnas.1416690112
73. Jang HS, Lee JH, Park YS, Kim YO, Park J, Yang TY, Jin K, Lee J, Park S, You JM, Jeong KW, Shin A, Oh IS, Kwon MK, Kim YI, Cho HH, Han HN, Kim Y, Chang YH, Paik SR, Nam KT, Lee YS (2014) Tyrosine-mediated two-dimensional peptide assembly and its role as a bio-inspired catalytic scaffold. Nat Commun 5. doi:ARTN 3665 DOI 10.1038/ncomms4665

74. Jiang T, Vail OA, Jiang Z, Zuo X, Conticello VP (2015) Rational Design of Multilayer Collagen Nanosheets with Compositional and Structural Control. J Am Chem Soc 137 (24):7793-7802. doi:10.1021/jacs.5b03326
75. Jiang T, Xu CF, Liu Y, Liu Z, Wall JS, Zuo XB, Lian TQ, Salaita K, Ni CY, Pochan D, Conticello VP (2014) Structurally Defined Nanoscale Sheets from Self-Assembly of Collagen-Mimetic Peptides. J Am Chem Soc 136 (11):4300-4308. doi:DOI 10.1021/ja412867z
76. Jiang T, Xu CF, Zuo XB, Conticello VP (2014) Structurally Homogeneous Nanosheets from Self-Assembly of a Collagen-Mimetic Peptide. Angew Chem Int Edit 53 (32):8367-8371. doi:DOI 10.1002/anie.201403780
77. Matmour R, De Cat I, George SJ, Adriaens W, Leclere P, Bomans PHH, Sommerdijk NAJM, Gielen JC, Christianen PCM, Heldens JT, van Hest JCM, Lowik DWPM, De Feyter S, Meijer EW, Schenning APHJ (2008) Oligo(p-phenylenevinylene)-Peptide Conjugates: Synthesis and Self-Assembly in Solution and at the Solid-Liquid Interface. J Am Chem Soc 130 (44):14576-14583. doi:DOI 10.1021/ja803026j
78. Matthaei JF, DiMaio F, Richards JJ, Pozzo LD, Baker D, Baneyx F (2015) Designing Two-Dimensional Protein Arrays through Fusion of Multimers and Interface Mutations. Nano Lett 15 (8):5235-5239. doi:10.1021/acs.nanolett.5b01499
79. McGuinness K, Khan IJ, Nanda V (2014) Morphological Diversity and Polymorphism of Self-Assembling Collagen Peptides Controlled by Length of Hydrophobic Domains. Acs Nano 8 (12):12514-12523. doi:DOI 10.1021/nn505369d
80. Nam KT, Shelby SA, Choi PH, Marciel AB, Chen R, Tan L, Chu TK, Mesch RA, Lee BC, Connolly MD, Kisielowski C, Zuckermann RN (2010) Free-floating ultrathin two-dimensional crystals from sequence-specific peptoid polymers. Nat Mater 9 (5):454-460. doi:Doi 10.1038/Nmat2742
81. Olivier GK, Cho A, Sanii B, Connolly MD, Tran H, Zuckermann RN (2013) Antibody-Mimetic Peptoid Nanosheets for Molecular Recognition. Acs Nano 7 (10):9276-9286. doi:DOI 10.1021/nn403899y
82. Pashuck ET, Stupp SI (2010) Direct Observation of Morphological Tranformation from Twisted Ribbons into Helical Ribbons. J Am Chem Soc 132 (26):8819-+. doi:DOI 10.1021/ja100613w
83. Przybyla DE, Chmielewski J (2010) Metal-Triggered Collagen Peptide Disk Formation. J Am Chem Soc 132 (23):7866-+. doi:DOI 10.1021/ja103148t
84. Robertson EJ, Oliver GK, Qian M, Proulx C, Zuckermann RN, Richmond GL (2014) Assembly and molecular order of two-dimensional peptoid nanosheets through the oil-water interface. P Natl Acad Sci USA 111 (37):13284-13289. doi:DOI 10.1073/pnas.1414843111
85. Sanii B, Haxton TK, Olivier GK, Cho A, Barton B, Proulx C, Whitelam S, Zuckermann RN (2014) Structure-Determining Step in the Hierarchical Assembly of Peptoid Nanosheets. Acs Nano 8 (11):11674-11684. doi:DOI 10.1021/nn505007u
86. Sanii B, Kudirka R, Cho A, Venkateswaran N, Olivier GK, Olson AM, Tran H, Harada RM, Tan L, Zuckermann RN (2011) Shaken, Not Stirred: Collapsing a Peptoid Monolayer To Produce Free-Floating, Stable Nanosheets. J Am Chem Soc 133 (51):20808-20815. doi:DOI 10.1021/ja206199d

87. Xu F, Khan IJ, McGuinness K, Parmar AS, Silva T, Murthy NS, Nanda V (2013) Self-Assembly of Left- and Right-Handed Molecular Screws. J Am Chem Soc 135 (50):18762-18765. doi:DOI 10.1021/ja4106545
88. Sinclair JC, Davies KM, Venien-Bryan C, Noble ME (2011) Generation of protein lattices by fusing proteins with matching rotational symmetry. Nat Nanotechnol 6 (9):558-562. doi:10.1038/nnano.2011.122
89. Childers WS, Anthony NR, Mehta AK, Berland KM, Lynn DG (2012) Phase networks of cross-beta peptide assemblies. Langmuir 28 (15):6386-6395. doi:10.1021/la300143j
90. Lu K, Jacob J, Thiyagarajan P, Conticello VP, Lynn DG (2003) Exploiting amyloid fibril lamination for nanotube self-assembly. J Am Chem Soc 125 (21):6391-6393. doi:10.1021/ja0341642
91. Richter F, Leaver-Fay A, Khare SD, Bjelic S, Baker D (2011) De novo enzyme design using Rosetta3. Plos One 6 (5):e19230. doi:10.1371/journal.pone.0019230
92. Lai YT, Cascio D, Yeates TO (2012) Structure of a 16-nm cage designed by using protein oligomers. Science 336 (6085):1129. doi:10.1126/science.1219351
93. Lai YT, Tsai KL, Sawaya MR, Asturias FJ, Yeates TO (2013) Structure and flexibility of nanoscale protein cages designed by symmetric self-assembly. J Am Chem Soc 135 (20):7738-7743. doi:10.1021/ja402277f
94. Padilla JE, Colovos C, Yeates TO (2001) Nanohedra: using symmetry to design self assembling protein cages, layers, crystals, and filaments. Proc Natl Acad Sci U S A 98 (5):2217-2221. doi:10.1073/pnas.041614998
95. Lai YT, Reading E, Hura GL, Tsai KL, Laganowsky A, Asturias FJ, Tainer JA, Robinson CV, Yeates TO (2014) Structure of a designed protein cage that self-assembles into a highly porous cube. Nat Chem 6 (12):1065-1071. doi:10.1038/nchem.2107
96. Fairman R, Chao HG, Lavoie TB, Villafranca JJ, Matsueda GR, Novotny J (1996) Design of heterotetrameric coiled coils: evidence for increased stabilization by Glu(-)-Lys(+) ion pair interactions. Biochemistry 35 (9):2824-2829. doi:10.1021/bi952784c
97. Plass KE, Grzesiak AL, Matzger AJ (2007) Molecular packing and symmetry of two-dimensional crystals. Acc Chem Res 40 (4):287-293. doi:10.1021/ar0500158

Chapter 2 Design and characterization of an α-helical peptide 3FD-IL which forms nanosheets

2.1 Introduction

The previous chapter discussed the current known examples of nanosheets in the literature and their modes of self-assembly. While many motifs have been utilized to create nanosheets, including β-sheets [1-3], collagen mimetic peptides [4-6], whole proteins [7-9], and peptoids [10-16], the α-helix has not been utilized to make two-dimensional structures. However, the α-helical coiled-coil motif has been utilized by our groups and others to create a wide range of peptide assemblies, including nanofibers [17-24], nanotubes[25-28] , hydrogels [29], and crystals [30]. Furthermore, crystal structures of α-helical peptides reveal two-dimensional layers within the overall three-dimensional structure, suggesting that it is possible to design an α-helical nanosheet [30-35].

In addition to developing methods to create nanosheets from α-helices, it would be advantageous to develop methods to control the arrangement or packing of monomers within the nanosheet. The Degrado and Saven groups have had success with controlling the packing of α-helices in a protein crystal through the use of computational design [30]. The protein **P6-d** formed a highly symmetric hexagonal crystal composed of trimeric coiled-coils. Interhelical contacts were stabilized by complementary electrostatic interactions and a glycine zipper motif, which enabled tight packing between coiled-coil trimers. As described in Chapter 1, Baker et al. also have utilized computational design to produce a protein TTM, which assembled into hexagonal, two-dimensional arrays of

space group p3. In addition, Conticello *et al*. have produced highly ordered nanosheets

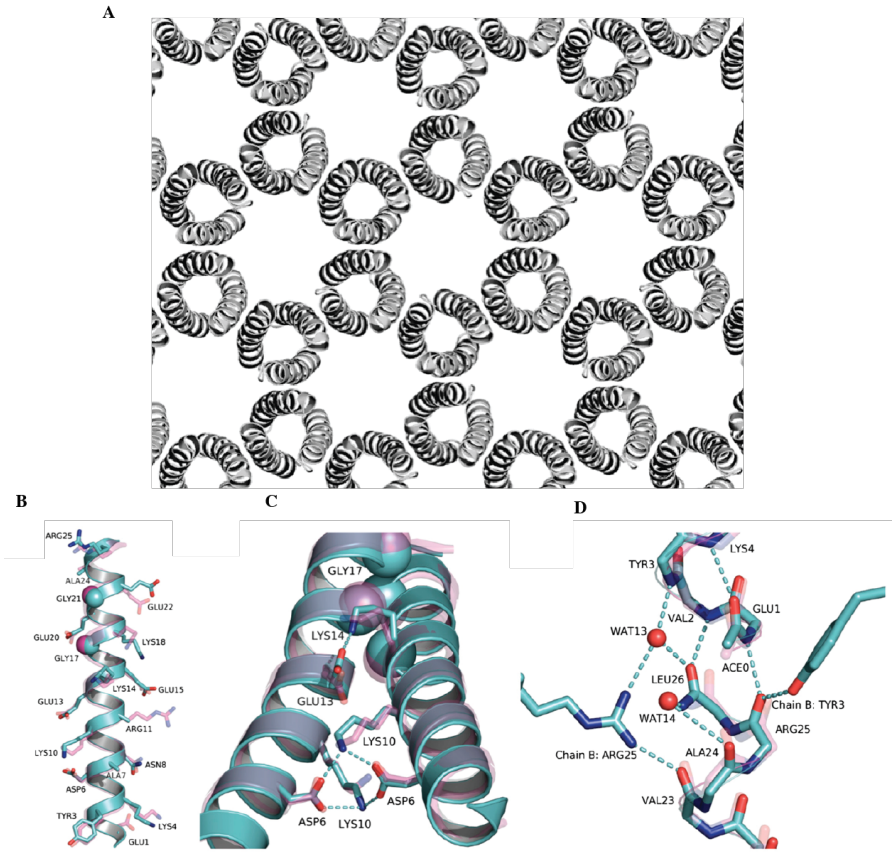

Figure 2.1 Computationally designed two-dimensional layer (a) cross section of a two-dimensional layer of P6-d (b) Single helix of P6-d displaying the side chains (c) glycine zipper (glycines displayed as spheres) and electrostatic interaction stabilization of interhelix contacts (d) hydrogen bonding across the interlayer interface. Reproduced with permission from [30]

from collagen mimetic peptides in which the triple helices pack in a tetragonal arrangement. Collagen-mimetic peptide structures can be sorted into two symmetry classes: pseudotetragonal and pseudohexagonal. However, although the **NSI** and **NSIII** nanosheets approximate the packing of the pseudotetragonal structures, the packing preference for collagen-mimetic peptides is not well understood [36] . An understanding of how to rationally design nanosheets, which contain monomers with specified packing

arrangements, would enhance the fabrication of materials with specified supramolecular structures.

2.2 Design of 3FD-IL nanosheets

The peptide **3FD-IL** was designed to form α-helical nanosheets with a high degree of internal order. The design of **3FD-IL** was based on the straight α-helical motif, which contains a repeat of 18 amino acids per five turns. The linear sequence of amino acids in one α-helical repeat, designated NH_2-abcdefghijklmnopr-COOH, can be projected on a helical wheel diagram, which allows for the visualization of amino acids on the same face of the α-helix. The thickness of the lines connecting the amino acid positions decreases from N- to C-terminus. The helical wheel can be divided into three identical faces consisting of six amino acids to generate a helix with three-fold symmetry, which allows for distinct packing between helices from each face. The peptide **3FD-IL** contained glutamate, lysine, alanine, isoleucine, and leucine on each face. Noncovalent interactions between faces of adjacent helices promoted two-dimensional assembly formation. More specifically, the design enabled hydrophobic interactions between leucine and isoleucine and salt bridge formation between lysine and glutamate (Figure 2.2). Finally, the presence of alanine, which is oftentimes found at the helix-helix interface of transmembrane proteins, allows for tight packing at the helix-helix interface [37]. Two 18 amino acid repeats are present in the sequence of the resultant α-helix **3FD-IL**, because α-helix stability increases with length [38,39]. The N-terminus of **3FD-IL** was capped with glutamic acid, and the C-terminus of **3FD-IL** was capped with lysine in order to stabilize the α-helix dipole [40]. The peptide **3FD-IL** was synthesized by solid-

phase peptide synthesis and purified using reverse phase liquid chromatography. The purity and identity of **3FD-IL** was confirmed using a combination of analytical high performance liquid chromatography and electrospray ionization mass spectrometry.

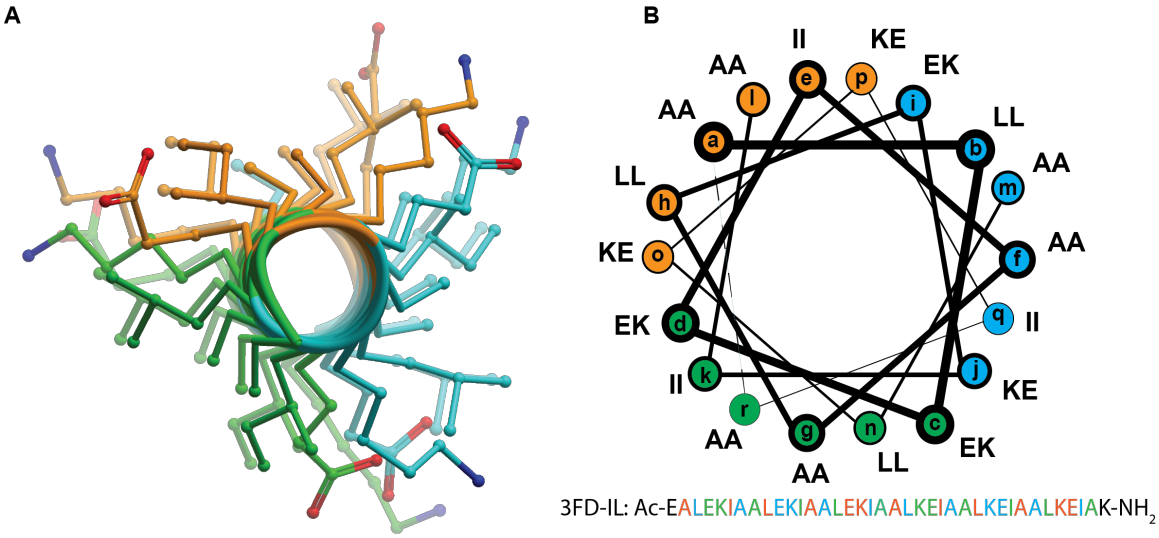

Figure 2.2 Design of 3FD-IL α-helix (a) cartoon representation of a three-fold helix with side chains from each face colored differently (b) helical wheel representation and linear sequence of peptide 3FD-IL color-coded in the same fashion as in (a)

2.3 Results and Discussion

2.3.1 Self Assembly of 3FD-IL

In order to determine if **3FD-IL** forms nanosheets, preliminary self-assembly experiments were conducted. Conditions that peptides are self assembled in, such as salt concentration, pH, and peptide concentration, can strongly affect the resultant structures that are formed. For instance, the peptide Ac-KLVFFAE-NH_2, the nucleating core of the Aβ peptide responsible for Alzheimer's disease forms either fibrils or nanotubes, depending on the pH of the solution [41]. A different amyloid model heptapeptide, NH_2-βAβAKLVFF-COOH, forms twisted fibrils at low salt concentration (100 mM NaCl) and

nanotubes at high salt concentration (250 mM NaCl) [1]. Circular dichroism spectroscopy was the first technique employed to characterize the self-assembly of **3FD-IL**, because it can be used to determine the secondary structure of the analytes. The absorbance of circularly polarized light by peptides induces both $n \rightarrow \pi^*$ and $\pi \rightarrow \pi^*$ electronic transitions. The intensity and energy of these transitions depend on the ϕ/ψ dihedral angles of the peptide backbone. According to the design of **3FD-IL**, this peptide should form an α-helical structure. The circular dichroism signature of an α-helical peptide contains a

maximum at 190 nm and minima at 208 nm and 222 nm.

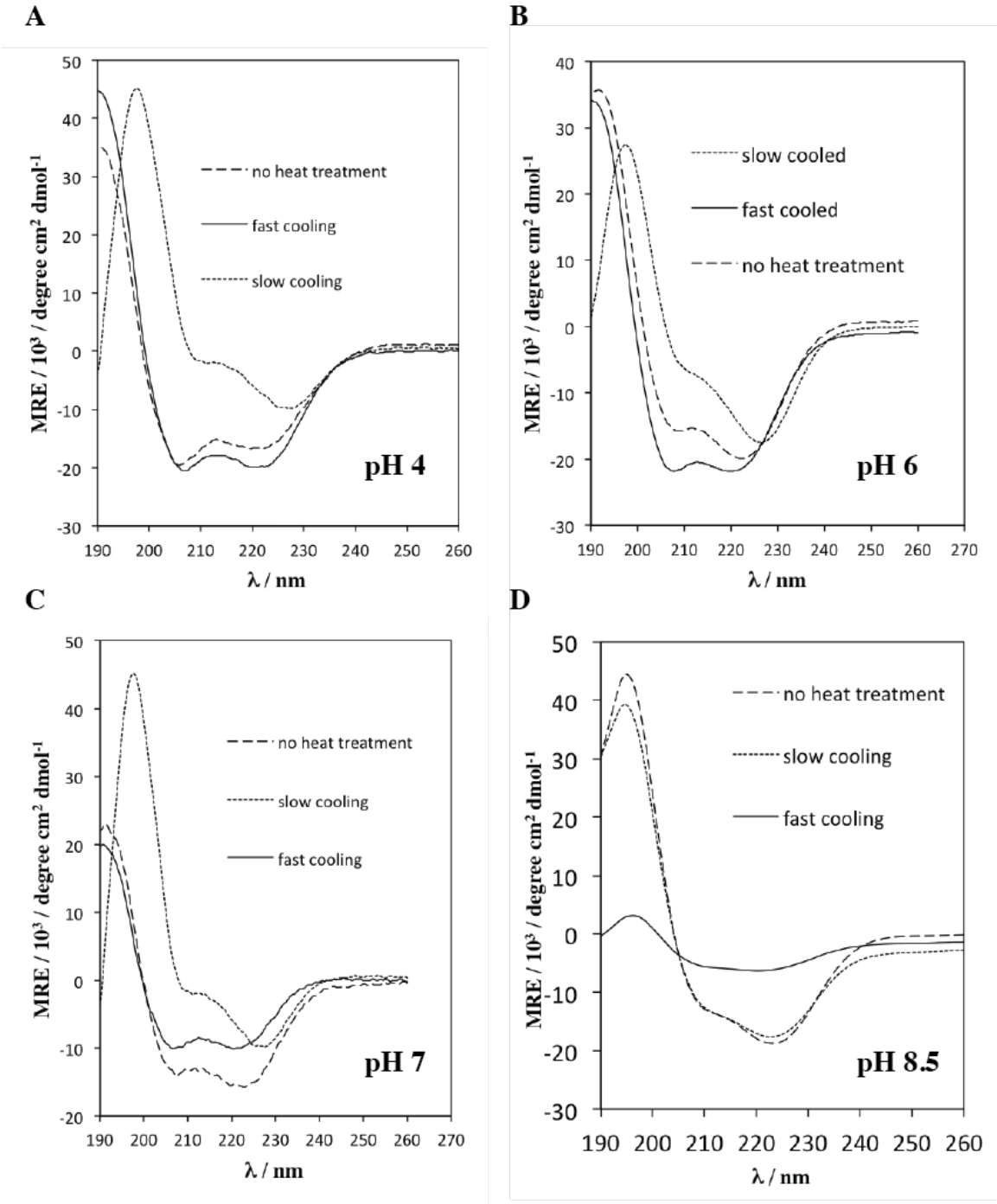

Figure 2.3 Dependence of circular dichroism spectra of 3FD-IL on pH. All CD curves were measured at a peptide concentration of 1 mg/mL. (a) pH 4, (b) pH 6, (c) pH 7, (d) pH 8.5

The peptide **3FD-IL** was assembled at pH 4, pH 6, pH 7, and pH 8.5. Within thirty minutes of assembly, the peptide **3FD-IL** formed an α-helical secondary structure at each pH (Figure 2.3). The minima are slightly red shifted from a standard α-helix, which contains negative minima at 208 nm and 222 nm due to light scattering. Light scattering occurs when the dimensions of the particles in solution are greater than 1/20th the wavelength of light [42]. Interestingly, heat treatment of **3FD-IL** affects the circular dichroism spectra. When **3FD-IL** is heated to 95 °C and cooled quickly (14 °C/minute) at pH 7 and 8.5, the intensity of the minima decrease, consistent with melting of secondary structure. A traditional α-helical circular dichroism spectra is obtained that does not appear to be affected by light scattering. At pH 4 and pH 6, 3FD-IL retains its secondary structure upon fast cooling. This is perhaps due to enhanced solubility of the pH 4 and pH 6 solutions compared to the pH 7 and pH 8.5 solutions. Across all pHs tested, after heating to 90 °C and slow cooling (0.2 °C / minute) to 40 °C, **3FD-IL** retains its α-helicity and the minima are red shifted from the standard α-helix.

In order to determine if the scattering effect observed in circular dichroism is correlated with the formation of nanosheets, transmission electron microscopy

experiments were performed.

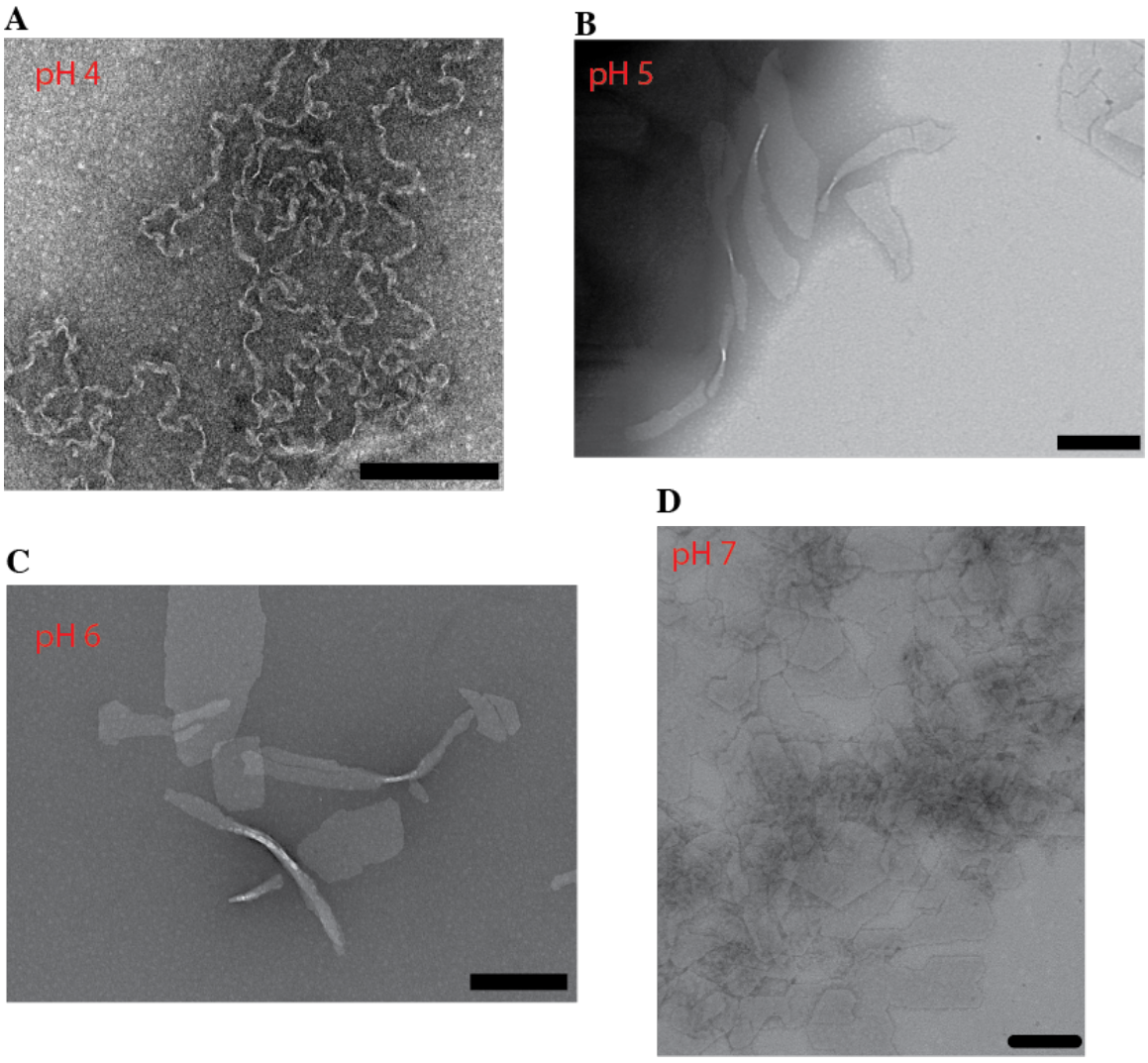

Figure 2.4 Transmission electron micrographs of thermally annealed 3FD-IL assemblies (approximately 5 mg/mL) at (a) pH 4 (b) pH 5 (c) pH 6, and (d) pH 7 (scale bars = 200 nm)

After slow cooling, **3FD-IL** formed large assemblies and fibrillar-like morphologies. The type of morphologies observed is dependent on pH. Large assemblies of **3FD-IL** (on the order of hundreds of nanometers to microns in side length) occur over a pH range from 5 to 8.5 (Figure 2.4). The isoelectric point of **3FD-IL** occurs at a pH of 7.41. At this pH, there is no net charge on the individual peptide helices, precluding

repulsion between adjacent helices and stimulating aggregation of the peptide helices. Interestingly, at pH 7 (10 mM MOPS buffer), the pH which is closest to the isoelectric point, **3FD-IL** forms large assemblies, but also forms structures which are flexible and fibrillar in morphology. Since pH 7 is close to the isoelectric point of **3FD-IL**, the attraction between helices and subsequent aggregation may occur rapidly, allowing for the formation of different peptide conformations or kinetic intermediates. At pH 5 (10 mM acetate) and pH 6 (10 mM MES buffer), **3FD-IL** also forms large assemblies in addition to elongated structures. At pH 4, in 10 mM acetate buffer, **3FD-IL** does not form large assemblies. Instead **3FD-IL** forms structures with morphologies that resemble twisted fibers. This suggests a role for glutamic acid in stabilizing the **3FD-IL** assemblies, since pH 4 is near the pK_a of the carboxylic side chain of glutamic acid. Glutamic acid most likely forms salt bridges with lysine.

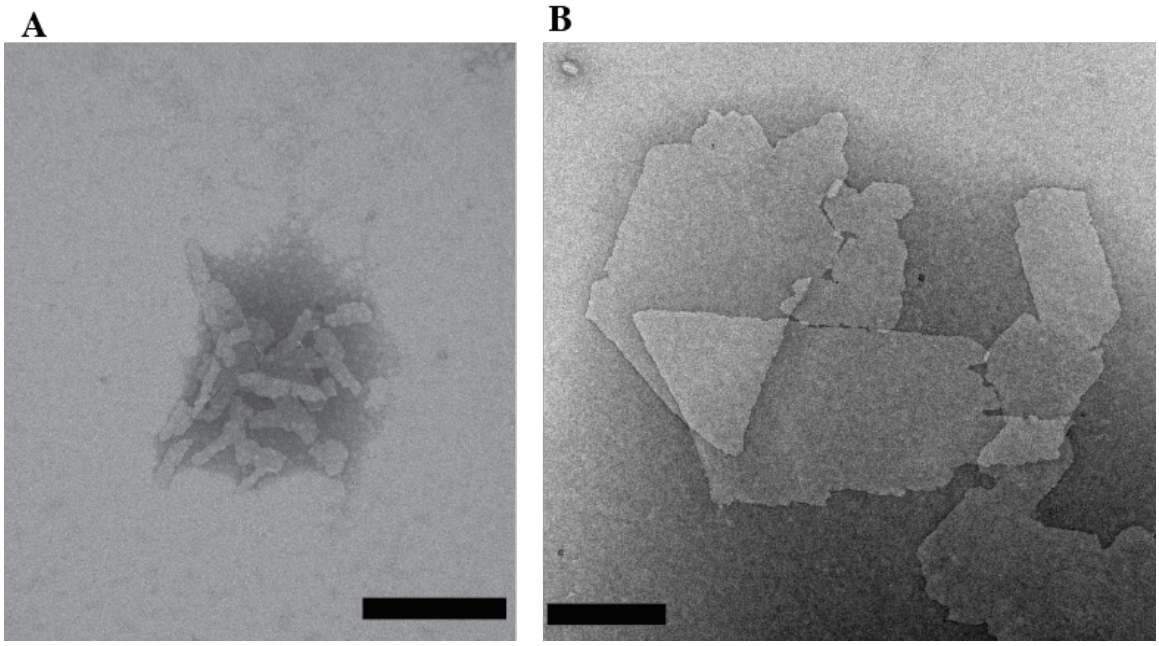

Figure 2.5 TEM images of 3FD-IL assembled in TAPS buffer pH 8.5 in the absence (a) and presence (b) of thermal annealing (scale bars = 200 nm)

After thermal annealing (slow cooling) at pH 8.5, **3FD-IL** forms a homogenous solution of large assemblies (Figure 2.5b). The assemblies formed have straight edges and in some cases form parallelograms. Since pH 8.5 is near the isoelectric point of **3FD-IL**, this pH promotes attractions between helices. Thermal annealing allows for error correction between monomers within the assemblies, allowing for the growth of micron sized assemblies. Since the large assemblies formed at pH 8.5 are homogenous, these conditions were used for future structural characterization. The circular dichroism spectra taken at pH 8.5 revealed a similar circular dichroism signature in the samples with no heat treatment and the sample prepared through thermal annealing, therefore additional transmission electron microscopy images of the sample with no heat treatment were taken. These images revealed the presence of assemblies, which are relatively smaller than the assemblies formed by thermal annealing (Figure 2.5). Additionally, the assemblies formed often have jagged edges. This experiment revealed the importance of thermal annealing for assembly formation.

In order to determine the thermal stability of the large assemblies formed at pH 8.5, circular dichroism melting studies were performed. The melting curves of **3FD-IL** assembled at pH 8.5 with no heat treatment and the **3FD-IL** solution prepared by the slow cooling method were conducted by monitoring the mean residue ellipticity at 222 nm. The melting temperatures of the samples were obtained by taking the first derivative of the respective melting curves. Without heat treatment, the melting temperature of the peptide is 81°C. After slow cooling, the melting temperature increased slightly to 84 °C (Figure 2.6). The similarity in melting temperatures may be attributed to the fact that in both assembly conditions, nanosheets are formed. The slight increase in melting

temperature could be due to the increase in size in the assemblies formed after slow cooling. The presence of side peaks in the first derivative curve for the annealed **3FD-IL** solution could indicate heterogeneity in melting due to the variety of nanosheet sizes in solution. Furthermore, the smaller nanosheets, which are formed in the absence of annealing may melt more homogenously, giving a single maximum.

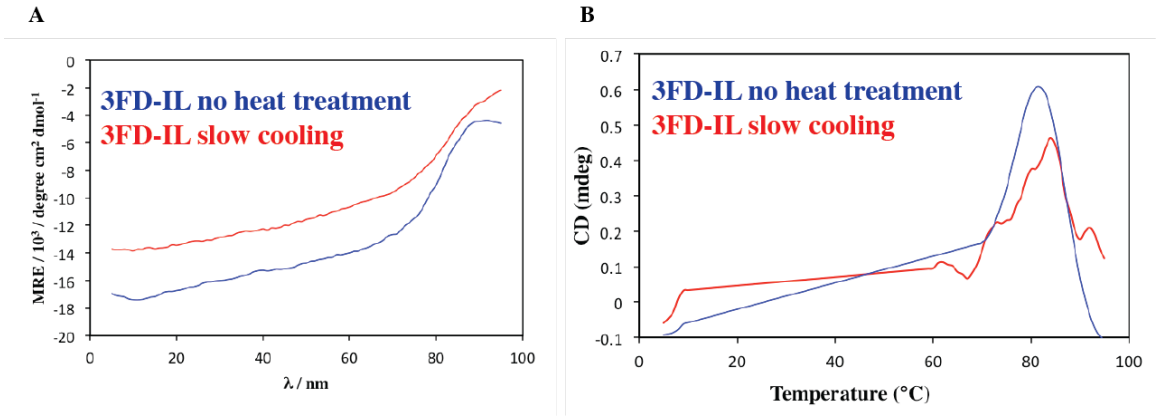

Figure 2.6 (a) Circular dichroism melting curves of 3FD-IL in the absence and presence of heat treatment recorded at 222 nm (b) first derivative of the CD melting curves utilized to reveal the melting temperature of the assemblies

In order to determine the forces that stabilize formation of the assemblies formed after thermal annealing, **3FD-IL** was assembled in the presence of sodium chloride concentrations up to 500 mM (Figure 2.7). As the concentration of sodium chloride increased, the assemblies became more cracked, suggesting that sodium chloride is having a charge screening effect on the assemblies.

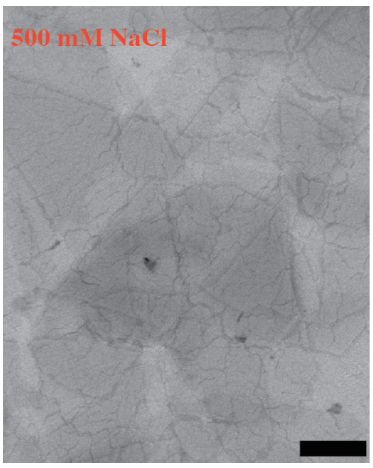

Figure 2.7 Transmission electron micrograph of 3FD-IL assembled in the presence of 500 mM sodium chloride (scale bar = 200 nm)

Sodium chloride can interrupt electrostatic interactions between lysine and glutamic acid. Interestingly, although the assemblies were cracked at high salt concentrations, the overall morphology of the assemblies was not interrupted. This suggests that hydrophobic interactions also play a role in stabilizing the self assembly of **3FD-IL**.

2.3.2 Small angle x-ray scattering

The next experiments performed attempted to better understand the structure of the **3FD-IL** assemblies formed. Small angle x-ray scattering (SAXS) experiments give

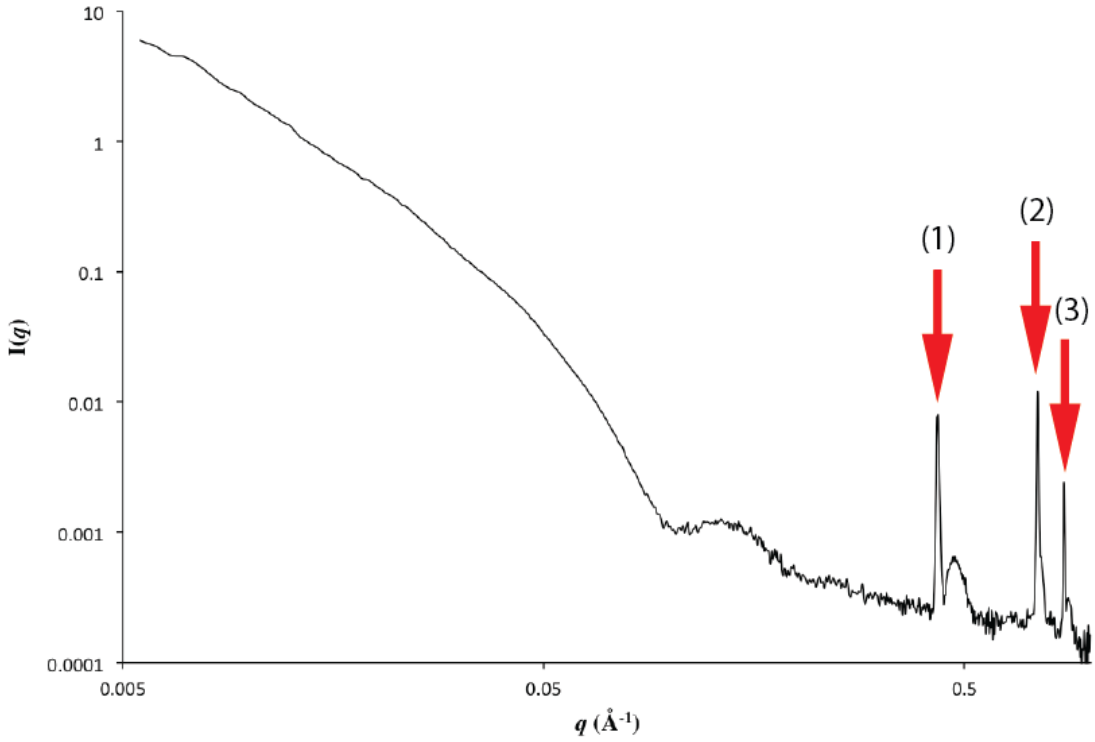

Figure 2.8 Small angle x-ray scattering curve of a solution of 3FD-IL assemblies; arrows correspond to Bragg diffraction peaks at (1) 14.54 Å, (2) 8.44 Å (3) 7.30 Å

information about the overall shape and internal structure of biomolecules. A solution of **3FD-IL** assemblies was exposed to a monochromatic x-ray beam (1.033 Å), and the intensities were recorded as a function of momentum transfer, q, where $q = 4\pi\sin\theta / \lambda$. A plot of q versus intensity gives rise to the small angle x-ray scattering curve. Different regions of the small angle x-ray scattering curve give different information about the structure of materials. Momentum transfer q is related to distance (d) by the equation $d = 2\pi / q$. Therefore, the low q region, which corresponds to greater distances, can give information about the overall shape of the assemblies, whereas the high q region corresponds to smaller distances within the structure of materials. A plot of momentum

transfer q versus intensity reveals that the **3FD-IL** assemblies are highly ordered, as evident by Bragg diffraction peaks in the high q region (Figure 2.8). In order to prove that the large assemblies formed by transmission electron microscopy are nanosheets, the intermediate q region of the scattering curve can be analyzed. The intensity in the intermediate q region of the scattering curve decays with q^{-2}, consistent with the

formation of disc-like

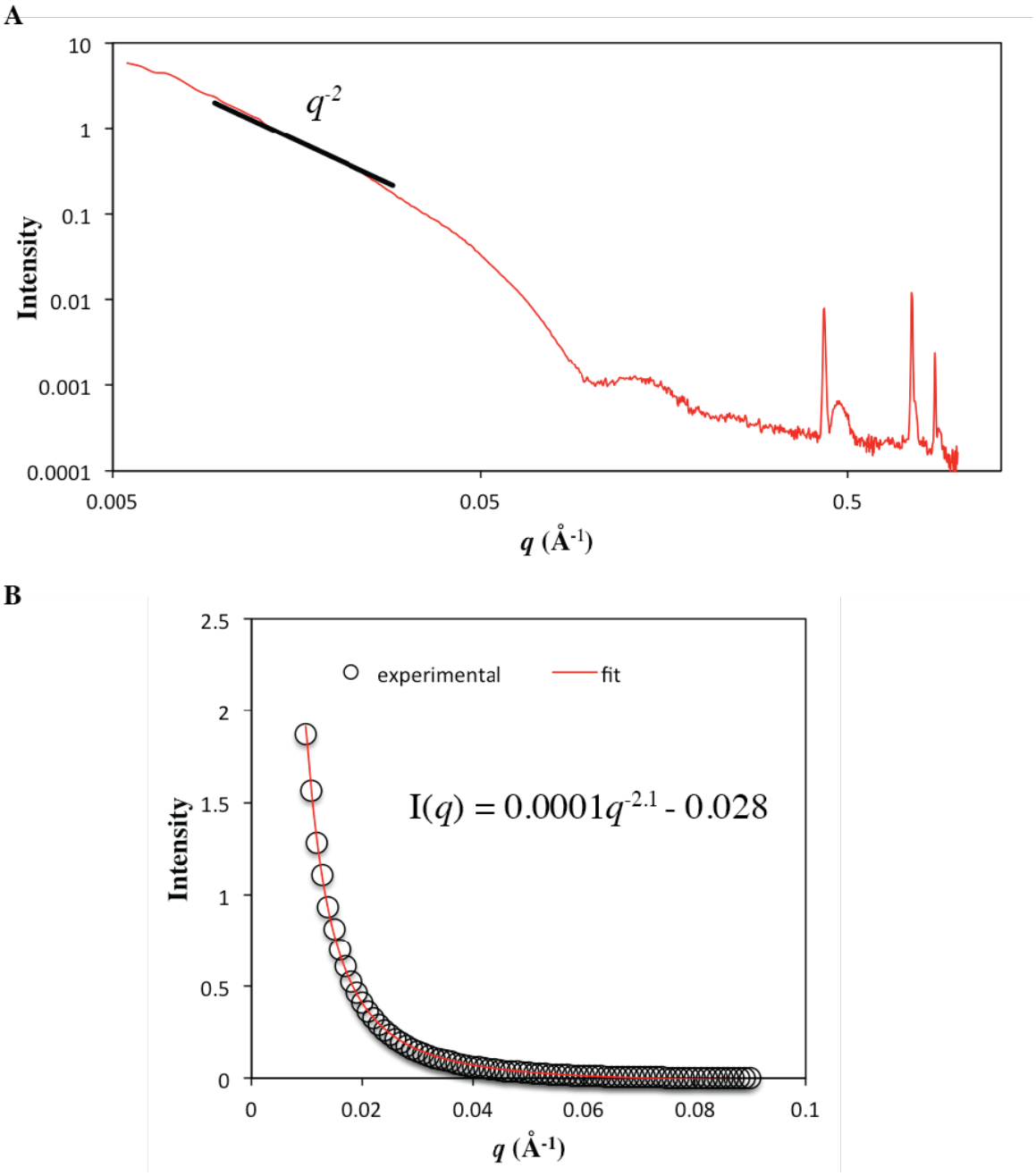

Figure 2.9 (a) Small angle x-ray scattering curve showing the dependency of I(q) is proportional to q^{-2} (b) fit of intermediate q region to an exponential function

objects (Figure 2.9). The Guinier region (low q) region of the scattering curve can be fit to an equation for sheet-like forms to obtain the radius of gyration, R_g, and subsequently the thickness, T, of the nanosheets (Figure 2.10). The radius of gyration was determined

to be 18.797 Å, and thus the thickness of the nanosheets was determined to be 65.117 Å. The Guinier approximation was judged to be valid, because (R_g*q_{max}) ≤ 1.3 (ref 15 Tao's paperangewandte).

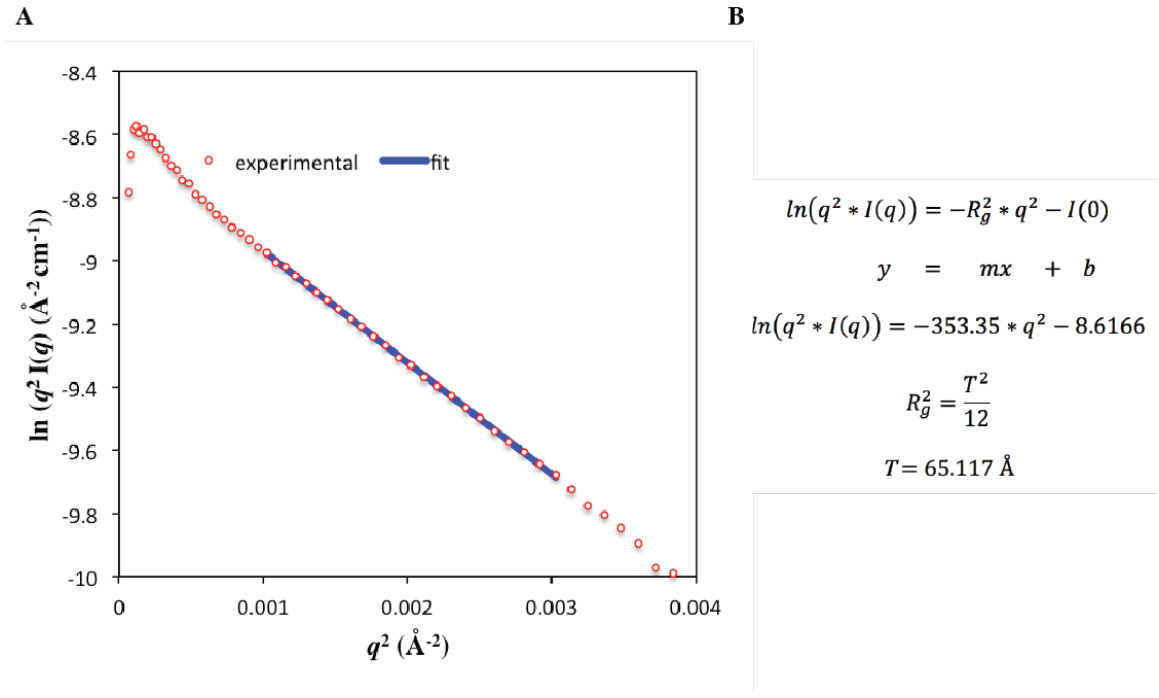

Figure 2.10 (a) Guinier plot of solution of 3FD-IL nanosheets and (b) derivation of thickness from linear region of the Guinier plot

The Bragg diffraction peaks in the high q region correspond to distances of 14.54 Å, 8.44 Å, and 7.30 Å. These three distances are in the ratio n: n/√3: n/√4 (Figure 2.11). The geometric relationship between these diffraction peaks indicates that the helices within the 3FD-IL nanosheets are packed in a hexagonal arrangement.

The SAXS data provided important information necessary to confirm the design for the peptide **3FD-IL**. It confirmed that **3FD-IL** does form nanosheets in solution. Additionally, the data supported a model for the **3FD-IL** nanosheets in which the thickness of a single nanosheet is equivalent to the length of the **3FD-IL** peptide. The theoretical length of the 3FD-IL peptide can be calculated by multiplying the number of

amino acids within the α-helix by the α-helix rise per residue of 1.5 Å. The theoretical length obtained corresponds to 5.7 Å, which is similar to the thickness obtained from the Guinier approximation (6.5 Å). This data also supports a model for helix packing in which the helices within the nanosheet are in a hexagonal orientation. Based on the three-fold design of the **3FD-IL** peptide, this is a reasonable geometry. The next sections of this chapter will attempt to confirm and explain the results obtained from the SAXS experiment. Questions involving the α-helix length, α-helix packing and orientation, and differences between the solution and powder form of the **3FD-IL** nanosheets will be investigated.

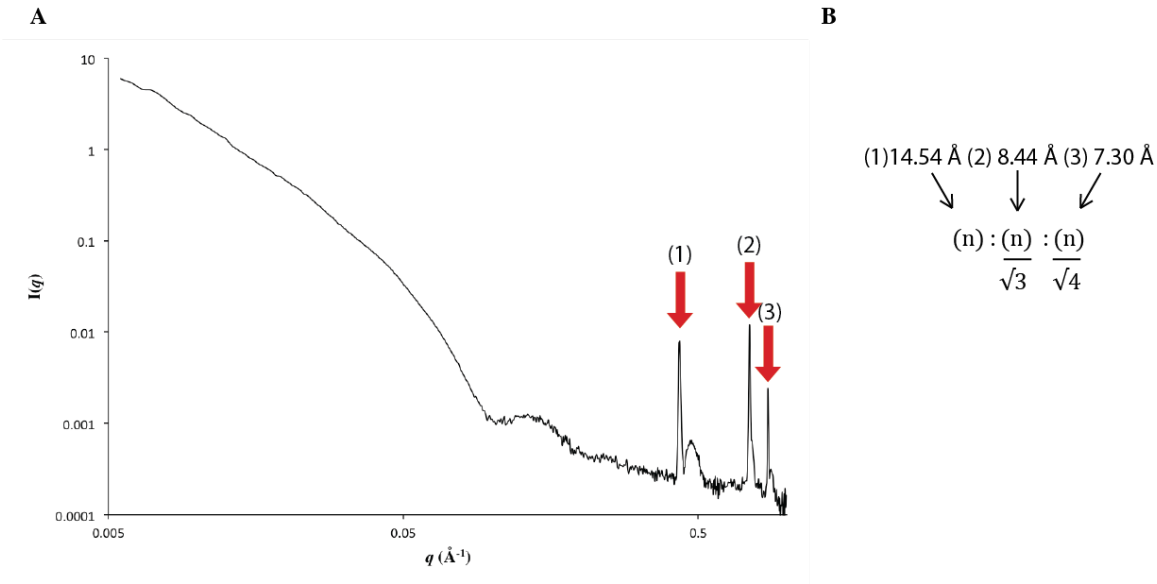

Figure 2.11 (a) Bragg diffraction peaks in the high *q* region of the SAXS scattering curve and (b) geometric relationship between the peaks

2.3.3 The thickness of the 3FD-IL nanosheets and its implications for structure

Atomic force microscopy experiments were conducted to confirm the thickness measurements obtained for the **3FD-IL** nanosheets in solution by small angle x-ray

scattering. The average height of the **3FD-IL** nanosheets was 6.13 nm (Figure 2.12). As mentioned previously, the theoretical length of the 3FD-IL α-helix is 5.7 nm. The combined data from AFM and SAXS suggested that the α-helices are oriented perpendicular to the plane of the nanosheets. There are a few explanations for the observed increased experimental thickness. The first possibility is that the helix termini are partially unfolded in solution. Since the termini are most exposed to the solvent, it is possible that they interact with the solvent and partially unfold. The second possibility is that the helices within the nanosheets are staggered with respect to each other.

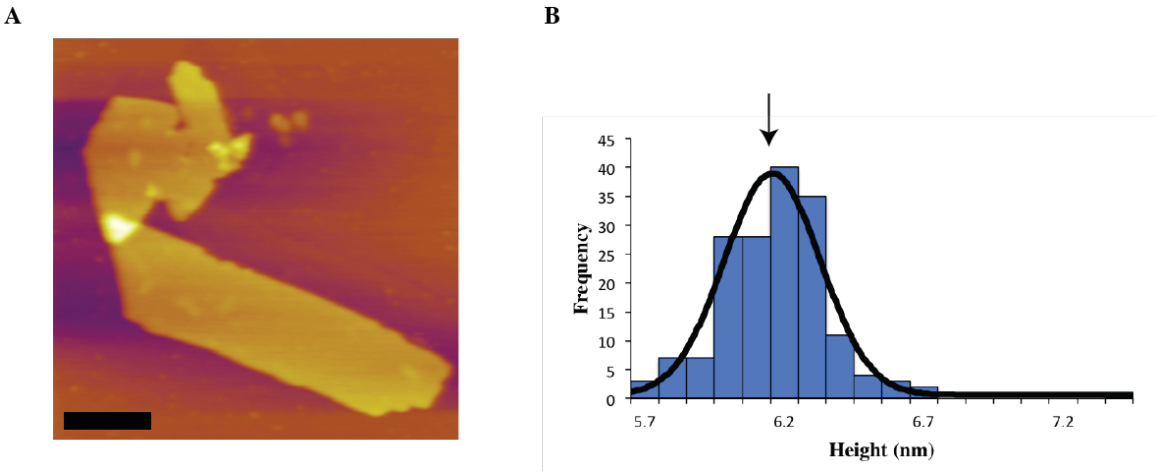

Figure 2.12 Atomic force microscopy measurements of 3FD-IL (a) representative AFM image (scale bar is 200 nm) (b) histogram of AFM measurements fit to a Gaussian distribution; arrow corresponds to the maximum in the Gaussian fit of 6.13 nm.

The third possibility is that instead of forming an α-helical conformation, **3FD-IL** adopts an alternative secondary structure such as a 3_{10} helix and that the red-shifted CD signature of **3FD-IL**, which is attributed to scattering, is really the signature of a 3_{10} helix. If **3FD-IL** formed a 3_{10} helix, all isoleucines and leucines would fall on the same face, and sheet formation could be stabilized by the hydrophobic effect. The CD signature for a 3_{10} helix has not been studied intensively [43]. A 3_{10} helix contains three

residues per turn of the helix and has a rise per residue of 2.0 Å. The theoretical length of the **3FD-IL** 3_{10} helix would therefore be 7.6 nm. In order to test this

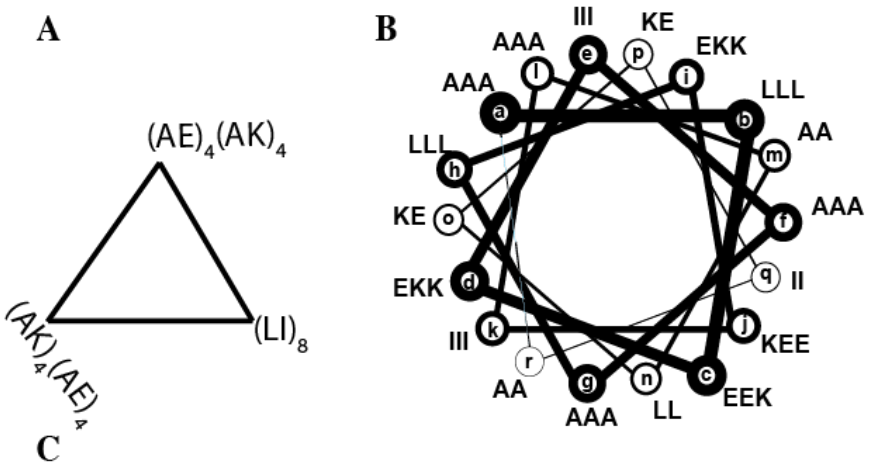

3FD-8IL: Ac-E ALEKIA ALEKIA ALEKIA ALEKIA ALKEIA ALKEIA ALKEIA ALKEIA K-NH_2

Figure 2.13 Sequence of 3FD-8IL represented as a (a) 3_{10} helix and as an (b) α-helix

hypothesis, the peptide **3FD-8IL** was synthesized in which the peptide sequence of **3FD-IL** was extended by twelve amino acids. This extension breaks the three-fold symmetry associated with **3FD-IL**, and should impair nanosheet formation if **3FD-IL** is an α-helix (Figure 2.13). However, a 3_{10} helix of **3FD-8IL** should be able to form nanosheets, because all leucines and isoleucines are on the same face of the 3_{10} helix, enabling nanosheet growth through the hydrophobic effect (Figure 2.13). The peptide **3FD-8IL**

was assembled in 10 mM TAPS buffer at

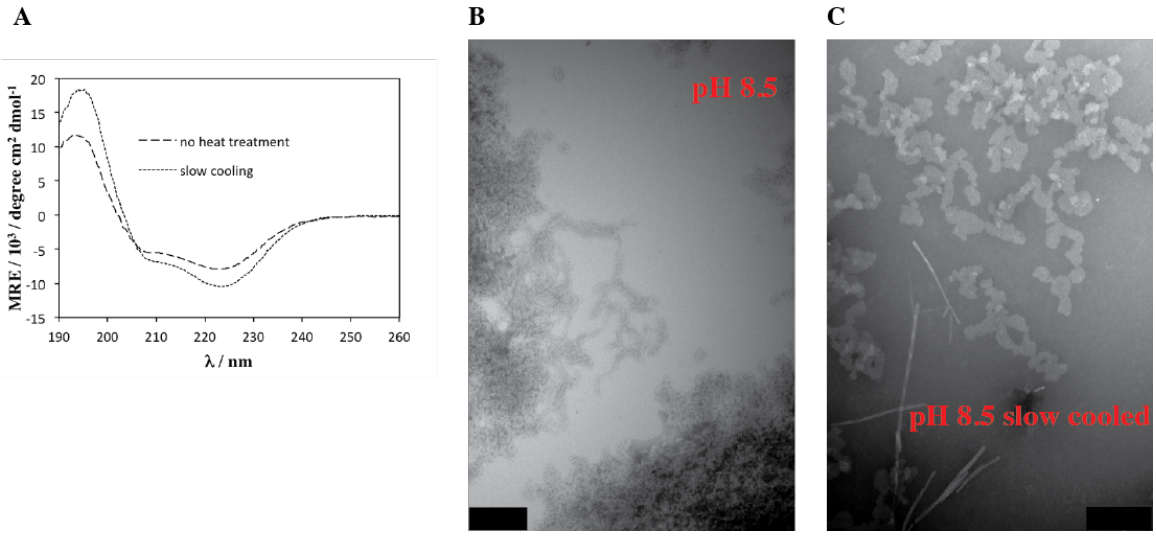

Figure 2.14 Characterization of 3FD-8IL. (a) CD spectrum obtained for 3FD-8IL in 10 mM TAPS buffer pH 8.5 (b) TEM image of 3FD-8IL after one day of assembly (c) TEM image of 3FD-8IL after thermal annealing; all scale bars correspond to 200 nm

pH 8.5. Circular dichroism spectropolarimetry reveals that **3FD-8IL** forms a similar CD signature to **3FD-IL** (Figure 2.14a). Transmission electron microscopy reveals that **3FD-8IL** formed fibrils after one day of assembly at pH 8.5; and after slow cooling, **3FD-8IL** appears to form small sheets and extended twisted fibrils (Figure 2.14b). Although **3FD-8IL** does appear to form nanosheets, these sheets are much smaller (maximum of 100 nm) than those formed by **3FD-IL** (Figure 2.14c). If **3FD-8IL** was a 3_{10} helix, I predict that the nanosheets formed should resemble those of **3FD-IL**. It is possible that the small nanosheets could form from an α-helix version of **3FD-8IL**, but with more difficulty because the faces of 3FD-8IL are each unique, and each unique face can only form complementary electrostatic interactions with itself. This could explain the smaller nanosheets formed by **3FD-8IL**, compared to **3FD-IL**.

Solid-state nuclear magnetic resonance was utilized to confirm the secondary structure of **3FD-IL**. A model of the **3FD-IL** nanosheets was created using molecular

dynamics simulations to measure potential distances within the α-helices and between α-helices. These models enabled the design of an isotope labeling scheme to determine the secondary structure of the peptide (Figure 2.15a). Two ^{13}C carbonyl labels were introduced at Ala-19 and Ala-20 of the **3FD-IL** peptide sequence (Figure 2.15b). These alanines were selected as their position in the middle of the sequence would be most likely folded, whereas the ends of the peptide could denature or unfold in solution. Furthermore, compared to other isotopically enriched amino acids (Glu, Lys, Ile, Leu), Fmoc-[1-^{13}C]Ala is the least expensive. Solid-state NMR DQF-DRAWS (double quantum filtered dipolar coupling with a windowless sequence), was utilized to measure the distance between the carbonyl carbon at Ala-19 to the carbonyl carbon at Ala-20[44,45]. It is important to note that the only dipolar coupling that will be observed is coupling between labeled amino acids on the same helix. The distance between alanine carbonyl carbons on adjacent helices is too far (> 6.92 Å) to have any observable dipolar coupling. The distance between backbone carbonyls in peptides is between 2.7-3.7 Å [46]. The DQF-DRAWS spectrum is very sensitive to variations in the dihedral angle

ϕ and can be thus utilized to determine secondary structure.

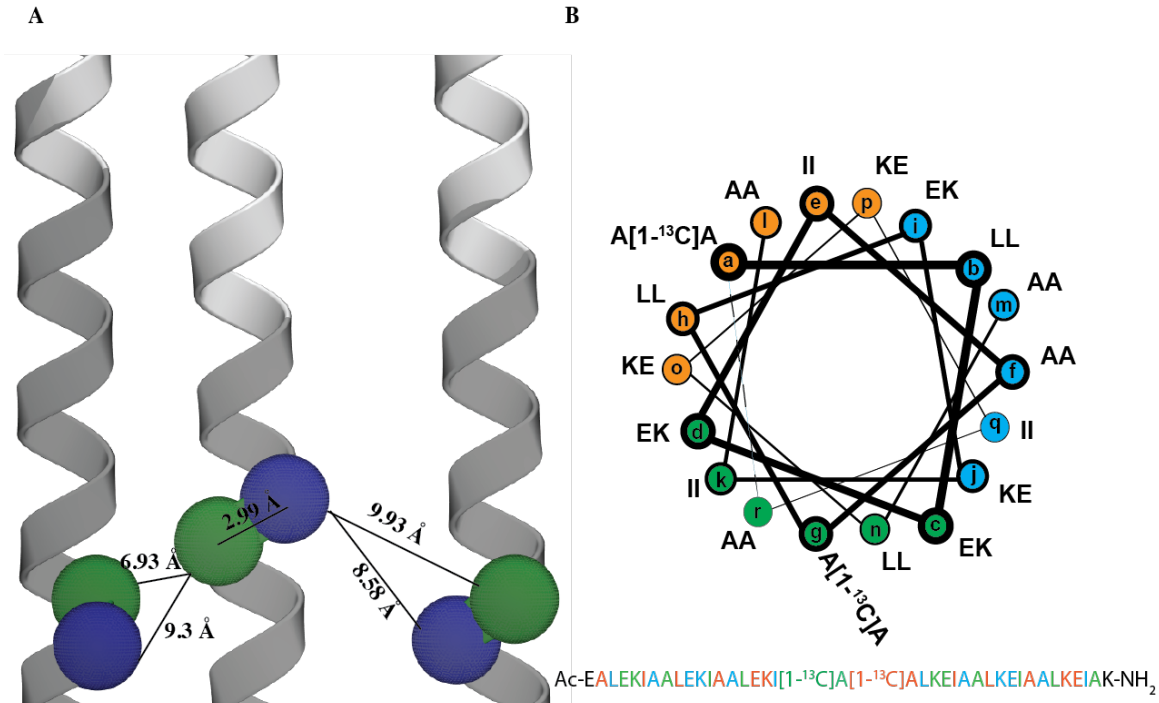

Figure 2.15 NMR Labeling Scheme for 3FD-IL_[1-^{13}C]Ala19, [1-^{13}C]Ala20 (a) structural model used for labeling (b) Helical wheel diagram and sequence of 3FD-IL_[1-^{13}C]Ala19, [1-^{13}C]Ala20

The ^{13}C spectrum contains two major resonances with chemical shifts at 179.6 ppm and at 176.6 ppm. The chemical shift at 176.6 ppm is consistent with the formation of an α-helix and is close to the chemical shift observed for the α-helical nanotubes

formed by the peptide

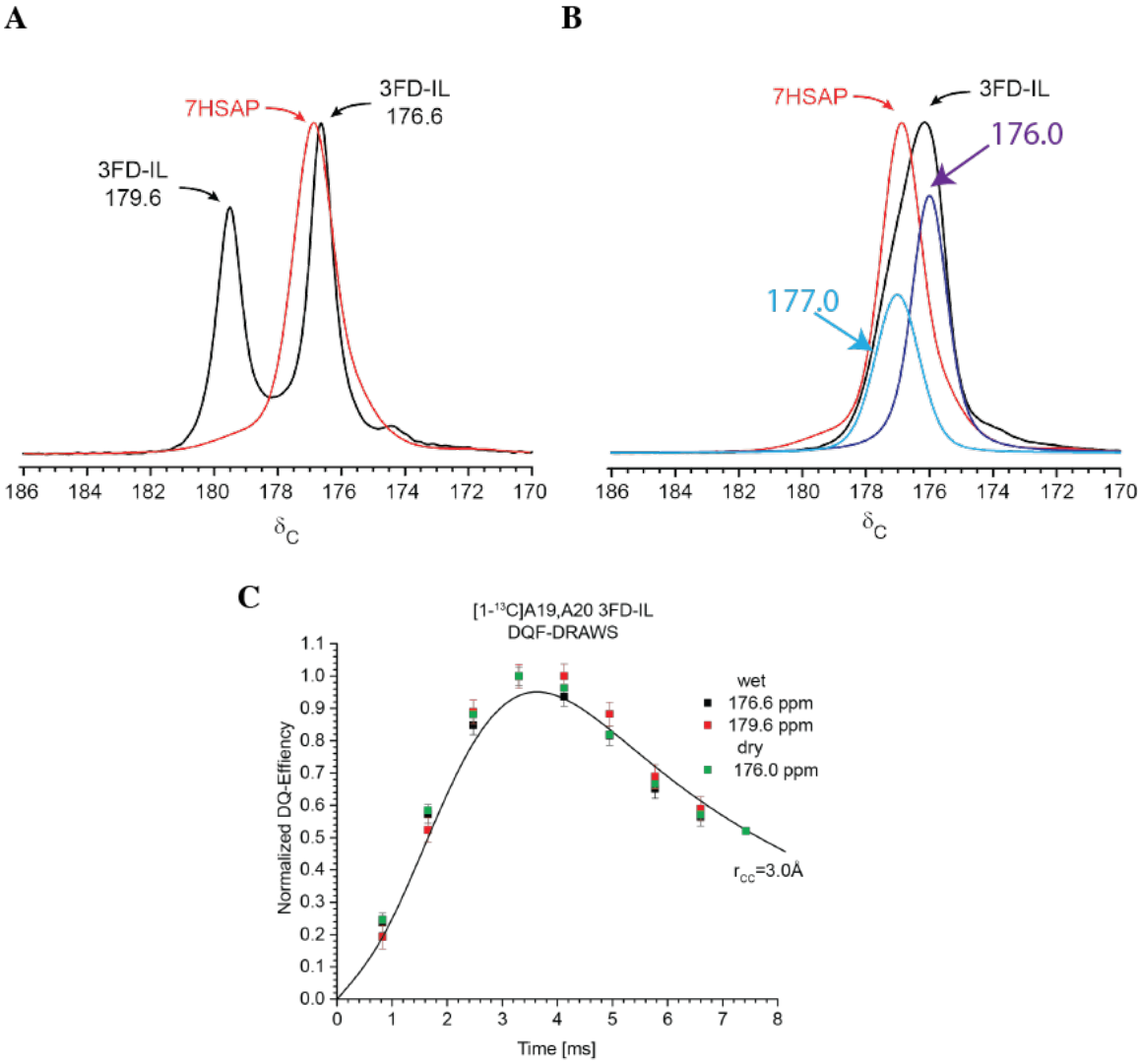

Figure 2.16 (a) ^{13}C spectrum of 3FD-IL_[1-^{13}C]Ala19, [1-^{13}C]-Ala20 nanosheets superimposed upon ^{13}C spectrum of α-helical peptide [1-^{13}C]Ala12-7HSAP (wet) (b) ^{13}C spectrum of 3FD-IL_[1-^{13}C]Ala19, [1-^{13}C]-Ala20 nanosheets superimposed upon ^{13}C spectrum of α-helical peptide [1-^{13}C]Ala12-7HSAP after further lyophilization (dry) (c) ^{13}C DQF-DRAWS curves of nanosheets formed from 3FD-IL_[1-^{13}C]Ala19, [1-^{13}C]-Ala20 can be fit to a ^{13}C-^{13}C distance of 3.0 Å for all three resonances observed

7HSAP-1 (Figure 2.16a, Figure 2.17a) [25]. Although the chemical shift observed at 179.6 ppm deviated from that observed for the **7HSAP-1** α-helices, DQF-DRAWS

analyses of the nanosheets showed that both peaks corresponded to a 3.0 Å distance between carbonyls, which is consistent with α-helical secondary structure (Figure 2.16c).

2.3.4 Solid-state NMR and the effect of hydration on structure

The presence of two resonances in the ^{13}C solid-state NMR spectrum could provide further information about the packing environment of the helices within the nanosheets. The presence of two peaks could indicate two possibilities, first, that the two peaks arise from different nuclei (i.e. one arises from Ala-19 and one arises from Ala-20) or second, that the two nuclei are in different packing environments. Because the ratio of the areas of the two peaks is 0.7:1, the first option is unlikely. It is more likely that there are two unique packing environments within the nanosheets. In membrane proteins, hydration affects the chemical shift and can be attributed to the presence of distinct domains within the membrane protein [47]. Because the original sample of the 3FD-IL_[1-^{13}C]Ala19, [1-^{13}C]-Ala20 nanosheets was lost, the peptide was resynthesized and assembled for additional NMR experiments. The ^{13}C spectrum of the new sample of nanosheets resembled that of the older sample and contained resonances at 179.6 and 176.6 ppm. The ratio of the areas of the peaks at 179.6 and 176.6 was also 0.7:1 (Figure 2.17b). In order to determine the effect of hydration on the chemical shifts within the ^{13}C spectrum, the The powder **3FD-IL** nanosheets were liapholized for three additional days to remove additional water. Upon liapholization, the ^{13}C spectrum revealed the presence of a broad peak, which could be fit to Gaussian distributions corresponding to resonances at 177.0 ppm and 176.0 ppm (Figure 2.17c). The ratio of the area of these two peaks remained the same, suggesting that the resonance at 177.0 ppm corresponded to the hydrated resonance at 179.6 ppm and that the resonance at 176.0 ppm corresponded to

the resonance of the hydrated sample at 176.6 ppm. Furthermore, fits of the DQF-DRAWS curves indicated that this spacing also corresponds to 3.0 Å (Figure 2.16c). This supports the hypothesis that the nuclei are in two different environments, one of which is more sensitive to hydration than the other.

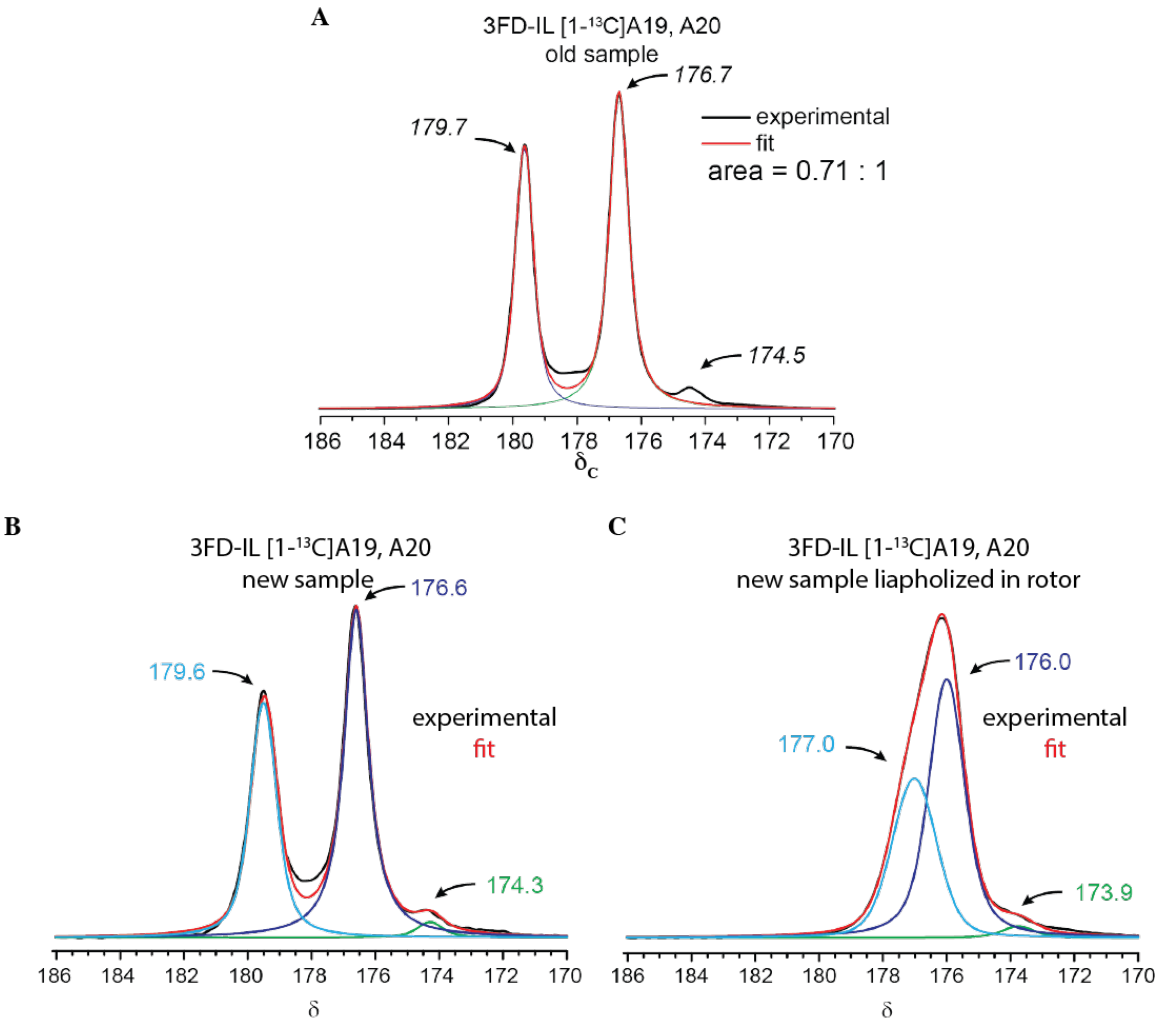

Figure 2.17 **^{13}C spectrums of different preparations of** 3FD-IL_[1-^{13}C]Ala19, [1-^{13}C]-Ala20 (a) older sample (b) new sample (c) new sample after liapholization

2.3.5 Powder Small Angle X-Ray Scattering

The solid-state NMR data indicated that the powder formulation of **3FD-IL** nanosheets could contain a different packing arrangement than that found in solution. Powder diffraction small angle x-ray scattering measurements were collected to examine the effect of drying down the nanosheets on internal structure. The powder diffraction revealed the possibility of a structural rearrangement from honeycomb to hexagonal close packed after liapholization of the **3FD-IL** nanosheets (Figure 2.18). The resultant small angle x-ray scattering measurements changed when the x-ray beam was shined on different positions of the powder sample. Both honeycomb and hexagonal close packed structures were detected. In comparison to solution, the distances for the diffraction peaks of the honeycomb structure were shifted to smaller distances. This likely corresponds to lattice shrinking upon drying down of the nanosheets due to dehydration. In the hexagonal close packed powder spectrum, only the middle peak which corresponded to

8.4 Å was observed.

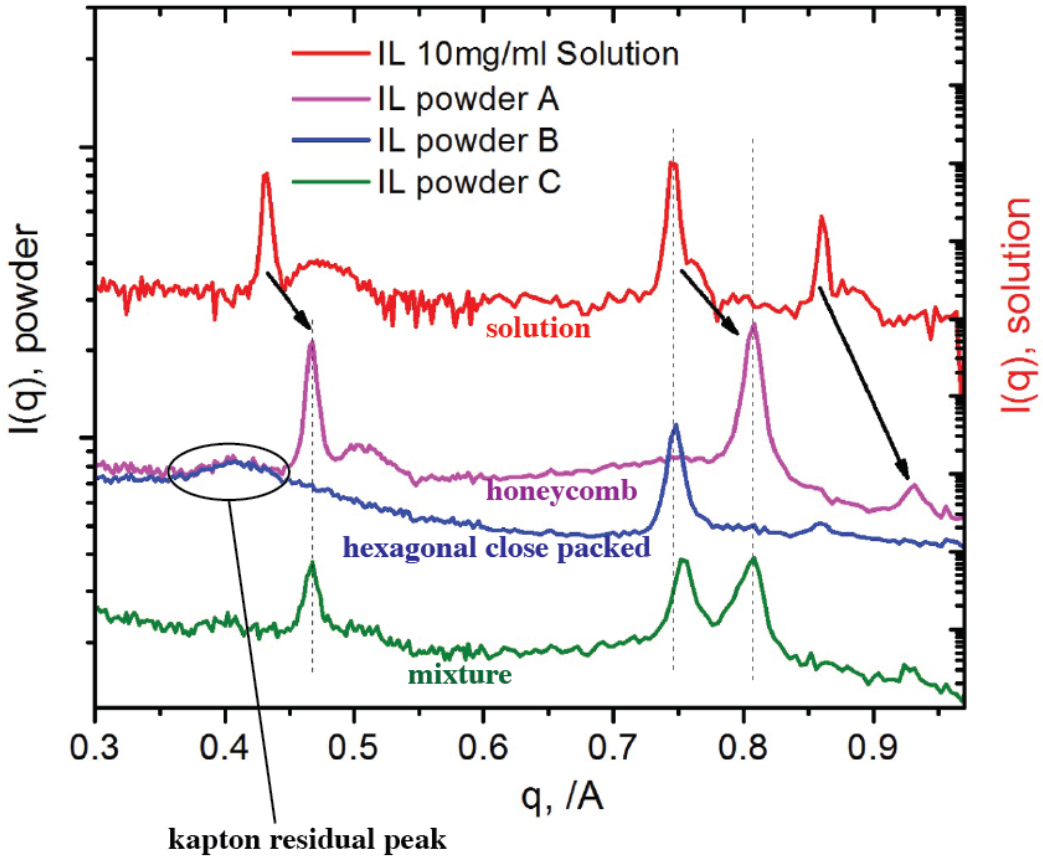

Figure 2.18 Small angle x-ray scattering powder diffraction measurements

2.3.6 Orientation of the 3FD-IL nanosheets

Fiber diffraction measurements can be performed to obtain structural information related to both helix packing and helix stacking of the **3FD-IL** nanosheets. Fibers were produced by drying a droplet of **3FD-IL** nanosheets within a capillary tube. Surface tension caused the droplet to dry into a fiber. Fiber diffraction reveals reflections, which corresponded to distances of 30 Å, 21.86 Å, 9.2 Å, and 4.5 Å. The first two distances corresponded to ½ the length of one **3FD-IL** α-helix and 1/3 the length of one 3FD-IL α-helix. The distance, which would result due to the length of the α-helix, is obscured

because of the beamstop. The latter two distances are related to the translation per residue along the α-helical axis. The distance of 4.5 Å is three times the α-helix translation of 1.5 Å per residue, and 9.2 Å is about six times the a-helix translation of 1.5 Å per residue. This data supports the formation of an α-helix with three-fold symmetry.

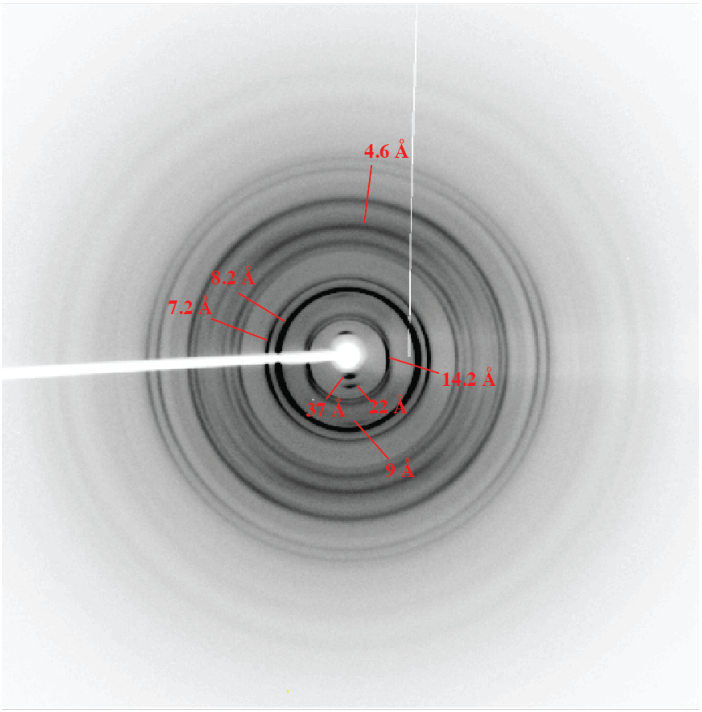

Figure 2.19 X-ray diffraction image of 3FD-IL fibers

Additional distances are obtained at 14.12 Å, 8.43 Å, 7.3 Å, which are related to the hexagonal packing of helices within the nanosheets (Figure 2.19).

The orientation of the nanosheets can be explored by shining the x-ray beam on either the face or the edge of the **3FD-IL** nanosheets when they are dried on parafilm to produce a film (Figure 2.20). Due to the large size in the xy plane, if the nanosheets are oriented they should dry such that the xy plane is parallel to the surface of the parafilm. When the x-ray beam is shined on the face of the film (xy plane), a series of rings are obtained which corresponded to distances of 14.48 Å, 8.44 Å, 7.3 Å. These distances are

identical to the Bragg diffraction peaks, which occurred in the small angle x-ray scattering spectra and correspond to the hexagonal packing of α-helices within the nanosheets. The presence of rings suggested that when the **3FD-IL** nanosheets were dried, the sheets were not all arranged in the same orientation, leading to azimuthal averaging. When the x-ray beam was shined on the edge of the nanosheet, spacings related to the hexagonal spacings of the α-helices obtained above are also obtained, but in this case meridional reflections are obtained rather than rings due to preferential orientation of the sheets with respect to the long axis of the fibril.

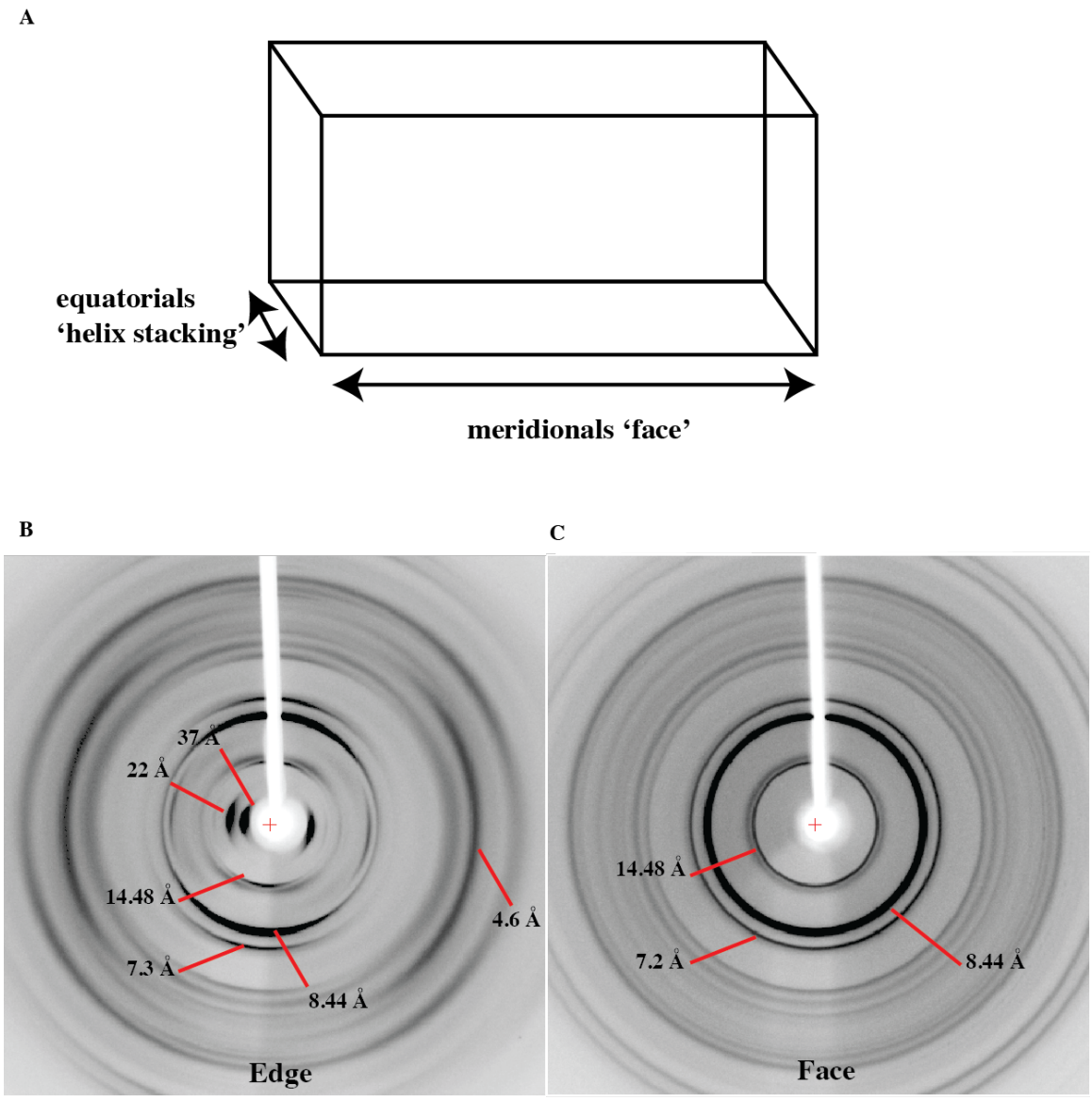

Figure 2.20 Oriented x-ray diffraction of 3FD-IL films (a) Schematic showing sheet-stacking and sheet-packing dimensions (b) x-ray diffraction images of the edge and face of the 3FD-IL films

Small angle x-ray scattering was also utilized to obtain information on the orientation of the **3FD-IL** two-dimensional assemblies. **3FD-IL** films were brought to Argonne National Laboratory for analysis. Small angle x-ray scattering of the edge revealed distances related to the length of the helix and hexagonal packing (Figure 2.21). In contrast to the fiber diffraction results, small angle x-ray scattering allowed for

observation of the full length of the **3FD-IL** α-helix or 65.42 Å. Distances are also observed at approximately half the length of the **3FD-IL** α-helix (36.30 Å) and two distances related to hexagonal packing of α-helices (8.46 Å and 7.32 Å). In contrast, on the face of the film only the 8.46 Å distance is revealed. This could suggest that upon drying there is a change in helix packing.

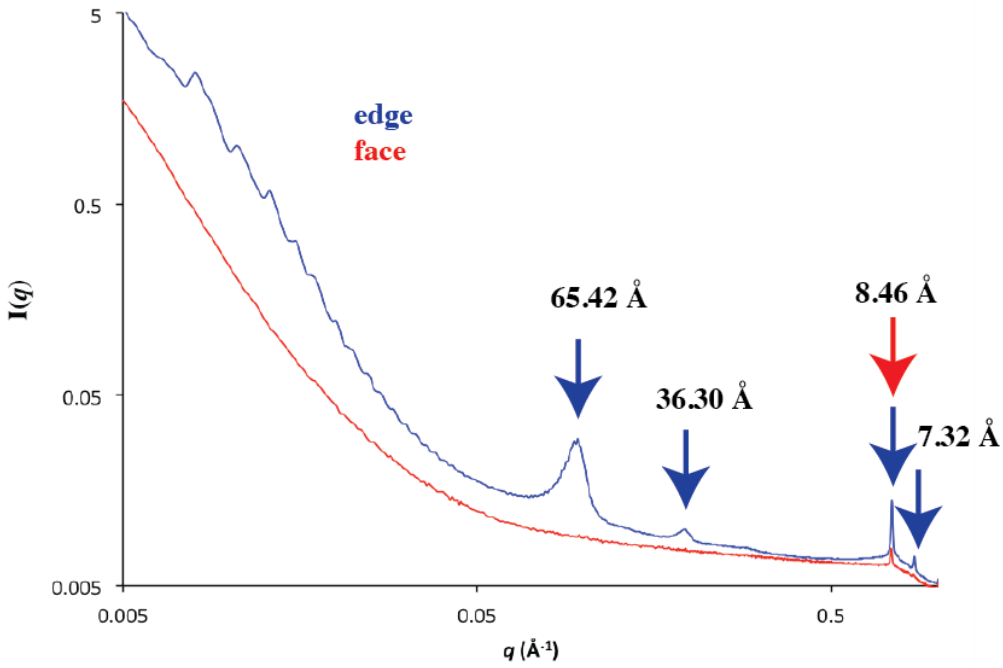

Figure 2.21 Oriented small angle x-ray scattering curves from the face and edge of the 3FD-IL films

2.3.5 Hexagonal lattice of 3FD-IL

As previously mentioned, the small angle x-ray scattering scattering curve, described above, shows Bragg diffraction peaks in the high q region that have a geometric relationship consistent with hexagonal packing of the helices within the

nanosheets. The three-fold design of the **3FD-IL** α-helices permits the helices to arrange in a hexagonal orientation through hydrophobic interactions and electrostatic interactions between each face.

There are two possible types of hexagonal packing, hexagonal close packed and hexagonal honeycomb. In the hexagonal close packed arrangement, six helices are arranged in a hexagon, and in the center of the hexagon, there is an additional helix (Figure 2.22a). In the honeycomb arrangement of helices, the center helix is removed (Figure 2.22b). In order to distinguish between these two types of hexagonal packing, scanning transmission electron microscopy experiments were performed. Scanning transmission electron microscopy allows for an experimental determination of the mass per area of the **3FD-IL** assemblies, which can be utilized to distinguish between different unit cells.

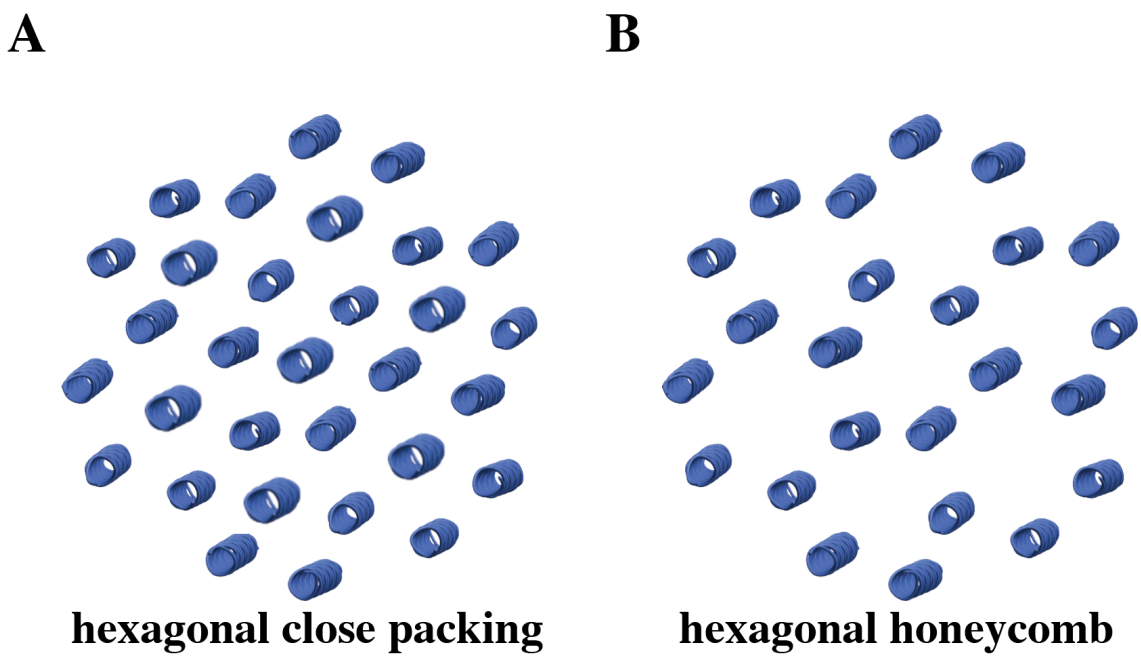

Figure 2.22 Two modes of hexagonal packing for the α-helices within the 3FD-IL nanosheets (a) hexagonal close packing and (b) hexagonal honeycomb packing

The mass of the two unit cells can be calculated by multiplying the mass of the **3FD-IL** helix times the number of helices in each unit cell. The hexagonal close packed unit cell contains four helices, which are shared equally between four adjacent unit cells, giving it one helix per cell (Figure 2.23a) and a mass of 4070 Da. The hexagonal honeycomb unit cell contains the two helices found in the center of the unit cell (Figure 2.23b), giving it a mass of 8140 Da. In order to calculate the area of each unit cell, the Bragg diffraction peaks from the small angle x-ray scattering data can be utilized to determine the interhelical distance **a**, which was calculated to be 9.7 Å (through basic trigonometry). The area of each of the proposed hexagonal unit cells can be calculated using the formula for area of a parallelogram or base times height. The height of each unit cell corresponds to the distance from the (100) and (010) lattice planes. The base of a hexagonal close packed unit cell is equivalent to the interhelical distance **a**, or 9.7 Å, and the base of a honeycomb unit cell is equal to $\sqrt{3}\mathbf{a}$ or 16.8 Å. The height of the hexagonal close packed unit cell is 8.4 Å, and the height of the honeycomb unit cell is 14.5 Å. The mass per area of a theoretical hexagonal close packed unit cell is the mass of one **3FD-IL** α-helix divided by the area or 49.9 Da /Å^2. In contrast, the mass per area for a theoretical hexagonal honeycomb unit cell is 33.4 Da / Å^2.

A histogram of the experimental mass per area measurements reveal the presence of one major mass per area peak and a second minor peak (Figure 2.24b). Gaussian functions fit to the experimental data yielded 31.2 Da/ Å^2 for the major distribution peak and 37.9 Da/ Å^2 for the minor peak. The major peak of 31.2 Da / Å^2 suggests that a majority of the nanosheets adopt a hexagonal honeycomb arrangement. The presence of the minor peak suggested that there is a small population of nanosheets, which adopted

the hexagonal close packed arrangement. Furthermore, an FFT of a negatively stained 3FD-IL nanosheet provided further evidence for a hexagonal lattice. The reflection observed in the FFT corresponded to a distance of 15.1 Å, which is closest to the largest Bragg diffraction peak from the small angle x-ray scattering curve (Figure 2.24a).

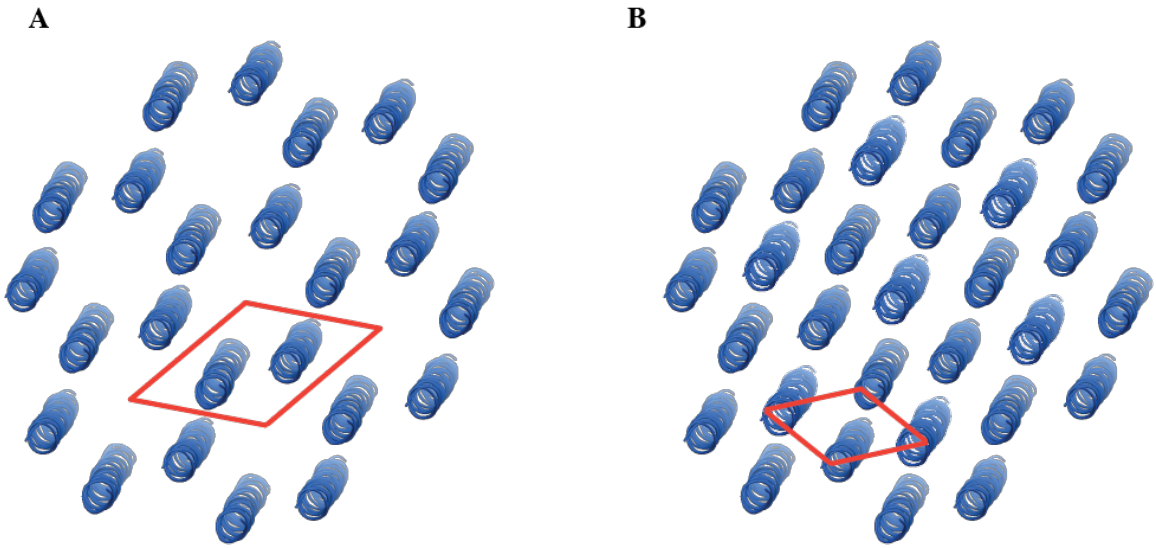

Figure 2.23 Unit cells (orange parallelograms) for (a) hexagonal honeycomb and (b) hexagonal close packed internal structures

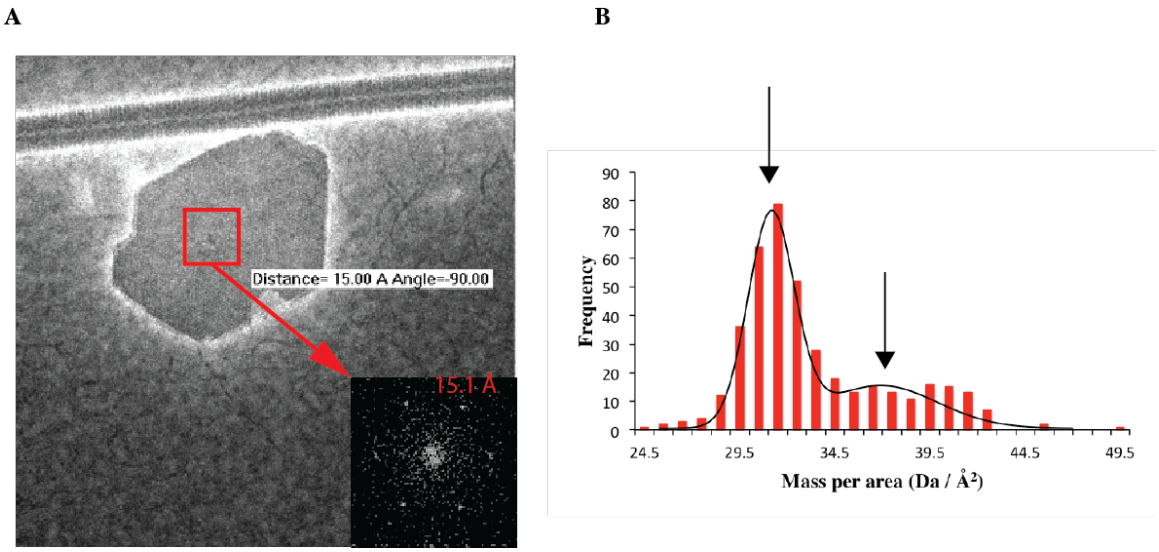

Figure 2.24 (a) Negative stained scanning transmission electron microscopy image of a 3FD-IL nanosheet and fast fourier transform which showed hexagonal symmetry and reflection at 15.1 Å (b) histogram of the mass per area measurements calculated from STEM data and a Gaussian fit which reveals a major distribution at ; 31.2 Da/ $Å^2$ and a minor distribution at 37.9 $Da/Å^2$.

Modeling of the small angle x-ray scattering data can also be utilized to obtain more evidence that the **3FD-IL** nanosheets adopted a honeycomb structure (Figure 2.25). Figure 2.25 shows the scattering profile of a single α-helix (cyan). The diffraction peak intensity of the experimental scattering data (red) roughly follows the scattering intensity of the single α-helix. Upon formation of a disc object, oscillations arise after a q value of 0.1 $Å^{-1}$ due to the sheet thickness. The experimental data closely resembles that of a honeycomb sheet (blue) or a honeycomb sheet filled with water (green). If a honeycomb sheet was filled with a peptide helix (red), i.e. or if it is in a hexagonal close packed arrangement, the scattering profile loses the first and third diffraction peaks. This data supported the STEM data, suggesting that the **3FD-IL** nanosheets adopt a hexagonal honeycomb arrangement. Furthermore, the data suggested that the internal channels within the **3FD-IL** nanosheets are filled with water.

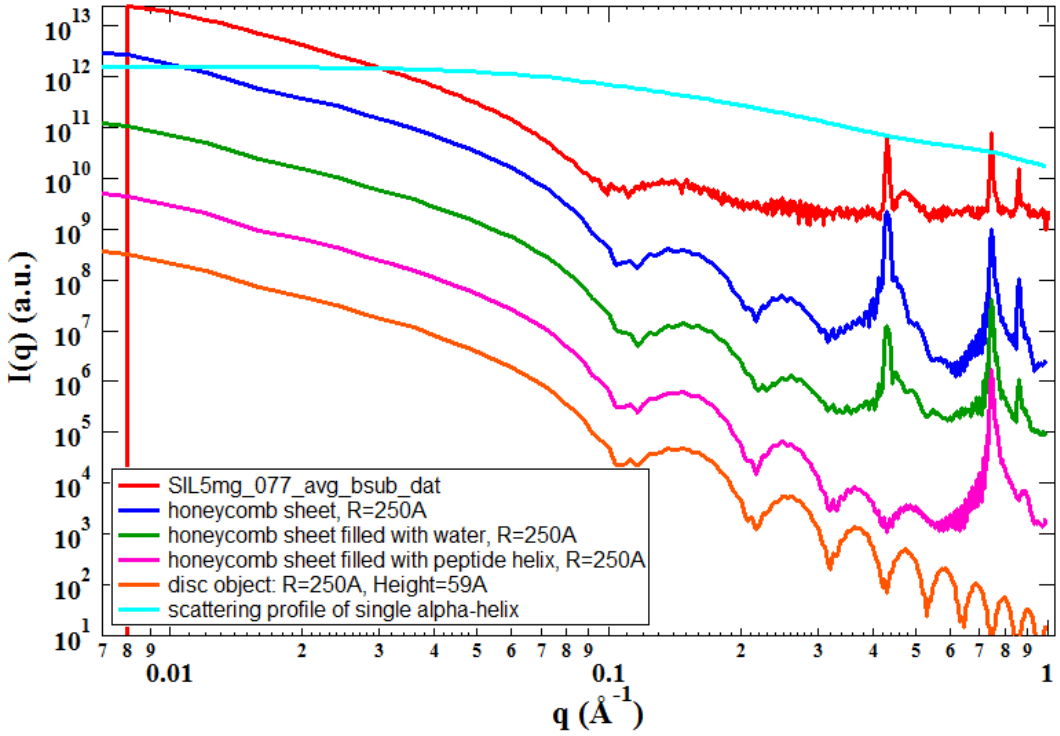

Figure 2.25 Modeling of the small angle x-ray scattering data to determine the packing arrangement of the helices within the 3FD-IL nanosheets

2.4 Conclusions

2.4.1 Model for Nanosheets

The peptide **3FD-IL** formed nanosheets on the order of hundreds of nanometers, which are persistent in solution. As the circular dichroism measurements and solid state NMR experiments showed, **3FD-IL** formed an α-helix, consistent with its design. As the fiber diffraction measurements showed, the **3FD-IL** helix contained three-fold symmetry, consistent with the design of the peptide nanosheets. The AFM and SAXS analysis indicated that the nanosheets have a thickness between 6.1 and 6.5 nanometers, which suggested that the helices within the nanosheets are perpendicular to the plane of the nanosheets. Small angle x-ray scattering and fiber diffraction measurements indicated that the nanosheets formed by **3FD-IL** are two-dimensional. The helices within the

nanosheets adopted a hexagonal honeycomb arrangement of helices with highly ordered internal structure. The diffraction peaks obtained from SAXS corresponded to distances from the (100) lattice plane (14.5 Å), the (200) lattice plane (7.3 Å), and the (110) lattice plane (8.4 Å) (Figure 2.26). Simple trigonometry yielded an inter-helical distance of 9.7 Å, which is consistent with interhelix spacings in crystal structures [48].

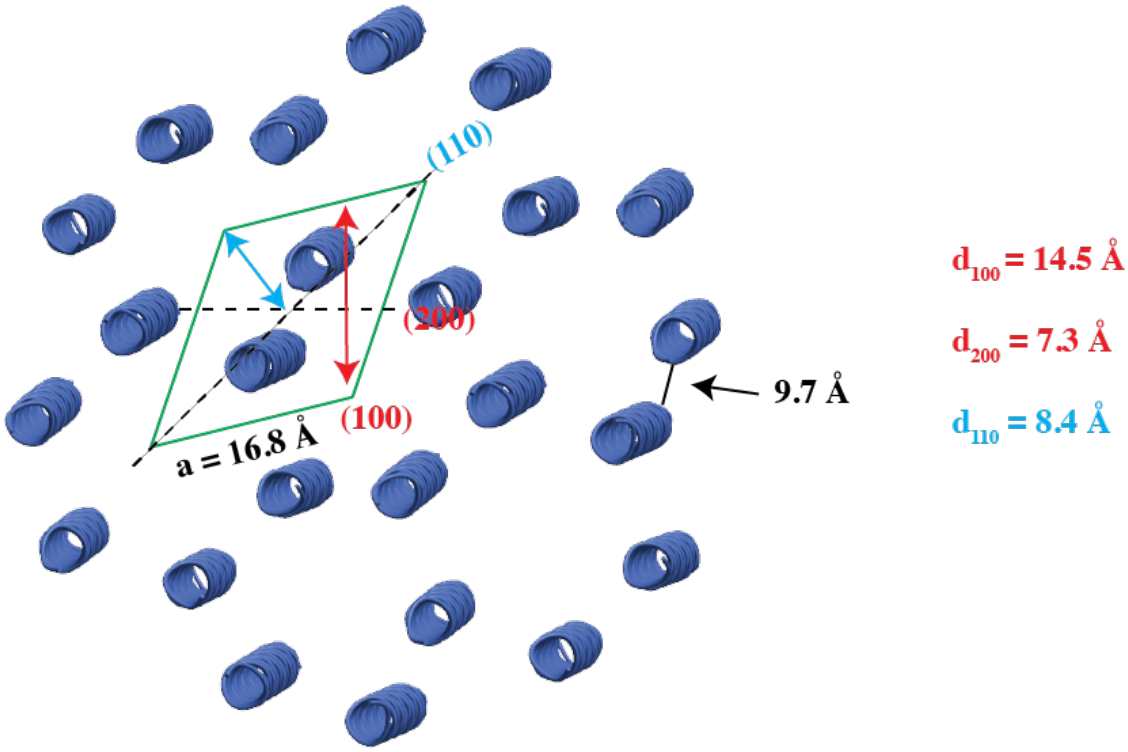

Figure 2.26 Model for the structure of the 3FD-IL nanosheets

2.4.2 Cryo-electron microscopy to determine the structure of the nanosheets

The final experiment performed on the **3FD-IL** nanosheets was cryo-electron microscopy imaging. Cryo-electron microscopy can be utilized to determine the structure

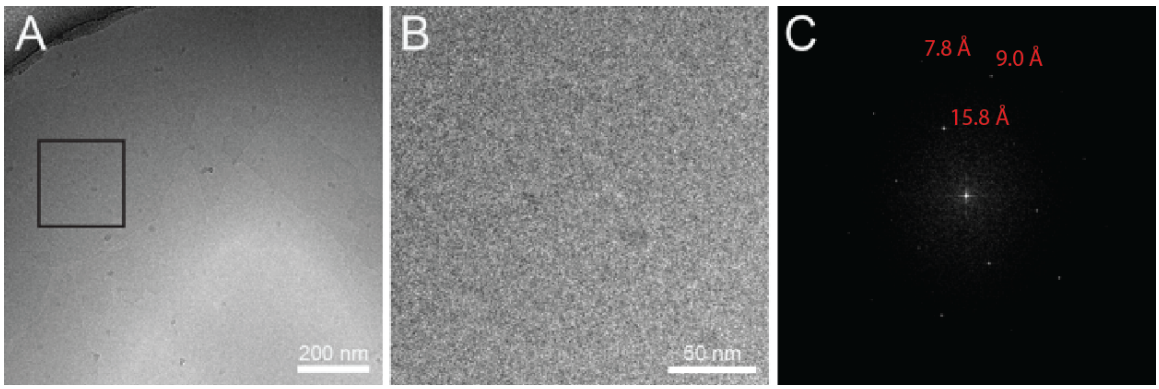

Figure 2.27 (a) Cryo-electron microscopy image of nanosheets (b) zoomed in image of the boxed region of (a) (c) Fourier transform of the boxed in region of (a) indicating the diffraction spacings

of peptide assemblies to atomic level resolution. Initial cryo-electron microscopy imaging revealed the presence of nanosheets. A fast fourier transform (FFT) of the nanosheet revealed the presence of a hexagonal lattice with lattice spacings at 15.8 Å, 9.0 Å, and 7.8 Å (Figure 2.27). An FFT of the ice outside of the region of the nanosheet contained an absence of reflections, confirming that the spacings observed by cryo-electron microscopy are

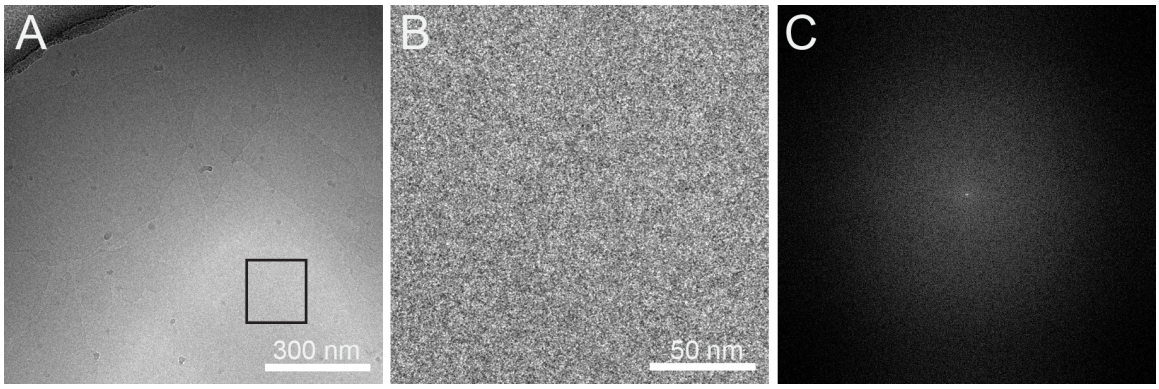

Figure 2.28 (a) cryo-EM image of 3FD-IL nanosheets (b) zoomed in image of the ice, or the boxed in region from (a) (c) FFT of the ice

observed due to the hexagonal lattice within the **3FD-IL** nanosheets (Figure 2.28).

The spacings observed are close to those determined from small angle x-ray scattering. Preliminary cryo-EM reconstruction revealed that the nanosheets contained a trigonal unit cell with p3 symmetry (Figure 2.29). The side length of the unit cell was 18 Å, which is slightly larger than the distance calculated from the SAXS measurements. The data from the reconstruction revealed that the structure resembled that of the model built from the other biophysical data. Future work on this project will use cryo-electron microscopy to determine the high resolution structure of the nanosheets. This will aid in potential application of the nanosheets for nanoarchitectonics.

These experiments highlight the potential of the three-fold α-helical design for the design of ordered assemblies. Although collagen mimetic peptide substrates have been utilized to create highly ordered nanosheets, the mechanism in which these substrates form highly ordered nanosheets is unclear.[4,6,49] The use of a three-fold α-helix allowed for the formation of hexagonal honeycomb nanosheets, which could be predicted based on the design. S-layer proteins form specific lattices, which are used as molecular sieves to contain or keep molecules in and out of the cell. The nanosheets formed by **3FD-IL** recapitulate the porous internal structure of some of these S-layer proteins.[50,51] In contrast to the sequences of S-layer proteins, which are not conserved and thus difficult to use as building blocks for nanosheets, the **3FD-IL** sequence platform represents a simple way to build porous nanosheets.

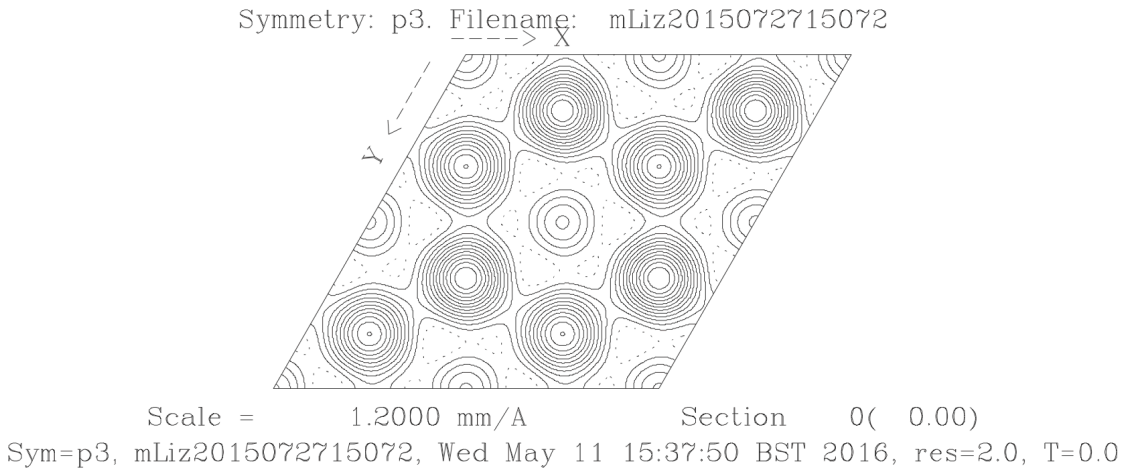

Figure 2.29 Preliminary cryo-EM reconstruction revealed that the 3FD-IL nanosheets contained a trigonal unit cell with symmetry p3

2.5 Methods and Supporting Information

Reagents: All Fmoc amino acids were purchased from Anaspec Inc. (Fremont, CA). The Fmoc-Peg-PAL-PS resin for solid-phase peptide synthesis was purchased from Applied Biosystems. All other chemicals were purchased from Sigma-Aldrich.

Peptide synthesis: The peptide 3FD-IL and its variants were synthesized using microwave-assisted synthesis on a CEM Liberty solid-phase peptide synthesizer. A Fmoc-PEG-PAL-PS resin (Applied Biosystems) was used for synthesis. Standard Fmoc protection chemistry was used for coupling, which was promoted using standard activation protocols based on DIEA/HBTU and base-induced deprotection of the Fmoc group (20 % piperidine in DMF). All peptides were acetylated at the N-terminus using

20 % acetic anhydride. The peptides were purified using reverse phase high performance liquid chromatography (HPLC) on a C18 column using a water-acetonitrile (0.1 % trifluoroacetic acid) gradient. The target HPLC fractions were collected and liapholized. The purity of the peptides was analyzed using electrospray ionization mass spectrometry and analytical HPLC.

Peptide Assembly: The peptide 3FD-IL was dissolved in 10 mM TAPS buffer at pH 8.5 unless otherwise noted. Nanosheets were produced after thermal annealing in a thermal cycler. The annealing method initially heated up the peptide to 90° C for ten minutes followed by cooling 0.2° C/ 5 minutes to a final temperature of 40 °C. The resultant nanosheets were stored at room temperature.

Circular Dichroism: CD spectra were recorded on a Jasco J-810 CD spectropolarimeter in 0.1 mm quartz cells (Hellma Analytics) at a peptide concentration of 1 mg/mL in 10 mM TAPS buffer pH 8.5. Spectra were recorded at a scanning rate of 50 nm/min and a resolution of 0.1 nm. CD melting experiments were performed in the temperature range from 5°C to 95°C at a heating rate of 40 °C/hour. The intensity of the CD signal at 222 nm was monitored as a function of temperature. Melting temperatures were obtained from the first derivative of the melting curves.

Transmission Electron Microscopy: TEM specimens were prepared from aqueous solutions of 3FD-IL (10 mg/mL) and its variants. The samples were deposited onto 200 mesh carbon-coated copper grids from Electron Microscopy Sciences (Hatfield, PA).

After a 1 min incubation period, the samples were washed with water and stained with an aqueous solution of 0.1 % phosphotungstate stain. Excess stain was wicked away from the grids after incubation on the grid for 30 s. TEM measurements were acquired on a JEOL JEM-1400 transmission electron microscope at an accelerating voltage of 120 kV.

Atomic force microscopy: AFM specimens were prepared from 10 mg/mL solutions of 3FD-IL. The 3FD-IL solution was diluted to 0.25 mg/mL using 0.5 mM TAPS buffer pH 8.5 right before deposition on a freshly cleaved mica substrate. The sample was spin-coated using a spin coater at a rate of 1.5 rpm for 1 min. The AFM experiments wereperformed using a MFP-3D-BIO from Asylum Research. Silicon AFM tips (MikronMasch) with a force constant (5.4-16 N/m) were used to image the specimens in tapping mode at a scan rate of 1 Hz.

Cryo-electron microscopy: 3FD-IL nanosheets (10 mg/mL) in 10 mM TAPS (pH 8.5) were utilized for cryo-electron microscopy. The nanosheets were diluted to a concentration of 1 mg/mL using 10 mM TAPS (pH 8.5) buffer. Cryo-EM specimens were prepared by applying 4 μl aliquots to glow-discharged 200 mesh copper Quantifoil grids and plunge freezing in liquid ethane using a Vitrobot Mark III (FEI, Hillsboro, Oregon). Cryo-EM data was collected using a JEOL JEM-2200FS 200 kV FEG-TEM with an in-column Omega energy filter (slit width 20 eV). Images were acquired on a Direct Electron, LP DE-20 direct electron detector (San Diego, CA) at a nominal magnification of 20,000× for a pixel size of 2.94 Å.

Scanning transmission electron microscopy: The STEM specimen was prepared by dialyzing a solution of 3FD-IL nanosheets (10 mg/mL) in 10 mM TAPS buffer (pH 8.5) against pure water. The STEM data were acquired at Brookhaven National Laboratory (BNL). The STEM instrument operates at 40 keV with a scanning probe of <0.3 nm diameter produced from a cold field- emission source. Every electron emerging from the specimen is detected by one of the scintillator-photomultiplier detectors collecting 0!15 mRadian (bright field), 15!40 mRadian (small- angle dark field), and 40!200 mRadian (large-angle dark field). The large-angle signal is proportional to the mass of atoms in the path of the beam. Specimen quality and mass calibration are checked by detailed comparison of the image to the known structure of tobacco mosaic virus (TMV). For mass-per-area (M/A) measurements, TMV rafts at a theoretical M/A value of 81.9 Da/Å^2 were employed for calibration.

Specimens are deposited on thin carbon (ca. 2 nm thick) supported on a thicker holey carbon film mounted on a titanium grid using the wet-film, hanging-drop method http://www.bnl. gov/biology/stem/SpecPrepDetails.asp. TMV is added to the grid first as an internal control, followed by injection buffer, then specimen solution (in 20 mM MOPS buffer, pH 7.0) for 1 min, then 10 washes of 20 mM ammonium acetate, pH 7.0. Excess solution is wicked from the edge with filter paper between each injection. After the last wash, the grid is wicked to a thin layer (ca. 1 μm), fast frozen by plunging into liquid nitrogen slush, and stored under liquid nitrogen. Grids are freeze dried overnight in an ion-pumped chamber with

an efficient cold trap and transferred under vacuum to the STEM cold stage (!160 °C). Imaging typically uses a dose of 20 el/Å^2 (causing <5% mass loss, corrected by comparison to TMV).

Mass measurements were performed off-line with customized software (PCMass, available at ftp.stem.bnl.gov). The program masks out objects significantly above background and computes the value for the thin carbon in the remaining areas, which is subtracted, and pixels within the contour of filaments are summed and divided by area to give mass-per-unit-area. Accuracy is determined by cleanliness of the background between objects and by counting statistics of the scattered electrons. For TMV, the program provides automatic searching and measurement, but manual selection was employed for the thin sheets. PCMass also provides statistics in a database for individual images or groups of images.

Small angle x-ray scattering: 3FD-IL was prepared for small angle x-ray scattering measurements at a peptide concentration of 10 mg/mL in 10 mM TAPS buffer, pH 8.5. The 3FD-IL solution was thermally annealed and the nanosheets and dialyzed against 10 mM TAPS (pH 8.5) to remove residual trifluoroacetic acid. Synchrotron SAXS/WAXS measurements were performed at the 12-ID-B beamline of Advanced Photon Source at Argonne National Laboratory. A simultaneous SAXS/WAXS setup was utilized, and the sample-to-detector distances were set such that the overall scattering momentum transfer, q, range was achieved from 0.005 to 2.4 Å–1, where $q = 4\pi\sin\theta/\lambda$, 2θ denoting the scattering angle and λ the X-ray wavelength. The wavelength was set at 1.033 Å during

the measurements. Scattered X-ray intensities were measured using a Pilatus 2 M (DECTRIS Ltd.) detector for SAXS and Pilatus 300K for WAXS. SAXS/WAXS measurements were performed on aqueous solutions of peptides at 25 °C. A quartz capillary flow cell (1.5 mm diameter) was employed to prevent radiation damage. Twenty images were collected for each sample and buffer. The 2D scattering images were converted to 1D SAXS curves through azimuthal averaging after solid angle correction and then normalizing with the intensity of the transmitted X-ray beam, using the software package at beamline 12ID-B. The 1D curves of the samples were averaged and subtracted with the background measured from the corresponding buffers.

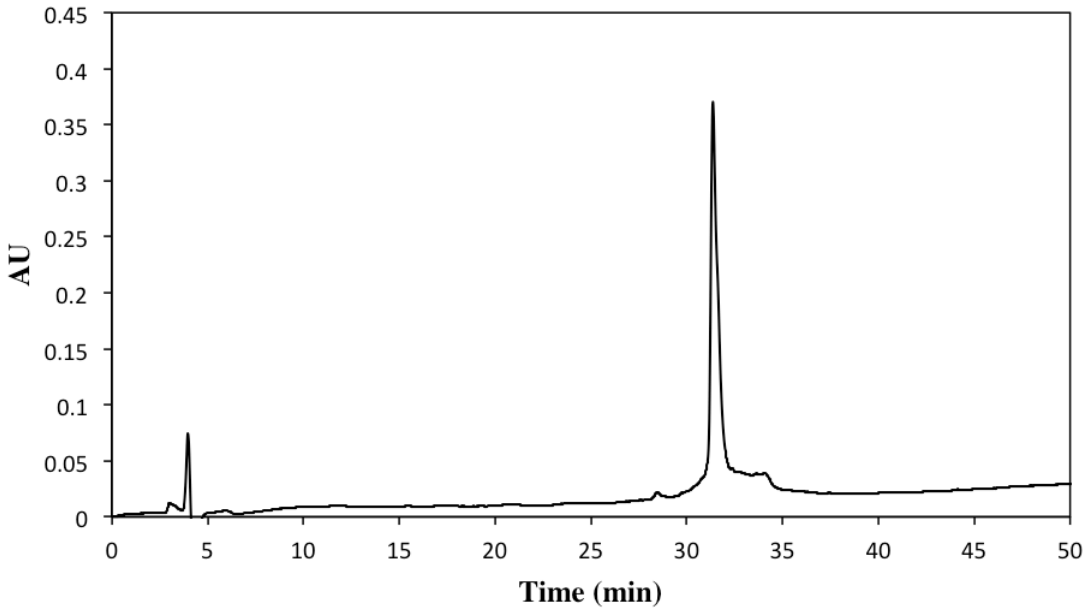

Figure 2.30 Analytical HPLC spectrum of 3FD-IL

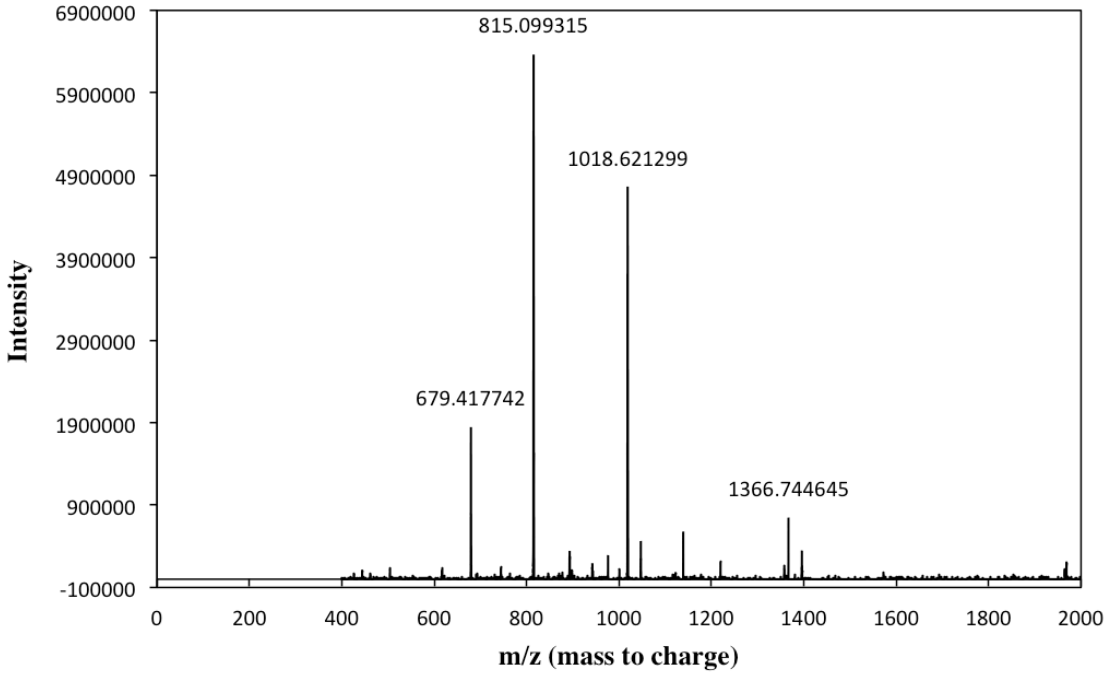

Figure 2.31 Mass spectrum of 3FD-IL

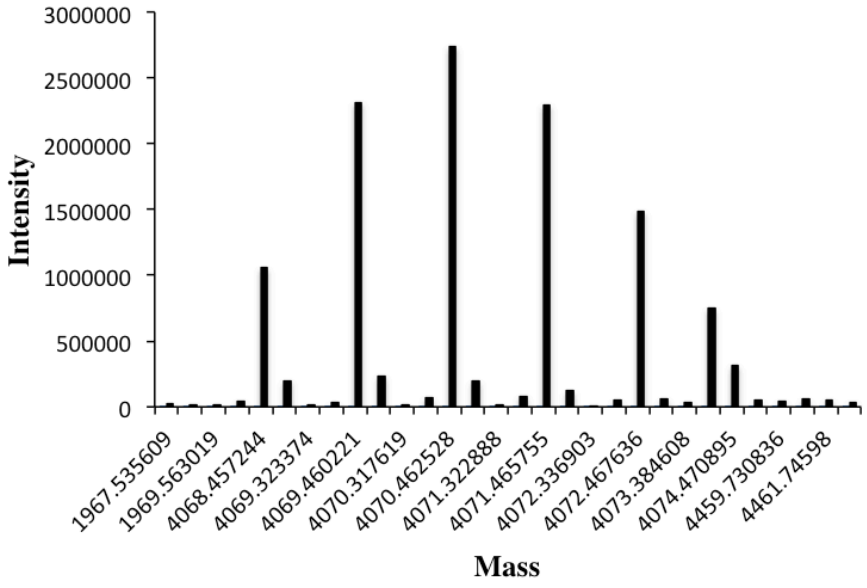

Figure 2.32 Deconvoluted mass spectrum of 3FD-IL

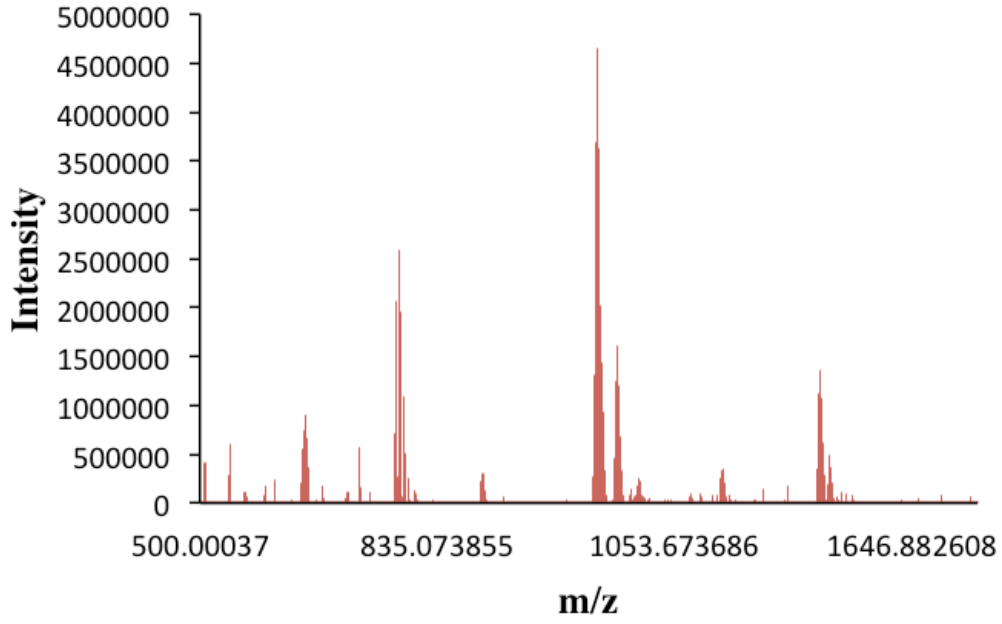

Figure 2.33 Mass spectrum of 3FD-IL-[1-^{13}C]Ala19-[1-^{13}C]Ala20

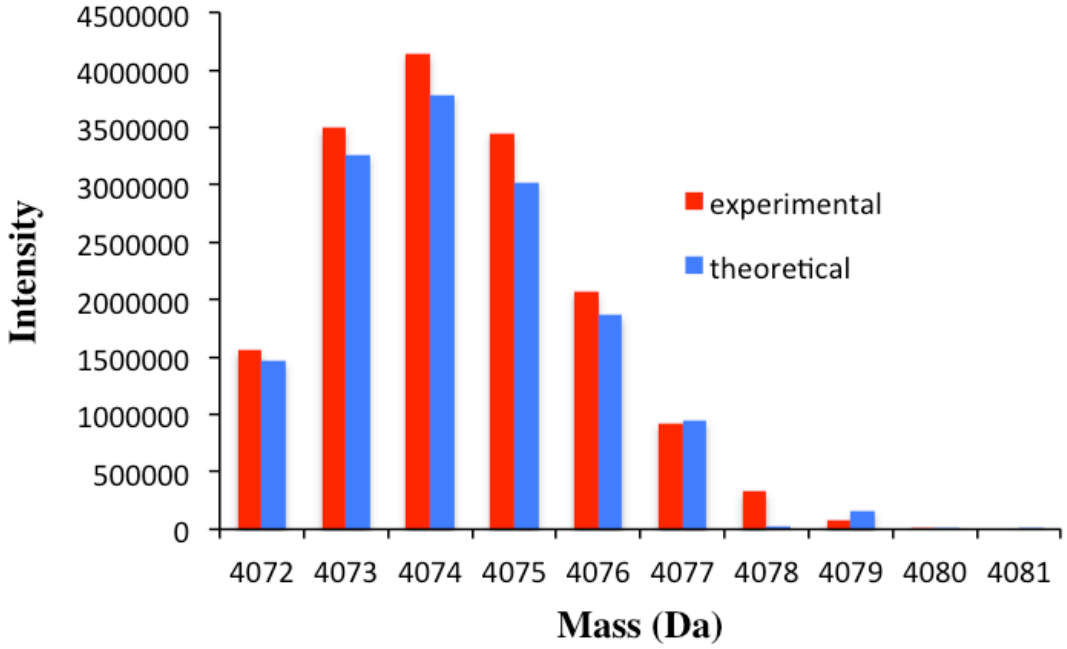

Figure 2.34 Deconvolution of 3FD-IL-[1-^{13}C]Ala19-[1-^{13}C]Ala20 mass spectrum

2.6 ReferencesUncategorized References

1. Castelletto V, Hamley IW, Cenker C, Olsson U (2010) Influence of Salt on the Self-Assembly of Two Model Amyloid Heptapeptides. J Phys Chem B 114 (23):8002-8008. doi:DOI 10.1021/jp102744g
2. Dai B, Li D, Xi W, Luo F, Zhang X, Zou M, Cao M, Hu J, Wang W, Wei G, Zhang Y, Liu C (2015) Tunable assembly of amyloid-forming peptides into nanosheets as a retrovirus carrier. Proc Natl Acad Sci U S A 112 (10):2996-3001. doi:10.1073/pnas.1416690112
3. Hamley IW, Dehsorkhi A, Castelletto V (2013) Self-assembled arginine-coated peptide nanosheets in water. Chem Commun 49 (18):1850-1852. doi:DOI 10.1039/c3cc39057h
4. Jiang T, Vail OA, Jiang Z, Zuo X, Conticello VP (2015) Rational Design of Multilayer Collagen Nanosheets with Compositional and Structural Control. J Am Chem Soc 137 (24):7793-7802. doi:10.1021/jacs.5b03326
5. Jiang T, Xu C, Zuo X, Conticello VP (2014) Structurally homogeneous nanosheets from self-assembly of a collagen-mimetic peptide. Angew Chem Int Ed Engl 53 (32):8367-8371. doi:10.1002/anie.201403780
6. Jiang T, Xu CF, Liu Y, Liu Z, Wall JS, Zuo XB, Lian TQ, Salaita K, Ni CY, Pochan D, Conticello VP (2014) Structurally Defined Nanoscale Sheets from Self-Assembly of Collagen-Mimetic Peptides. J Am Chem Soc 136 (11):4300-4308. doi:DOI 10.1021/ja412867z
7. Brodin JD, Ambroggio XI, Tang CY, Parent KN, Baker TS, Tezcan FA (2012) Metal-directed, chemically tunable assembly of one-, two- and three-dimensional crystalline protein arrays. Nat Chem 4 (5):375-382. doi:Doi 10.1038/Nchem.1290
8. Brodin JD, Carr JR, Sontz PA, Tezcan FA (2014) Exceptionally stable, redox-active supramolecular protein assemblies with emergent properties. P Natl Acad Sci USA 111 (8):2897-2902. doi:DOI 10.1073/pnas.1319866111
9. Matthaei JF, DiMaio F, Richards JJ, Pozzo LD, Baker D, Baneyx F (2015) Designing Two-Dimensional Protein Arrays through Fusion of Multimers and Interface Mutations. Nano Lett 15 (8):5235-5239. doi:10.1021/acs.nanolett.5b01499
10. Nam KT, Shelby SA, Choi PH, Marciel AB, Chen R, Tan L, Chu TK, Mesch RA, Lee BC, Connolly MD, Kisielowski C, Zuckermann RN (2010) Free-floating ultrathin two-dimensional crystals from sequence-specific peptoid polymers. Nat Mater 9 (5):454-460. doi:Doi 10.1038/Nmat2742
11. Olivier GK, Cho A, Sanii B, Connolly MD, Tran H, Zuckermann RN (2013) Antibody-Mimetic Peptoid Nanosheets for Molecular Recognition. Acs Nano 7 (10):9276-9286. doi:DOI 10.1021/nn403899y
12. Richmond GL, Kittredge CT, Robertson E, Zuckermann R (2014) Novel peptoid nanosheet assembly at the oil-water interface. Abstr Pap Am Chem S 248
13. Robertson EJ, Oliver GK, Qian M, Proulx C, Zuckermann RN, Richmond GL (2014) Assembly and molecular order of two-dimensional peptoid nanosheets through the oil-water interface. P Natl Acad Sci USA 111 (37):13284-13289. doi:DOI 10.1073/pnas.1414843111
14. Sanii B, Haxton TK, Olivier GK, Cho A, Barton B, Proulx C, Whitelam S, Zuckermann RN (2014) Structure-Determining Step in the Hierarchical Assembly of Peptoid Nanosheets. Acs Nano 8 (11):11674-11684. doi:DOI 10.1021/nn505007u

15. Sanii B, Kudirka R, Cho A, Tran H, Tan L, Zuckermann RN (2011) Creating Peptoid Nanosheets by Buckling a Gibbs Monolayer. Biophys J 100 (3):57-57
16. Sanii B, Kudirka R, Cho A, Venkateswaran N, Olivier GK, Olson AM, Tran H, Harada RM, Tan L, Zuckermann RN (2012) Shaken, Not Stirred: Collapsing a Peptoid Monolayer to Produce Free-Floating, Stable Nanosheets. Biophys J 102 (3):269a-269a
17. Pandya MJ, Spooner GM, Sunde M, Thorpe JR, Rodger A, Woolfson DN (2000) Sticky-end assembly of a designed peptide fiber provides insight into protein fibrillogenesis. Biochemistry 39 (30):8728-8734
18. Dublin S, Zimenkov Y, Conticello VP (2009) Engineering responsive mechanisms to control the assembly of peptide-based nanostructures. Biochem Soc Trans 37 (Pt 4):653-659. doi:10.1042/BST0370653
19. Dublin SN, Conticello VP (2008) Design of a selective metal ion switch for self-assembly of peptide-based fibrils. J Am Chem Soc 130 (1):49-51. doi:10.1021/ja0775016
20. Anzini P, Xu C, Hughes S, Magnotti E, Jiang T, Hemmingsen L, Demeler B, Conticello VP (2013) Controlling self-assembly of a peptide-based material via metal-ion induced registry shift. J Am Chem Soc 135 (28):10278-10281. doi:10.1021/ja404677c
21. Zimenkov Y, Dublin SN, Ni R, Tu RS, Breedveld V, Apkarian RP, Conticello VP (2006) Rational design of a reversible pH-responsive switch for peptide self-assembly. J Am Chem Soc 128 (21):6770-6771. doi:10.1021/ja0605974
22. Papapostolou D, Smith AM, Atkins ED, Oliver SJ, Ryadnov MG, Serpell LC, Woolfson DN (2007) Engineering nanoscale order into a designed protein fiber. Proc Natl Acad Sci U S A 104 (26):10853-10858. doi:10.1073/pnas.0700801104
23. Ryadnov MG, Woolfson DN (2003) Engineering the morphology of a self-assembling protein fibre. Nat Mater 2 (5):329-332. doi:10.1038/nmat885
24. Sharp TH, Bruning M, Mantell J, Sessions RB, Thomson AR, Zaccai NR, Brady RL, Verkade P, Woolfson DN (2012) Cryo-transmission electron microscopy structure of a gigadalton peptide fiber of de novo design. Proc Natl Acad Sci U S A 109 (33):13266-13271. doi:10.1073/pnas.1118622109
25. Xu C, Liu R, Mehta AK, Guerrero-Ferreira RC, Wright ER, Dunin-Horkawicz S, Morris K, Serpell LC, Zuo X, Wall JS, Conticello VP (2013) Rational design of helical nanotubes from self-assembly of coiled-coil lock washers. J Am Chem Soc 135 (41):15565-15578. doi:10.1021/ja4074529
26. Burgess NC, Sharp TH, Thomas F, Wood CW, Thomson AR, Zaccai NR, Brady RL, Serpell LC, Woolfson DN (2015) Modular Design of Self-Assembling Peptide-Based Nanotubes. J Am Chem Soc 137 (33):10554-10562. doi:10.1021/jacs.5b03973
27. Thomas F, Burgess NC, Thomson AR, Woolfson DN (2016) Controlling the Assembly of Coiled-Coil Peptide Nanotubes. Angew Chem Int Ed Engl 55 (3):987-991. doi:10.1002/anie.201509304
28. Egelman EH, Xu C, DiMaio F, Magnotti E, Modlin C, Yu X, Wright E, Baker D, Conticello VP (2015) Structural plasticity of helical nanotubes based on coiled-coil assemblies. Structure 23 (2):280-289. doi:10.1016/j.str.2014.12.008
29. Mehrban N, Zhu B, Tamagnini F, Young FI, Wasmuth A, Hudson KL, Thomson AR, Birchall MA, Randall AD, Song B, Woolfson DN (2015) Functionalized alpha-Helical Peptide Hydrogels for Neural Tissue Engineering. ACS Biomater Sci Eng 1 (6):431-439. doi:10.1021/acsbiomaterials.5b00051

30. Lanci CJ, MacDermaid CM, Kang SG, Acharya R, North B, Yang X, Qiu XJ, DeGrado WF, Saven JG (2012) Computational design of a protein crystal. Proc Natl Acad Sci U S A 109 (19):7304-7309. doi:10.1073/pnas.1112595109
31. Anderson DH, Weiss MS, Eisenberg D (1996) A challenging case for protein crystal structure determination: the mating pheromone Er-1 from Euplotes raikovi. Acta Crystallogr D Biol Crystallogr 52 (Pt 3):469-480. doi:10.1107/S0907444995014235
32. Ogihara NL, Ghirlanda G, Bryson JW, Gingery M, DeGrado WF, Eisenberg D (2001) Design of three-dimensional domain-swapped dimers and fibrous oligomers. Proc Natl Acad Sci U S A 98 (4):1404-1409. doi:10.1073/pnas.98.4.1404
33. Ogihara NL, Weiss MS, Degrado WF, Eisenberg D (1997) The crystal structure of the designed trimeric coiled coil coil-VaLd: implications for engineering crystals and supramolecular assemblies. Protein Sci 6 (1):80-88. doi:10.1002/pro.5560060109
34. Prive GG, Anderson DH, Wesson L, Cascio D, Eisenberg D (1999) Packed protein bilayers in the 0.90 angstrom resolution structure of a designed alpha helical bundle. Protein Sci 8 (7):1400-1409
35. Taylor KS, Lou MZ, Chin TM, Yang NC, Garavito RM (1996) A novel, multilayer structure of a helical peptide. Protein Sci 5 (3):414-421
36. Jiang T, Xu C, Liu Y, Liu Z, Wall JS, Zuo X, Lian T, Salaita K, Ni C, Pochan D, Conticello VP (2014) Structurally defined nanoscale sheets from self-assembly of collagen-mimetic peptides. J Am Chem Soc 136 (11):4300-4308. doi:10.1021/ja412867z
37. Javadpour MM, Eilers M, Groesbeek M, Smith SO (1999) Helix packing in polytopic membrane proteins: role of glycine in transmembrane helix association. Biophys J 77 (3):1609-1618. doi:10.1016/S0006-3495(99)77009-8
38. Rohl CA, Scholtz JM, York EJ, Stewart JM, Baldwin RL (1992) Kinetics of amide proton exchange in helical peptides of varying chain lengths. Interpretation by the Lifson-Roig equation. Biochemistry 31 (5):1263-1269
39. Scholtz JM, Qian H, York EJ, Stewart JM, Baldwin RL (1991) Parameters of helix-coil transition theory for alanine-based peptides of varying chain lengths in water. Biopolymers 31 (13):1463-1470. doi:10.1002/bip.360311304
40. Sheridan RP, Levy RM, Salemme FR (1982) alpha-Helix dipole model and electrostatic stabilization of 4-alpha-helical proteins. Proc Natl Acad Sci U S A 79 (15):4545-4549
41. Liang Y, Pingali SV, Jogalekar AS, Snyder JP, Thiyagarajan P, Lynn DG (2008) Cross-strand pairing and amyloid assembly. Biochemistry 47 (38):10018-10026. doi:10.1021/bi801081c
42. Bustamante C, Tinoco I, Jr., Maestre MF (1983) Circular differential scattering can be an important part of the circular dichroism of macromolecules. Proc Natl Acad Sci U S A 80 (12):3568-3572
43. Andersen NH, Liu Z, Prickett KS (1996) Efforts toward deriving the CD spectrum of a 3(10) helix in aqueous medium. FEBS Lett 399 (1-2):47-52
44. Gregory DM, Benzinger TL, Burkoth TS, Miller-Auer H, Lynn DG, Meredith SC, Botto RE (1998) Dipolar recoupling NMR of biomolecular self-assemblies: determining inter- and intrastrand distances in fibrilized Alzheimer's beta-amyloid peptide. Solid State Nucl Magn Reson 13 (3):149-166

45. Hong M (1999) Determination of multiple ***φ***-torsion angles in proteins by selective and extensive (13)C labeling and two-dimensional solid-state NMR. J Magn Reson 139 (2):389-401. doi:10.1006/jmre.1999.1805
46. Bower PO, N.; Mehta, A.; Long, J.; Stayton, P.; Drobny, G. (1999) Determination of Torsion Angles in Proteins and Peptides Using Solid State NMR. J Am Chem Soc 121:8373-8375
47. Zhang Z, Chen Y, Tang X, Li J, Wang L, Yang J (2014) Solid-state NMR shows that dynamically different domains of membrane proteins have different hydration dependence. J Phys Chem B 118 (32):9553-9564. doi:10.1021/jp503032h
48. Chothia C, Levitt M, Richardson D (1981) Helix to helix packing in proteins. J Mol Biol 145 (1):215-250
49. Jiang T, Xu CF, Zuo XB, Conticello VP (2014) Structurally Homogeneous Nanosheets from Self-Assembly of a Collagen-Mimetic Peptide. Angew Chem Int Edit 53 (32):8367-8371. doi:DOI 10.1002/anie.201403780
50. Sleytr UB, Egelseer EM, Ilk N, Pum D, Schuster B (2007) S-Layers as a basic building block in a molecular construction kit. Febs J 274 (2):323-334. doi:10.1111/j.1742-4658.2006.05606.x
51. Sleytr UB, Schuster B, Egelseer EM, Pum D (2014) S-layers: principles and applications. Fems Microbiol Rev 38 (5):823-864. doi:Doi 10.1111/1574-6976.12063

Chapter 3: Manipulating Electrostatic Interactions to Obtain Information about structure of 3FD-IL and to access new conformations

3.1 Introduction

Coulombic interactions stabilize a wide variety of peptide assemblies. The two-dimensional nanosheets formed by collagen mimetic peptides and peptoids are just two examples of structures highly stabilized by ionic interactions [1-7].

Manipulation of the charged amino acids has been used to create structures of different morphologies using both β-sheet peptides and α-helical peptides as substrates. The class of peptides called molecular lego peptides are β-sheets, which contained distinct hydrophobic and hydrophilic surfaces [8]. The following three peptides contained the same composition of amino acids, but have different arrangement of charged amino acids. The peptides **EAK16-I** (sequence: AEAKAEAKAEAKAEAK) and **EAK16-II** (sequence: AEAEAKAKAEAEAKAK) formed fibrous structures regardless of pH. The peptide **EAK16-IV** (sequence: AEAEAEAEAKAKAKAK) formed globular structures between pH 6.5 and 7.5 and fibrous assemblies outside of this range. Fourier transform infrared spectroscopy revealed that all three of the aforementioned peptides form β-sheet peptides, but the peptide **EAK16-IV** forms turns. As a result, there is a significant amount of bending within the **EAK16-IV** structure. Theoretically, **EAK16-I**, **EAK16-II**, and **EAK16-IV** could each form turn structures through folding to form complementary electrostatic interactions.

To understand why **EAK16-IV** preferentially formed turns whereas **EAK16-I** and **EAK16-II** did not, Jun *et al*. evaluated the lowest energy conformation of each of these peptides. For **EAK16-I**, the ground state conformation of the peptide was a stretched worm (i.e. a linear β-strand), because of the weak charge polarity of the chain (Figure 3.1a). For **EAK16-IV**, the lowest energy conformation of the peptide was the hairpin (Figure 3.1e). **EAK16-II** contained two ground state conformations, the stretched worm and the hairpin (Figure 3.1b and Figure 3.1c). The authors hypothesized that **EAK16-IV** folded first into hairpins, exposing their hydrophobic faces, and the hairpins aggregated into globules, which are stabilized by hydrophobic interactions. The situation for **EAK16-II** was more complicated. At very low concentrations, less than 0.08 mg/mL, the authors observed the absence of fibrillar structures and the presence of globules by atomic force microscopy. Above 0.08 mg/mL fibrillar structures were observed. This concentration was designated the critical aggregation concentration for **EAK16-II**. However, since globules are expected for turn structures, it would be expected that **EAK16-II** formed turns below the critical aggregation concentration. FTIR does not show the presence of turns for **EAK16-II** below the critical aggregation concentration. This was attributed to the fact that the FTIR spectrum records the distribution of all molecules. Since one out of 10^4 molecules were determined to be in the hairpin conformation, this conformation is not revealed by FTIR. AFM, however, can detect the few molecules, which have aggregated into globules. This study indicated that the

arrangement of charged amino acids within a peptide sequence is crucial to self assembly.

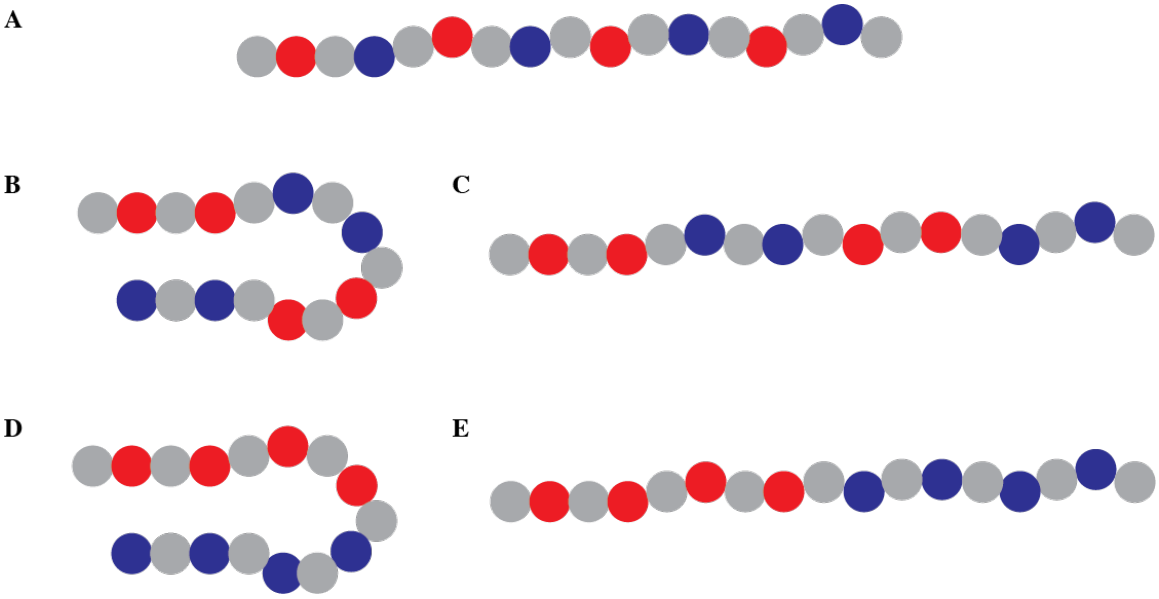

Figure 3.1 Sequences of molecular lego peptides color-coded by charge, where red corresponds to glutamic acid, blue corresponds to lysine, and grey corresponded to alanine (a) stretched worm conformation of EAK16-I (b) hairpin conformation of EAK-16-II (c) stretched worm conformation of EAK16-II (d) hairpin conformation of EAK-16-IV (e) stretched worm conformation of EAK16-IV

The arrangement of charged amino acids also affected the aggregation of α-helical peptides. The best example of the utility of charged amino acids for controlling self-assembly is the concept of sticky-ended fibrillogenesis developed by the Woolfson group (Figure 3.2a) [9]. The Woolfson group designed two coiled-coil peptides, **SAF-p1** and **SAF-p2**, which assembled into an extended coiled-coil fiber when mixed together (Figure 3.2b). When one molecule of **SAF-p1** interacts with one molecule of **SAF-p2**, the peptides associate in a staggered conformation. The first fourteen amino acids of **SAF-p2** interact with the last fourteen amino acids of **SAF-p1**. In this arrangement, sticky-ends are formed which promote longitudinal association of the peptides into extended fibers. Conticello *et al*. also utilized coiled-coil peptides to design a pH responsive fiber, **TZ1H** [10].The peptide **TZ1H** formed a trimeric coiled-coil in which a staggered conformation

of peptides was enforced between adjacent peptides. This led to the formation of sticky ends, which subsequently led to fibrillization. Fibrillization was controlled through the presence of histidine within the **TZ1H** sequence. At pH values below the pK_a of **TZ1H**, the imidazole side chains within TZ1H were protonated, leading to repulsion between molecules within **TZ1H** and ultimately destabilizing the α-helical conformation and preventing fibrillization. Both of these examples highlight the utility in utilizing electrostatic interactions to design novel architectures.

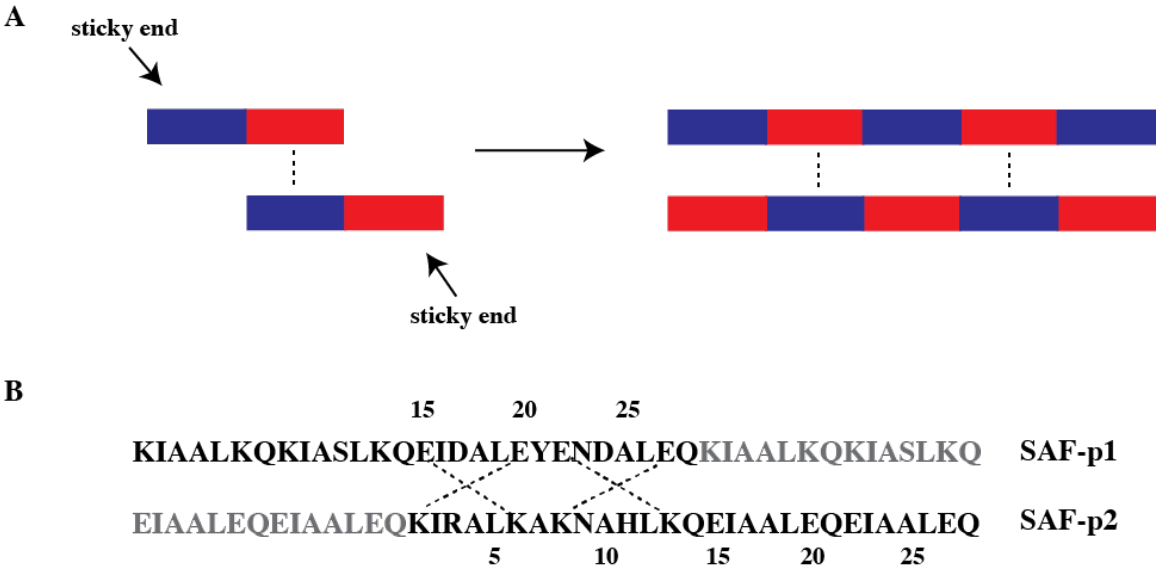

Figure 3.2 (a) schematic of sticky-end fibrillogenesis designed by the Woolfson group (b) design of SAF-p1 and SAF-p2 fibers; dashed lines refer to salt bridges between the peptides in the out of register conformation

A final example of the importance of charged amino acids for self-assembly was realized in structural studies of two α-helical coiled-coil peptides, which form nanotubes [11]. Each of these nanotube forming peptides was designed using the coiled-coil motif. The sequence of the **Form I** and **Form II** nanotube forming peptides are based on a coiled-coil design (Figure 3.3a). The **Form I** peptide contained arginine as its positively charged residue whereas in **Form II**, all arginines are replaced by lysine. Cryo-electron

microscopy measurements of the diameters of the nanotubes revealed that the **Form II** nanotubes were twice the diameter of the **Form I** nanotubes (Figure 3.3b and Figure 3.3c). Furthermore, the helices of both peptides are oriented perpendicular to the long axis of the nanotubes. The underlying molecular structures of the two nanotubes were significantly different. The **Form I** nanotubes contained 4.1 subunits per turn whereas the **form II** nanotubes contained 3.1 subunits per turn. Therefore, a cross section of the **Form I** nanotubes was square (Figure 3.3d). A cross section of the **Form II** nanotubes was not triangular, but circular, due to curvature within the α-helix subunits (Figure 3.3e). The asymmetric unit of **Form I** contained a single α-helix whereas the asymmetric unit of **Form II** contained two α-helices. The structure of the **Form II** nanotubes revealed that there were two layers, an inner and outer layer, which explained the presence of two α-helices in the asymmetric unit of **Form II**. This study showed that drastic conformational changes result through manipulation of the charged amino acids within the peptide sequence.

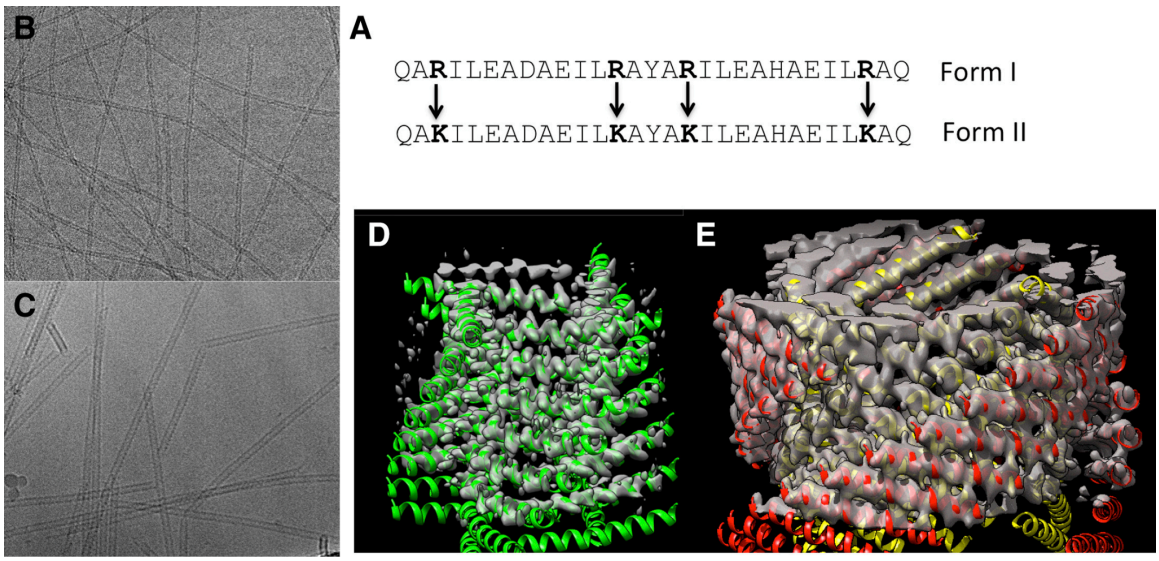

Figure 3.3 (a) the sequences of Form 1 and Form 2 nanotubes (b) cryo-EM image of Form 1 nanotubes (c) cryo-EM image of Form 2 nanotubes (d) structure of Form 1 nanotubes (e) structure of Form 2 nanotubes

Therefore, in this chapter, the charged amino acids of the peptide **3FD-IL** were rearranged or mutated to gain structural information about the **3FD-IL** nanosheets and to determine if **3FD-IL** can adopt alternate conformations.

3.2 Design of peptides with altered charge pattern to probe helix orientation

In order to determine whether the helices within the **3FD-IL** nanosheets were parallel or perpendicular, three peptides were synthesized and characterized. All three peptides retained the same sequence of hydrophobic amino acids of parent peptide **3FD-IL** but have differing orders of charged amino acids. The peptides **3FD-IL-EK** and **3FD-IL-KE** have a sequence of charged amino acids that only allows the peptides to form complementary electrostatic interactions when there is a parallel arrangement of α-helices (Figure 3.4).

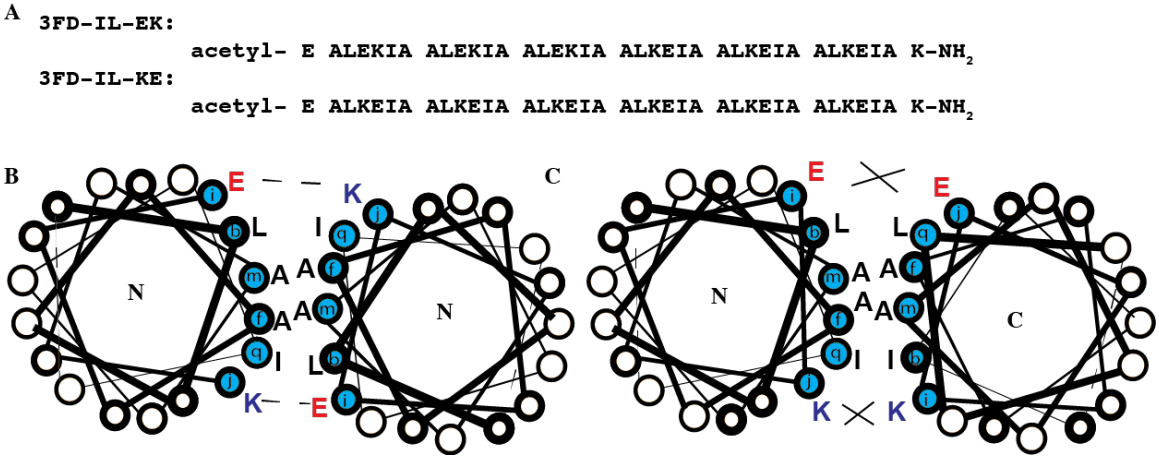

Figure 3.4 (a) sequences of parallel peptides 3FD-IL-EK and 3FD-IL-KE and (b) attractive electrostatic interactions of 3FD-IL-KE and 3FD-IL-EK in the parallel orientation (c) repulsive electrostatic interactions of 3FD-IL-KE and 3FD-IL-EK in the antiparallel orientation

On the other hand, **3FD-IL-EEKK** only has complementary electrostatic interactions in the antiparallel orientation (Figure 3.5).

A 3FD-IL-EEKK:
acetyl- E ALEEIA ALEEIA ALEEIA ALKKIA ALKKIA ALKKIA K-NH_2

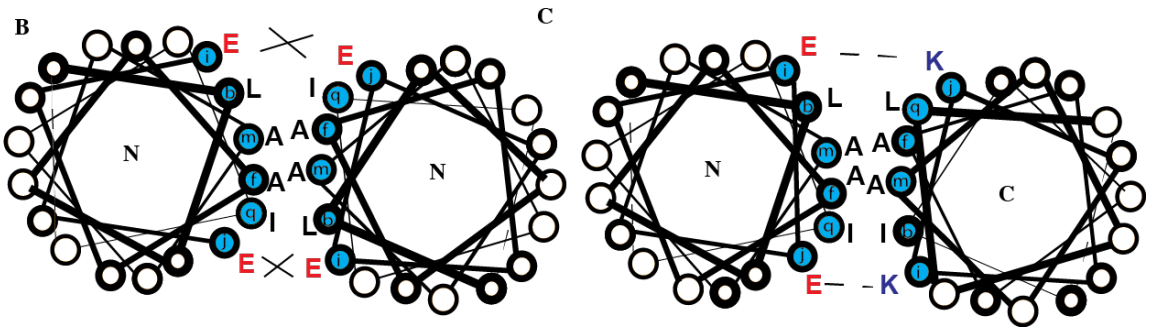

Figure 3.5 (a) Sequence of antiparallel peptide 3FD-IL-EEKK (b) repulsive electrostatic interactions of 3FD-IL-EEKK in the parallel orientation (c) attractive electrostatic interactions between 3FD-IL-EEKK in the antiparallel conformation

In contrast to these three peptides, **3FD-IL** could form complementary electrostatic interactions in both the parallel and antiparallel orientation of α-helices (Figure 3.6).

A 3FD-IL:
acetyl- E ALEKIA ALEKIA ALEKIA ALKEIA ALKEIA ALKEIA K-NH_2

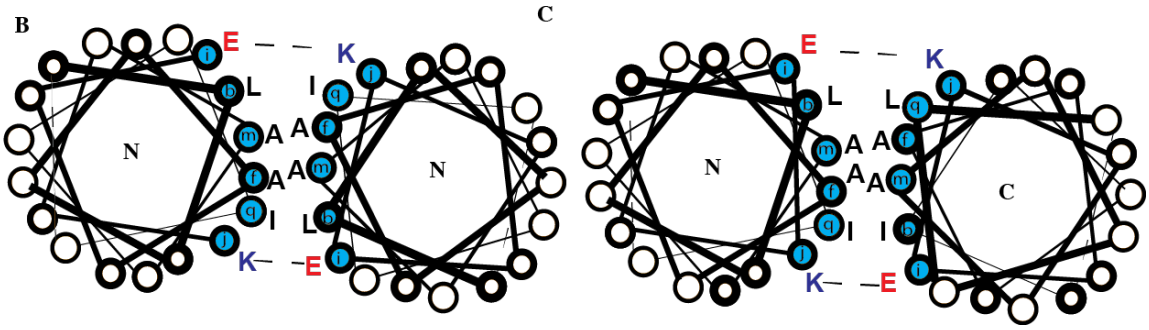

Figure 3.6 (a) sequence of peptide 3FD-IL (b) attractive electrostatic interactions between adjacent 3FD-IL helices in both the parallel and (c) antiparallel orientations

I hypothesized that the mutant that formed nanosheets will recapitulate the orientation of the helices contained within the **3FD-IL** nanosheets.

Self Assembly of Peptides with Altered Charge Patterns

The three mutant peptides were assembled under the same conditions that **3FD-IL**

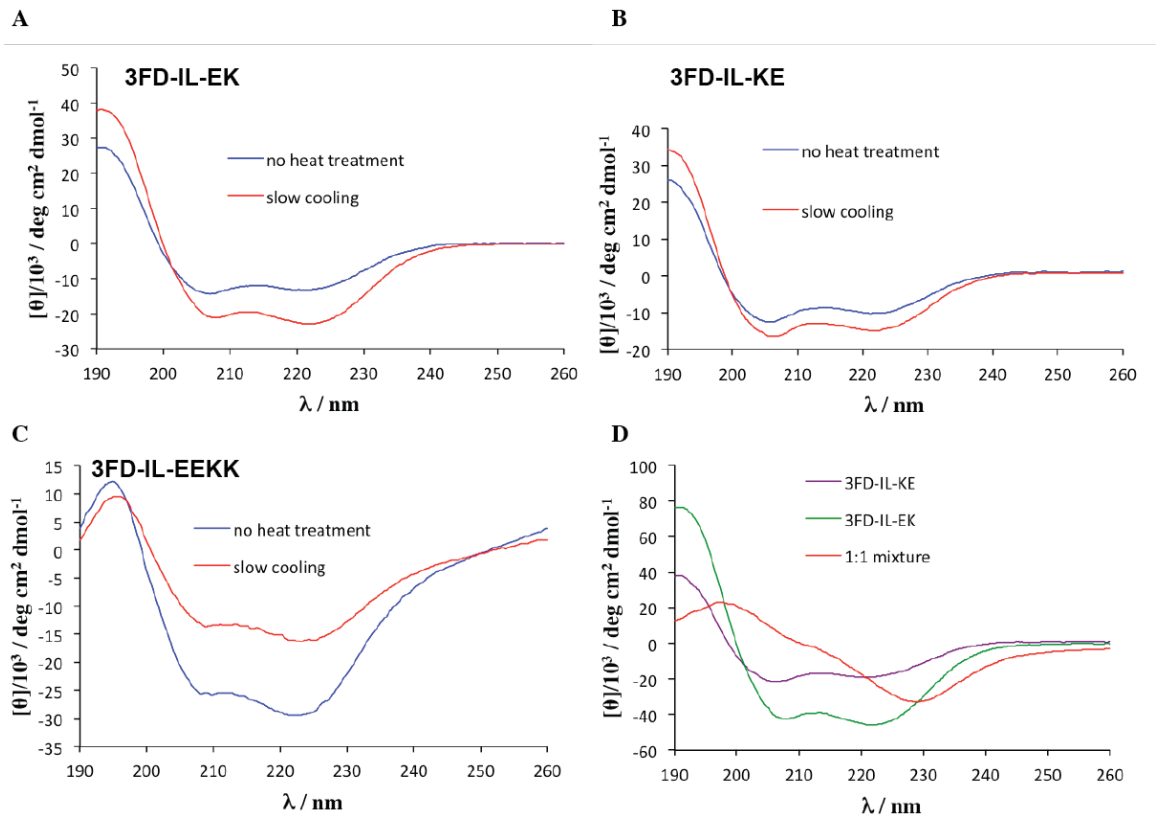

Figure 3.7 Circular dichroism spectra of parallel and antiparallel peptides in 10 mM TAPS buffer, pH 8.5 (a) CD spectra of 3FD-IL-EK (b) CD spectra of 3FD-IL-KE (c) CD spectra of 3FD-IL-EEKK (d) CD spectra of 3FD-IL-KE, 3FD-IL-EK, and a 1:1 mixture of 3FD-IL-KE and 3FD-IL-EK

formed nanosheets (in 10 mM TAPS buffer, pH 8.5). All three peptides exhibited α-helical circular dichroism signatures in the presence and absence of thermal annealing (Figure 3.7). Interestingly, the circular dichroism signature of the peptide **3FD-IL-EEKK**

most resembled that of **3FD-IL**. The circular dichroism spectra was

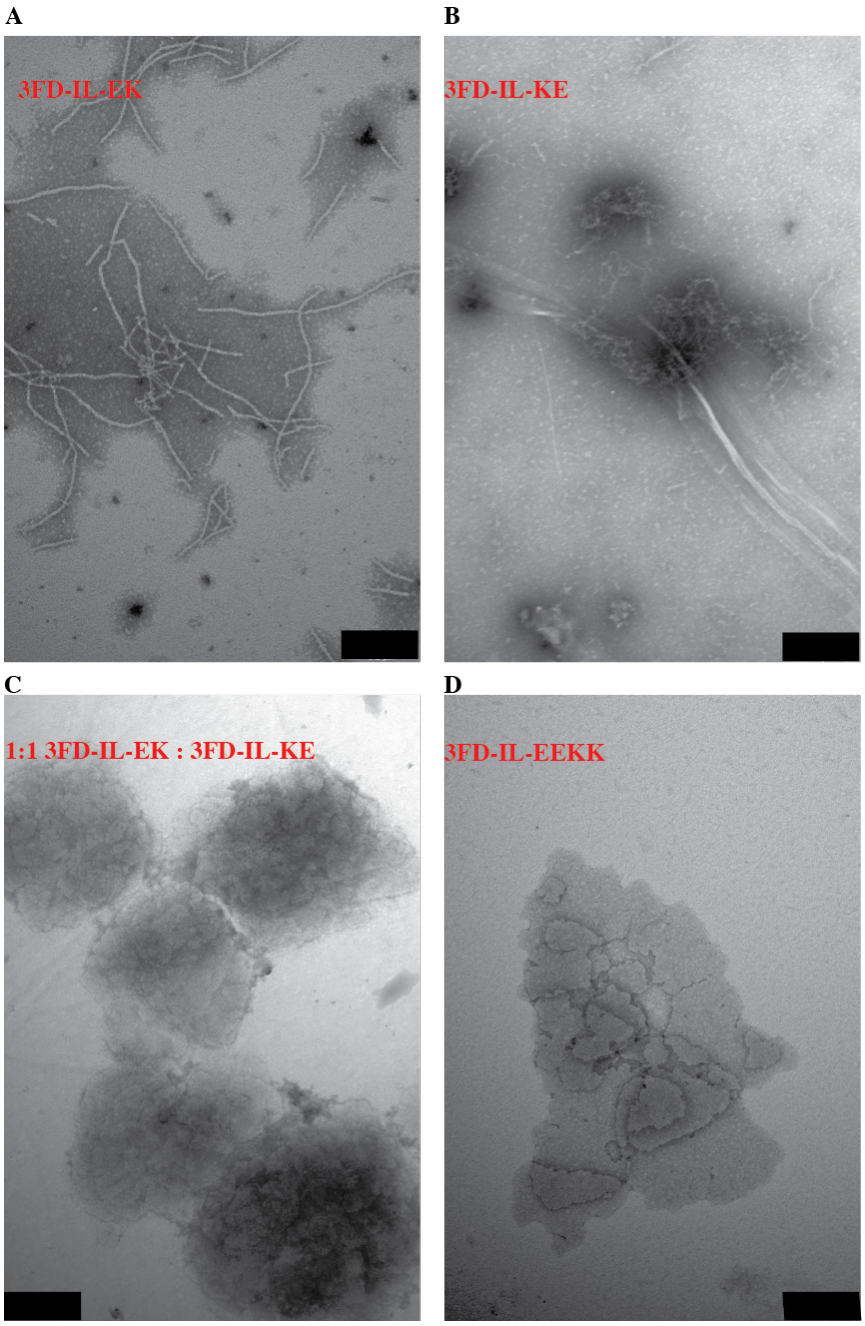

Figure 3.8 Transmission electron micrographs of (a) 3FD-IL-EK, (b) 3FD-IL-KE, (c) a 1:1 mixture of 3FD-IL-EK to 3FD-IL-KE (d) 3FD-IL-EEKK; all scale bars correspond to 200 nm

correlated with transmission electron microscopy (TEM) to determine if any of the aforementioned peptides are capable of forming nanosheets. TEM revealed that the

peptides **3FD-IL-EK** and **3FD-IL-KE** formed fibrillar structures, whereas the peptide **3FD-IL-EEKK** formed assemblies that resembled nanosheets (Figure 3.8). The nanosheets formed by **3FD-IL-EEKK** were smaller and contained less defined edges than those formed by parent peptide **3FD-IL**. Furthermore, the nanosheets formed by **3FD-IL-EEKK** are stacked. Small angle x-ray scattering measurements were performed to determine if the nanosheets formed by **3FD-IL-EEKK** are similar in structure to **3FD-IL**. The nanosheets formed by **3FD-IL-EEKK** have strong diffraction peaks in the high q region, which correspond to distances of 14.67 Å, 8.49 Å, and 7.33 Å (Figure 3.9a). These distances were nearly identical to those of **3FD-IL** and consequently have the same geometric relationship suggestive of hexagonally packed helices. Furthermore, in the intermediate q region, the intensity decays with the exponential function q^{-2}, suggesting that the assemblies observed by TEM are nanosheets (Figure 3.9a). Guinier analysis suggested that the nanosheets have a thickness of about 6.3 nm (Figure 3.9b and Figure 3.9c). The small angle x-ray scattering data suggested that the **3FD-IL-EEKK** nanosheets are similar in structure to those of **3FD-IL**. Collectively, this data supported a model for antiparallel packing of helices within the **3FD-IL** nanosheets, despite the differences in morphology between the nanosheets formed by the **3FD-IL-EEKK** and

3FD-IL. This data supported the preliminary cryo-EM structural model of **3FD-IL**.

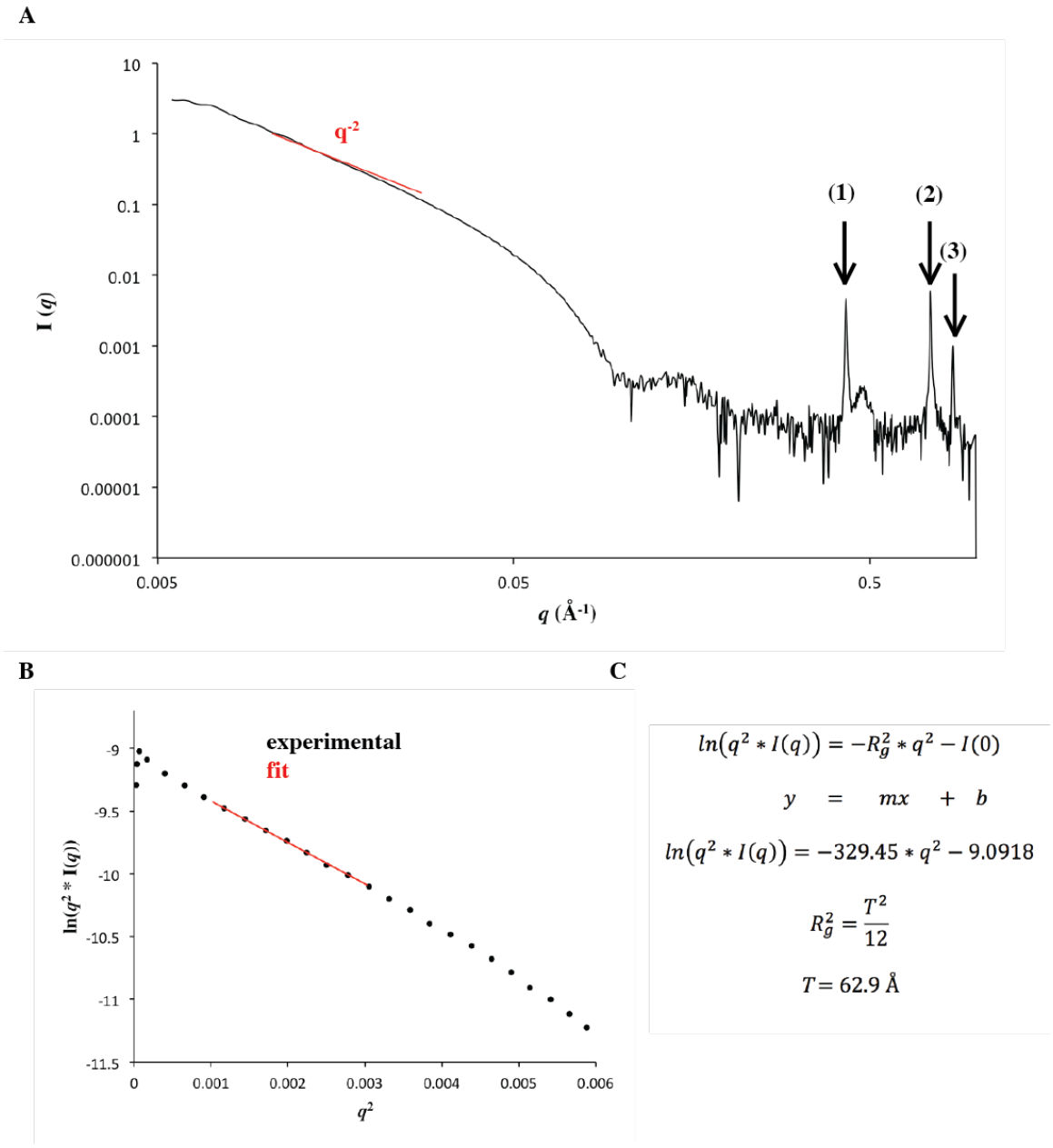

Figure 3.9 (a) Small angle x-ray scattering curve of 3FD-IL-EEKK which revealed the dependence of intensity on the exponential q^{-2} and Bragg diffraction peaks which corresponded to distances of 14.67 Å, 8.49 Å, and 7.33 Å (b) Guinier fit of 3FD-IL-EEKK (c) fit of the Guinier plot to an equation for sheet-like forms which revealed a sheet thickness of 62.9 Å

To understand the difference in morphology between the **3FD-IL** and **3FD-IL-EEKK** nanosheets, the sequence difference between the two peptides was analyzed. At

pH 8.5, **3FD-IL-EEKK** contained five negative charges at the N-terminus and five positive charges at the C-terminus. This sequence has high charge polarity, similar to the β-sheet peptide **EAK16-IV**, which was described in the introduction. The high charge polarity allows for two potential mechanisms of peptide assembly, lateral assembly of peptide molecules in the xy plane through an antiparallel in-register arrangement of helices and the possibility of growth in the z-dimension or sheet stacking through interaction between two parallel out of register peptides. These two mechanisms are in competition with each other. Nanosheet growth in the z-dimension blocks one face available for sheet growth in the xy plane, preventing the nanosheets from growing in the

xy plane (Figure 3.10).

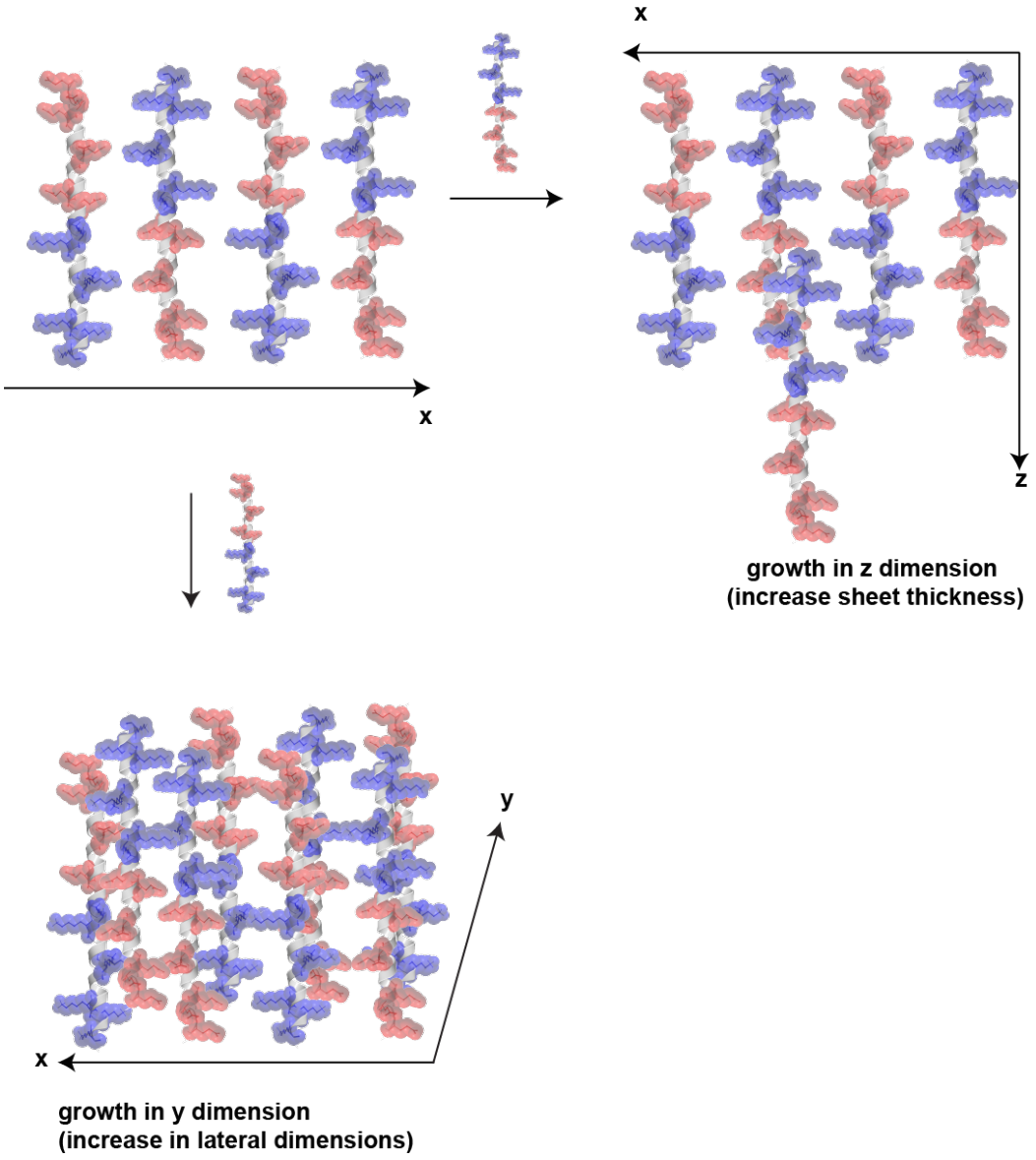

Figure 3.10 Model for competing pathways of nanosheet growth, either in register interhelical interactions in the xy plane or through staggered z-dimension growth

In contrast, the terminal charges of the peptide **3FD-IL** prevent z-dimension growth (Figure 3.11).

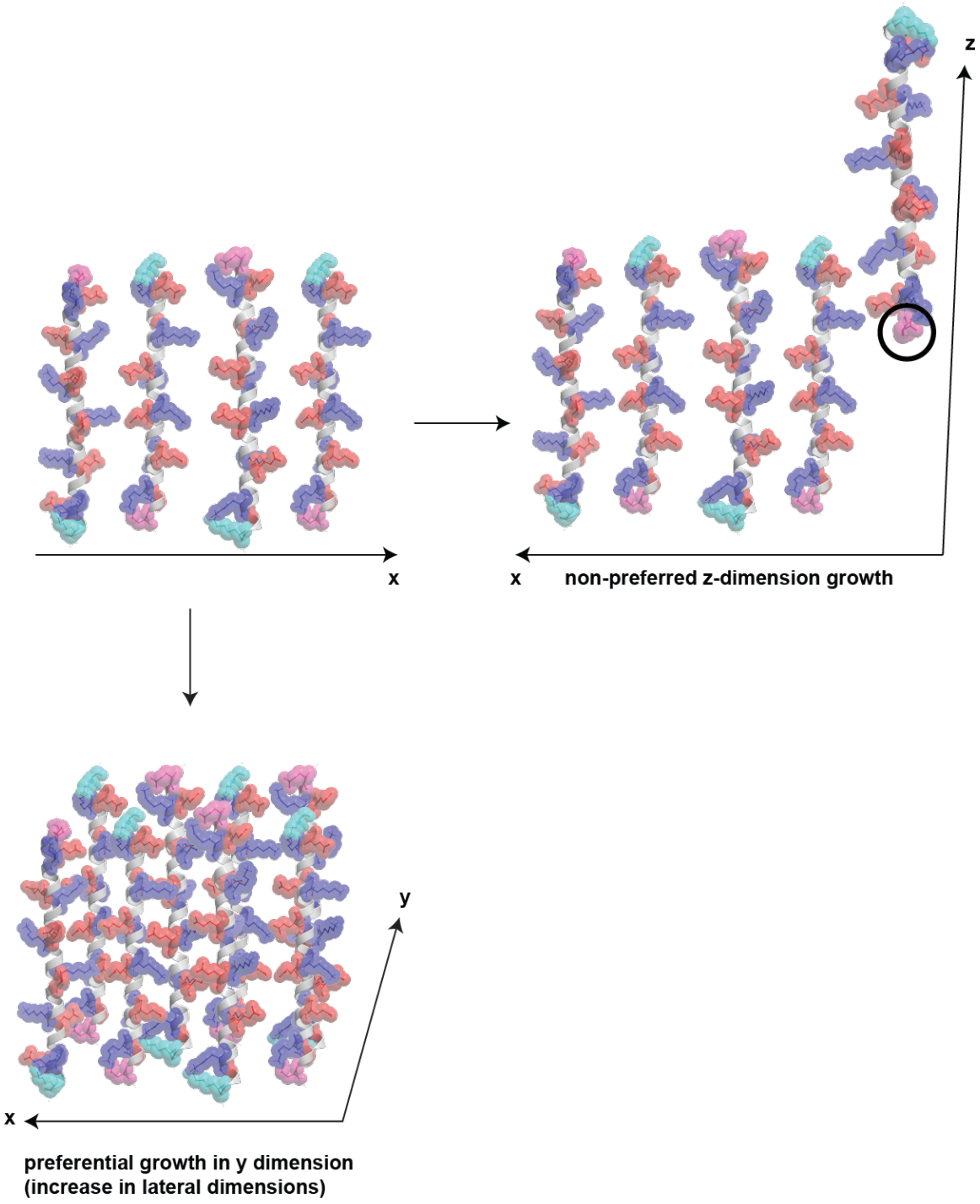

Figure 3.11 Mechanism for 3FD-IL self-assembly; terminal capping groups (circled) preclude z-dimension growth

A second experiment was performed to confirm that the helices within the **3FD-IL** nanosheets are arranged in an antiparallel orientation. While antiparallel packing of the peptides **3FD-IL-EK** and **3FD-IL-KE** is precluded when the peptides are assembled

A

3FD-IL-EK:
acetyl- E ALEKIA ALEKIA ALEKIA ALEKIA ALEKIA ALEKIA K-NH_2
3FD-IL-KE:
acetyl- E ALKEIA ALKEIA ALKEIA ALKEIA ALKEIA ALKEIA K-NH_2

B

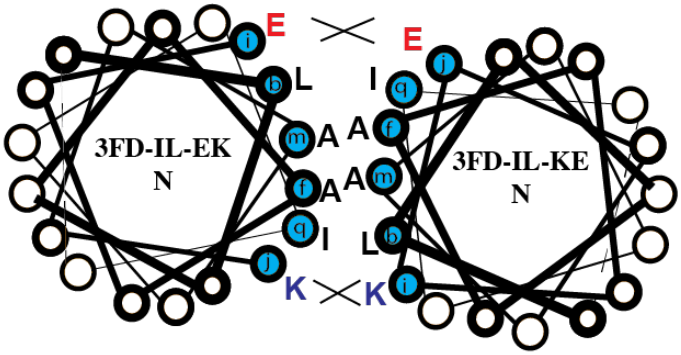

C

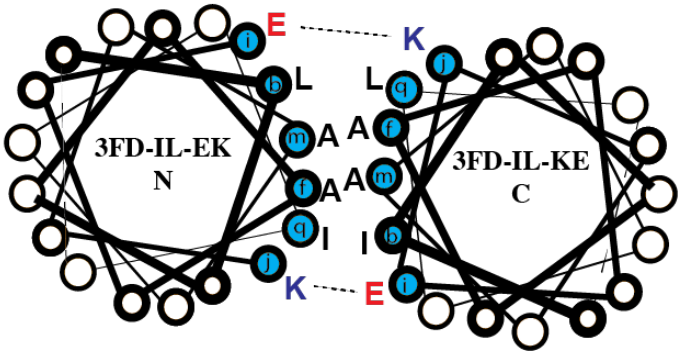

Figure 3.12 (a) sequences of 3FD-IL-EK and 3FD-IL-KE (b) repulsive electrostatic interactions formed by 3FD-IL-EK and 3FD-IL-KE in the parallel orientation (c) complementary electrostatic interactions formed by 3FD-IL-EK and 3FD-IL-KE in the antiparallel orientation

separately, a mixture of the two peptides allowed for an antiparallel packing arrangement of helices (Figure 3.12). A 1:1 mixture of the peptides **3FD-IL-KE** and **3FD-IL-EK** was prepared. Interestingly, although the CD behavior of the two peptides separately followed that of a standard α-helix, the CD signature of a mixture of the two peptides is red-shifted

from that of the individual peptides, suggesting a scattering effect similar to that observed for **3FD-IL** (Figure 3.7d). Transmission electron microscopy imaging shows that the mixture of two peptides formed nanosheets, which exhibited a similar morphology to those formed by the antiparallel peptide **3FD-IL-EEKK** (Figure 3.8c). Finally, small angle x-ray scattering experiments were performed on the mixture of peptides. The small angle x-ray scattering curve revealed diffraction peaks at 14.57 Å, 8.42 Å, and 7.29 Å, which exhibited a geometric relationship consistent with hexagonal packing of α-helices (Figure 13.3a).

A

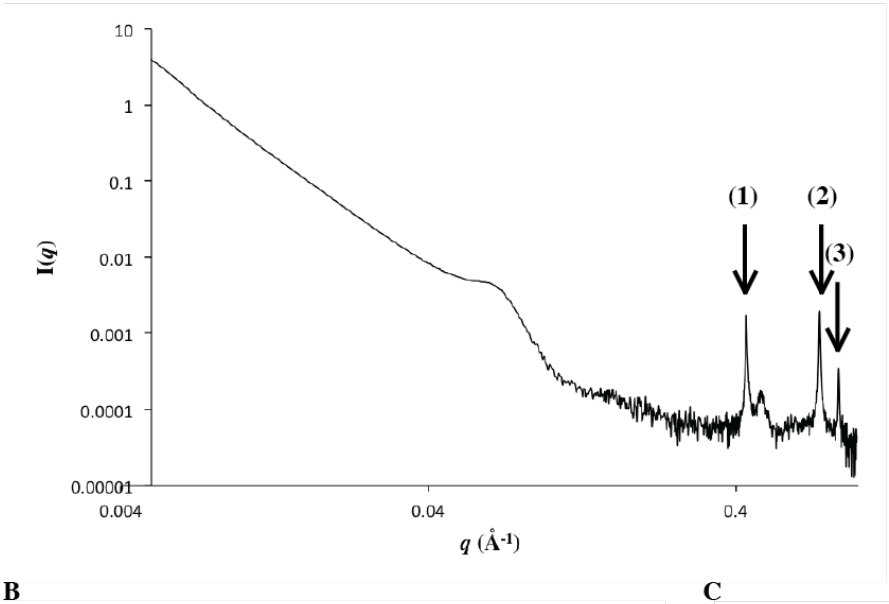

B

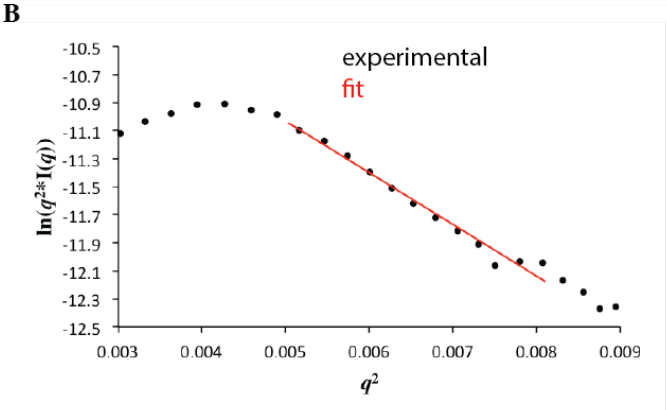

C

$$ln(q^2 * I(q)) = -R_g^2 * q^2 - I(0)$$

$$y = mx + b$$

$$ln(q^2 * I(q)) = -368.81 * q^2 - 9.187$$

$$R_g^2 = \frac{T^2}{12}$$

$$T = 66.5 \text{ Å}$$

Figure 3.13 (a) Small angle x-ray scattering curve of a 1:1 mixture of 3FD-IL-KE and 3FD-IL-EK which revealed diffraction peaks indicated by arrows at (1) 14.57 Å, (2) 8.42 Å, and (3) 7.29 Å (b) Guinier fit of peptide mixture revealed thickness of 66.5 Å

Furthermore, Guinier analysis revealed that the thickness of the nanosheets obtained from the mixture of **3FD-IL-EK** and **3FD-IL-KE** is 6.6 nm, which is almost exactly the thickness obtained from similar analysis of the **3FD-IL** nanosheets (Figure 13.3b). In comparison to the nanosheets formed by **3FD-IL**, the nanosheets formed by the mixture of peptides **3FD-IL-EK** and **3FD-IL-KE** are not as well defined. This observation can be explained due to the kinetics of association and dissociation of the two peptides. The nanosheets are formed from a mixture of two peptides, and it is possible for the peptides to either interact with each other or to assemble independently. Since **3FD-IL-KE** and **3FD-IL-EK** cannot form nanosheets independently, the inappropriate association of a molecule within the nanosheet with the same molecule would halt nanosheet growth.

These experiments proved that the orientation of the helices within the **3FD-IL** nanosheets is antiparallel. Furthermore, these experiments highlighted the utility of using charge to understand the structure of peptide assemblies.

3.3 The effect of charge reversal on self-assembly of 3FD-IL

The previous experiments showed that the sequence of charged amino acids vastly affects the self-assembly process. Although the sheet forming peptide **3FD-IL-EEKK** formed nanosheets, the nanosheets formed were different in morphology from **3FD-IL.** An additional peptide **3FD-IL-RC** was designed to test the effect of charge reversal on peptide self-assembly. **In 3FD-IL-RC**, the glutamate and lysine residues are switched (Figure 3.14a). In a similar fashion to **3FD-IL**, **3FD-IL-RC** can form complementary electrostatic interactions in both the parallel and antiparallel helix

orientations (Figure 3.14b and 3.14c).

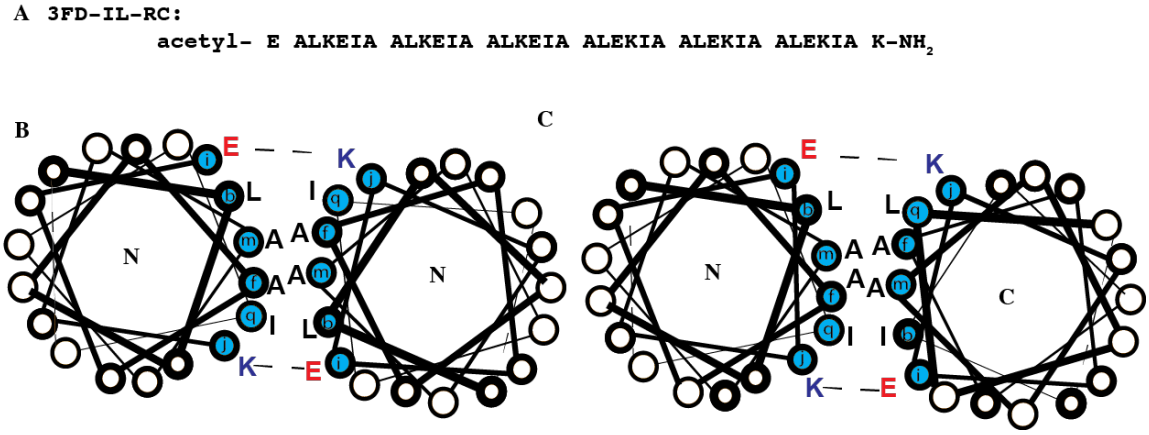

Figure 3.14 (a) the sequence of peptide 3FD-IL-RC (b) complementary electrostatic interactions of 3FD-IL-RC in both the parallel and (c) antiparallel orientation of helices

The peptide was assembled in a pH range between 6 and 8.5. The self-assembly of **3FD-IL-RC** was monitored in the absence of heat treatment and after thermal annealing.

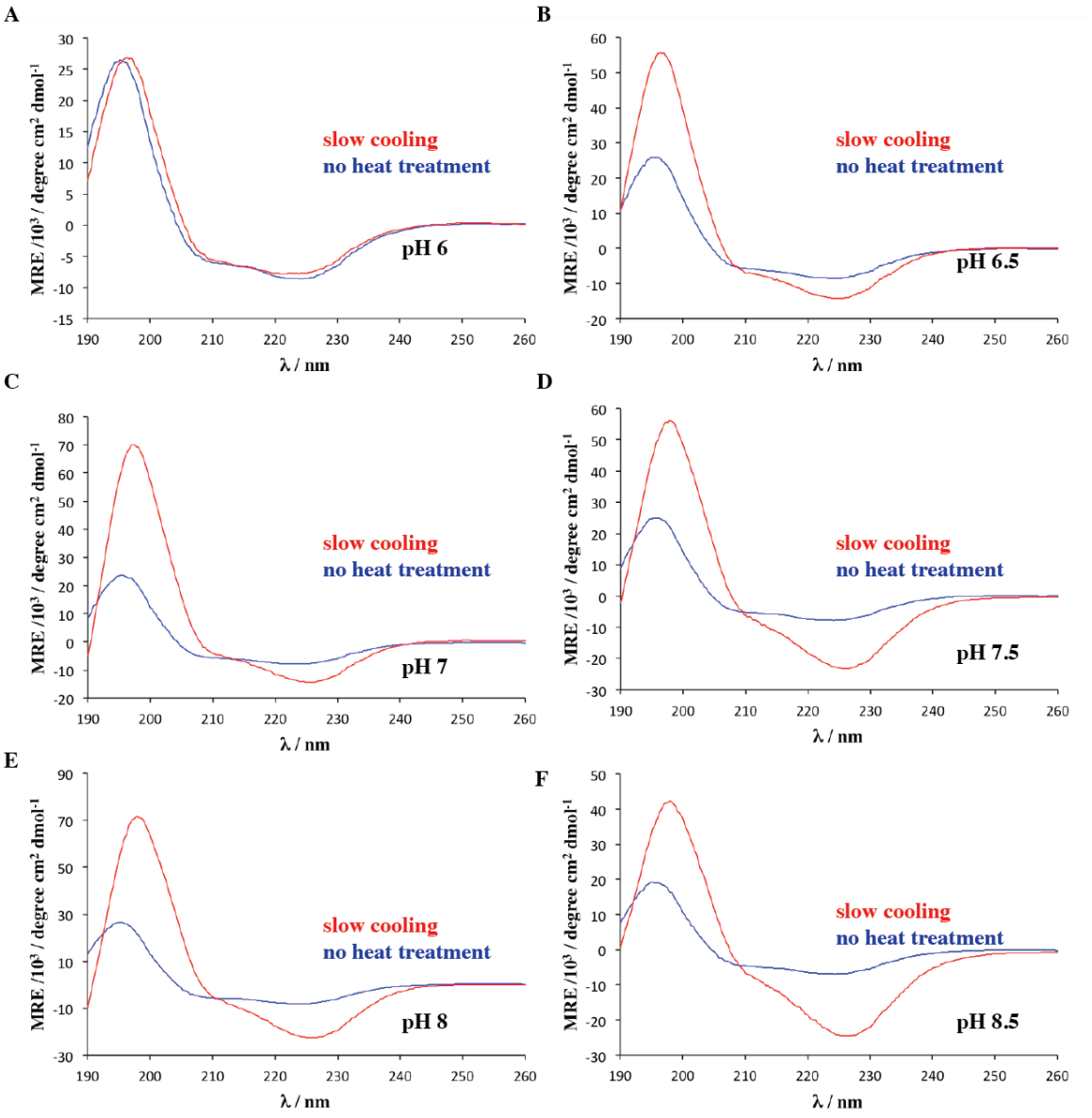

Figure 3.15 pH dependence of 3FD-IL-RC CD behavior (a) pH 6 (b) pH 6.5 (c) pH 7 (d) pH 7.5 (e) pH 8 (f) pH 8.5

The peptide **3FD-IL-RC** formed an α-helical signature over the pH range studied (Figure 3.15). After thermal annealing, the CD signature is shifted to longer wavelengths, which is attributed to a scattering effect. Transmission electron microscopy was utilized to visualize the morphologies of the assemblies formed at different pHs. Across pH 6 to 8.5,

3FD-IL-RC formed what appeared to be nanosheets in the absence of thermal annealing.

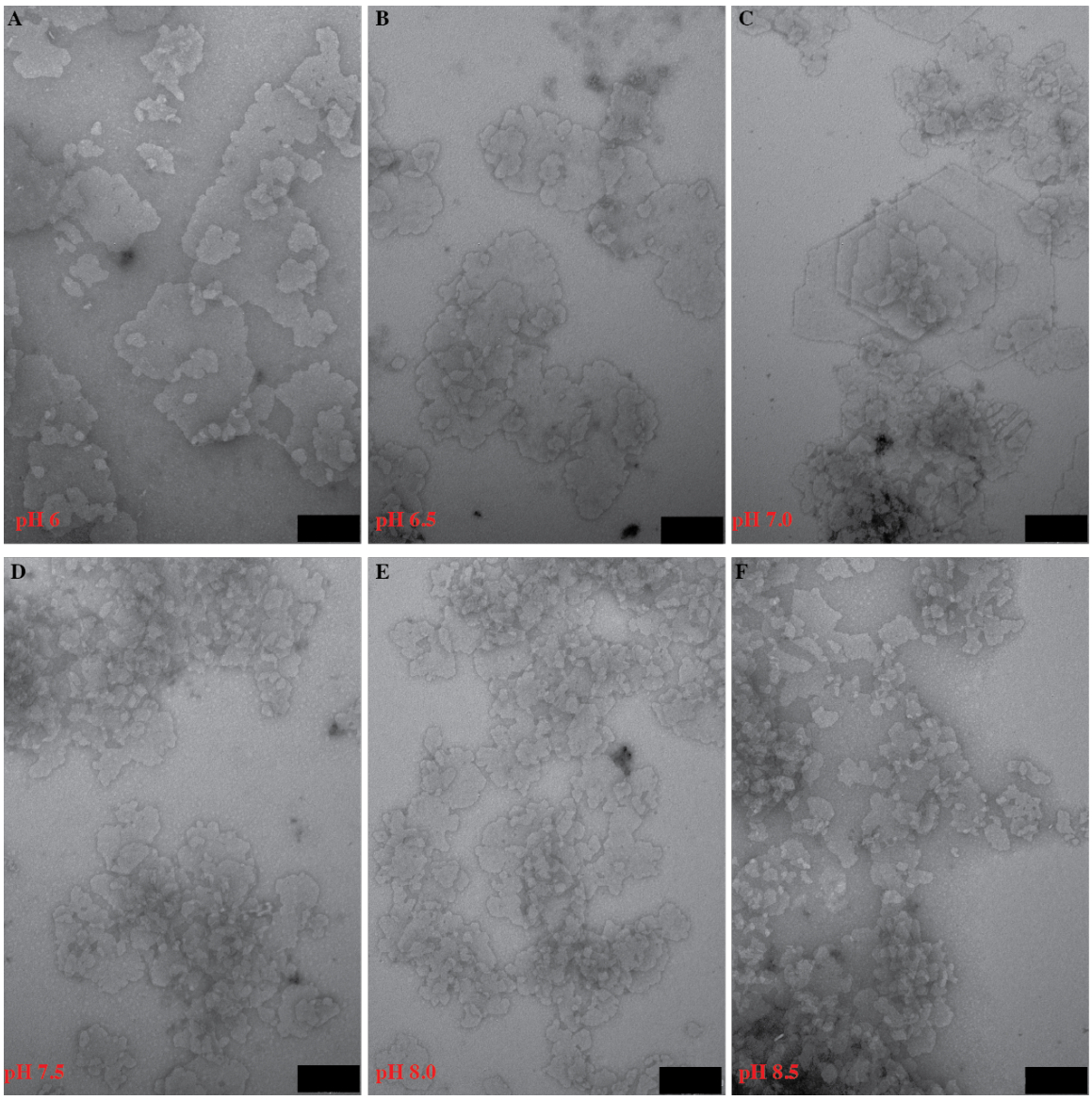

Figure 3.16 Transmission electron micrographs of 3FD-IL-RC in the absence of thermal annealing at (a) pH 6, (b) pH 6.5, (c) pH 7, (d) pH 7.5, (e) pH 8, (f) pH 8.5

The nanosheets appeared to be similar in morphology to those formed by **3FD-IL** without heat treatment at most pHs. However, at pH 7, nanosheets that look like hexagons are observed. After thermal annealing, many more hexagons observed in

addition to fibrous structures (Figure 3.17). The fibrous structures are very well aligned.

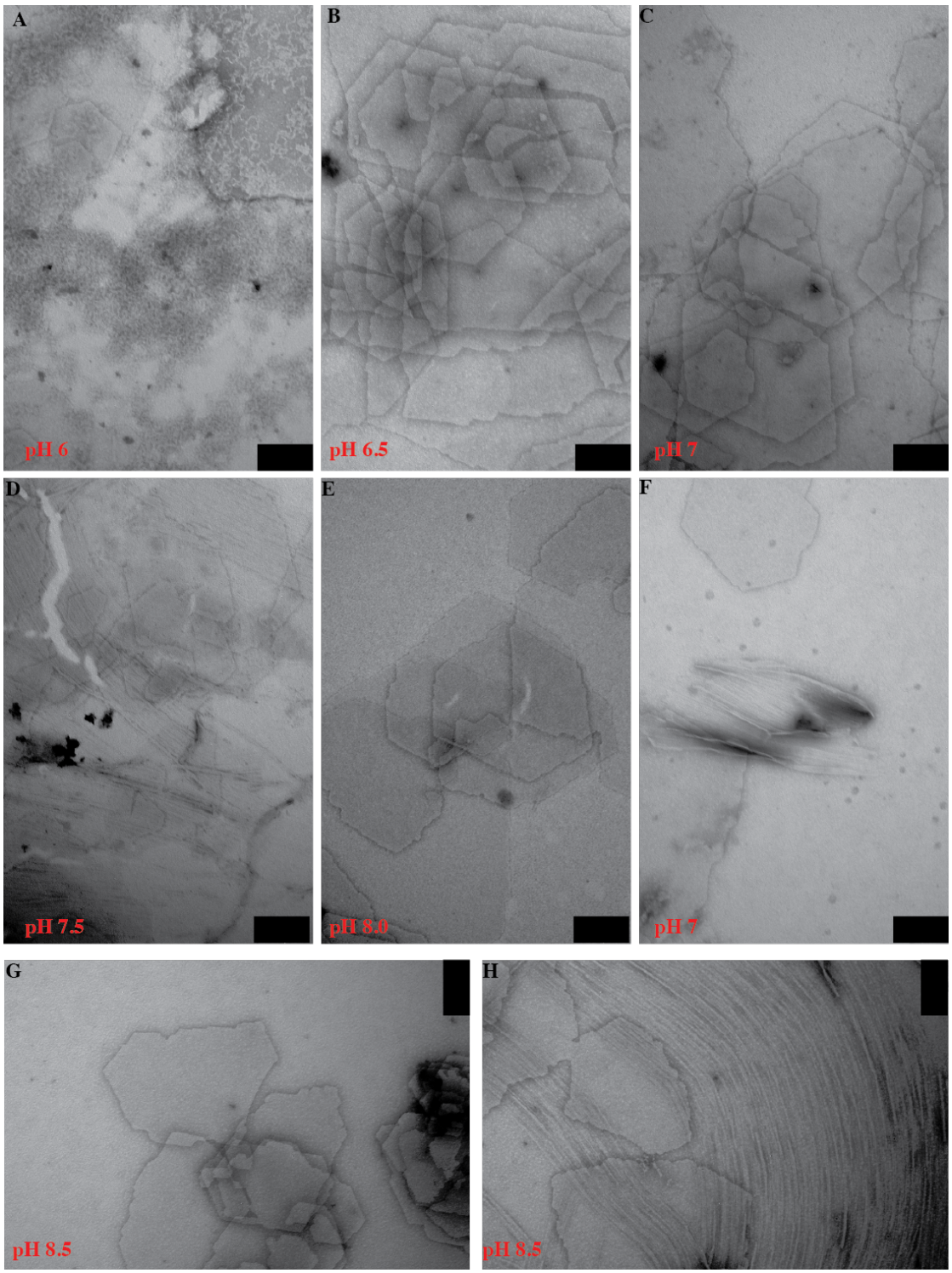

Figure 3.17 Transmission electron micrographs of 3FD-IL-RC after thermal annealing at pH 6, (a) pH 6 (b) pH 6.5 (c) pH 7 (d) pH 7.5 (e) pH 8 (f) pH 7 (g) pH 8.5 (h) pH 8.5

Unfortunately, the presence of a mixture of morphologies within the peptide **3FD-IL-RC** prevented further structural determination of these assemblies through small angle x-ray scattering. The sequence differences between **3FD-IL** and **3FD-IL-RC** may explain the difference in assembly formation between these two peptides. Both **3FD-IL** and **3FD-IL-RC** contained potential intrahelical Glu-Lys (i, i+5) and (i, i+1) interactions. The α-helical structure places side chains which are (i, i+5) and (i, i+1) on different faces of the α-helix, preventing the formation of intrahelical ion pairs [12]. In contrast to **3FD-IL**, **3FD-IL-RC** also contained two potential intrahelical Glu-Lys (i, i+3) ion pairs at the termini of the α-helix. These interactions in **3FD-IL** are repulsive. These intrahelical interactions could change the modes of lateral association between adjacent α-helices. Interestingly, the peptide **3FD-IL-KE**, which contained the same potential intrahelical ion pairs, also formed well-aligned fibrous structures, suggesting a role for the terminal amino acids of **3FD-IL** in promoting lateral association of peptides into nanosheets.

3.4 Design of arginine and aspartic acid mutants

As described in the introduction, small changes in the charged amino acids of peptide sequences can result in vastly different structures. Three mutant peptides were produced with different charged amino acids than in the parent peptide **3FD-IL**. The mutant peptides retained the overall charge pattern of **3FD-IL**, because previously this was deemed critical for nanosheet formation (Figure 3.18). In the peptide **3FD-IL-DK**, the glutamic acid residues of **3FD-IL** were replaced by aspartic acid. In the peptide **3FD-IL-ER**, the lysine residues of **3FD-IL** were replaced by arginine. In the third peptide **3FD-IL-DR**, the glutamic acid residues of **3FD-IL** were replaced by aspartic acid and the

lysines were replaced by arginine.

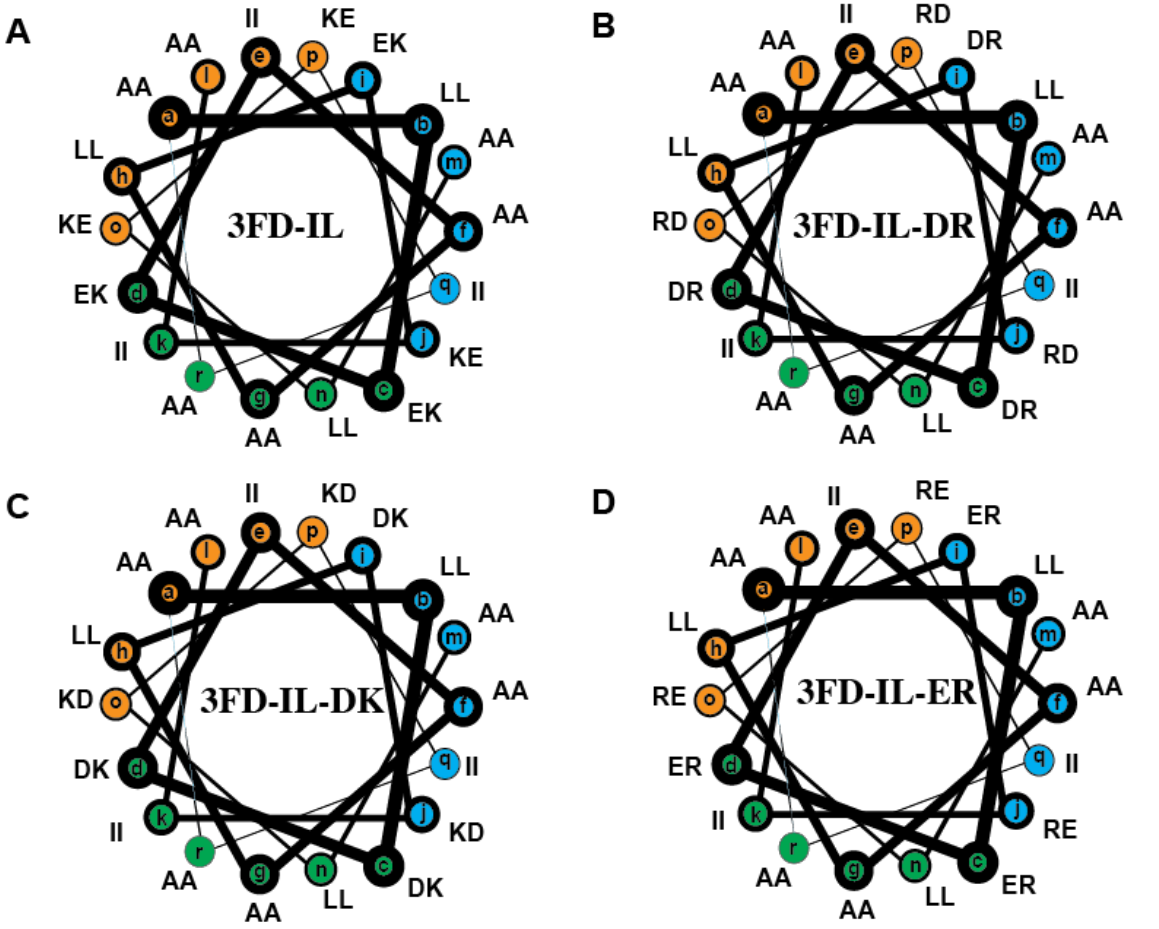

Figure 3.18 Helical wheel representation of (a) 3FD-IL (b) 3FD-IL-DR (c) 3FD-IL-DK, and (d) 3FD-IL-ER (e) linear sequences of previously mentioned peptides

3.5 Self-Assembly of Aspartate and Arginine Charge Mutants

Next, the self-assembly of the charge mutants **3FD-IL-DR**, **3FD-IL-DK**, and **3FD-IL-ER** was studied. The peptides **3FD-IL-DK** and **3FD-IL-DR** were assembled at pH 8.5 under the same conditions as **3FD-IL**. Circular dichroism experiments were

performed to determine the secondary structure of the charge mutants. The peptide **3FD-IL-DK** exhibited the same secondary structure before and after thermal annealing (Figure

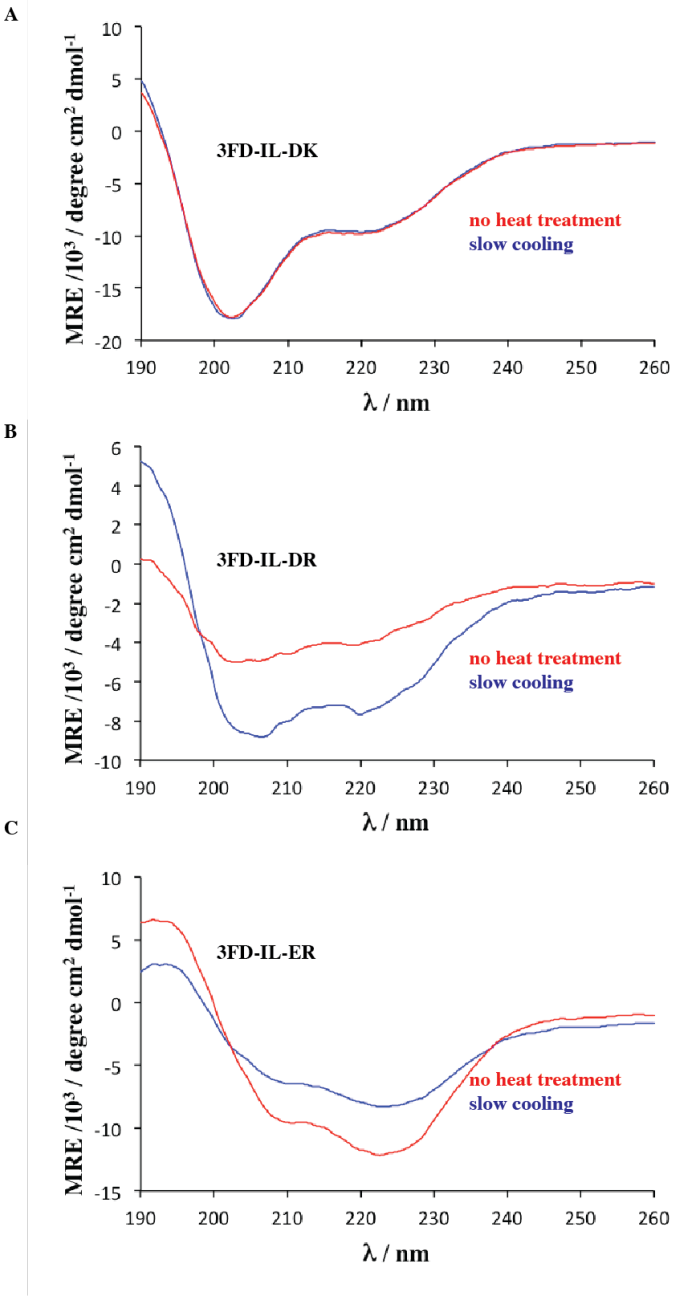

Figure 3.19 **CD spectra of (a)** 3FD-IL-DK **(b)** 3FD-IL-DR **and (c)** 3FD-IL-ER

3.19a). In comparison to **3FD-IL**, the CD signature of **3FD-IL-DK** contained reduced α-helical content. The presence of a new minimum at 204 nm was consistent with the

formation of a random coil secondary structure (Figure 3.19a). Similarly, the CD signature of **3FD-IL-DR** also revealed a decrease in α-helical secondary structure, and the formation of random coil secondary structure (Figure 3.19b). The decrease in α-helicity in the **3FD-IL-DK** and **3FD-IL-DR** mutants can be attributed to the length of the aspartic acid side chain. In comparison to glutamic acid, the negative charge of the aspartic acid is closer to the α-helical backbone. A study by Lu *et al*. showed that α-helical propensity is decreased as charge approaches the α-helical backbone due to interference of the charge with intramolecular hydrogen bonding [13]. As expected, neither **3FD-IL-DK** nor **3FD-IL-DR** formed assemblies observed by transmission electron microscopy.

In contrast, the peptide **3FD-IL-ER**, formed an α-helical circular dichroism signature in the absence of heat treatment and with thermal annealing. In comparison to **3FD-IL** (Figure 3.19c), which has a theoretical isoelectric point at a pH of 7.41, **3FD-IL-ER** has an isoelectric point at a pH of 8.13. As a result **3FD-IL-ER** is not soluble at the pH used to assemble **3FD-IL**. **3FD-IL-ER** was instead assembled at pH 6 in 10 mM MES buffer. Transmission electron microscopy revealed the presence of both large assemblies, which looked like the nanosheets formed by **3FD-IL** (Figure 3.20a) and twisted structures (Figure 3.20b), which appeared to be rolled up nanosheets. Sometimes, twisted structures were observed growing from nanosheets (Figure 3.20d), and nanosheets were observed folding (Figure 3.20c).

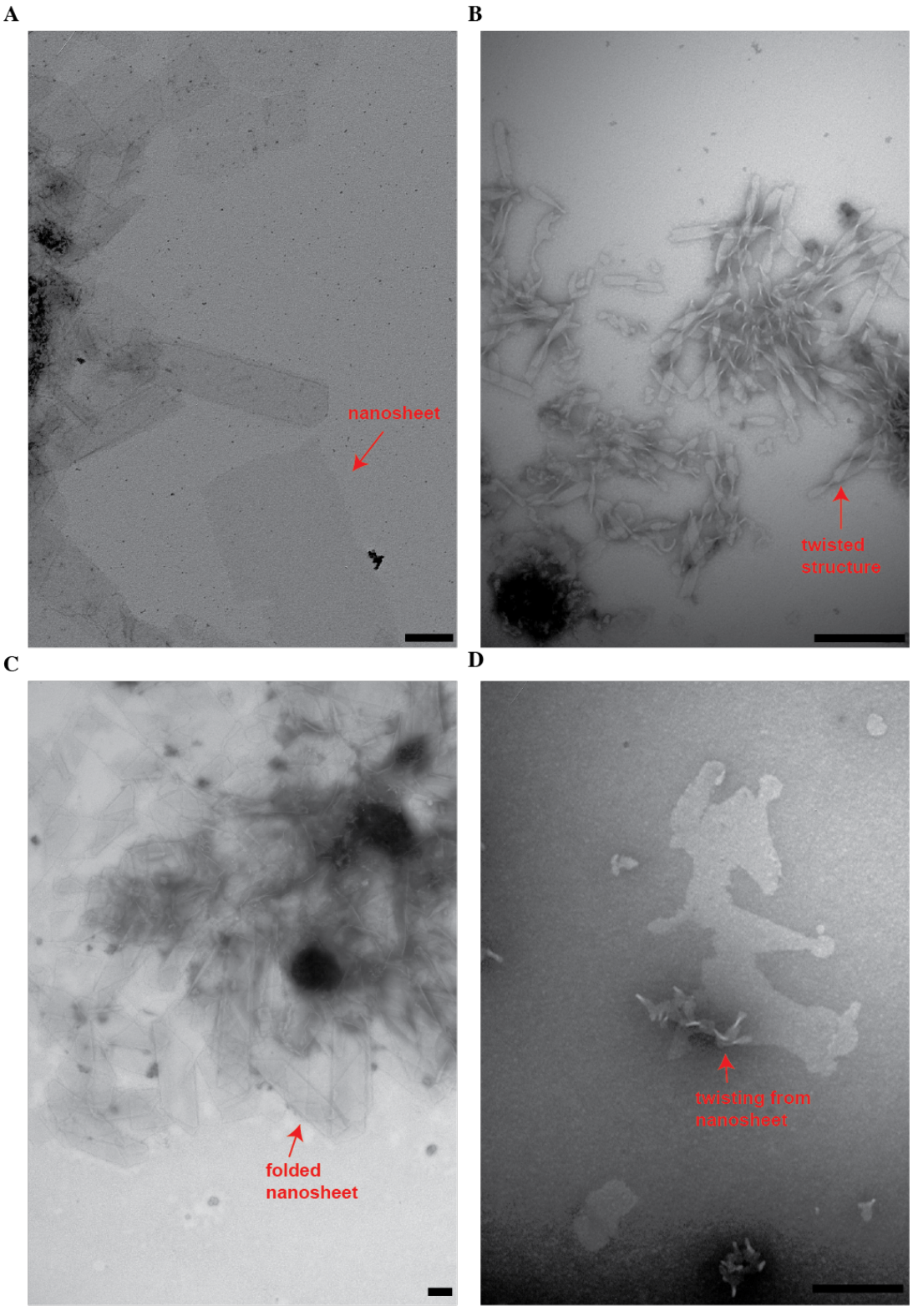
A
nanosheet
B
twisted
structure
C
folded
nanosheet
D
twisting from
nanosheet

Figure 3.20 Electron microscopy images of peptide 3FD-IL-ER after thermal annealing (a) possible nanosheet formation (b) formation of twisted structures (c) folding of nanosheets (d) twisting from nanosheets

A solution of these structures was taken for small angle x-ray scattering analysis. The small angle x-ray scattering curve revealed the presence of broad diffraction peaks, suggesting that the assemblies formed by **3FD-IL-ER** contained less internal order than those formed by **3FD-IL**. The diffraction spacings occurred at distances of 14.5 Å, 13.5 Å, 12.7 Å, 9.2 Å, and 8.4 Å. The distances 14.5 Å and 8.4 Å also showed up in the **3FD-IL** nanosheets, indicating some conservation of structure between **3FD-IL-ER** and **3FD-IL** (Figure 3.21).

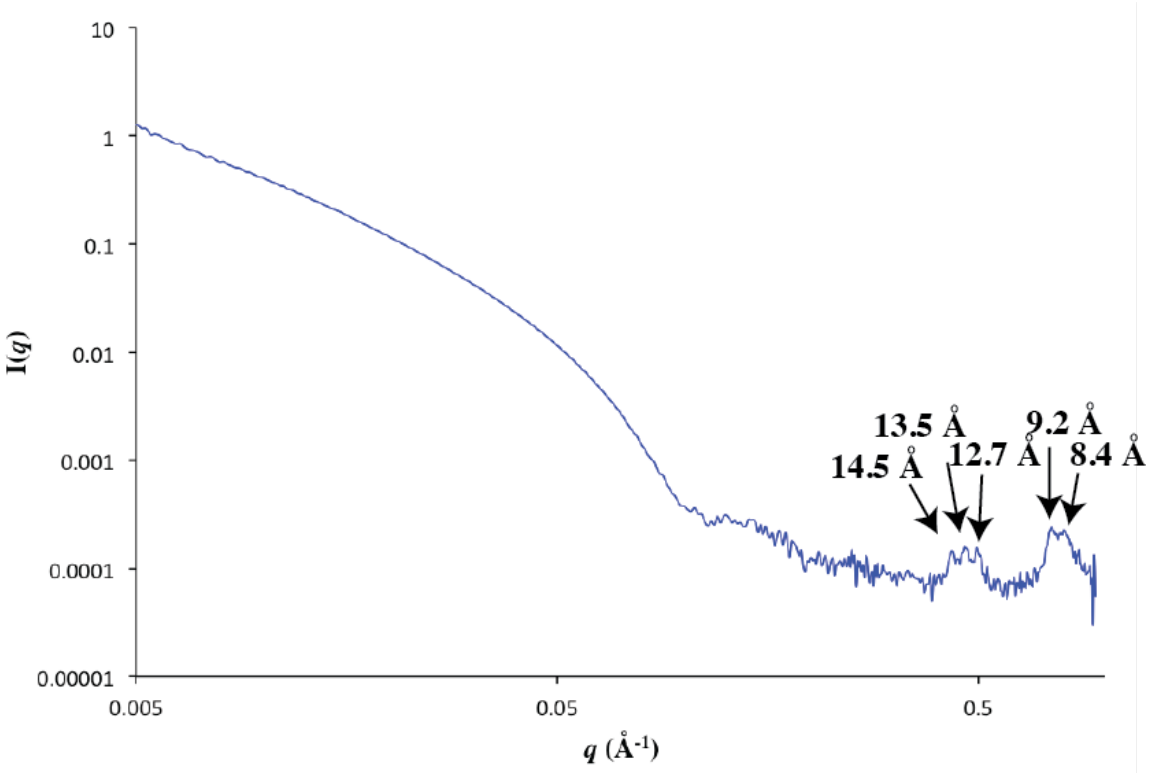

Figure 3.21 Small angle x-ray scattering curve of 3FD-IL-ER solution at pH 6 revealed weaker, more broad diffraction peaks than those formed by 3FD-IL

Interestingly, the intensity of the scattering in the intermediate q region decayed with $q^{-1.51}$, consistent with the heterogeneity of the sample as seen by TEM.

A

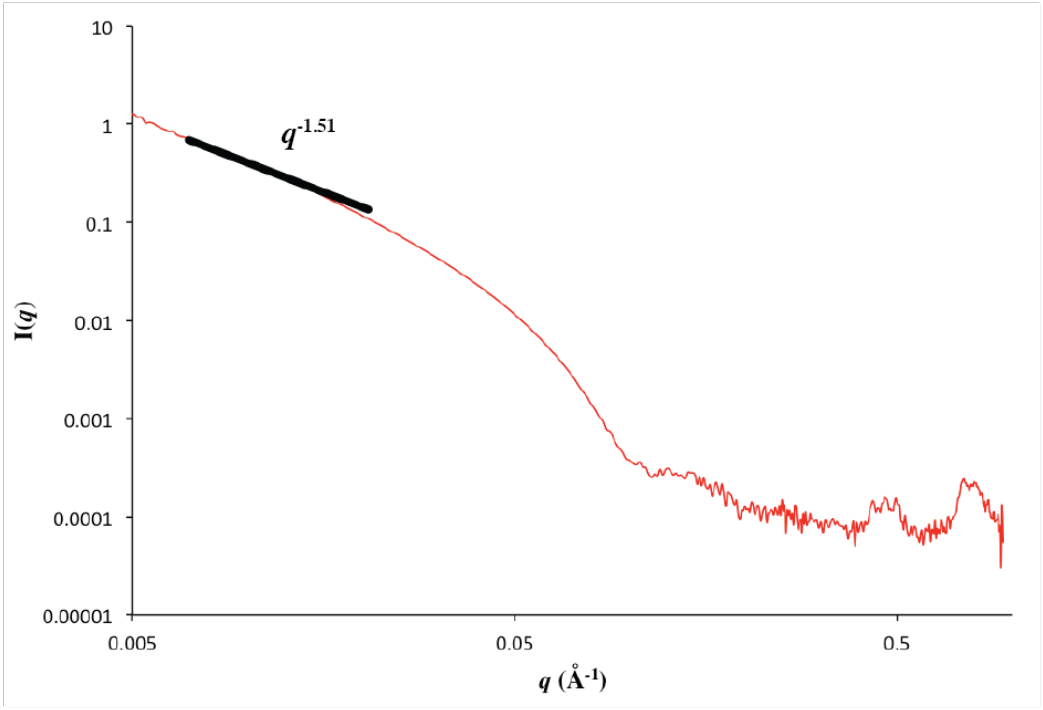

B

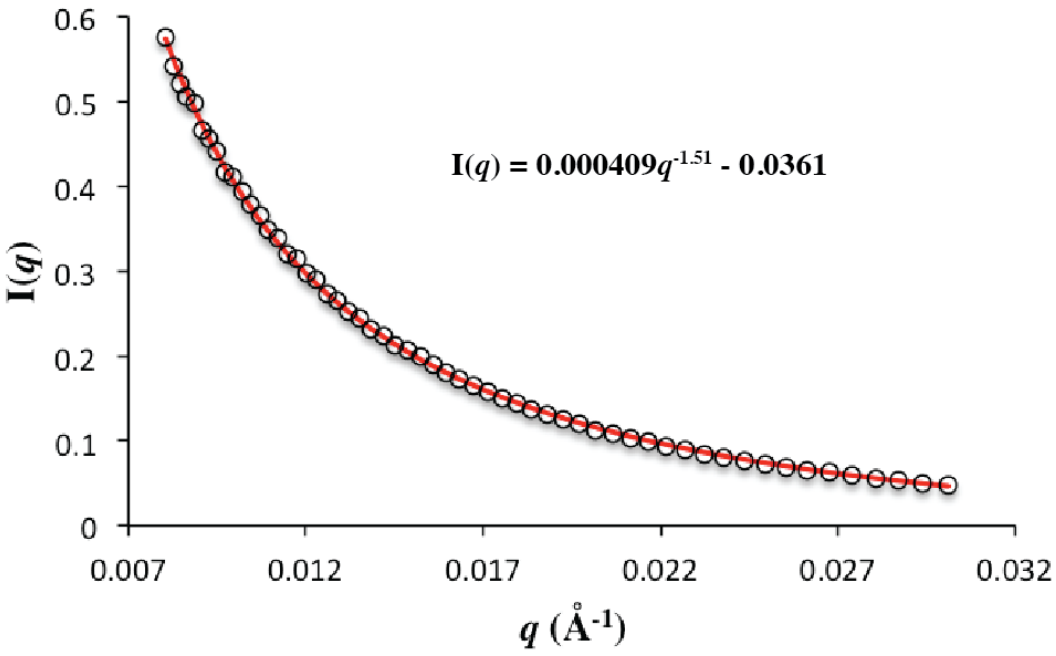

Figure 3.22 (a) dependency of I(q) on q-1.51 and (b) fit of intensity to an exponential function

A Guinier approximation of the low q region revealed that the nanosheets have a radius of gyration of 17.26 Å and a sheet thickness of 5.99 nm, consistent with a model for the nanosheets in which the long axis of the α-helix is perpendicular to the surface of the nanosheets (Figure 3.23).

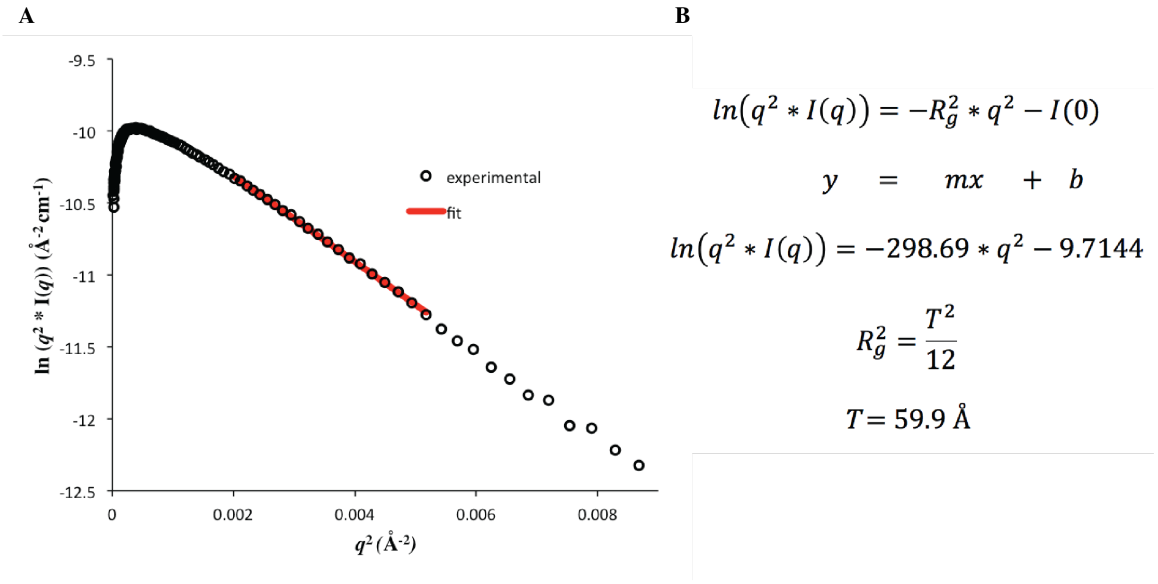

Figure 3.23 (a) Guinier fit of **3FD-IL-ER** scattering curve (b) determination of thickness for **3FD-IL-ER** nanosheets using the Guinier approximation for sheet-like objects

The conformational diversity that peptide **3FD-IL-ER** exhibited can be understood by comparing the side chain of arginine to lysine. Due to delocalization of charge, the guanidinium group of the arginine side chain can form bidentate hydrogen bonds. The peptide **A_6R**, described in Chapter 1, formed thin nanosheets or nanotubes, which were dependent on peptide concentration [14]. At low concentration, the peptide formed thin nanosheets. The nanosheets are stabilized by the interaction of **A_6R** peptides

in an antiparallel orientation, which is stabilized by electrostatic interactions between the arginine side chain and the C-terminal carboxyls. At high concentration, packing frustration of the arginine groups caused curvature of the **A_6R** nanosheets.

The dependence of **3FD-IL-ER** self-assembly on peptide concentration was tested. In contrast to **A_6R**, **3FD-IL-ER** formed a homogenous solution of twisted structures at a peptide concentration of 0.5 mg/mL. As the concentration of **3FD-IL-ER** was increased to 10 mg/mL, nanosheets were observed that coexisted with twisted structures (Figure 3.24).

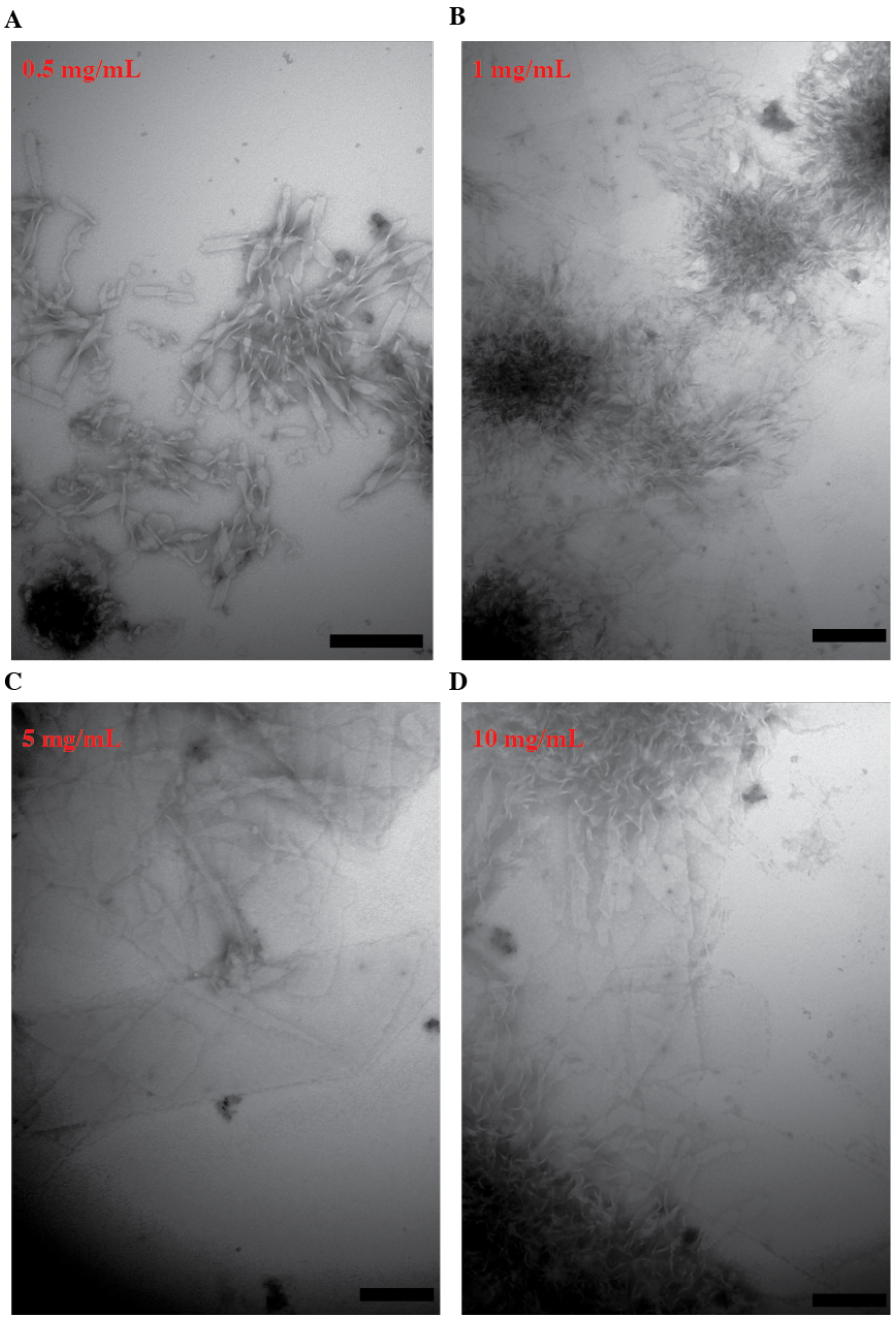

Figure 3.24 Dependence of 3FD-IL-ER self-assembly on concentration; Electron micrographs taken at approximate peptide concentrations of (a) 0.5 mg/mL, (b) 1 mg/mL, (c) 5 mg/mL, (d) 10 mg/mL

The assemblies were monitored over time to determine if either the twisted structures or nanosheets are unstable intermediates. After a period of nine days, the twisted structures

predominated the microscopy images, and after six weeks, no nanosheets were found by transmission electron microscopy (Figure 3.25).

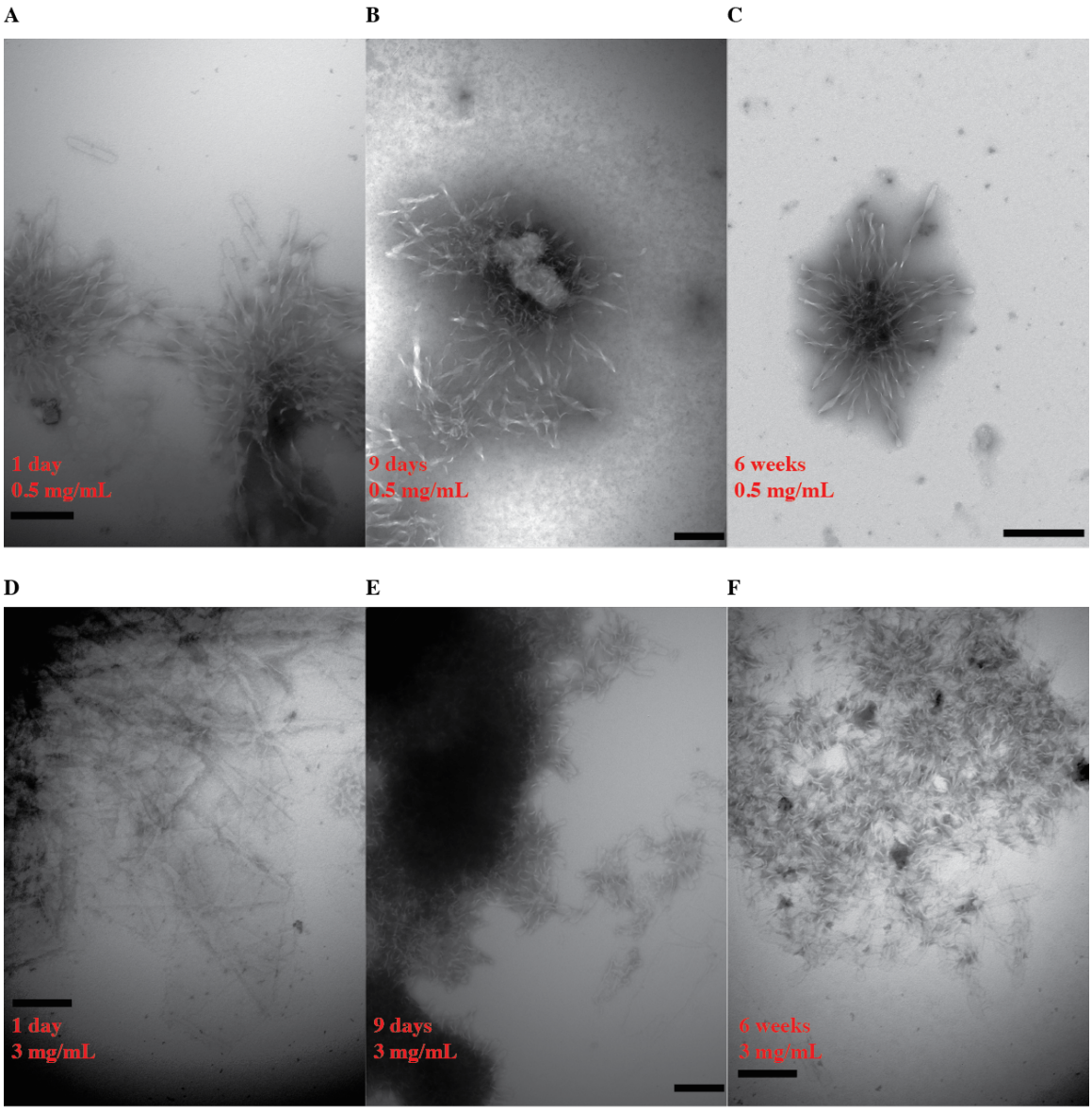

Figure 3.25 Time dependence of 3FD-IL-ER assembly (a) 0.5 mg/mL, 1 day 3FD-IL-ER assemblies (b) 0.5 mg/mL, 9 day 3FD-IL-ER assemblies, (c) 0.5 mg/mL, 6 weeks 3FD-IL-ER assemblies, (d) 3 mg/mL, 1 day 3FD-IL-ER assemblies, (e) 3 mg/mL, 9 days 3FD-IL-ER assemblies, (f) 3 mg/mL, 6 weeks 3FD-IL-ER assemblies

Based on this data, I propose that at high peptide concentrations, nanosheets are formed in which the α-helices are oriented perpendicular to the nanosheet surface. The

bulky arginine side chain does not pack into nanosheets as efficiently as lysine, and twisting could stabilize the packing of arginine. Based on the observation that nanosheets disappear as a function of time, I predict that these products are not the thermodynamically favorable product. With enough incubation time or at low concentrations, the thermodynamically stable product, the twisted structures are formed.

3.6 Conclusions

The experiments from this chapter indicated that charge manipulation provides valuable structural information about the **3FD-IL** nanosheets. As the assembly of **3FD-IL** in the presence of salt indicated, specific salt bridges are essential for maintaining the structural integrity of the nanosheets. Variations in the sequence of the charged amino acids drastically change peptide self-assembly. The α-helical macrodipole is one factor that contributes to the requirement of specific charge interactions in the **3FD-IL** nanosheets. The macrodipole is stabilized when the **3FD-IL** nanosheets are in the antiparallel conformation. The sequence of charged amino acids either prevents or allows an antiparallel conformation of helices. Arrangement of helices in the parallel orientation causes the formation of structures of different morphology.

Seemingly slight mutations in charged amino acids, such as aspartate for glutamate, or arginine for lysine, also impact the resultant morphologies observed. The former mutation causes a change in the secondary structure of the peptide, which prohibits nanosheet formation. The latter mutation introduces a guanidino group into the peptide sequence. Arginine side chains have more opportunities to hydrogen bond and have interactions in different directions. Therefore, the observation of additional morphologies such as twisted nanosheets is not surprising. The energy landscape

involved in peptide self-assembly is very complex and slight changes in sequence can drastically change this landscape. The 3FD-IL nanosheets contain specific ionic interactions. The knowledge obtained in this chapter will aid in further design of structures based on **3FD-IL**. Furthermore, a high-resolution structure of **3FD-IL** will greatly aid our understanding of the charge variants described in this chapter.

3.7 Methods and Supporting Information

Reagents: All Fmoc amino acids were purchased from Anaspec Inc. (Fremont, CA). The Fmoc-Peg-PAL-PS resin for solid-phase peptide synthesis was purchased from Applied Biosystems. All other chemicals were purchased from Sigma-Aldrich.

Peptide synthesis: The peptides were synthesized using microwave-assisted synthesis on a CEM Liberty solid-phase peptide synthesizer. A Fmoc-PEG-PAL-PS resin (Applied Biosystems) was used for synthesis. Standard Fmoc protection chemistry was used for coupling, which was promoted using standard activation protocols based on DIEA/HBTU and base-induced deprotection of the Fmoc group (20 % piperidine in DMF). All peptides were acetylated at the N-terminus using 20 % acetic anhydride. The peptides were purified using reverse phase high performance liquid chromatography (HPLC) on a C18 column using a water-acetonitrile (0.1 % trifluoroacetic acid) gradient. The target HPLC fractions were collected and liapholized. The purity of the peptides was analyzed using electrospray ionization mass spectrometry and analytical HPLC.

Peptide Assembly: The peptides **3FD-IL-KE**, **3FD-IL-EK**, and **3FD-IL-EEKK** were dissolved in 10 mM TAPS buffer at pH 8.5. Nanosheets and fibrils were produced after thermal annealing in a thermal cycler. The peptides 3FD-IL-DR (10 mg/mL) and **3FD-IL-DK** (10 mg/mL) were also prepared in 10 mM TAPS buffer at pH 8.5. The peptide **3FD-IL-ER** was assembled in 10 mM MES buffer at pH 6.0 (range of concentrations from 0.5 mg/mL to 10 mg/mL). The nanosheets formed from the mixture of **3FD-IL-EK** and **3FD-IL-KE** were assembled by dissolving 1 mg of each peptide (in the same tube) in 50 μL of trifluoroethanol. The trifluoroethanol was allowed to evaporate completely in the dessicator, and subsequently 200 μL of 10 mM TAPS buffer was added to the tube. Sheets were formed after annealing this solution. The annealing method used in all of these cases was the same as that used for 3FD-IL. The peptide solutions were initially heated up to 90° C for ten minutes followed by cooling 0.2° C/ 5 minutes to a final temperature of 40 °C. The resultant nanosheets were stored at room temperature.

Circular Dichroism: CD spectra were recorded on a Jasco J-810 CD spectropolarimeter in 0.1 mm quartz cells (Hellma Analytics) at a peptide concentration of 1 mg/mL in 10 mM TAPS buffer pH 8.5. Spectra were recorded at a scanning rate of 50 nm/min and a resolution of 0.1 nm. CD melting experiments were performed in the temperature range from 5°C to 95°C at a heating rate of 40 °C/hour. The intensity of the CD signal at 222 nm was monitored as a function of temperature. Melting temperatures were obtained from the first derivative of the melting curves.

Transmission Electron Microscopy: TEM specimens were prepared from aqueous

solutions of 3FD-IL (10 mg/mL) and its variants. The samples were deposited onto 200 mesh carbon-coated copper grids from Electron Microscopy Sciences (Hatfield, PA). After a 1 min incubation period, the samples were washed with water and stained with an aqueous solution of 0.1 % methylamine tungstate stain. Excess stain was wicked away from the grids after incubation on the grid for 30 s. TEM measurements were acquired on a JEOL JEM-1400 transmission electron microscope at an accelerating voltage of 120 kV.

Small angle x-ray scattering: 3FD-IL-ER was prepared for small angle x-ray scattering measurements at a peptide concentration of 10 mg/mL in 10 mM TAPS buffer, pH 8.5. The peptide **3FD-IL-EEKK** and the mixture of **3FD-IL-EK** and **3FD-IL-KE** were also assembled at peptide concentrations of 10 mg/mL. After nanosheets were formed by thermal annealing, all solutions except for **3FD-IL-ER** were dialyzed against 10 mM TAPS (pH 8.5) to remove residual trifluoroacetic acid. For the twisted structures of **3FD-IL-ER**, radiation damage was observed, and therefore this solution was dialyzed against a butter that contained 10 mM TAPS buffer and 1 % glycerol. The dialysis solutions were used as buffer blanks. This aspect is essential for accurate background subtraction of the small angle x-ray scattering curve.

Synchrotron SAXS/WAXS measurements were performed at the 12-ID-B beamline of Advanced Photon Source at Argonne National Laboratory. A simultaneous SAXS/WAXS setup was utilized, and the sample-to-detector distances were set such that the overall scattering momentum transfer, q, range was achieved from 0.005 to 2.4 Å–1, where $q = 4\pi\sin\theta/\lambda$, 2θ denoting the scattering angle and λ the X-ray wavelength. The wavelength was set at 1.033 Å during the measurements. Scattered X-ray intensities were

measured using a Pilatus 2 M (DECTRIS Ltd.) detector for SAXS and Pilatus 300K for WAXS. SAXS/WAXS measurements were performed on aqueous solutions of peptides at 25 °C. A quartz capillary flow cell (1.5 mm diameter) was employed to prevent radiation damage. Twenty images were collected for each sample and buffer. The 2D scattering images were converted to 1D SAXS curves through azimuthal averaging after solid angle correction and then normalizing with the intensity of the transmitted X-ray beam, using the software package at beamline 12ID-B. The 1D curves of the samples were averaged and subtracted with the background measured from the corresponding buffers.

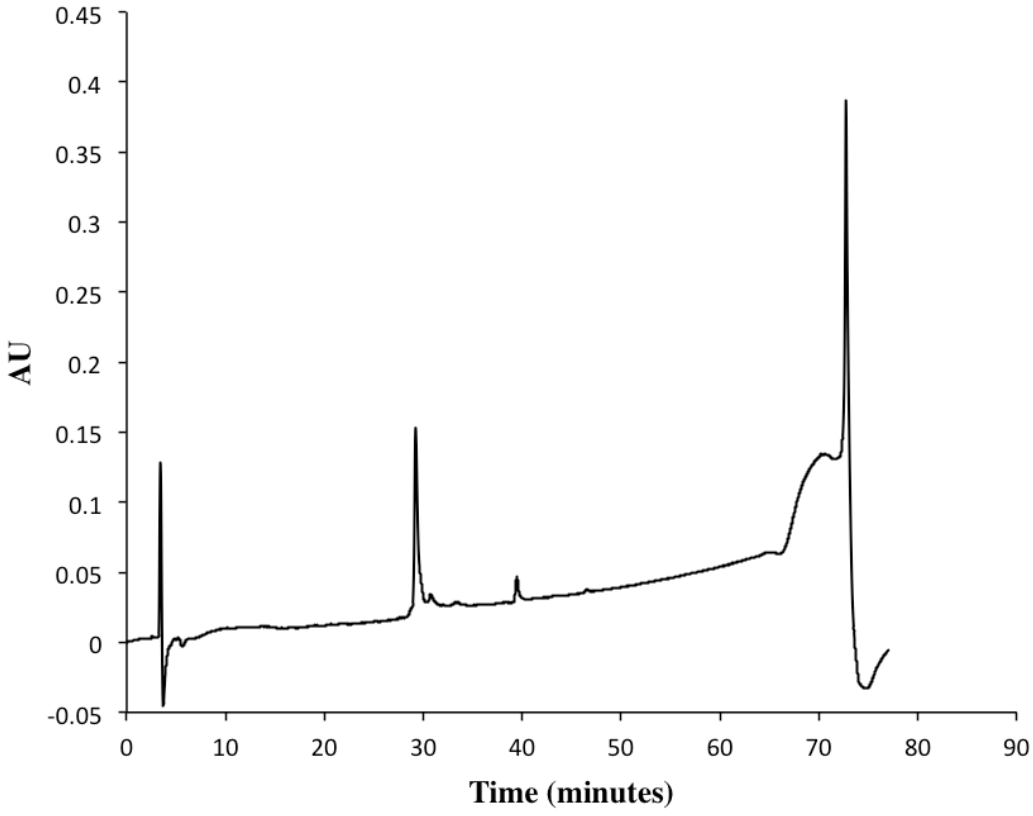

Figure 3.26 Analytical HPLC spectrum of **3FD-IL-KE**

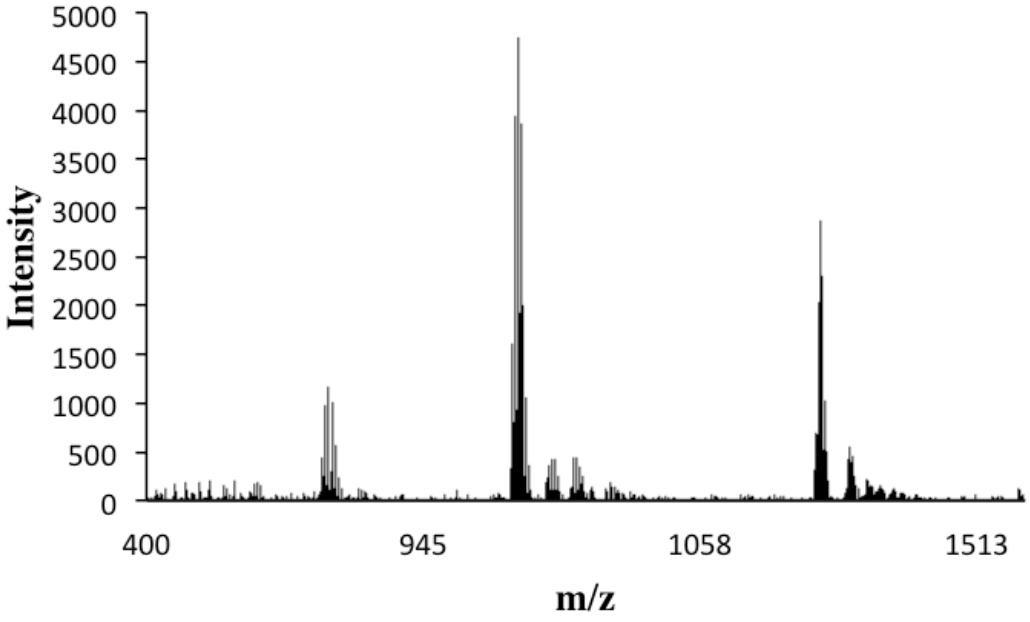

Figure 3.27 Mass spectrum of **3FD-IL-KE**

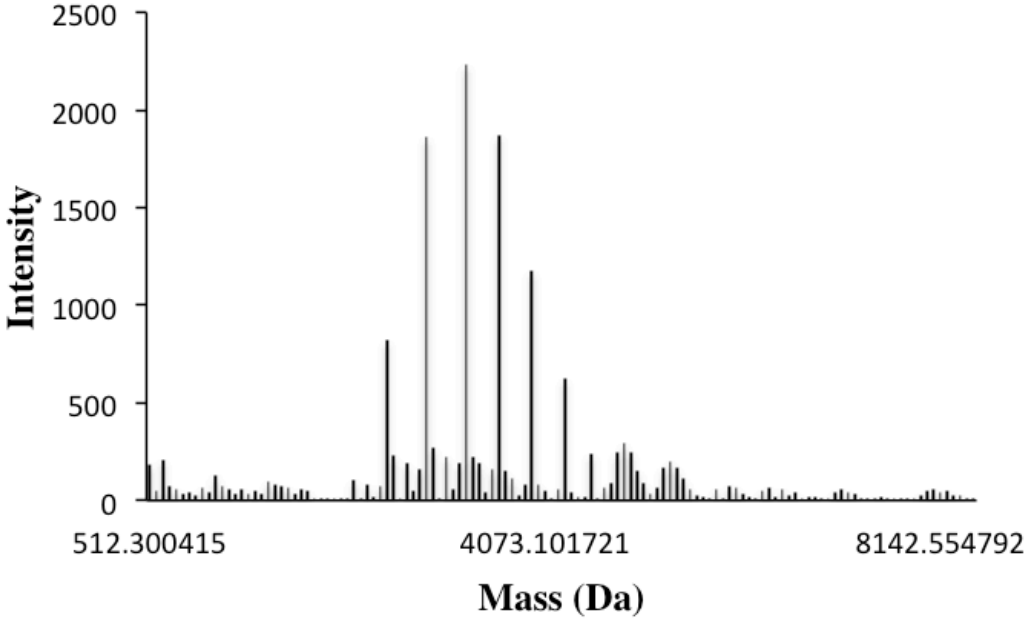

Figure 3.28 Deconvoluted mass spectrum of **3FD-IL-KE**

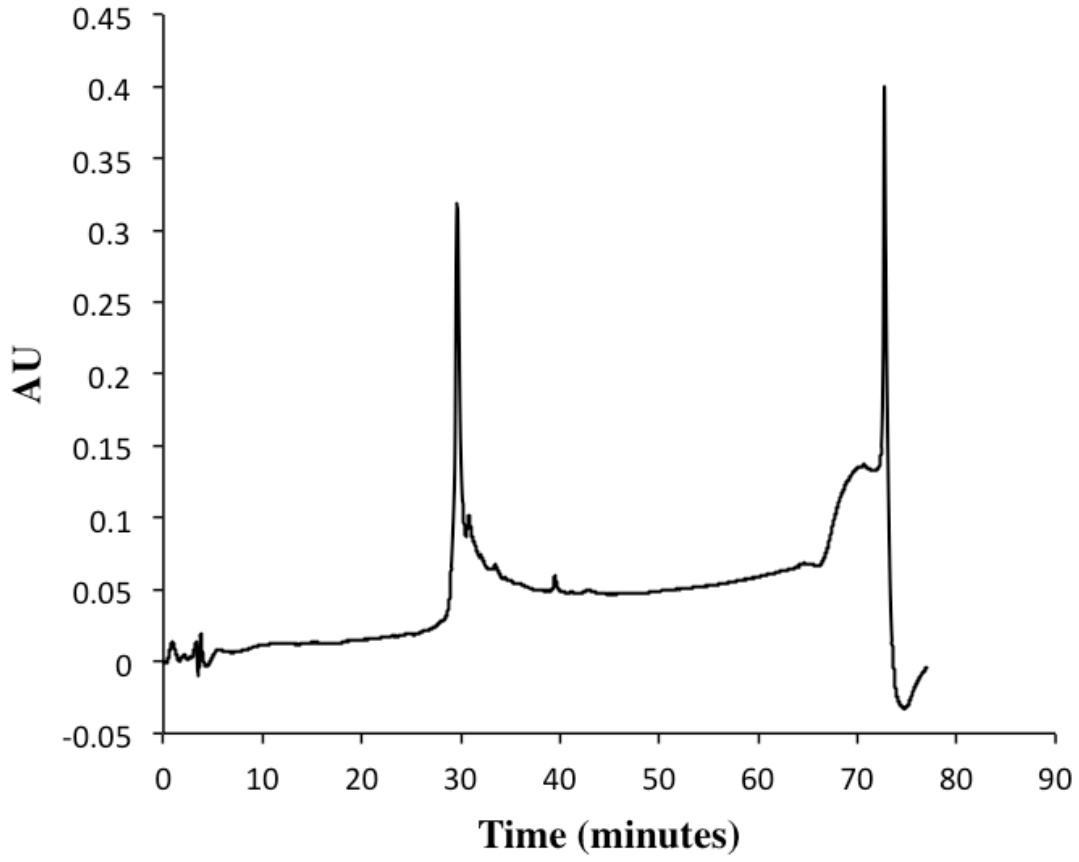

Figure 3.29 Analytical HPLC spectrum of **3FD-IL-EK**

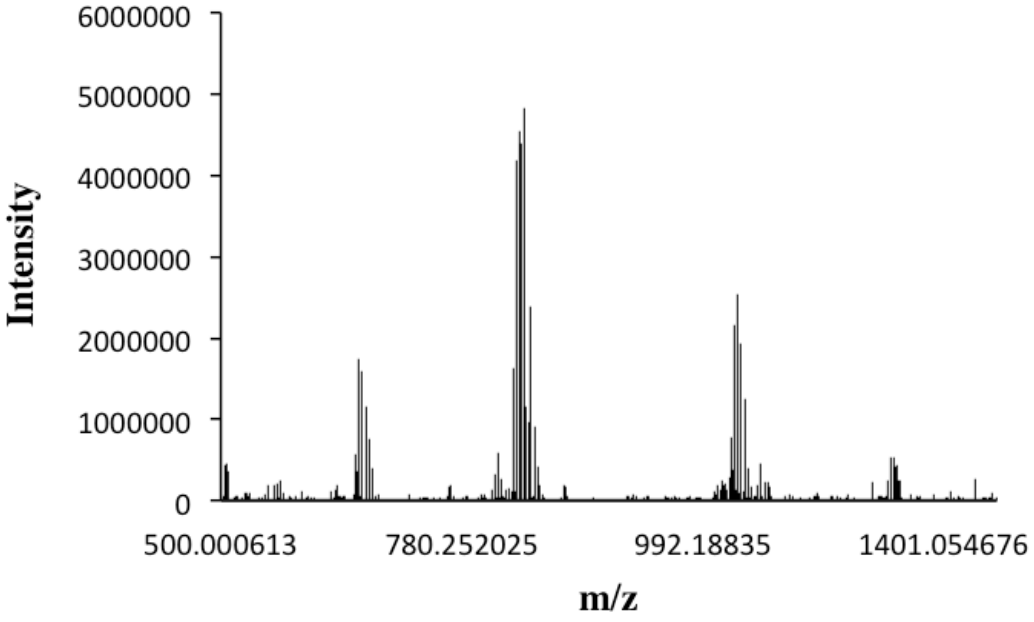

Figure 3.30 Mass spectrum of **3FD-IL-EK**

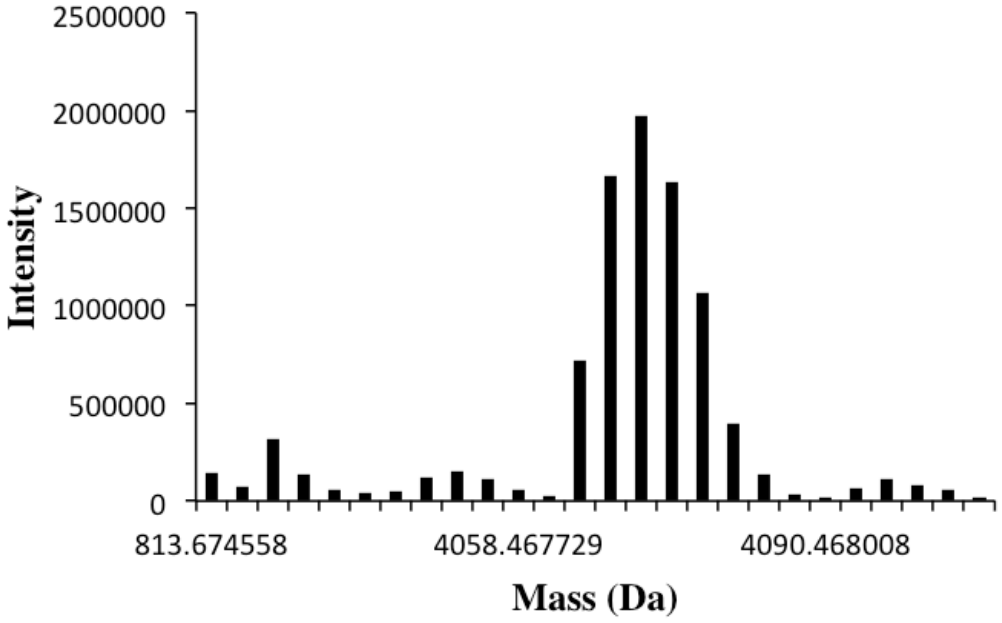

Figure 3.31 Deconvoluted mass spectrum of **3FD-IL-EK**

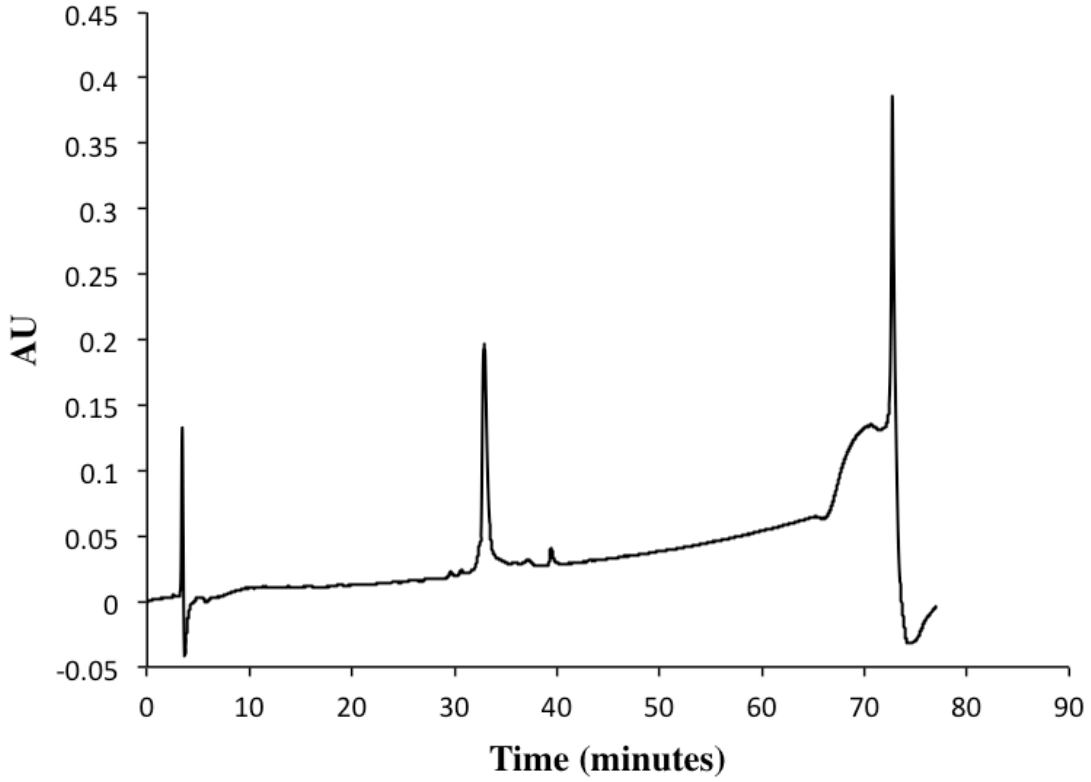

Figure 3.32 Analytical HPLC spectrum of **3FD-IL-EEKK**

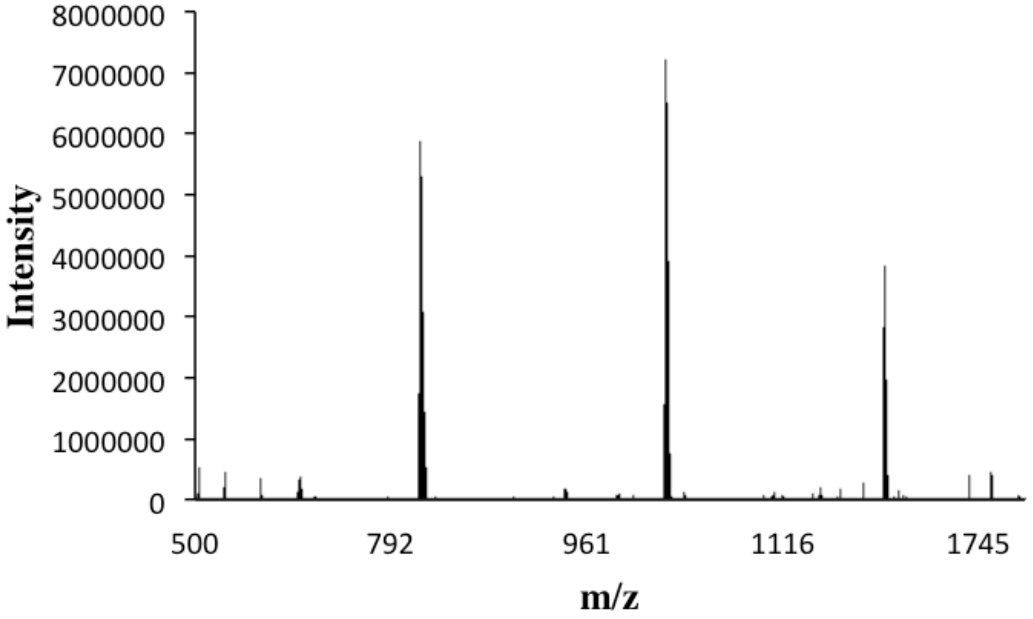

Figure 3.33 Mass spectrum of 3FD-IL-EEKK

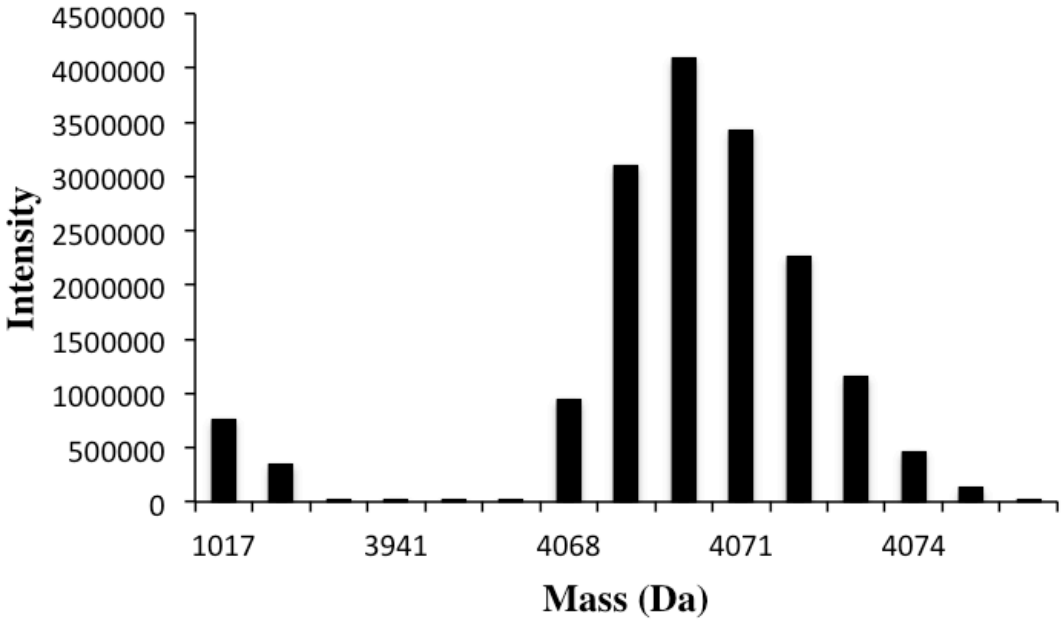

Figure 3.34 Deconvoluted mass spectrum of **3FD-IL-EEKK**

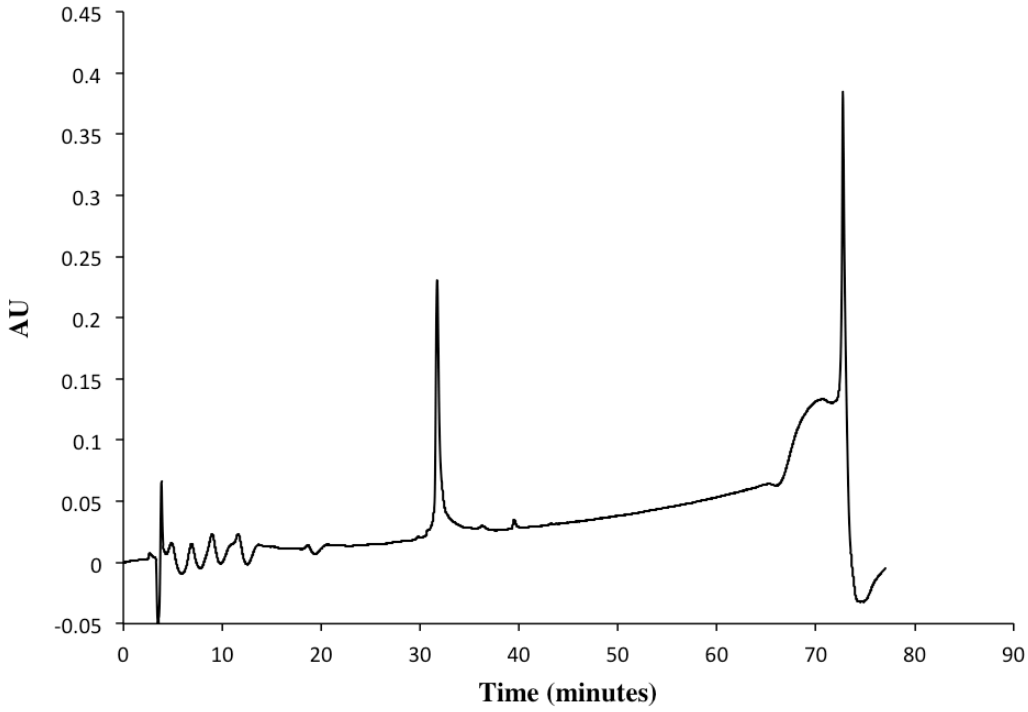

Figure 3.35 Analytical HPLC spectrum of **3FD-IL-ER**

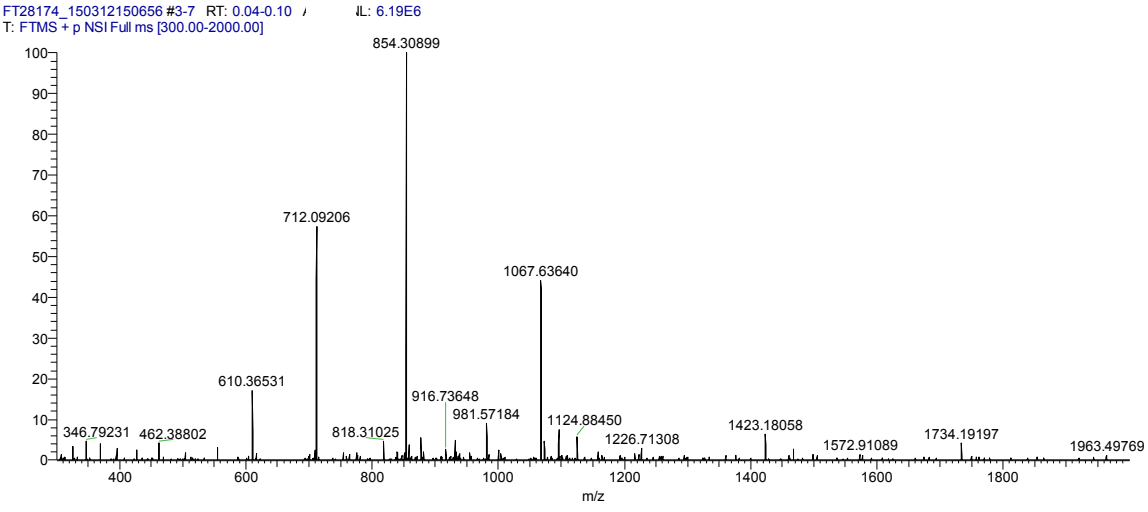

Figure 3.36 Mass spectrum of **3FD-IL-ER**

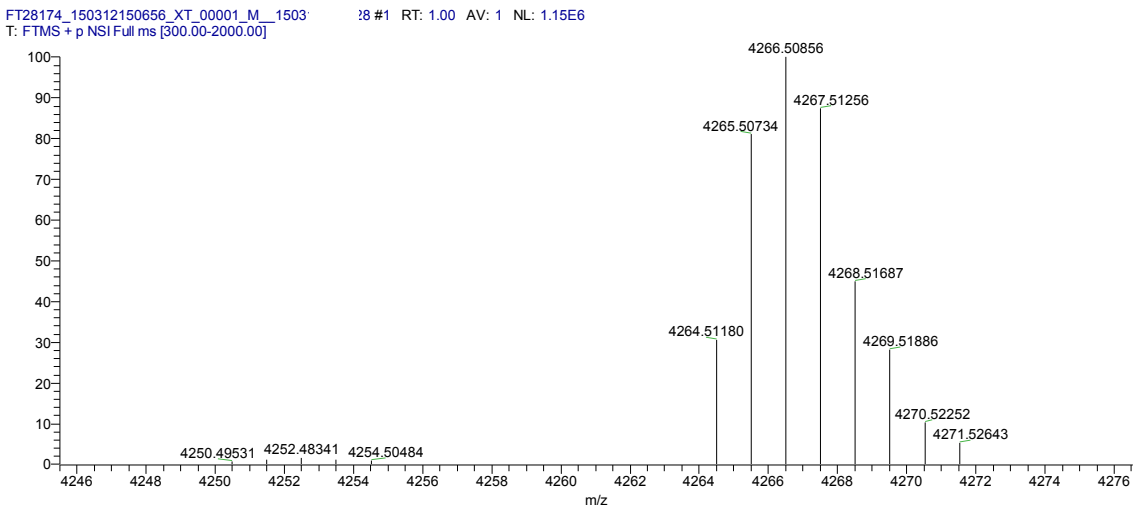

Figure 3.37 Deconvoluted mass spectrum of **3FD-IL-ER**

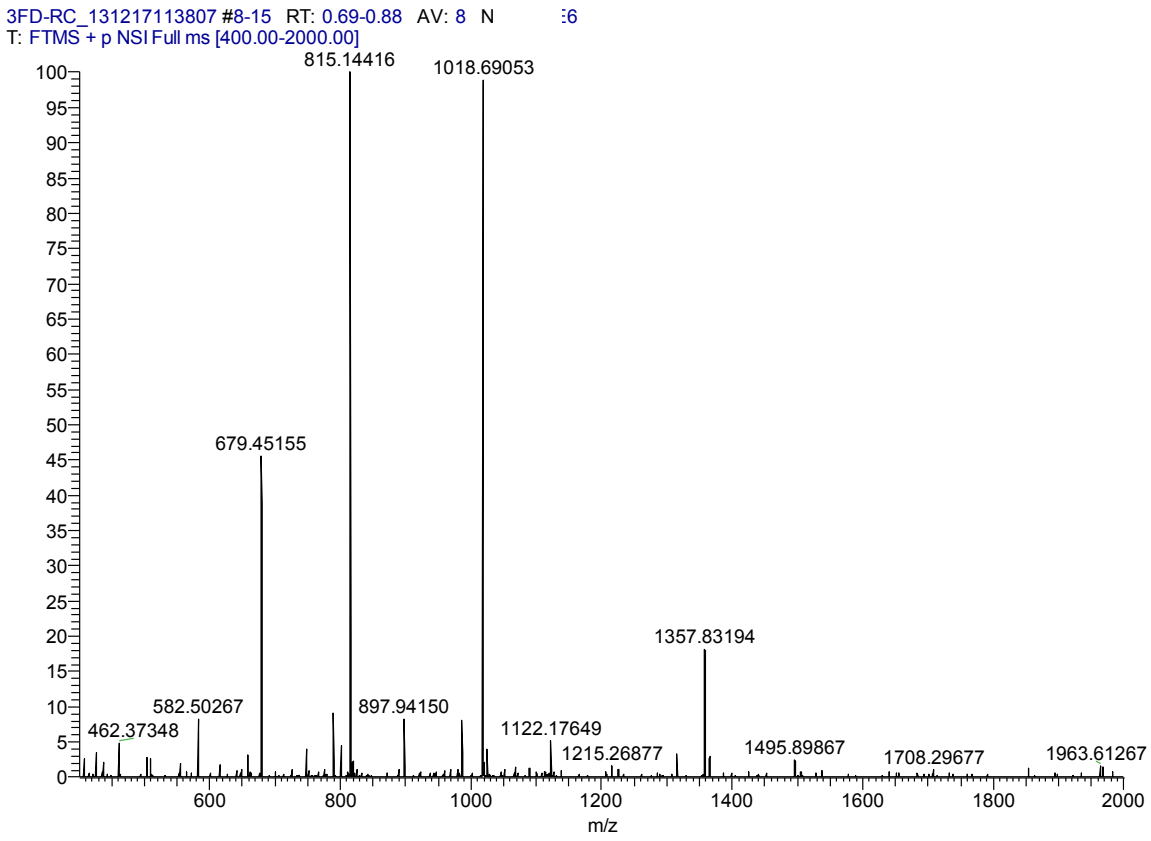

Figure 3.38 Mass spectrum of **3FD-IL-RC**

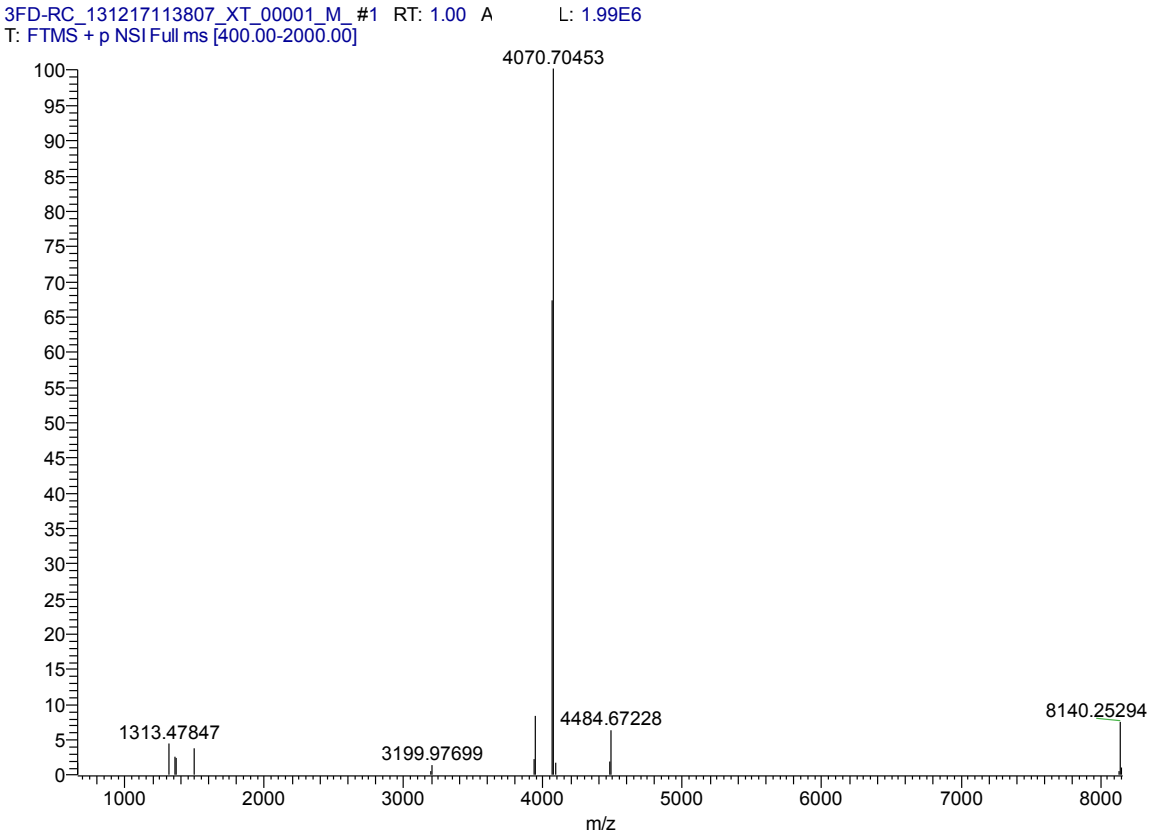

Figure 3.39 Deconvolution of mass spectrum of **3FD-IL-RC**

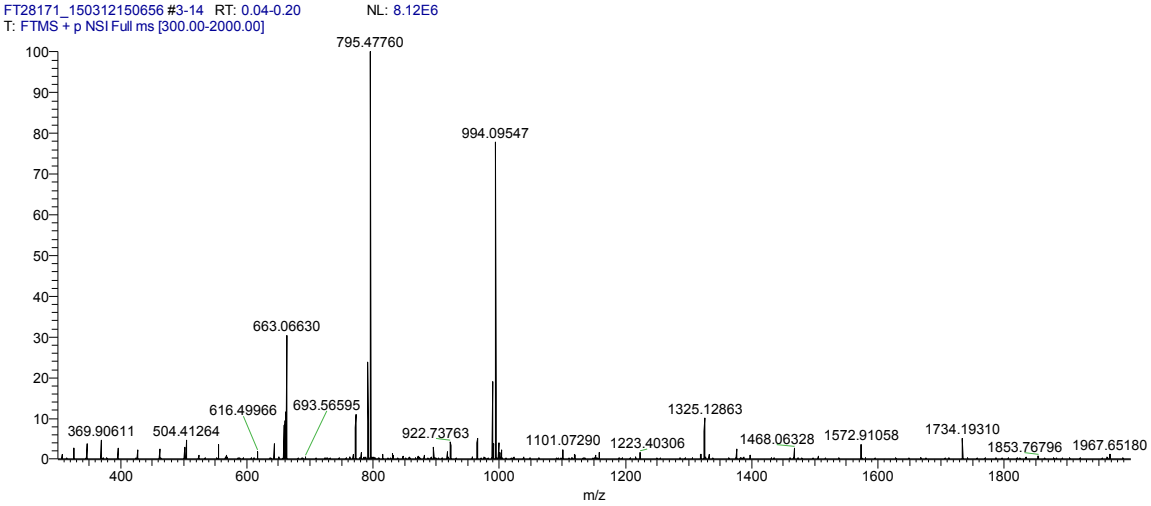

Figure 3.40 Mass spectrum of **3FD-IL-DK**

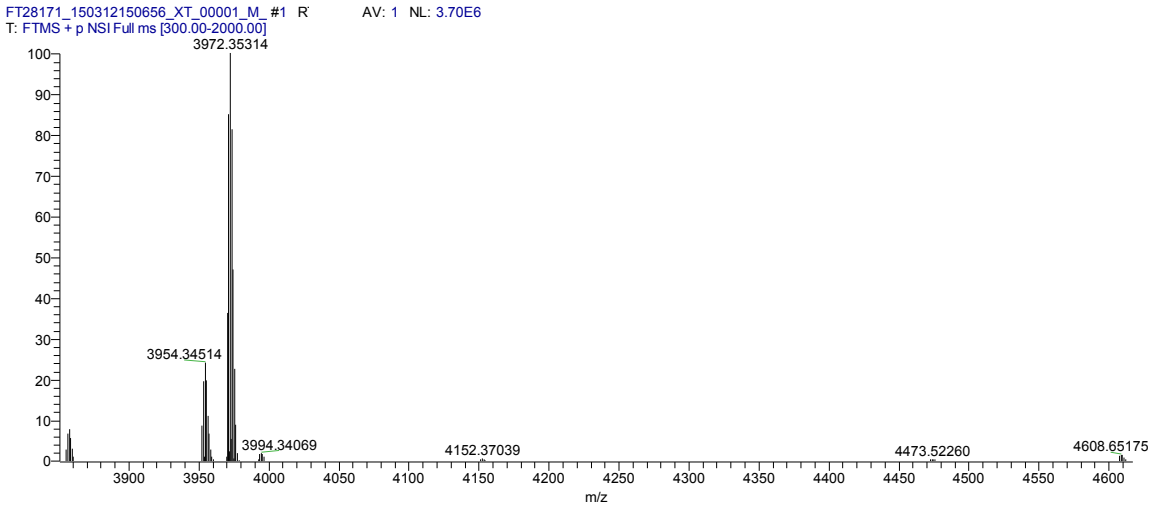

Figure 3.41 Deconvolution of mass spectrum of **3FD-IL-DK**

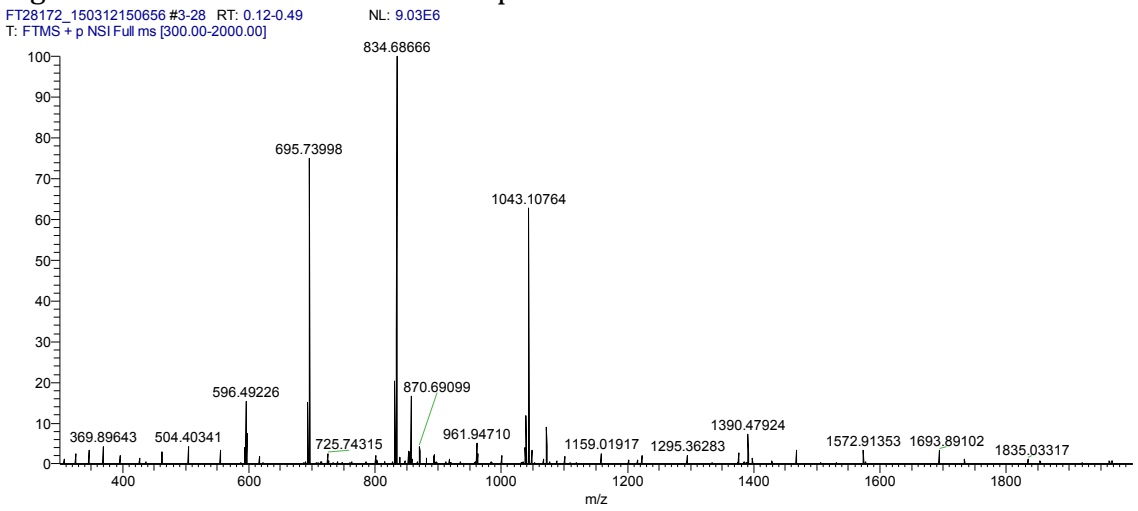

Figure 3.42 Mass spectrum of **3FD-IL-DR**

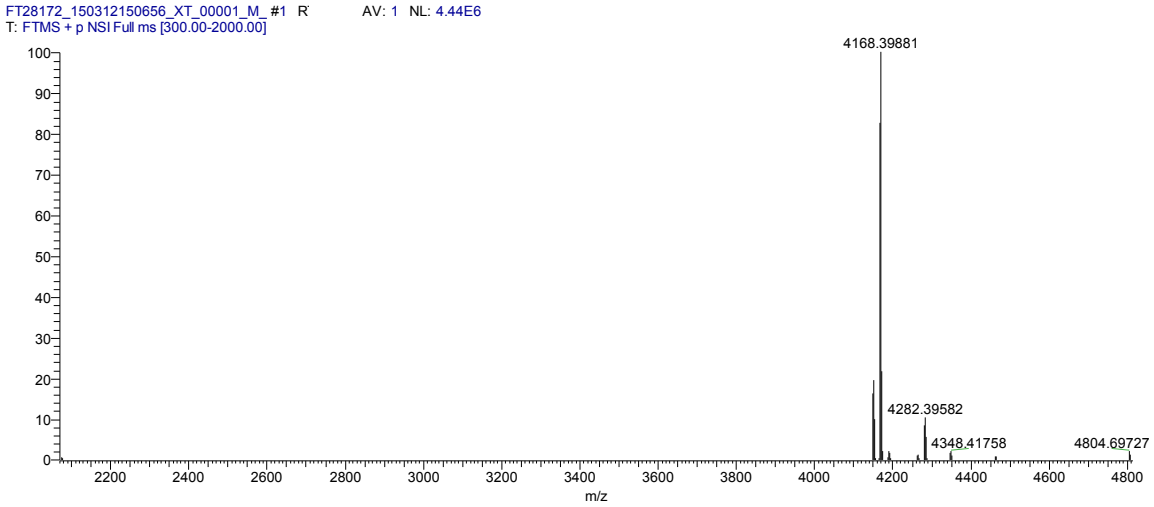

Figure 3.43 Deconvolution of **3FD-IL-DR**

ReferencesUncategorized References

1. Jiang T, Xu CF, Zuo XB, Conticello VP (2014) Structurally Homogeneous Nanosheets from Self-Assembly of a Collagen-Mimetic Peptide. Angew Chem Int Edit 53 (32):8367-8371. doi:DOI 10.1002/anie.201403780
2. Jiang T, Xu CF, Liu Y, Liu Z, Wall JS, Zuo XB, Lian TQ, Salaita K, Ni CY, Pochan D, Conticello VP (2014) Structurally Defined Nanoscale Sheets from Self-Assembly of Collagen-Mimetic Peptides. J Am Chem Soc 136 (11):4300-4308. doi:DOI 10.1021/ja412867z
3. Jiang T, Vail OA, Jiang Z, Zuo X, Conticello VP (2015) Rational Design of Multilayer Collagen Nanosheets with Compositional and Structural Control. J Am Chem Soc 137 (24):7793-7802. doi:10.1021/jacs.5b03326
4. Nam KT, Shelby SA, Choi PH, Marciel AB, Chen R, Tan L, Chu TK, Mesch RA, Lee BC, Connolly MD, Kisielowski C, Zuckermann RN (2010) Free-floating ultrathin two-dimensional crystals from sequence-specific peptoid polymers. Nat Mater 9 (5):454-460. doi:Doi 10.1038/Nmat2742
5. Olivier GK, Cho A, Sanii B, Connolly MD, Tran H, Zuckermann RN (2013) Antibody-Mimetic Peptoid Nanosheets for Molecular Recognition. Acs Nano 7 (10):9276-9286. doi:DOI 10.1021/nn403899y
6. Sanii B, Haxton TK, Olivier GK, Cho A, Barton B, Proulx C, Whitelam S, Zuckermann RN (2014) Structure-Determining Step in the Hierarchical Assembly of Peptoid Nanosheets. Acs Nano 8 (11):11674-11684. doi:DOI 10.1021/nn505007u
7. Sanii B, Kudirka R, Cho A, Venkateswaran N, Olivier GK, Olson AM, Tran H, Harada RM, Tan L, Zuckermann RN (2011) Shaken, Not Stirred: Collapsing a Peptoid Monolayer To Produce Free-Floating, Stable Nanosheets. J Am Chem Soc 133 (51):20808-20815. doi:DOI 10.1021/ja206199d
8. Jun S, Hong Y, Imamura H, Ha BY, Bechhoefer J, Chen P (2004) Self-assembly of the ionic peptide EAK16: the effect of charge distributions on self-assembly. Biophys J 87 (2):1249-1259. doi:10.1529/biophysj.103.038166
9. Pandya MJ, Spooner GM, Sunde M, Thorpe JR, Rodger A, Woolfson DN (2000) Sticky-end assembly of a designed peptide fiber provides insight into protein fibrillogenesis. Biochemistry 39 (30):8728-8734
10. Zimenkov Y, Dublin SN, Ni R, Tu RS, Breedveld V, Apkarian RP, Conticello VP (2006) Rational design of a reversible pH-responsive switch for peptide self-assembly. J Am Chem Soc 128 (21):6770-6771. doi:10.1021/ja0605974
11. Egelman EH, Xu C, DiMaio F, Magnotti E, Modlin C, Yu X, Wright E, Baker D, Conticello VP (2015) Structural plasticity of helical nanotubes based on coiled-coil assemblies. Structure 23 (2):280-289. doi:10.1016/j.str.2014.12.008
12. Cheng RP, Girinath P, Ahmad R (2007) Effect of lysine side chain length on intra-helical glutamate--lysine ion pairing interactions. Biochemistry 46 (37):10528-10537. doi:10.1021/bi700701z

13. Lu H, Wang J, Bai Y, Lang JW, Liu S, Lin Y, Cheng J (2011) Ionic polypeptides with unusual helical stability. Nat Commun 2:206. doi:10.1038/ncomms1209
14. Hamley IW, Dehsorkhi A, Castelletto V (2013) Self-assembled arginine-coated peptide nanosheets in water. Chem Commun 49 (18):1850-1852. doi:DOI 10.1039/c3cc39057h

Chapter 4 Design and Characterization of Hydrophobic Mutants of Peptide 3FD-IL

4.1 Introduction:

In Chapter 2, I described the design and structural characterization of the nanosheet forming peptide **3FD-IL**. The peptide **3FD-IL** was designed to form nanosheets through a combination of hydrophobic and electrostatic interactions. From Chapter 3, it is clear that electrostatic interactions play a large role in stabilizing nanosheet self-assembly. In this chapter, I investigated the effect of mutating the hydrophobic amino acids with the **3FD-IL** sequence.

Hydrophobic interactions stabilize a wide range of peptide assemblies, and conservative mutations, such as isoleucine to leucine, can greatly impact the resultant structure. This is especially evident in the case of coiled-coil peptides (sometimes called leucine zippers), which consist of two or more α-helices supercoiled around each other. The primary structure of coiled-coil peptides contains repeating heptad motifs, the hallmark of a coiled-coil. Each heptad motif consists of seven amino acids: *abcdefg*, in which hydrophobic residues occur at positions *a* and *d*. These hydrophobic (core) residues make up left-handed hydrophobic stripes within the coiled-coil structure (Figure 4.1a). Coiled-coil oligomers are generated when left-handed hydrophobic stripes are packed into hydrophobic seams. Coiled-coil motifs allow for unique packing between adjacent helices, called knob-into-hole (KIH) packing. A side chain on one α-helix makes up a knob interdigitating into a hole formed by four side chains on an adjacent

helix. In coiled-coil peptides, the identity of amino acids at the *a* and *d* positions can dictate oligomerization state [1-3]. For example, the sequence of the transcription factor GCN4, which biologically exists as a coiled-coil dimer, can be modulated to change GCN4 to a trimer or a tetramer. When isoleucine occupies the *a* position and leucine occupies the *d* position, GCN4 forms a dimer. When both the *a* and *d* positions of GCN4 are isoleucine, GCN4 forms a trimer, and when leucine occupies the *a* position and isoleucine occupies

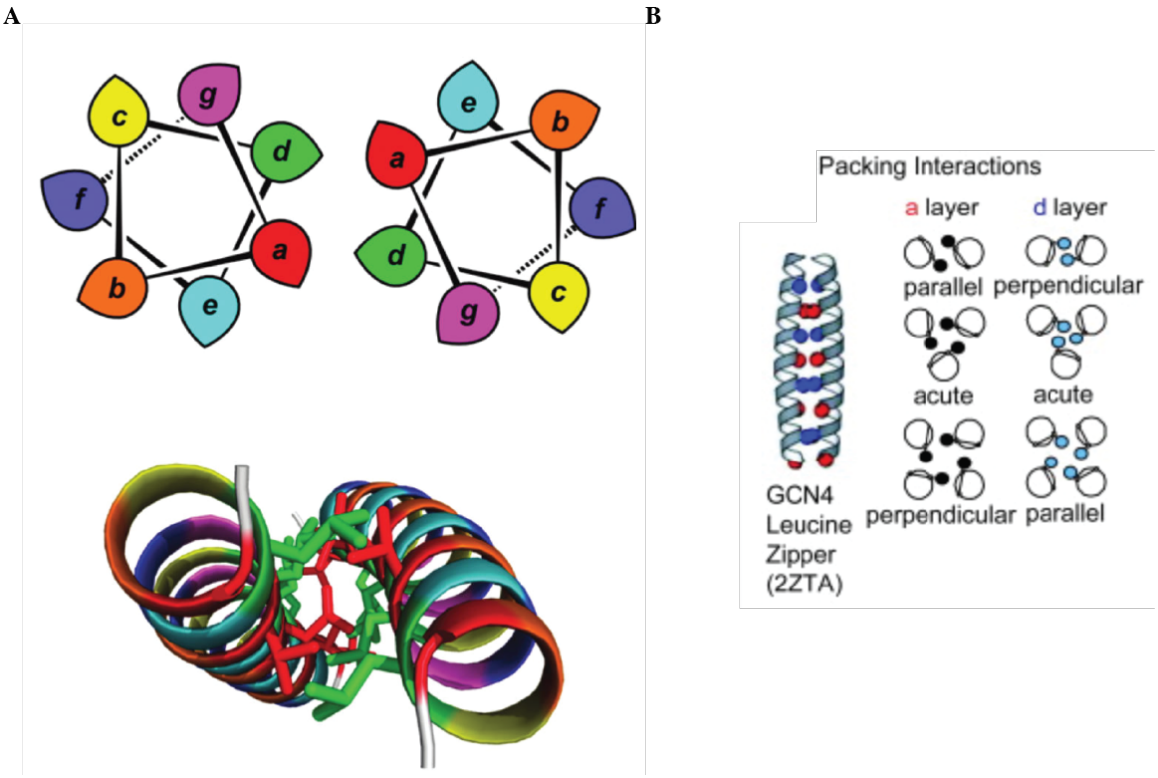

Figure 4.1 (a) coiled-coil heptad motif projected on a helical wheel where a and d positions form a hydrophobic stripe which enables oligomerization (Reproduced with permission from [2] (b) Packing interactions in different coiled-coil oligomerization states (Reproduced with permission from [3].)

the *d* position, GCN4 forms a tetramer. Harbury et al. analyzed the crystal structures of the **GCN4** dimer, trimer, and tetramer to explain why these subtle mutations affect the oligomerization state of **GCN4**. At the *d*-level of the dimer, the Cα-Cβ bond of each

leucine knob is perpendicular to the Cα-Cα vector at the bottom of the hole into which it packs. This is known as perpendicular knob-into-hole packing. Conversely, at the *a*-level of the dimer, the Cα-Cβ bond of each isoleucine knob is parallel to the Cα-Cα vector at the bottom of the hole on the adjacent helix. This packing is known as parallel KIH packing (Figure 4.1b). The crystal structure of tetrameric GCN4 reveals the exact opposite packing pattern to the dimer. The Cα-Cβ bond of the *a*-level knobs exhibit perpendicular KIH packing whereas the *d*-level knobs exhibit parallel KIH packing (Figure 4.1b). In contrast to the dimer and the tetramer, the knobs formed by isoleucine's Cα-Cβ bond pack at a 60° angle to the Cα-Cα vector at the bottom of the recipient helix. This type of KIH packing is called acute packing (Figure 4.1b). This study highlights the difference in packing preference between amino acids, which are similar in structure. Different packing arrangements place the β-carbons on adjacent helices at different distances from each other. For instance, perpendicular KIH packing places the β-carbons of adjacent helices 2 Å closer than in the parallel KIH packing arrangement. Therefore, leucine, which is not a β-branched amino acid and is less sterically hindered at the C-β-position than isoleucine, can be sterically accommodated when its Cα-Cβ bond packs perpendicular to the Cα-Cα vector at the bottom of the recipient hole. On the other hand, ideal van der Waals interactions are formed when the Cα-Cβ knob of isoleucine, which is a beta branched amino acid, is parallel to the Cα-Cα vector at the bottom of the hole formed on the recipient helix [4]. When isoleucine occurs at both a and d positions, it packs in the acute arrangement to minimize the number of isoleucines participating in perpendicular KIH interactions.

A series of β-sheet peptides of sequence Ac-XKXE-NH_2 with varying hydrophobicities also shows the effect of hydrophobicity on peptide self-assembly [5]. Peptides **1**-**4** (X = Phe, Ala, Val, Leu, respectively) exhibited differing degrees of β-sheet formation and assembly into amyloid fibrils. Peptide **1**, which is the most hydrophobic, exhibited a high degree of β-sheet formation and self-assembled into varying fibrillar assemblies, which depended on concentration. Conversely, peptide **2**, which contained alanine, did not self-assemble, consistent with its relatively low hydrophobicity. Peptide **3** is less hydrophobic than peptide **1**; but it contains valine which has the highest β-sheet forming propensity of canonical amino acids. Peptide **3** formed well-defined, homogenous fibrils and β-sheet secondary structure at 2 mM and 4 mM peptide concentrations. This shows that in addition to hydrophobicity, the formation of stable secondary structure also contributes to self-assembly. Peptide **4**, which is more hydrophobic than peptide **3** and comparable in hydrophobicity to peptide **1**, displays peptide concentration dependent self-assembly [5]. At a 4 mM peptide concentration, peptide **4** adopts a strong β-sheet signature and forms fibrils accompanied by globular, amorphous assemblies. Since leucine has a lower preference to form β-sheet structure and is more commonly found in α-helical structures, peptide **4** may have a higher degree of variation in its intrastrand and interstrand packing, leading to conformational polymorphism. This study shows that the identity of the hydrophobic amino acid plays a role in both the formation of stable secondary structure and packing mode. The aforementioned studies suggest that the identity of hydrophobic amino acids within the peptide sequence can greatly affect self-assembly.

4.2 Design of Hydrophobic Peptide Variants

In order to test the effect of changing hydrophobic residues on nanosheet formation, four peptides were synthesized, **3FD-LL**, **3FD-LI**, **3FD-II**, and **3FD-ILLI**. Each peptide contained the same arrangement of charged amino acids as in **3FD-IL**, but they alter in the identity and location of the hydrophobic amino acids (Figure 4.2). The peptide **3FD-LL** contained leucines at all hydrophobic positions of the 3FD-IL sequence. The peptide **3FD-II** contained isoleucine at all hydrophobic positions within the **3FD-IL** sequence. In the peptide **3FD-LI**, the leucine and isoleucine positions are switched as compared to the **3FD-IL** sequence. In the peptide **3FD-LIIL**, the first eighteen amino acids retained the same sequence of hydrophobic amino acids as in **3FD-IL**, but in the

second half of the peptide, isoleucine and leucine are switched.

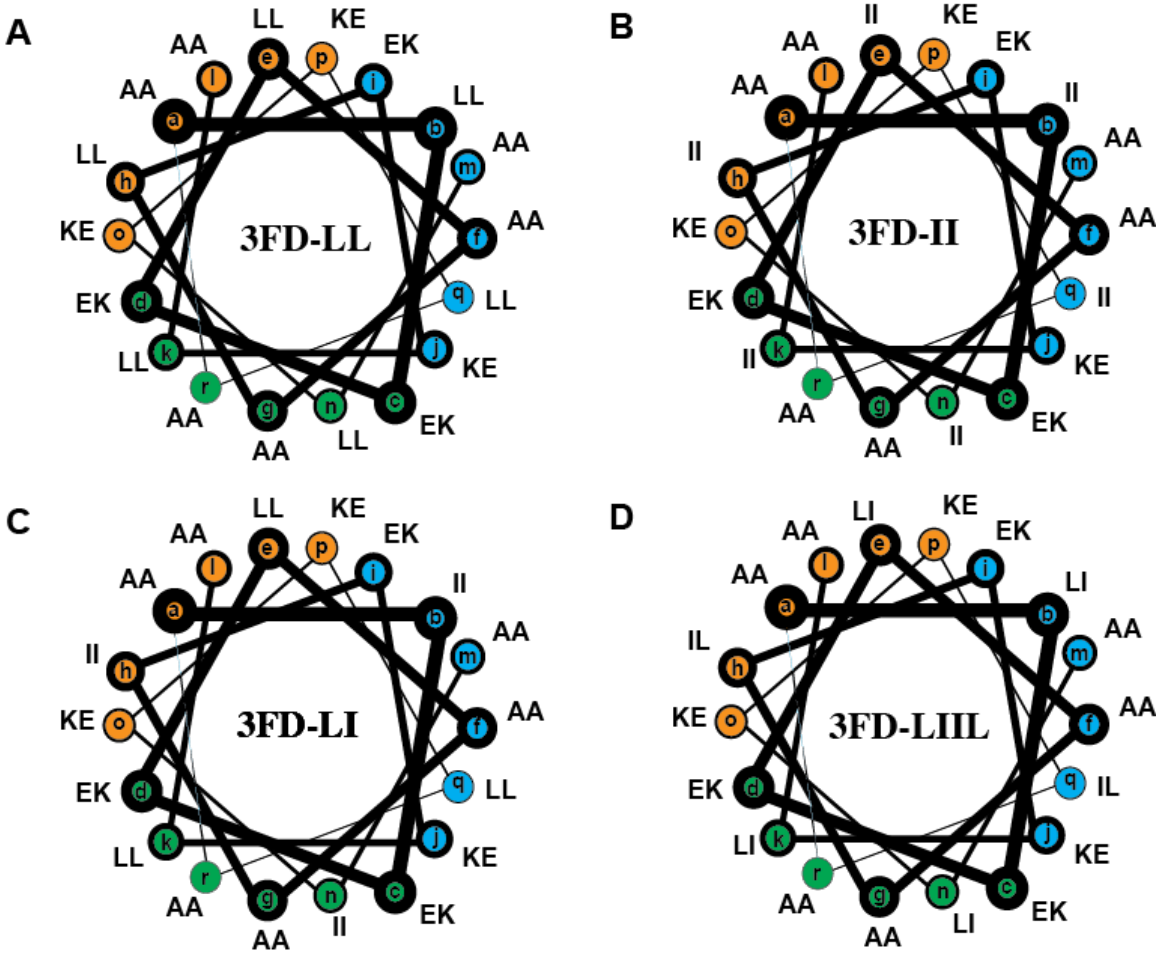

Figure 4.2 Helical wheel representations of (a) 3FD-LL (b) 3FD-II (c) 3FD-LI, and (d) 3FD-LIIL (e) linear sequence of aforementioned peptides

4.3 Results and Discussion

4.3.1 Effect of Changing the Identity of Hydrophobic Amino Acids on Self Assembly

The peptides **3FD-II** and **3FD-LL** were created to test the effect of changing the identity of the hydrophobic amino acids on self-assembly. The peptide **3FD-II** was assembled over a range of pHs from 4 to 8.5. The circular dichroism behavior was also observed over this pH range (Figure 4.3). Over this pH range, it appears that in the absence of heat treatment, **3FD-II** adopted an α-helical secondary structure. From pH 6 to pH 8.5, the shape of the circular dichroism curve resembled that of **3FD-IL**. Interestingly, after heat treatment **3FD-II** appeared to change conformation. The high number of isoleucines in the sequence of **3FD-II** could give this peptide a propensity to

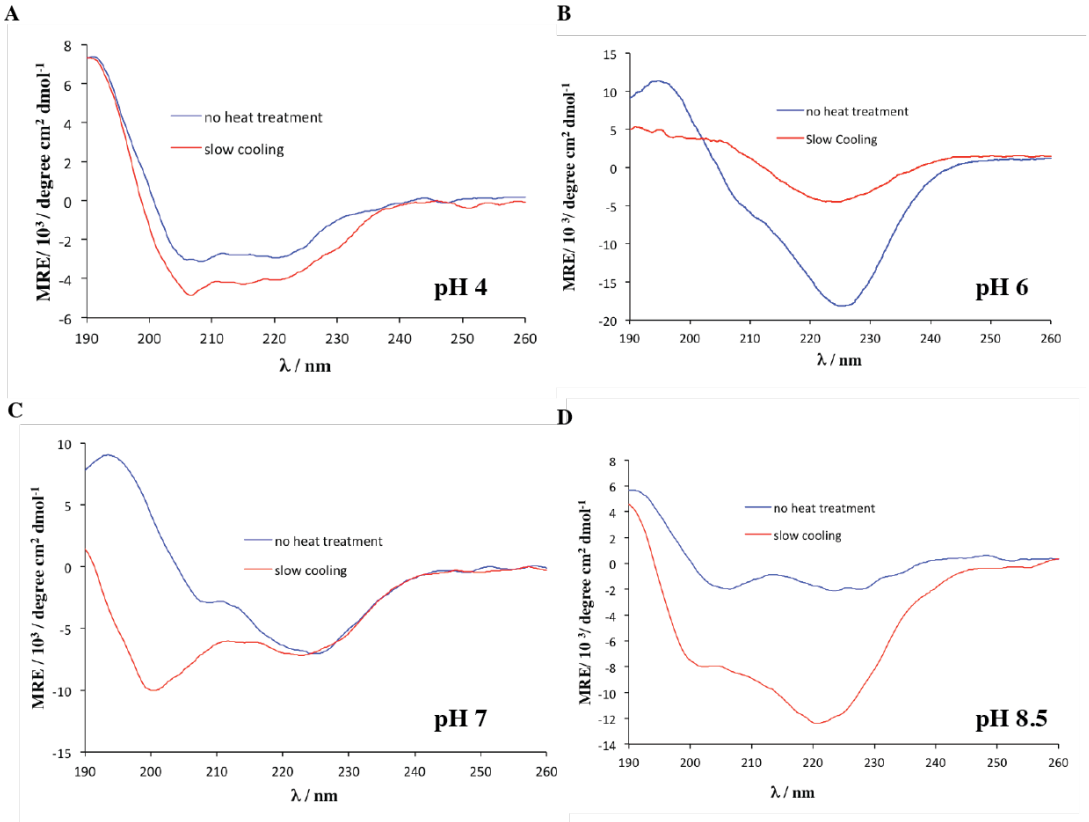

Figure 4.3 pH dependence of the CD spectra of 3FD-II

form β-sheet secondary structure rather than α-helical secondary structure. Isoleucine, which is a β-branched amino acid, can occupy less conformational space relative to alanine. The conformational space available to isoleucine is mostly restricted to regions

outside of the α-helix [6]. However, the CD signature of **3FD-II** after heat treatment does not resemble that of a traditional β-sheet, which exhibits a single minimum around 215 nm. Nonetheless, the structural diversity of β-sheet structures as a result of variation in peptide length, orientation of neighboring β-strands (i.e. antiparallel or antiparallel), twist, and distortion of β-sheets can result in spectral diversity of some β-sheet rich proteins [7]. In order to confirm the hypothesis that after heat treatment, the 3FD-II assemblies form β-sheet secondary structure, Fourier transform infrared spectroscopy-attenuated total reflection (-ATR) experiments were performed. After thermal annealing (labeled RT on graphs), β-sheet is the prevalent conformation that **3FD-II** adopts, assigned by the low frequency amide I stretch at 1619 cm^{-1} (Figure 4.4) There existed some α-helical character (1651 cm^{-1}) but this has not been quantified. The β-sheets appeared to be antiparallel in arrangement, as can be assigned by the visible high frequency amide I stretch at 1693 cm^{-1}. At 4 °C, α-helix is the prevalent conformation that **3FD-II** adopted, assigned by the amide I stretch at 1651 cm^{-1} (Figure 4.4).

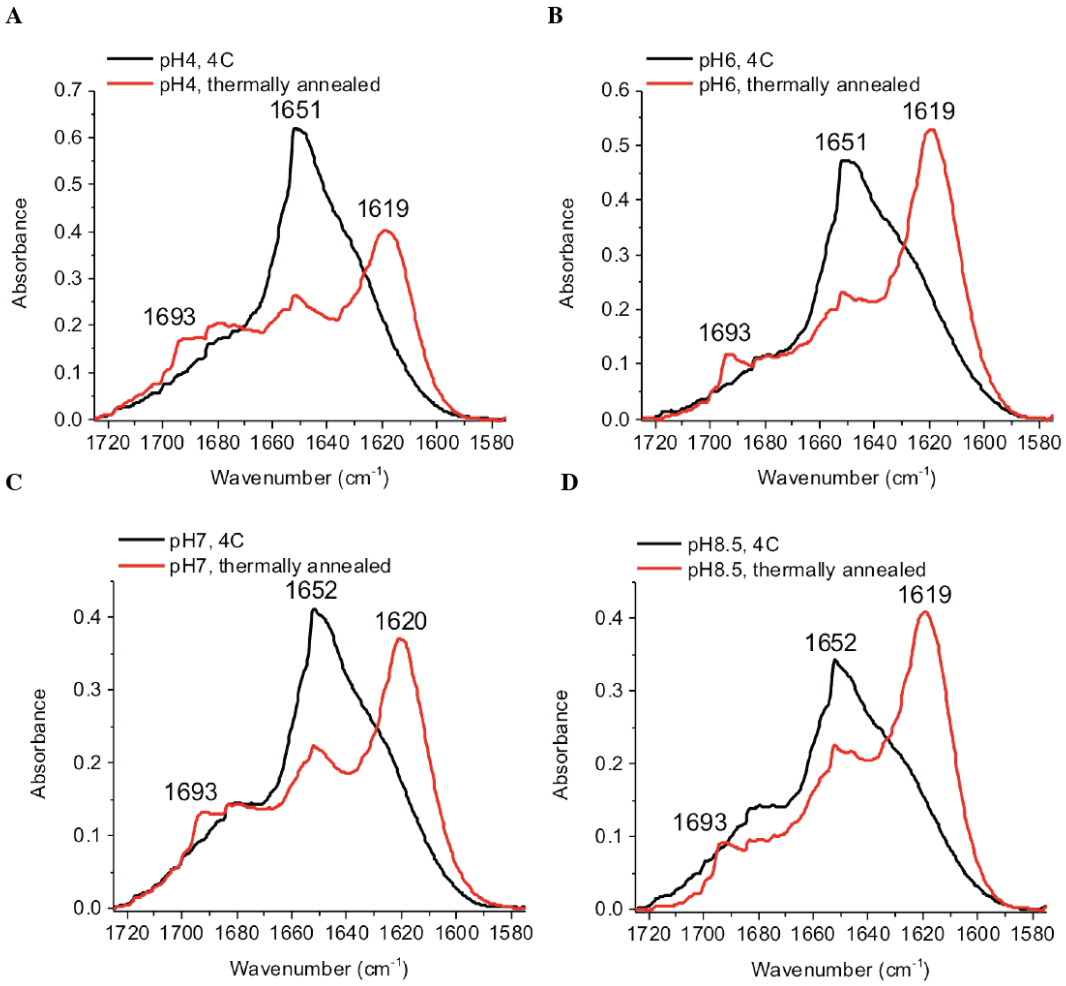

Figure 4.4 Temperature dependent ATR-FTIR spectra of **3FD-II** (a) pH 4 (b) pH 6 (c) pH 7 (d) pH 8.5

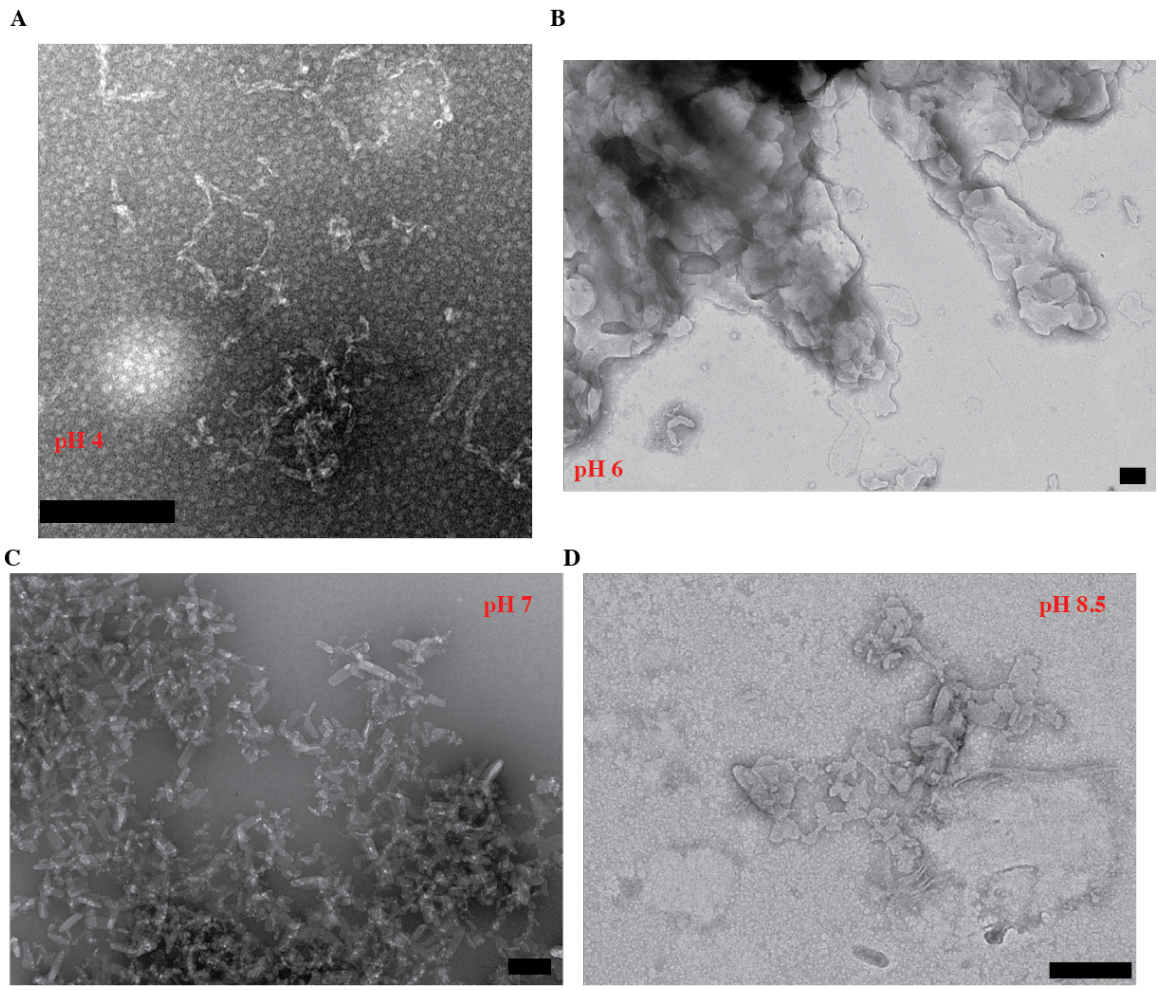

Figure 4.5 TEM images of 3FD-II (approximate peptide concentration = 5 mg/mL) at (a) pH 4, (b) pH 6, (c) pH 7, and (d) pH 8.5 after one week of incubation at 25 °C (all scale bars = 200 nm)

The secondary structure experiments were correlated with transmission electron microscopy to determine the presence of assemblies. The heat treated assemblies did not form assemblies under the conditions tested, consistent with their loss of α-helicity. Interestingly, irregular assemblies of **3FD-II** were observed after an incubation of one week at 25 °C (Figure 4.5). However, if the **3FD-II** solutions were incubated at 4 °C, well-defined rectangular assemblies were observed (Figure 4.6). In contrast to the nanosheets formed by **3FD-IL**, the **3FD-II** nanosheets were more asymmetric in the

lateral dimensions. The shorter side of the rectangular assemblies reached a maximum of 100 nm, whereas the longer side of the rectangular assemblies can be up to several hundred nanometers in length. Interestingly, after two years and nine months of assembly at 4 °C, **3FD-II** forms a homogenous mixture of sheet-like assemblies (Figure 4.6e). These assemblies are about 100-200 nm in diameter and have lengths up to several microns. The fact that these assemblies form at low temperatures suggests that the low temperature restricts the conformational motion of the peptide monomers, allowing for the formation of ordered assemblies.

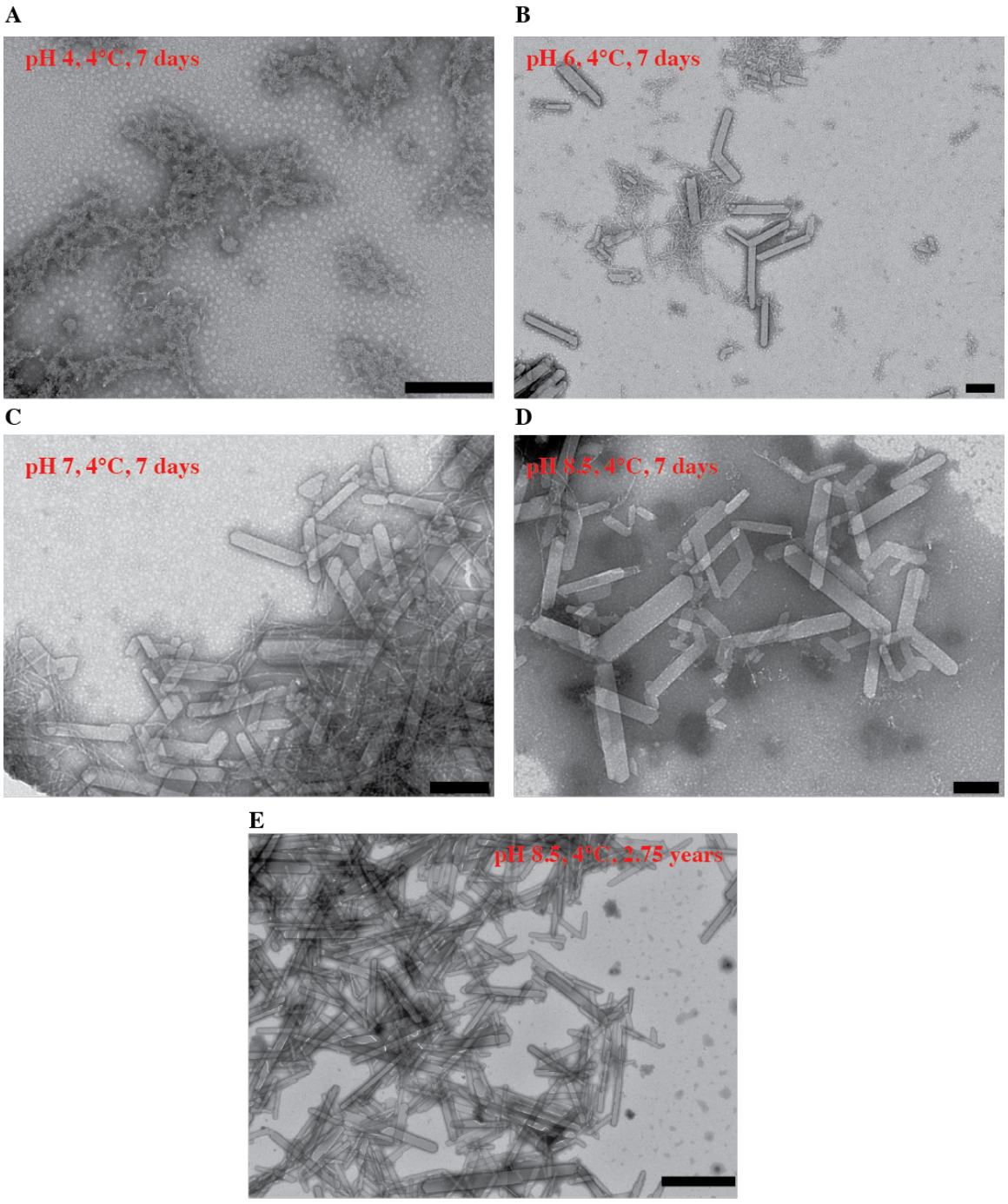

Figure 4.6 Transmission electron micrographs of 3FD-II assembled at 4°C; (a) pH 4, 1 week (scale bar = 200 nm), (b) pH 6, 1 week (scale bar = 200 nm), (c) pH 7, 1 week (scale bar = 200 nm), (d) pH 8.5, 1 week (scale bar = 200 nm), (e) pH 8.5, 2.75 years (scale bar = 2.0 µm)

Next, the self-assembly of **3FD-LL** was studied as a function of pH and temperature. **3FD-LL** contains leucines at each hydrophobic position within the sequence. Since **3FD-LL** contains all leucines, this peptide should exhibit more α-helical character than **3FD-II**. Since the parent peptide **3FD-IL** formed the most regular solution of nanosheets at pH 8.5, the self assembly of **3FD-LL** was initially tested at pH 8.5. At pH 8.5, **3FD-LL** formed an α-helical circular dichroism signature, similar to that observed by **3FD-IL**. When **3FD-LL** was heated up to 90 °C and cooled slowly, it retained its α-helical signature. Conversely, when **3FD-LL** was heated up to 90 °C and cooled quickly, it shifted conformation from an α-helix to a random coil (Figure 4.7d), indicating that the peptide is kinetically trapped. **3FD-LL** exhibited the same CD behavior at self assembly conditions of pH 4, pH 6, and pH 7 (Figure 4.7a, Figure 4.7b, Figure 4.7c). In comparison to **3FD-II**, the solutions of **3FD-LL** exhibited greater α-helical character as evident by the more negative minima at 222 nm. Next, the circular

dichroism behavior of **3FD-LL** was correlated with transmission electron microscopy.

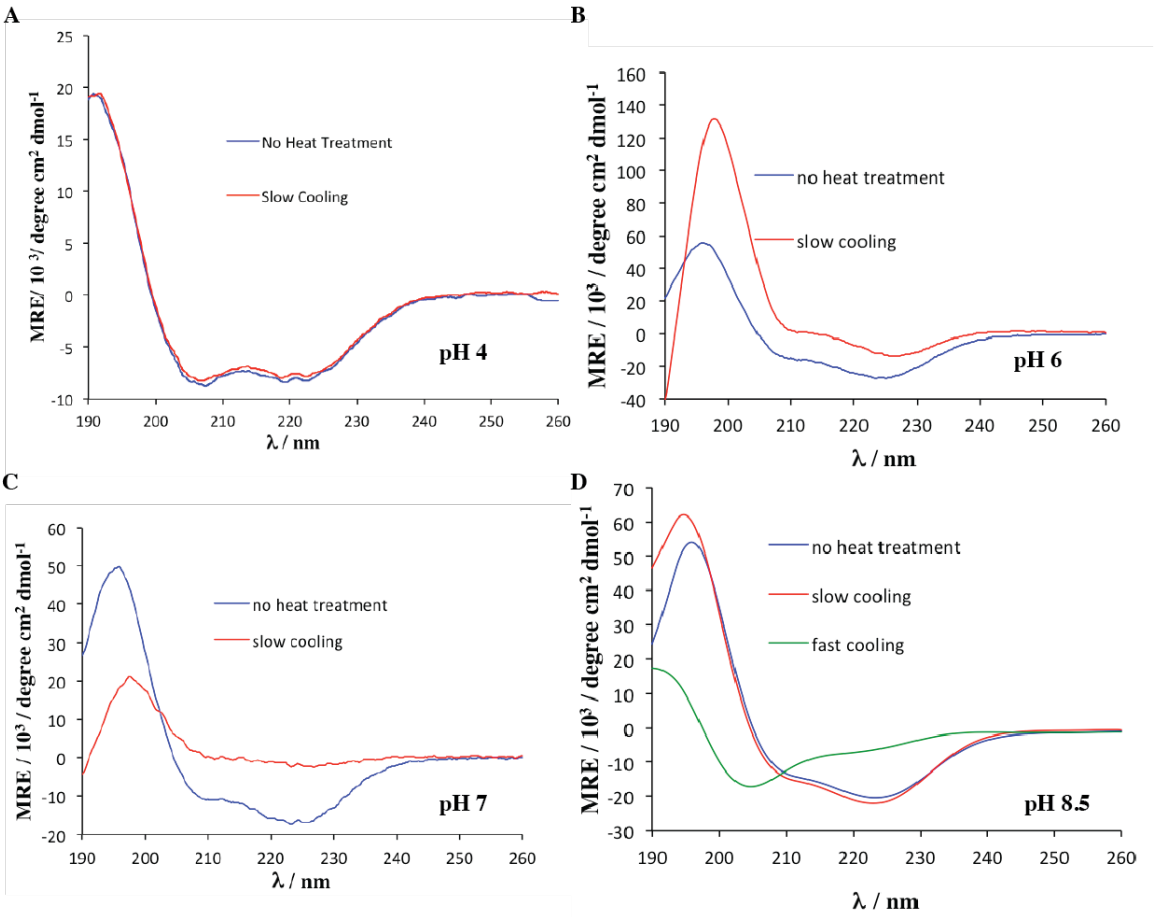

Figure 4.7 Circular dichroism behavior of 3FD-LL as a function of pH (a) pH 4, (b) pH 6, (c) pH 7, (d) pH 8.5

Similarly to **3FD-IL**, the peptide **3FD-LL** formed large assemblies across the pH range from 6 to 8.5 in the presence of thermal annealing or slow cooling (Figure 4.8).

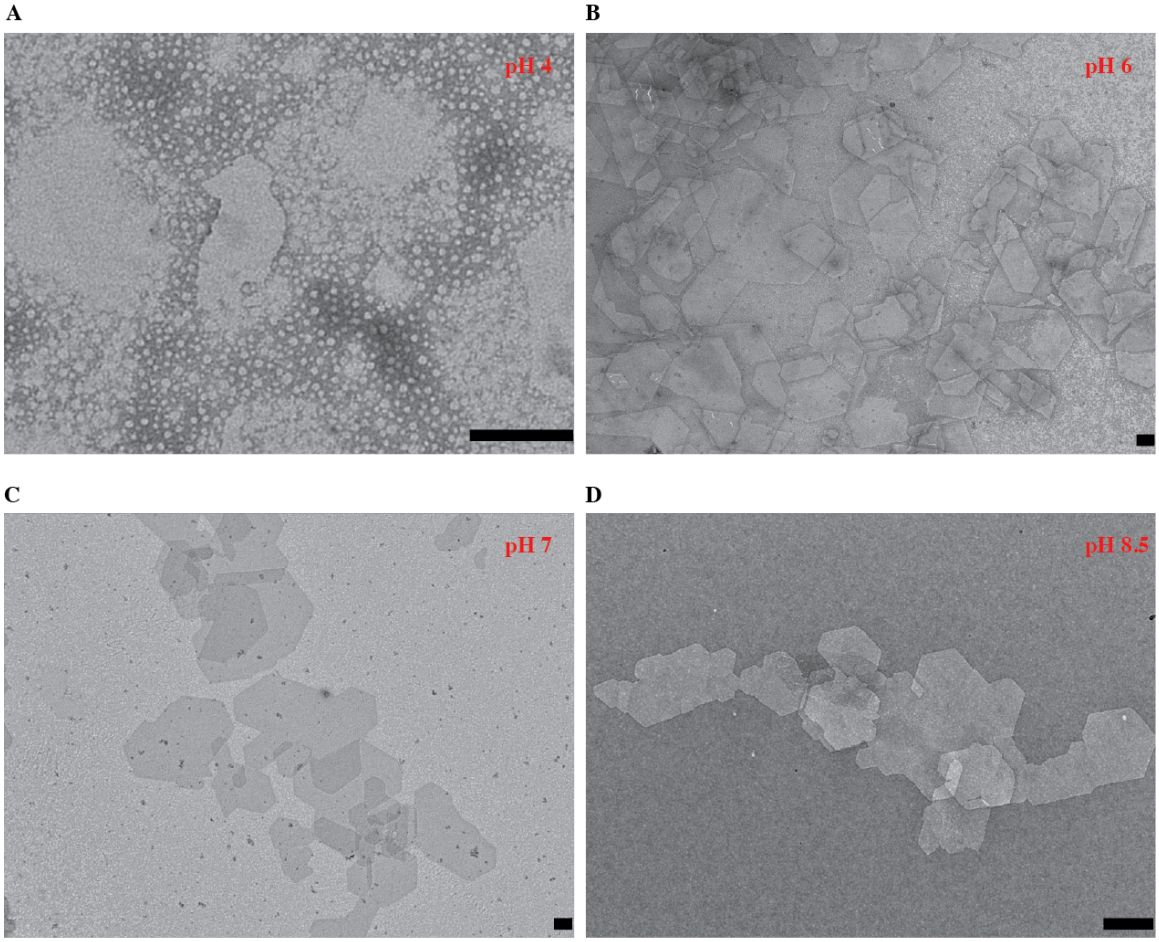

Figure 4.8 Representative transmission electron micrographs of 3FD-LL assemblies formed after thermal annealing at (a) pH 4 (b) pH 6, (c) pH 7, and (d) pH 8.5

Sometimes these nanosheets were accompanied by fibrils. In the absence of thermal annealing, the peptide **3FD-LL** forms assemblies, which appear to have more jagged

edges and are smaller than those formed in the presence of slow cooling (Figure 4.9).

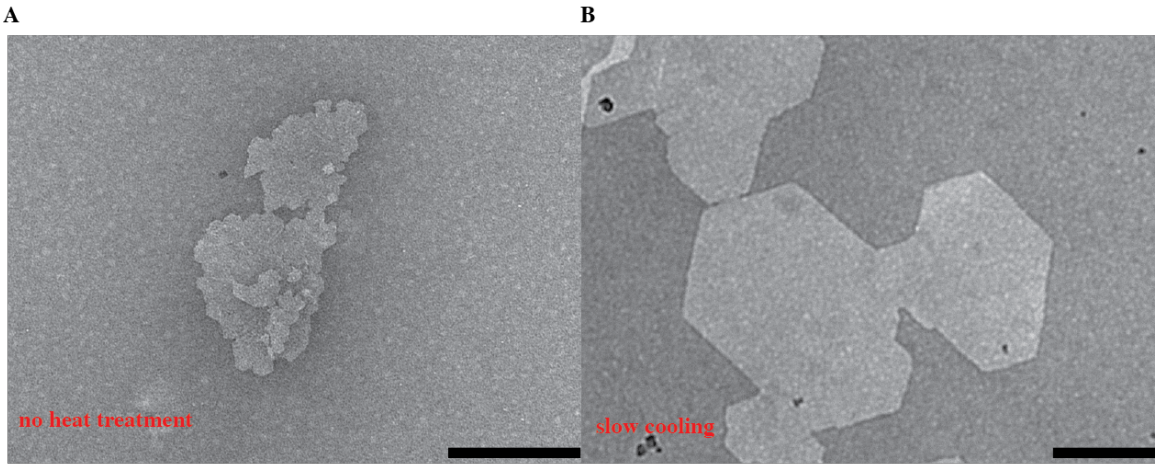

Figure 4.9 3FD-LL assemblies in the (a) absence and (b) presence of thermal annealing

After thermal annealing, **3FD-LL** formed assemblies, which ranged in size from hundreds of nanometers to microns and contained well-defined edges. In contrast to the **3FD-IL** nanosheets, many of the **3FD-LL** nanosheets observed by TEM formed hexagons. In some cases, these hexagons are connected by bridging peptide (Figure 4.10). Since the largest and most homogenous assemblies of **3FD-LL** were formed at pH 8.5 with thermal annealing, these assembly conditions were chosen for further biophysical characterization. In order to determine the thermal stability of the assemblies

formed by 3FD-LL the melting

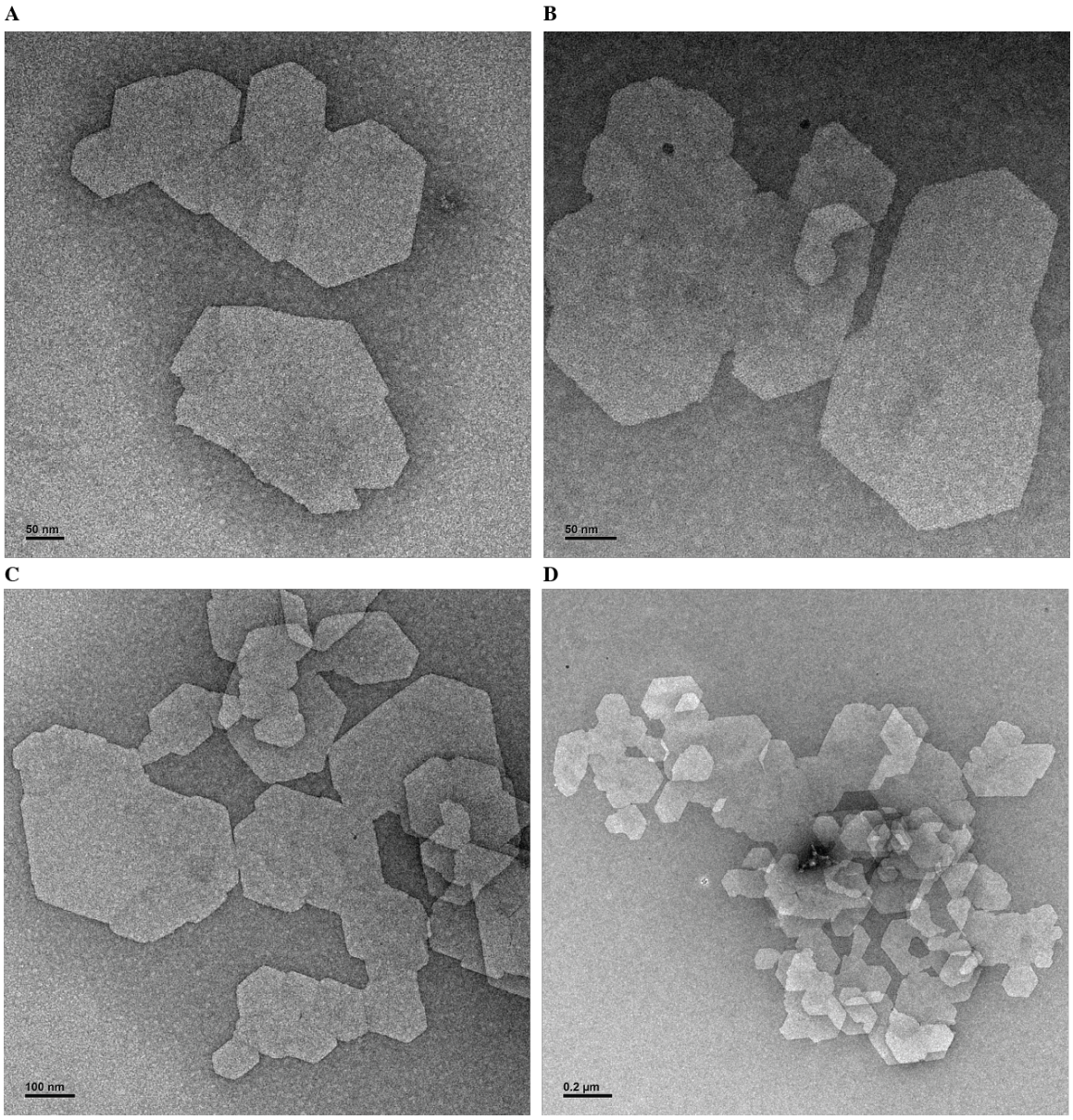

Figure 4.10 TEM images of large 3FD-LL assemblies

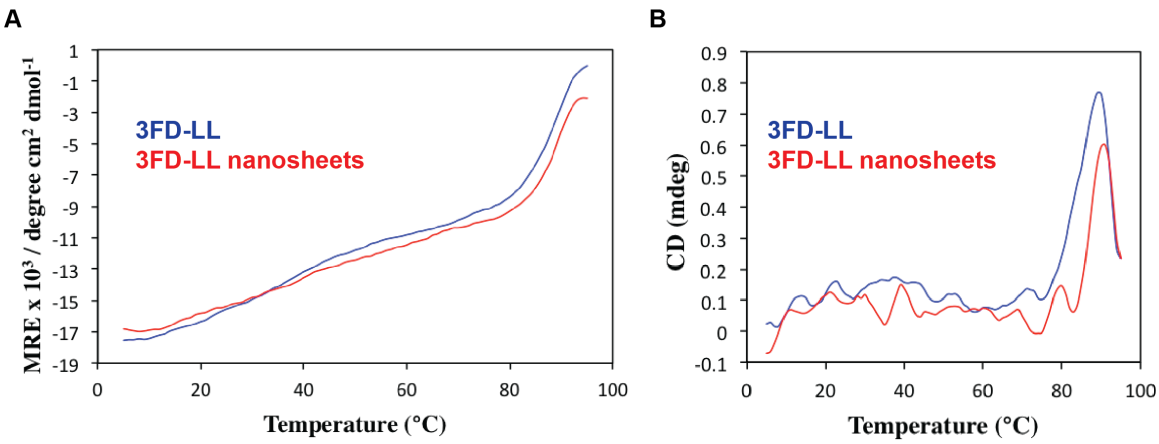

Figure 4.11 (a) CD melting curves of 3FD-LL monitored at 222 nm, and (b) first derivatives of melting curves from (a) revealed the melting temperatures for the 3FD-LL assemblies

temperature was determined by circular dichroism. The circular dichroism signal was monitored at 222 nm, and the **3FD-LL** solutions were heated from 5°C to 95° C (Figure 4.11a). The first derivative of a melting curve of **3FD-LL** revealed a melting temperature of 89 °C for the **3FD-LL** sample, which is not heat treated and a melting temperature of 90 °C for the peptide solution which has been annealed (Figure 4.11b). These temperatures are higher than those obtained for **3FD-IL**. Next, **3FD-LL** was assembled in the presence of salt to determine whether electrostatic interactions contribute to the formation of the **3FD-LL** assemblies. **3FD-LL** assembled into homogenous assemblies that were stable at salt concentrations up to 500 mM (Figure 4.12). This indicates that the **3FD-LL** assemblies are more robust than those formed by **3FD-IL**. One explanation for the difference between **3FD-IL** and **3FD-LL** is that the leucine and isoleucine side chains in the respective sequences have different packing preferences, leading to different sheet morphologies. α-helical interfaces in coiled-coil peptides are very sensitive to the identity of the hydrophobic amino acids, because isoleucine has different rotameric preferences than leucine, due to its β-branched character [1]. This suggests that hydrophobicity can

drastically affect resultant quaternary structure.

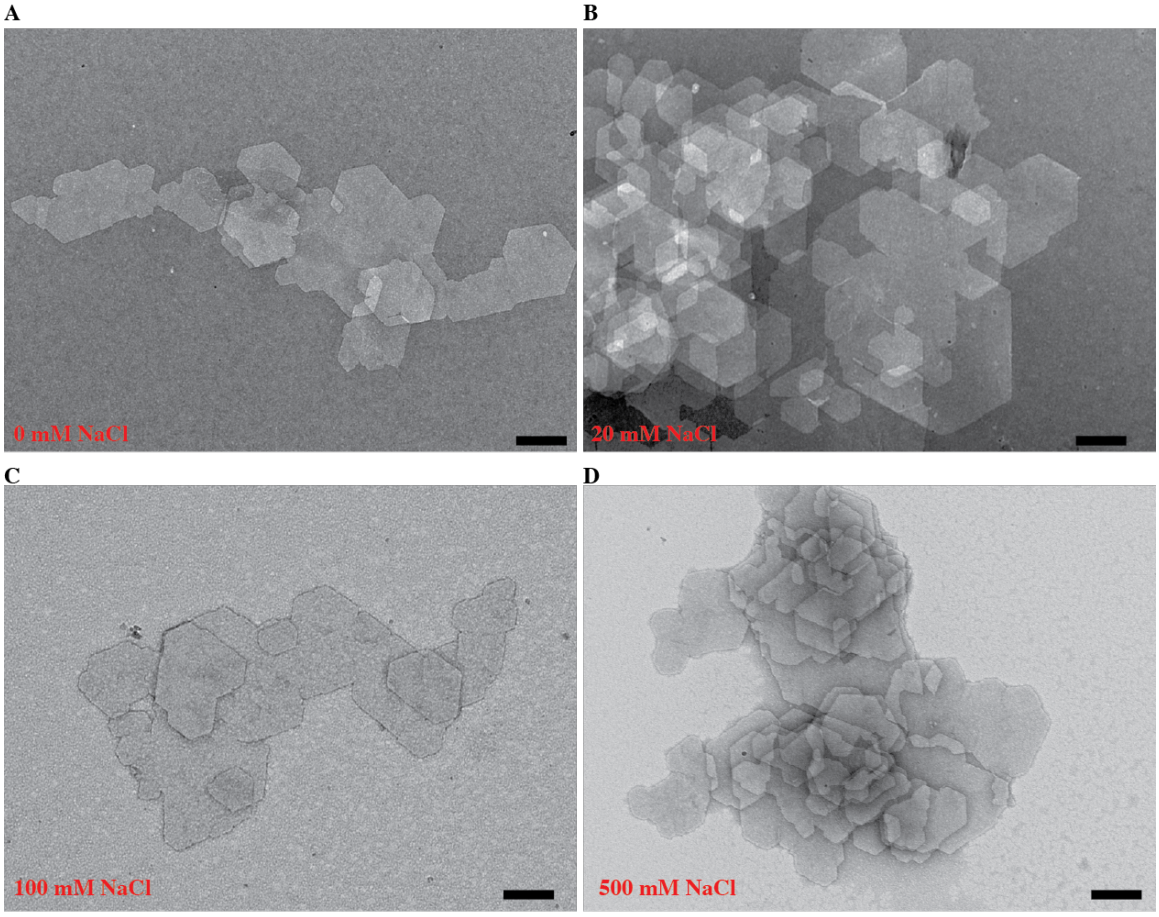

Figure 4.12 The effect of salt on 3FD-LL assembly (a) absence of salt (b) 20 mM NaCl (c) 100 mM NaCl (d) 500 mM NaCl

4.3.2 Effect of changing the Arrangement of Isoleucines and Leucines on Self-Assembly

The peptides **3FD-LI** and **3FD-ILLI** were synthesized to test the effect of the order of hydrophobic amino acids on self-assembly. The sequence of the peptide **3FD-LI** had the sequence of all leucines and isoleucines reversed whereas the peptide **3FD-ILLI** only contained a reversal of hydrophobic amino acids in the second half of the peptide sequence. The self-assembly of both peptides was evaluated at pH 8.5, the pH at which **3FD-IL** and **3FD-LL** formed the most homogenous solution of assemblies. Both **3FD-LI**

and **3FD-ILLI** formed α-helical circular dichroism signatures at pH 8.5 (Figure 4.13). The total α-helical content of the two peptides appeared to be less than that formed by **3FD-IL**, as evident by the less negative minimum in the CD signature at 222 nm. The CD curves were correlated with TEM to determine if these two peptides were capable of forming nanosheets.

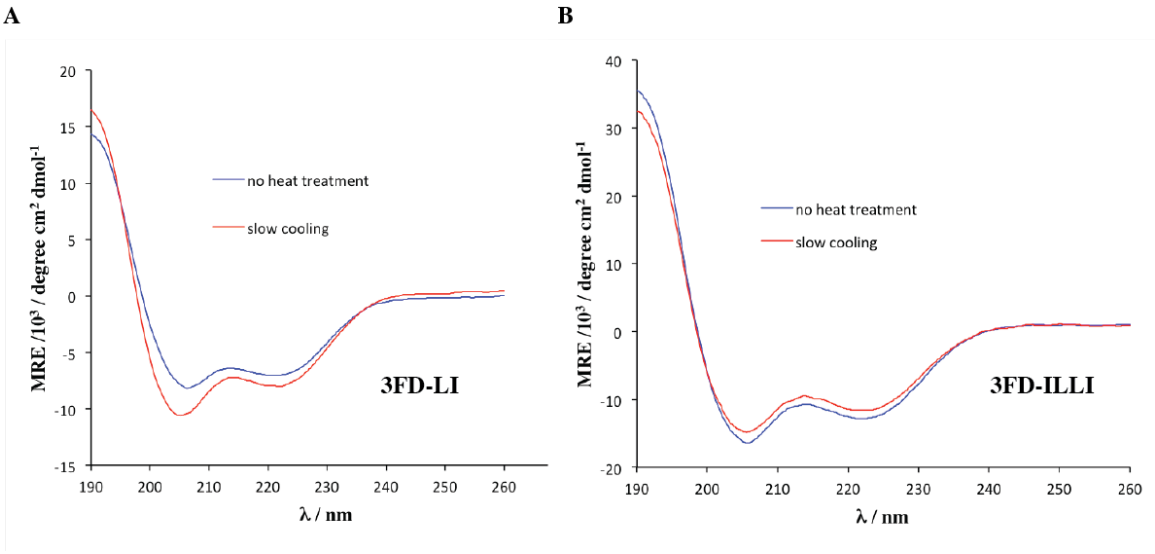

Figure 4.13 CD spectra of (a) 3FD-LI and (b) 3FD-ILLI

In the absence of thermal annealing, neither **3FD-LI** nor **3FD-ILLI** formed ordered assemblies. In the presence of thermal annealing, **3FD-ILLI** appeared to form nanosheets. These nanosheets were accompanied by small aggregates. In comparison to **3FD-IL**, these nanosheets had less defined edges. The peptide **3FD-LI** formed elongated structures (4.14a and Figure 4.14c), which were accompanied by small aggregates, which resembled those formed by **3FD-ILLI** (Figure 4.14a). These experiments showed that seemingly small changes in peptide sequence can result in large changes in peptide structure. Presumably the peptides **3FD-LI** and **3FD-ILLI** contain different modes of hydrophobic packing than that exhibited by **3FD-IL**.

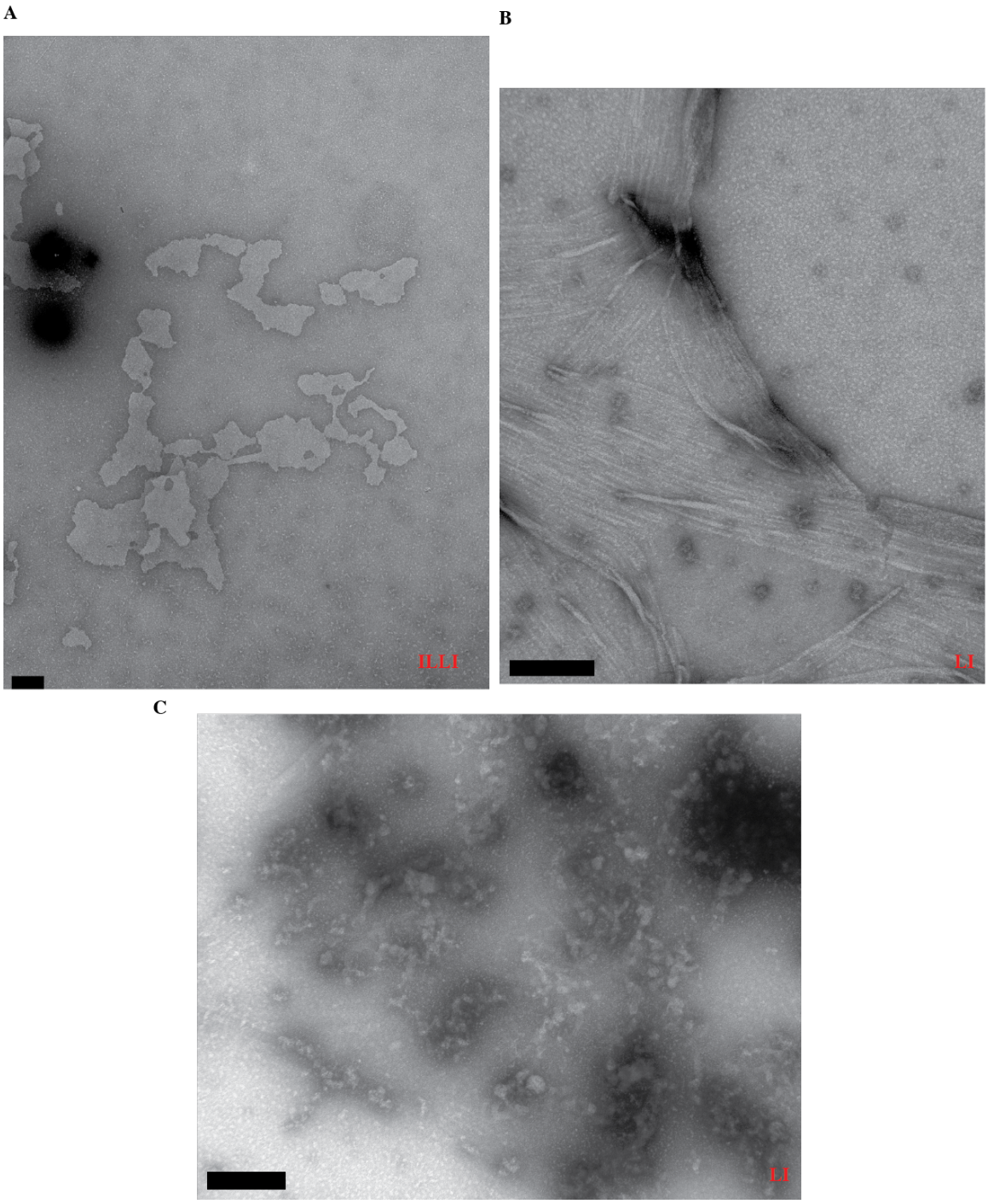

Figure 4.14 TEM images of (a) 3FD-ILLI and (b) 3FD-LI aligned fibrils and aggregates (c)

4.3.3 Small angle x-ray scattering

Small angle x-ray scattering experiments were performed to analyze the shape of **3FD-LL** and the internal structure of the **3FD-LL** assemblies. Similarly to **3FD-IL**, the resultant small angle x-ray scattering curve revealed the presence of highly ordered assemblies in solution, as demonstrated by the presence of Bragg diffraction peaks in the high q region of the scattering curve (Figure 4.15).

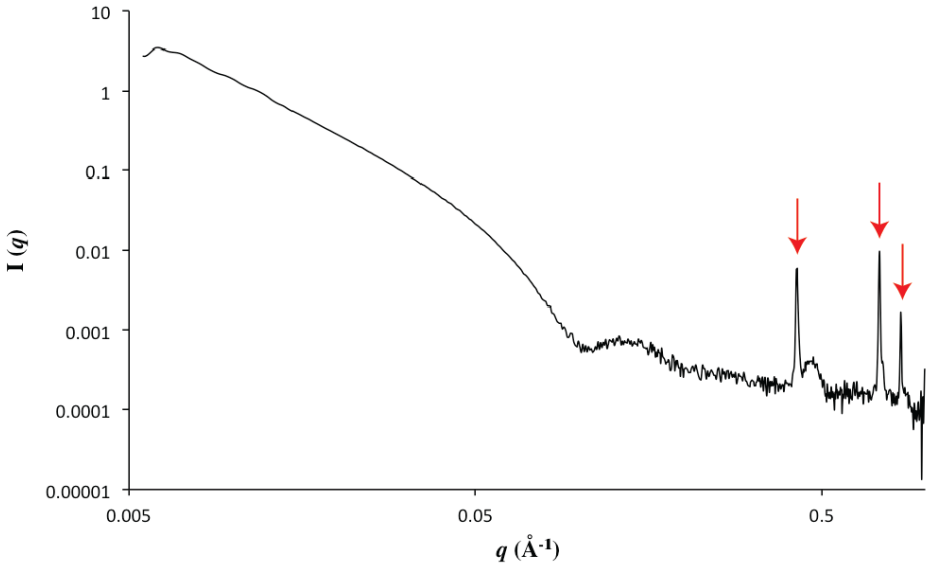

Figure 4.15 Small angle x-ray scattering curve for **3FD-LL**, arrows indicate the presence of Bragg diffraction peaks in the high q region

The scattering intensity in the Porod region of the scattering curve followed a power law dependence of the momentum transfer (q^{-2}), suggesting the presence of sheet-like assemblies (Figure 4.16). The Bragg diffraction peaks in the high q region corresponded to d-spacings of 14.74 Å, 8.53 Å, and 7.41 Å. The mathematical relationship between the three diffraction spacings, n, n/√3, n/√4 (n= 14.74 Å), corresponded to a hexagonal geometrical arrangement of α-helices within the **3FD-LL** nanosheets (Figure 4.17). The data in the Guinier region of the scattering curve ($q_{max}R_c \leq 1.0$) was fit to a model for

sheet-like forms. A value of 73 Å for the sheet thickness was calculated using the Guinier plot (Figure 4.18).

A

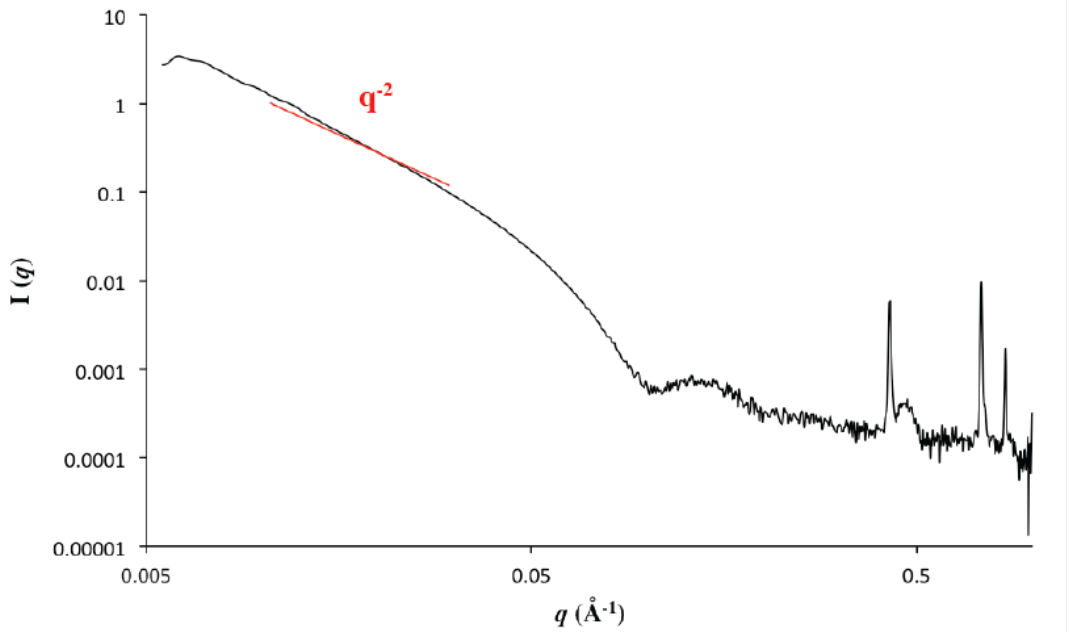

B

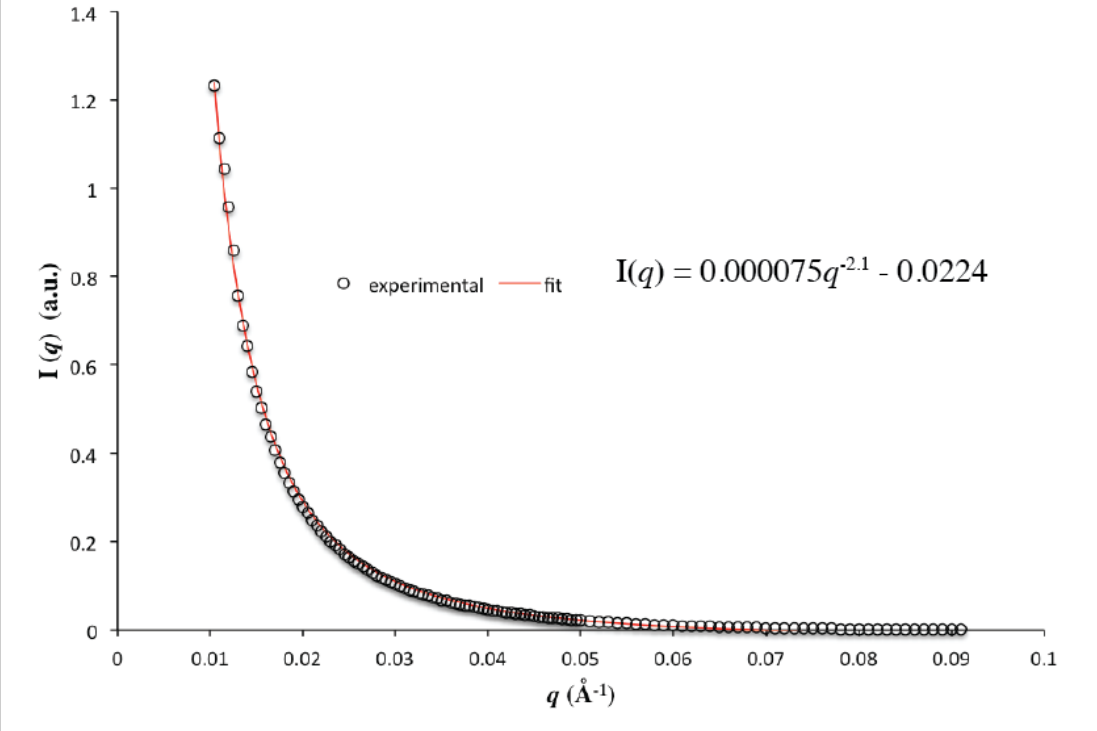

Figure 4.16 (a) Small angle x-ray scattering curve of **3FD-LL** showing that the decay of intensity in the intermediate q region is proportional to q^{-2} and (b) fit of intermediate q region to an exponential

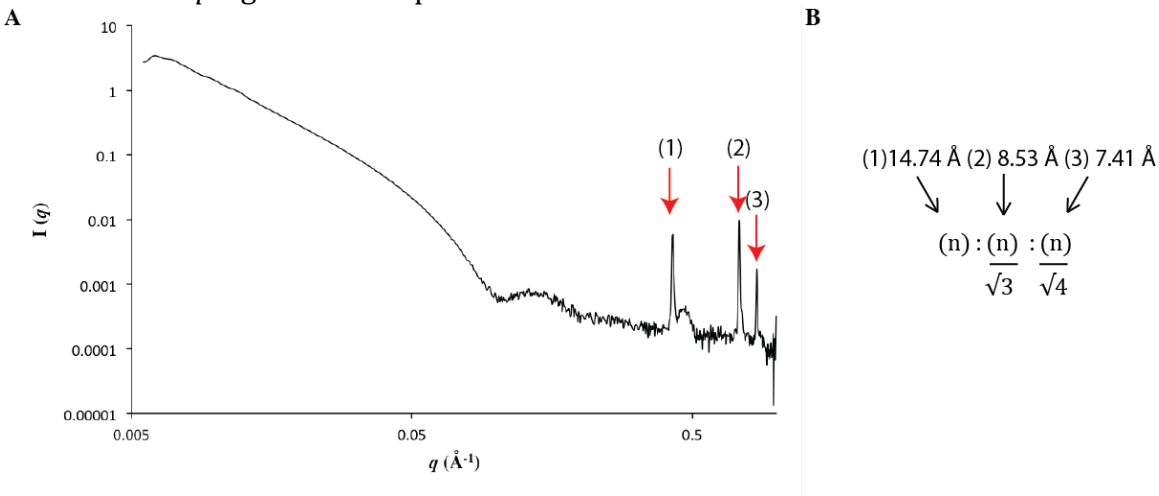

Figure 4.17 (a) Small angle x-ray scattering curve showing the Bragg diffraction peaks, which are indicated by red peaks (b) and their mathematical relationship

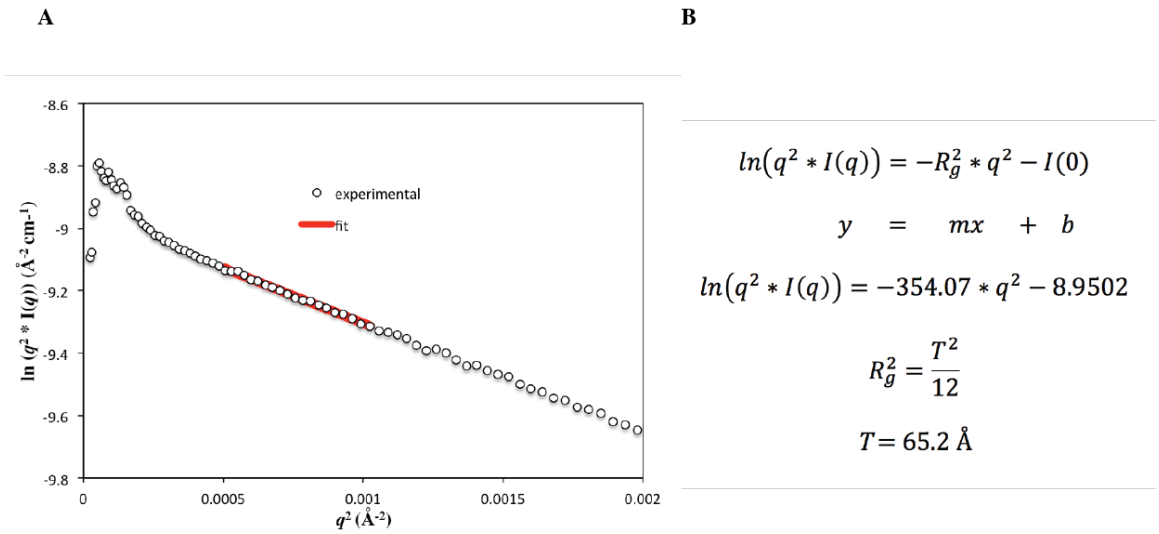

Figure 4.18 (a) Guinier fit of the small angle x-ray scattering curve (b) fit of Guinier region to an equation for sheet-like forms used to determine the thickness of the **3FD-LL** nanosheets

4.3.4 Atomic Force Microscopy

Atomic force microscopy measurements were made to confirm the thickness of the nanosheets obtained from small angle x-ray scattering. The morphology of the nanosheets was very similar to the morphology observed by TEM (Figure 4.19a). Furthermore, the height measurements of the nanosheets could be fit to a Gaussian distribution which contained one maxima at 5.8463 Å, corresponding to the average height (Figure 4.19c). This data is consistent with a perpendicular arrangement of helices with respect to the surface of the **3FD-LL** nanosheets.

A

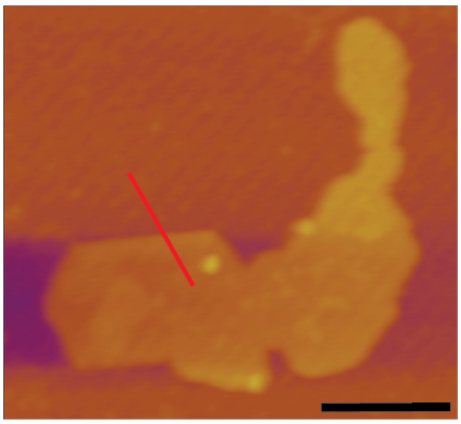

A

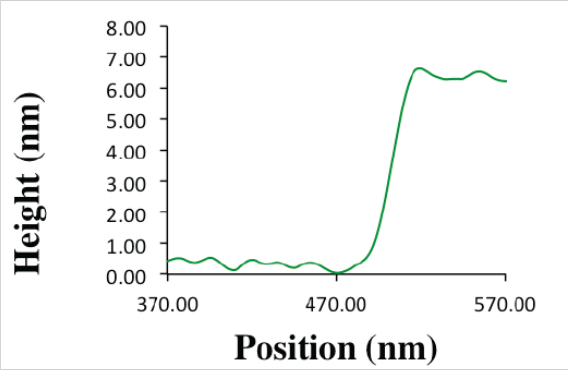

C

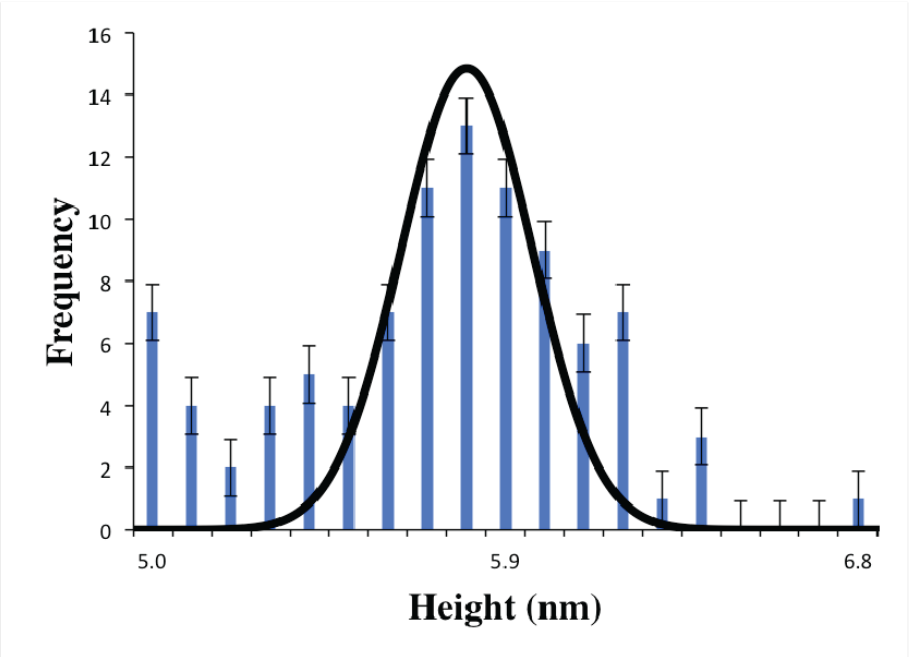

Figure 4.19 (a) Representative AFM image of **3FD-LL** nanosheets (scale bar = 200 nm) (b) AFM measurement of sheet in (a) (c) AFM height statistics reveals an average height for the nanosheets of 5.8463 Å

4.3.5 Orientation of 3FD-LL nanosheets

Fiber diffraction measurements were utilized to obtain structural information for the **3FD-LL** nanosheets (Figure 4.20). A fiber was of 3FD-LL nanosheets was produced by drying a small volume of nanosheets inside a capillary. Surface tension caused fiber formation. Fiber diffraction revealed the presence of both equatorial and meridional spacings. Equatorial spacings occur which are related to the stacking of α-helices. Reflections occurred at distances of 30 Å, 21.86 Å, and 4.5 Å. The first two distances corresponded to ½ the length of one **3FD-LL** α-helix and 1/3 the length of one **3FD-LL** α-helix. The distance, which occured due to the length of the α-helix, is obscured due to the beamstop. The latter two distances are related to the translation per residue along the α-helical axis. The distance of 4.5 Å is three times the α-helix translation of 1.5 Å per residue. This data supported the formation of an α-helix with three-fold symmetry. Meridional reflections occurred at 14.12 Å, 8.43 Å, 7.3 Å, which are related to the hexagonal packing of helices within the nanosheets.

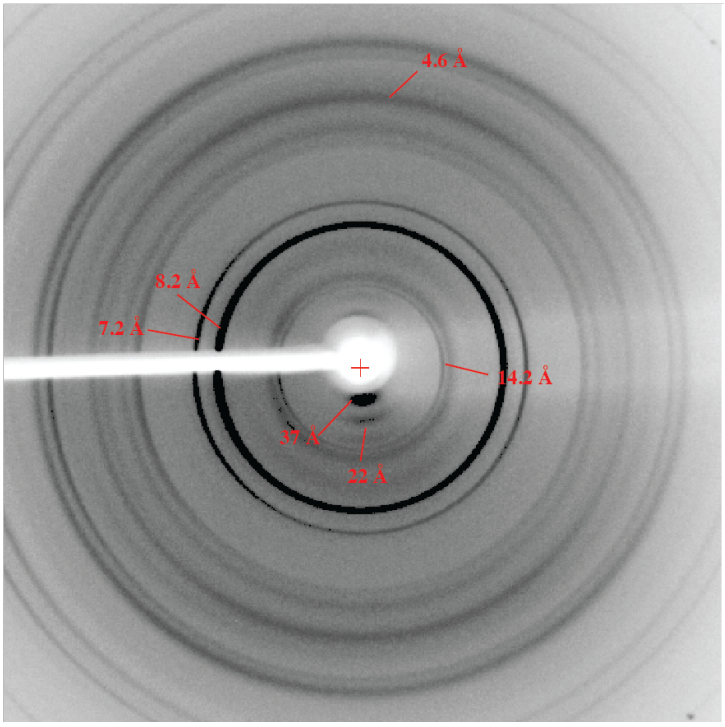

Figure 4.20 X-ray fiber diffraction image revealing reflections related to the structure of the 3FD-LL nanosheets

The orientation of the nanosheets was further explored by shining the x-ray beam on either the face or the edge of the nanosheets. A small volume of **3FD-LL** nanosheets was dried on parafilm to produce a film of **3FD-LL** nanosheets. When the x-ray beam is shined on the face of the film, a series of rings are obtained which corresponded to distances of 14.48 Å, 8.44 Å, 7.3 Å (Figure 4.21c) These distances are identical to the Bragg diffraction peaks, which occurred in the small angle x-ray scattering spectra and corresponded to the hexagonal packing of α-helices within the nanosheets. The presence of rings suggested that when the **3FD-LL** nanosheets are dried, the sheets are not all arranged in the same orientation, leading to azimuthal averaging. When the x-ray beam is shined on the edge of the nanosheet, spacings related to the hexagonal spacings of the α-helices obtained above are also obtained, but in this case meridional reflections are

obtained rather than rings due to preferential orientation of the sheets with respect to the long axis of the fibril (Figure 4.21b). In addition, layer lines and ro lines were observed, which indicated a high degree of order of the **3FD-LL** for the nanosheets.

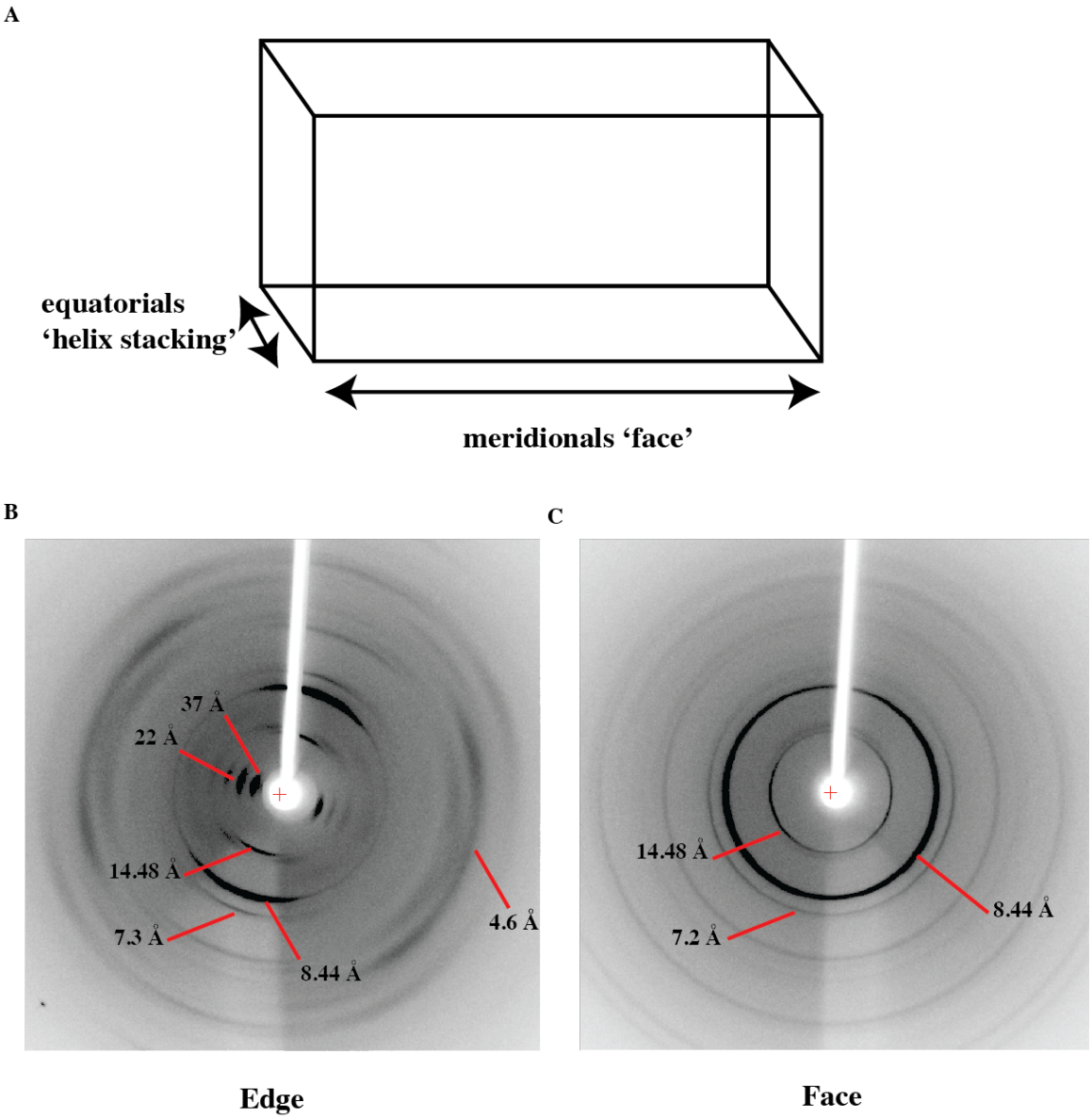

Figure 4.21 Schematic showing the edge and face of a two-dimensional object (b) x-ray diffraction image of edge of the **3FD-LL** film, and (c) x-ray diffraction image of the face of the **3FD-LL** film

Small angle x-ray scattering was also utilized to attempt to get information about orientation. Unfortunately, the films produced were insufficient to obtain orientation

information and x-ray diffraction from the face was identical to that measured from the edge (Figure 4.22). However, a reflection from the length of the α-helix, 77.5 Å, was observed. This reflection was obscured in fiber diffraction due to the beam stop.

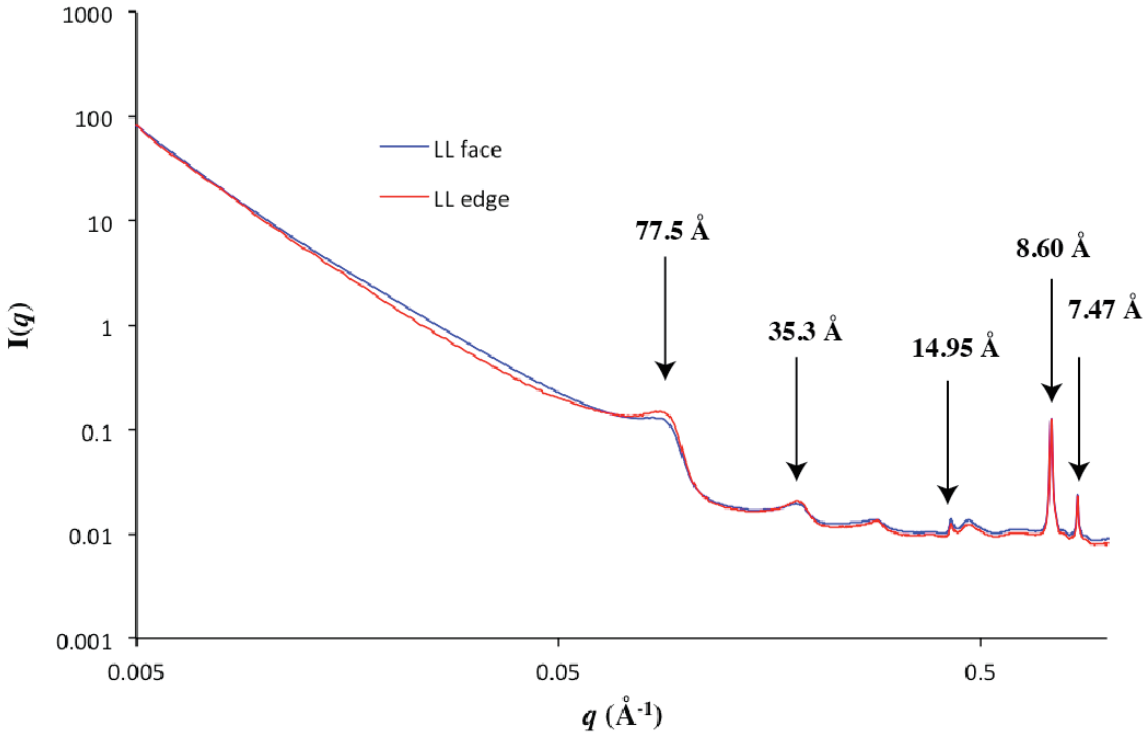

Figure 4.22 Small angle x-ray scattering of **3FD-LL** film

4.3.6 Hexagonal Packing of 3FD-LL nanosheets

In order to elucidate the type of hexagonal unit cell occupied by the 3FD-LL α-helices, scanning transmission electron microscopy was performed. The molecular mass of one **3FD-LL** helix is approximately 4070 Da. For a hexagonal close packed unit cell, there are three helices per unit cell whereas for a honeycomb hexagonal unit cell, there are two helices per cell. Using the value of *a* calculated from the SAXS diffraction peaks, 7.08 Å and a height of 14.8 Å, the area of a hexagonal parallogram is 252.78 Å^2. The

theoretical mass per area of a hexagonal close packed nanosheet is 48.3 Da / Å^2 whereas the mass per area of a hexagonally packed honeycomb nanosheet is 32.2 Da / Å^2. The scanning transmission electron microscopy images revealed the presence of nanosheets which look similar to those observed by AFM and TEM (Figure 4.23a). Unfortunately, the negative-stain STEM image did not give information about the hexagonal lattice, suggesting that the sample becomes disordered in the STEM sample preparation phase. The mass per area obtained from the experimental data for the **3FD-LL** nanosheets was 28.3 Da / Å^2 which agrees within experimental error with the honeycomb arrangement of **3FD-LL** α-helices (Figure 4.23b).

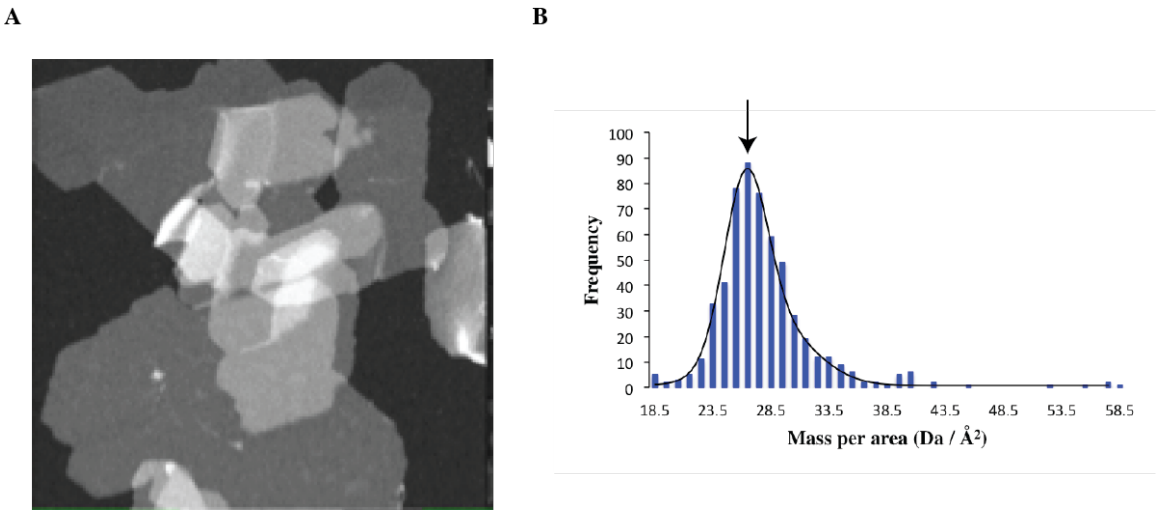

Figure 4.23 (a) freeze dried STEM image of **3FD-LL** nanosheets (b) histogram of mass per area measurements obtained for **3FD-LL** which showed the presence of a single distribution with an average mass per area of 28.3 Da/ Å^2

4.4 Conclusions

4.41 Cryo-electron microscopy

The final experiment performed on the **3FD-LL** nanosheets was cryo-electron microscopy. Preliminary cryo-EM data revealed the presence of large nanosheets. A Fourier transform of the nanosheets revealed a hexagonal lattice, which contained

reflections at 15.8 Å, 9.0 Å, and 7.8 Å. The future goal for this peptide is to obtain the high resolution structure of **3FD-LL** by cryo-EM to determine why larger, more robust nanosheets are observed from a single mutation.

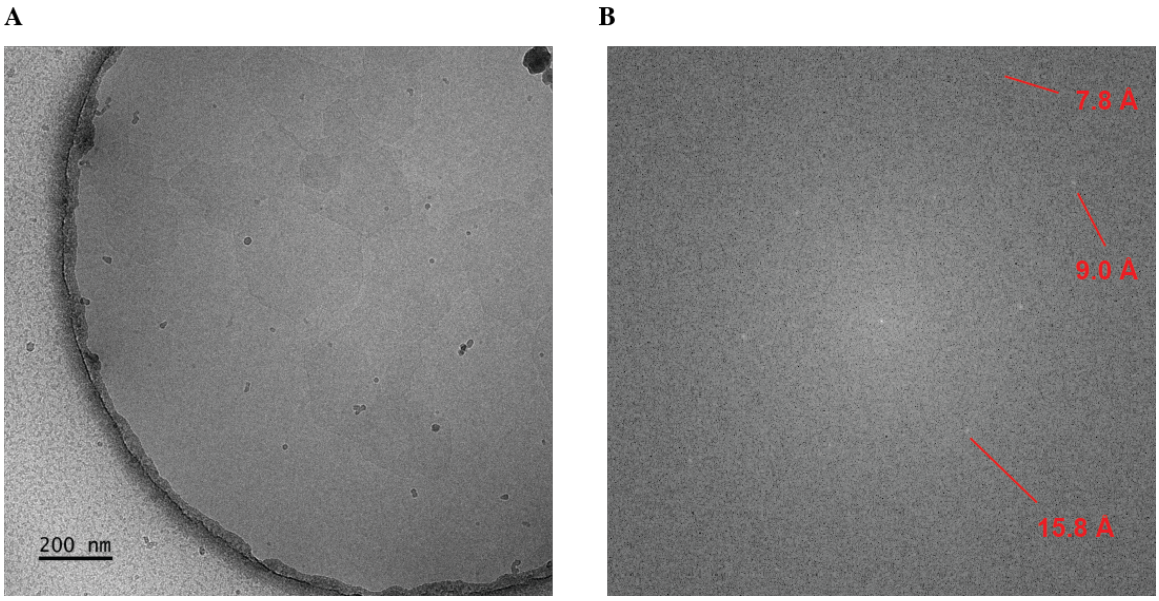

Figure 4.24 (a) Cryo-EM image of **3FD-LL** nanosheets (b) FFT of **3FD-LL** nanosheets

4.42 Conclusions

This chapter emphasized the importance of hydrophobic packing in the formation of the **3FD-IL** nanosheets. As could be predicted based on knowledge that coiled-coils adopt different oligomeric states based on the identity of their hydrophobic amino acids, slight changes in the hydrophobic amino acids resulted in drastic changes in assembly formation. These changes can be attributed to both a change in the resultant ability of the peptide to form an α-helix and different modes of hydrophobic packing which are possible for the different hydrophobic amino acids. Thermodynamics could also play a role in the differences between the observed assemblies. The reversibility of the helix-

helix interaction enables for error correction and the formation of more robust nanosheets.

A comparison of the self-assembly of **3FD-IL** to the behavior exhibited by **3FD-II** and **3FD-LL** is very interesting. **3FD-IL** formed hexagonal nanosheets, which range in size from hundreds of nanometers to microns. In contrast, **3FD-LL** formed nanosheets which are typically larger, micron size and contain sharp edges. The structures formed by **3FD-LL** will be optimized for future use due to their apparent homogeneity in structure based on the scanning transmission electron microscopy data. **3FD-II** formed longer, more narrow assemblies, which resemble sharpened pencils. Interestingly, **3FD-II** only formed assemblies at 4°C. Higher resolution structures will aid in an understanding of the self-assembly differences between these three peptides. Furthermore, most studies on the effect of hydrophobicity on helix-helix interactions involve coiled-coil peptides. This work provides a way to understand hydrophobic packing in straight α-helices.

4.5 Supporting Information

Reagents: All Fmoc amino acids were purchased from Anaspec Inc. (Fremont, CA). The Fmoc-Peg-PAL-PS resin for solid-phase peptide synthesis was purchased from Applied Biosystems. All other chemicals were purchased from Sigma-Aldrich.

Peptide synthesis: The peptides **3FD-LI**, **3FD-II**, and **3FD-LL** were synthesized using microwave-assisted synthesis on a CEM Liberty solid-phase peptide synthesizer. A Fmoc-PEG-PAL-PS resin (Applied Biosystems) was used for synthesis. Standard Fmoc protection chemistry was used for coupling, which was promoted using standard activation protocols based on DIEA/HBTU and base-induced deprotection of the Fmoc

group (20 % piperidine in DMF). All peptides were acetylated at the N-terminus using 20 % acetic anhydride. The peptides were purified using reverse phase high performance liquid chromatography (HPLC) on a C18 column using a water-acetonitrile (0.1 % trifluoroacetic acid) gradient. The target HPLC fractions were collected and liapholized. The purity of the peptides was analyzed using electrospray ionization mass spectrometry and analytical HPLC.

Peptide Assembly: The peptides **3FD-LI** and **3FD-LL** were dissolved in 10 mM TAPS buffer at pH 8.5 unless otherwise noted. Nanosheets were produced after thermal annealing in a thermal cycler. The annealing method initially heated up the peptide to 90° C for ten minutes followed by cooling 0.2° C/ 5 minutes to a final temperature of 40 °C. The resultant nanosheets were stored at room temperature. Nanosheets from peptide **3FD-II** were produced by incubating the peptide (5 mg/mL) in 10 mM TAPS buffer, pH 8.5 at 4°C for several weeks.

Circular Dichroism: CD spectra were recorded on a Jasco J-810 CD spectropolarimeter in 0.1 mm quartz cells (Hellma Analytics) at a peptide concentration of 1 mg/mL in 10 mM TAPS buffer pH 8.5. Spectra were recorded at a scanning rate of 50 nm/min and a resolution of 0.1 nm. CD melting experiments were performed in the temperature range from 5°C to 95°C at a heating rate of 40 °C/hour. The intensity of the CD signal at 222 nm was monitored as a function of temperature. Melting temperatures were obtained from the first derivative of the melting curves.

Transmission Electron Microscopy: TEM specimens were prepared from aqueous solutions of 3FD-LL (10 mg/mL) and its variants. The samples were deposited onto 200 mesh carbon-coated copper grids from Electron Microscopy Sciences (Hatfield, PA). After a 1 min incubation period, the samples were washed with water and stained with an aqueous solution of 0.1 % phosphotungstate stain. Excess stain was wicked away from the grids after incubation on the grid for 30 s. TEM measurements were acquired on a JEOL JEM-1400 transmission electron microscope at an accelerating voltage of 120 kV.

Atomic force microscopy: AFM specimens were prepared from 10 mg/mL solutions of **3FD-LL**. The 3FD-IL solution was diluted to 0.25 mg/mL using 0.5 mM TAPS buffer pH 8.5 right before deposition on a freshly cleaved mica substrate. The sample was spin-coated using a spin coater at a rate of 1.5 rpm for 1 min. The AFM experiments wereperformed using a MFP-3D-BIO from Asylum Research. Silicon AFM tips (MikronMasch) with a force constant (5.4-16 N/m) were used to image the specimens in tapping mode at a scan rate of 1 Hz.

Cryo-electron microscopy: 3FD-LL nanosheets (10 mg/mL) in 10 mM TAPS (pH 8.5) were utilized for cryo-electron microscopy. The nanosheets were diluted to a concentration of 1 mg/mL using 10 mM TAPS (pH 8.5) buffer and dialyzed into 10 mM TAPS buffer pH 8.5. Cryo-EM specimens were prepared by applying 4 µl aliquots to glow-discharged 200 mesh copper Quantifoil grids and plunge freezing in liquid ethane using a Vitrobot Mark III (FEI, Hillsboro, Oregon). Cryo-EM data was collected using a JEOL JEM-2200FS 200 kV FEG-TEM with an in-column Omega energy filter (slit width

20 eV). Images were acquired on a Direct Electron, LP DE-20 direct electron detector (San Diego, CA) at a nominal magnification of 20,000× for a pixel size of 2.94 Å.

Scanning transmission electron microscopy: The STEM specimen was prepared by dialyzing a solution of 3FD-IL nanosheets (10 mg/mL) in 10 mM TAPS buffer (pH 8.5) against pure water. INSERT JOE WALL

Small angle x-ray scattering: 3FD-LL was prepared for small angle x-ray scattering measurements at a peptide concentration of 10 mg/mL in 10 mM TAPS buffer, pH 8.5. The 3FD-IL solution was thermally annealed and the nanosheets and dialyzed against 10 mM TAPS (pH 8.5) to remove residual trifluoroacetic acid. Synchrotron SAXS/WAXS measurements were performed at the 12-ID-B beamline of Advanced Photon Source at Argonne National Laboratory. A simultaneous SAXS/WAXS setup was utilized, and the sample-to-detector distances were set such that the overall scattering momentum transfer, q, range was achieved from 0.005 to 2.4 Å–1, where $q = 4\pi\sin\theta/\lambda$, 2θ denoting the scattering angle and λ the X-ray wavelength. The wavelength was set at 1.033 Å during the measurements. Scattered X-ray intensities were measured using a Pilatus 2 M (DECTRIS Ltd.) detector for SAXS and Pilatus 300K for WAXS. SAXS/WAXS measurements were performed on aqueous solutions of peptides at 25 °C. A quartz capillary flow cell (1.5 mm diameter) was employed to prevent radiation damage. Twenty images were collected for each sample and buffer. The 2D scattering images were converted to 1D SAXS curves through azimuthal averaging after solid angle correction and then normalizing with the intensity of the transmitted X-ray beam, using the software

package at beamline 12ID-B. The 1D curves of the samples were averaged and subtracted with the background measured from the corresponding buffers.

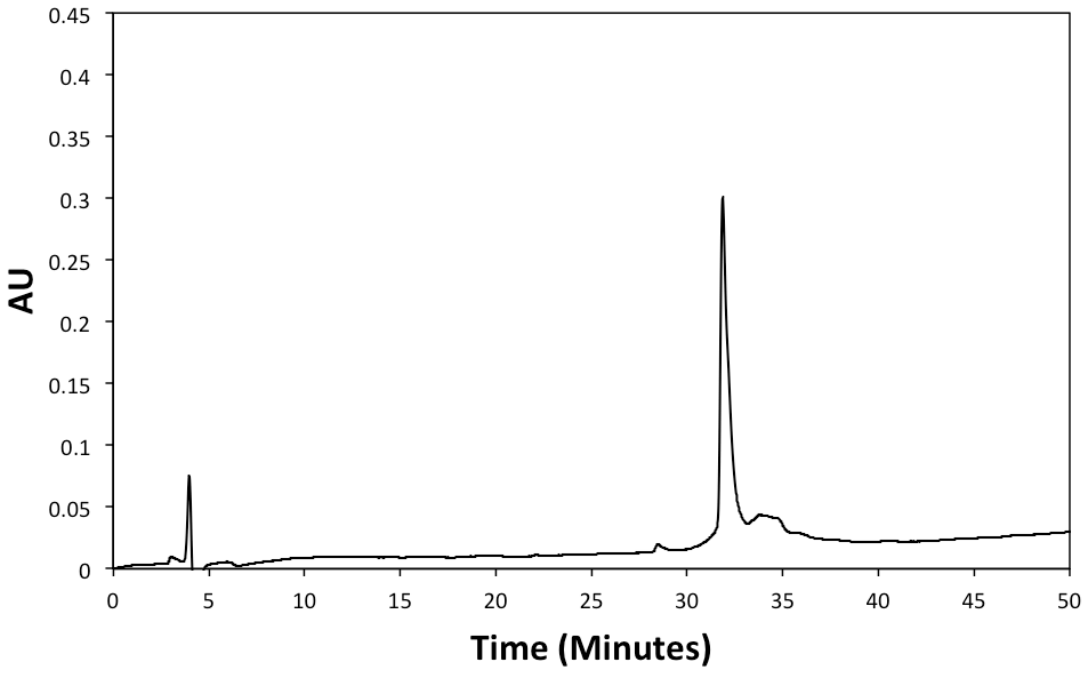

Figure 4.25 Analytical HPLC spectrum of 3FD-LL

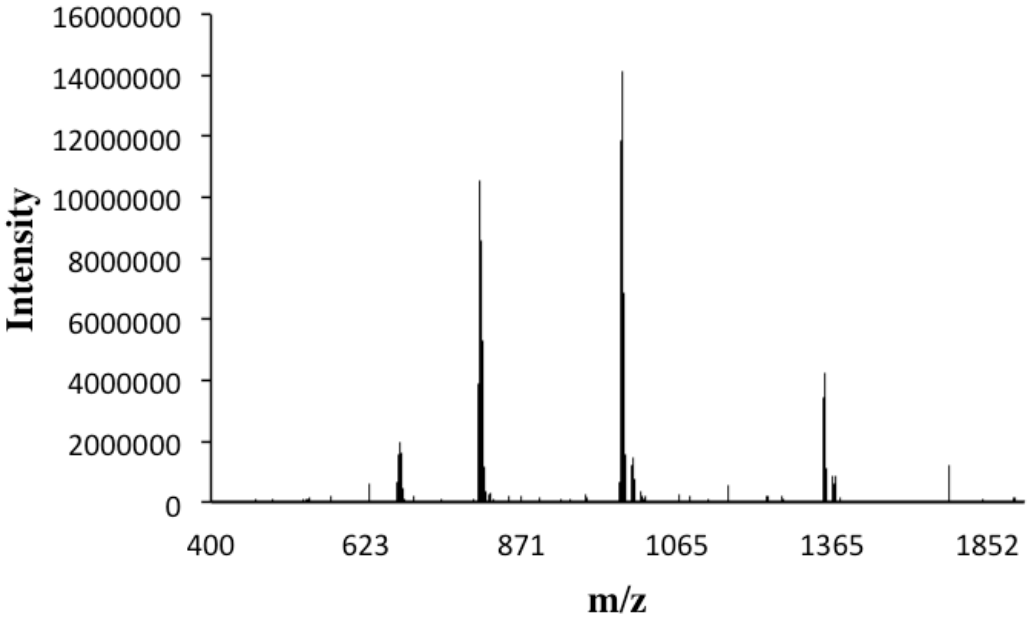

Figure 4.26 Mass spectrum of 3FD-LL

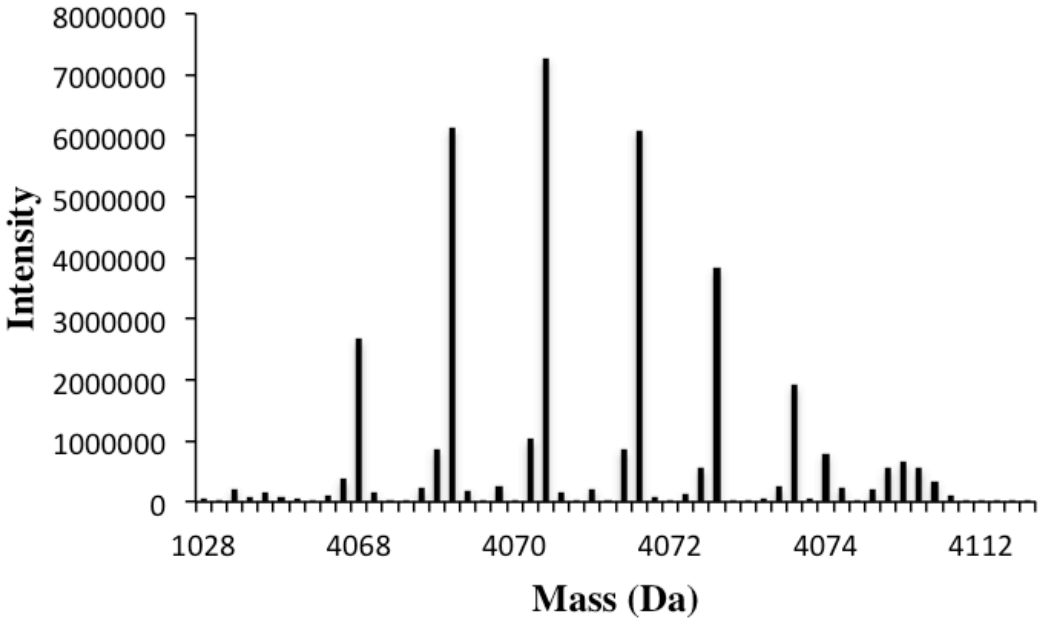

Figure 4.27 Deconvoluted mass spectrum of 3FD-LL

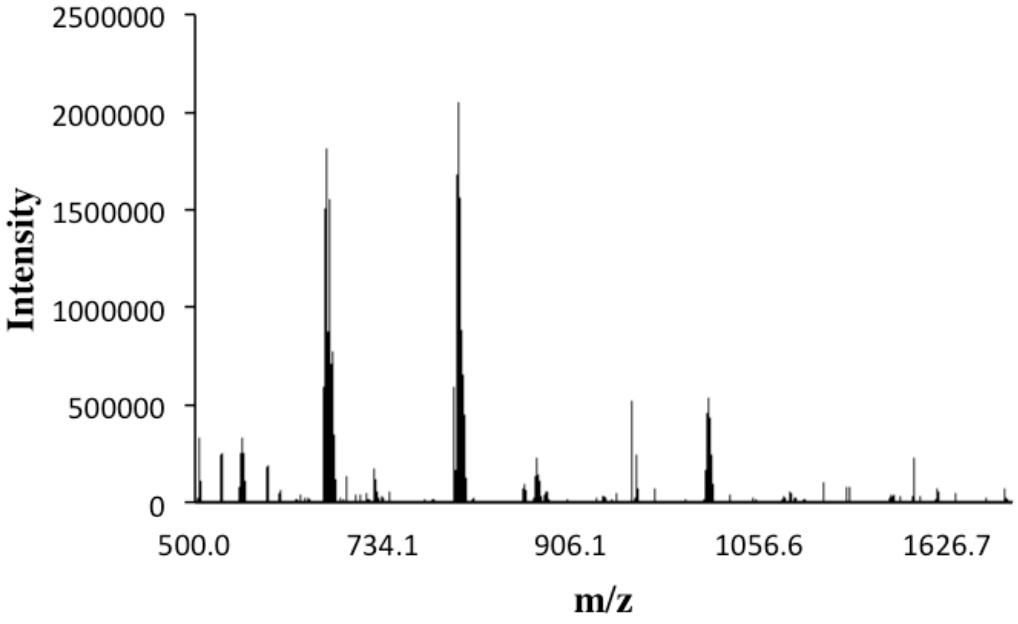

Figure 4.28 Mass spectrum of 3FD-II

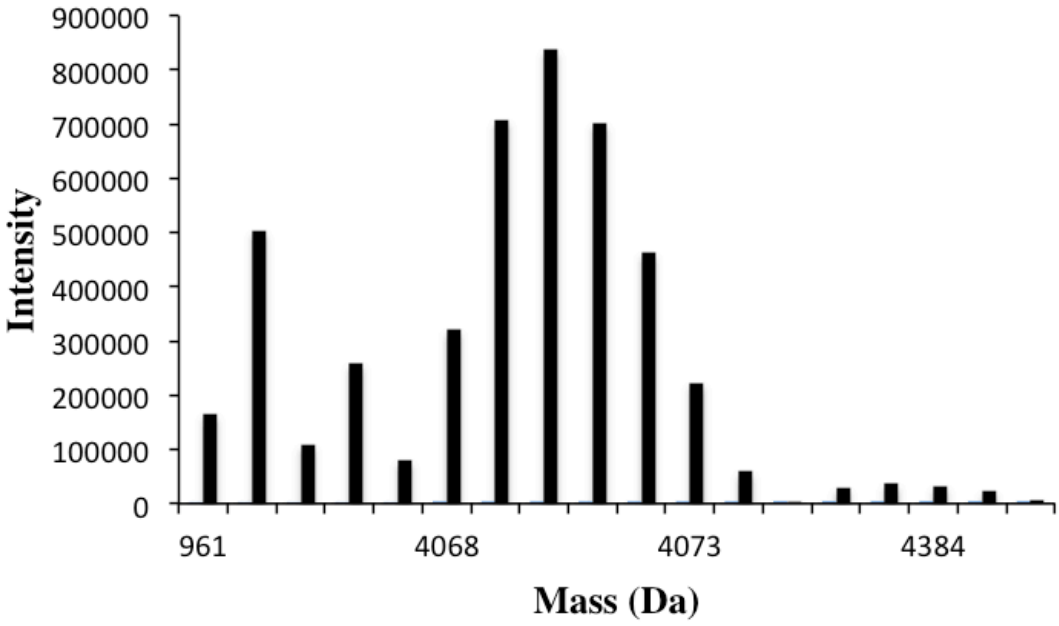

Figure 4.29 Deconvoluted mass spectrum of 3FD-II

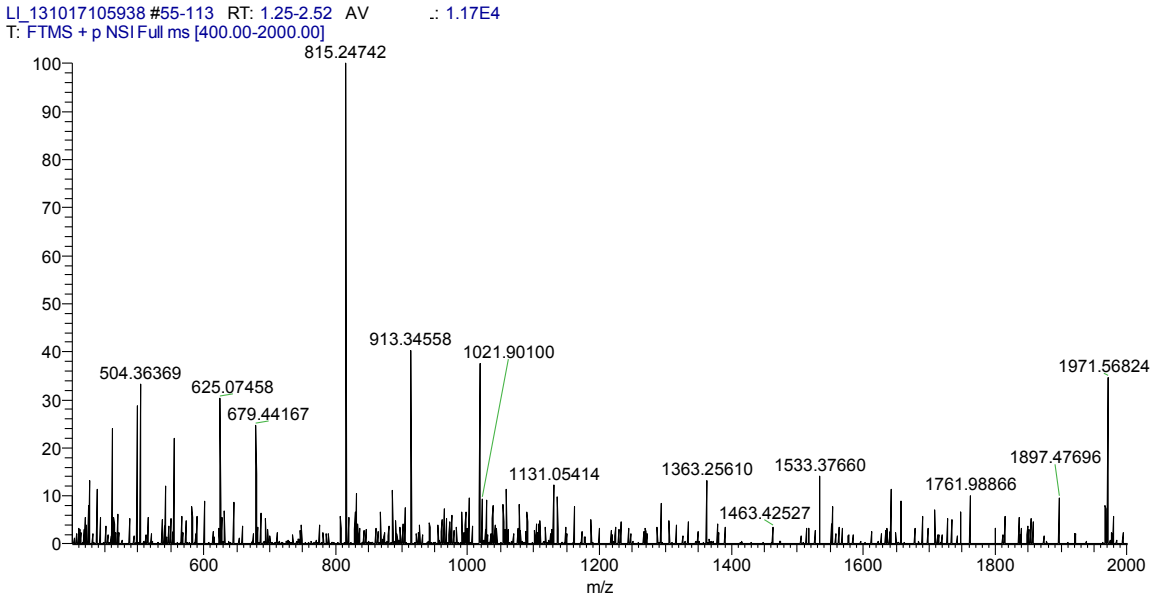

Figure 4.30 Mass spectrum of **3FD-LI**

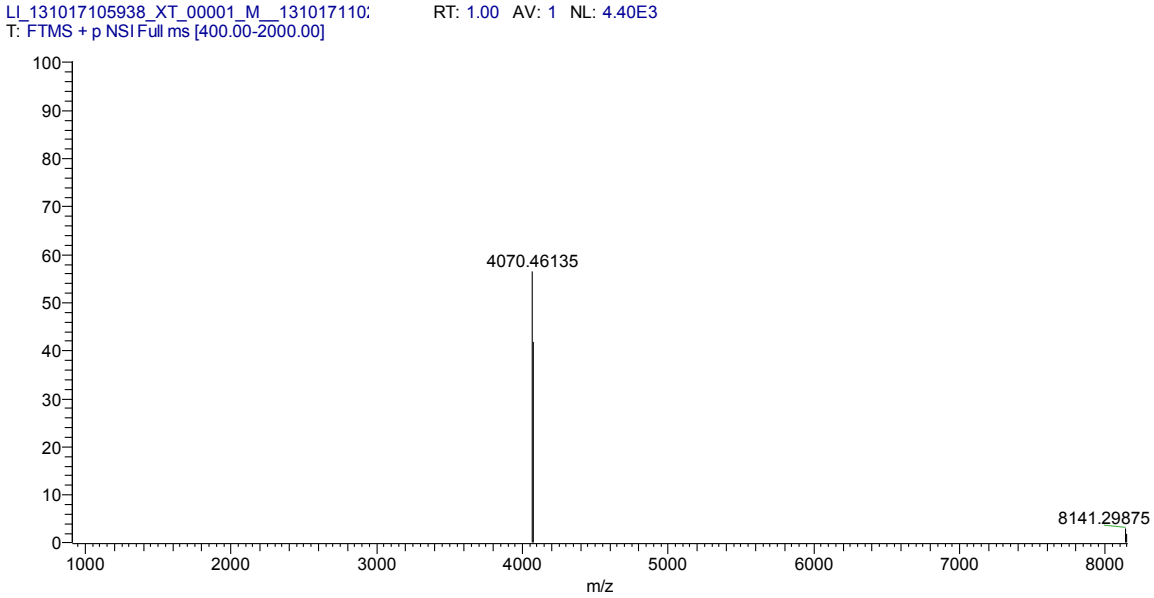

Figure 4.31 Deconvoluted mass spectrum of **3FD-LI**

4.4 References Uncategorized References

1. Harbury PB, Zhang T, Kim PS, Alber T (1993) A switch between two-, three-, and four-stranded coiled coils in GCN4 leucine zipper mutants. Science 262 (5138):1401-1407

2. Fletcher JM, Boyle AL, Bruning M, Bartlett GJ, Vincent TL, Zaccai NR, Armstrong CT, Bromley EH, Booth PJ, Brady RL, Thomson AR, Woolfson DN (2012) A basis set

of de novo coiled-coil peptide oligomers for rational protein design and synthetic biology. ACS Synth Biol 1 (6):240-250. doi:10.1021/sb300028q
3. Lupas AN, Gruber M (2005) The structure of alpha-helical coiled coils. Adv Protein Chem 70:37-78. doi:10.1016/S0065-3233(05)70003-6
4. Zhu BY, Zhou NE, Kay CM, Hodges RS (1993) Packing and hydrophobicity effects on protein folding and stability: effects of beta-branched amino acids, valine and isoleucine, on the formation and stability of two-stranded alpha-helical coiled coils/leucine zippers. Protein Sci 2 (3):383-394. doi:10.1002/pro.5560020310
5. Bowerman CJ, Ryan DM, Nissan DA, Nilsson BL (2009) The effect of increasing hydrophobicity on the self-assembly of amphipathic beta-sheet peptides. Mol Biosyst 5 (9):1058-1069. doi:10.1039/b904439f
6. Lyu PC, Sherman JC, Chen A, Kallenbach NR (1991) Alpha-helix stabilization by natural and unnatural amino acids with alkyl side chains. Proc Natl Acad Sci U S A 88 (12):5317-5320
7. Micsonai A, Wien F, Kernya L, Lee YH, Goto Y, Refregiers M, Kardos J (2015) Accurate secondary structure prediction and fold recognition for circular dichroism spectroscopy. Proc Natl Acad Sci U S A 112 (24):E3095-3103. doi:10.1073/pnas.1500851112

Chapter 5: Conclusions

In the previous three chapters, the first rationally designed α-helical nanosheets were described. The creation of an α-helix with three-fold symmetry allowed for the generation of nanosheets with a high degree of internal order. The porous structures formed by **3FD-IL** were directed using an α-helix with three-fold screw symmetry that allowed for the formation of hexagonal honeycomb architectures. Hexagonal honeycomb structures have not been achieved for peptides. Current nanosheets which adopt this packing arrangement are created using supramolecular organic frameworks.[1] It may be serendipitious that the first peptide **3FD-IL** formed nanosheets, as slight changes in the **3FD-IL** sequence can result in different architectures, such as the twisted structures formed by **3FD-IL-ER** and the fibrils formed by **3FD-LI**. In order to better understand these structural changes, a high-resolution structure of the **3FD-IL** nanosheets is necessary. This platform will enable a deeper understanding of interactions between straight α-helices. To date, these interactions are primarily understood through studies of coiled-coil peptides.

Cryo-electron microscopy represents a superior technique for structure determination, because it allows for an examination of the structural features of biological samples in their hydrated states. Furthermore, advances in cryo-electron microscopy, such as direct electron detection and improved image processing, have enhanced the ability of this technique to be utilized for the determination of high-resolution structures. A high resolution structure of the 3FD-IL nanosheets would allow

for an understanding of the hydrophobic and electrostatic interactions within the sheets and enable eventual functionalization of these nanosheets for nanoarchitectonic purposes.

One attractive avenue for nanosheet functionalization results from the existence of potential hydrophilic channels within these nanosheets. The **3FD-IL** nanosheets contain pores of defined dimensions within them due to their honeycomb packing arrangement. Although the diameter of these nanotubes is not known, based on the diameter of the six helix coiled-coil bundle **CC-Hex**, we anticipate that the diameter is around 6 Å [2]. In contrast to coiled-coil bundles, which are lined with hydrophobic residues, the pores of **3FD-IL** contain charged moieties, due to the existence of seven glutamic acids and seven lysines in the **3FD-IL** sequence. Therefore, the 3FD-IL nanosheets could be utilized in proton channels. Polymer electrolyte membranes (PEMs), which utilize proton transfer to drive the hydrolysis of water, are one of the main components of fuel cells. The prototypical PEM is made up of Nafion, which is a synthetic perfluoronated copolymer, which is punctuated by sulphonate moieties [3]. The sulphonate moieties allow for the formation of charged channels within the PEM, which can be readily hydrated. In an ideal PEM, the charged channels are perpendicular to the surface of the membrane. In Nafion, this orientation may be accomplished through uniaxial deformation. The channels within the **3FD-IL** nanosheets are oriented perpendicular to the surface of the nanosheets. The structural data for the **3FD-IL** nanosheets suggests that the **3FD-IL** nanosheets are hydrated, which would make them suitable materials for proton transfer. Proteins are utilized frequently in biology for proton transfer. This phenomenon is exemplified by the BM2 protein, which is found in the viral envelope of the influenza B virus. The BM2 protein forms a tetrameric channel, based on a left-handed coiled-coil motif, which is

lined by polar amino acids, glutamine, arginine, histidine, and serine [4]. The polar amino acids within the channels allow the BM2 protein to transfer protons at higher rates than mutants which contain more hydrophobic interiors.

A

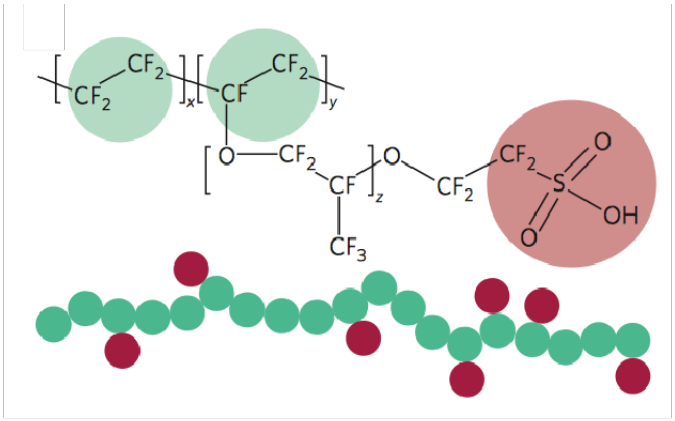

B

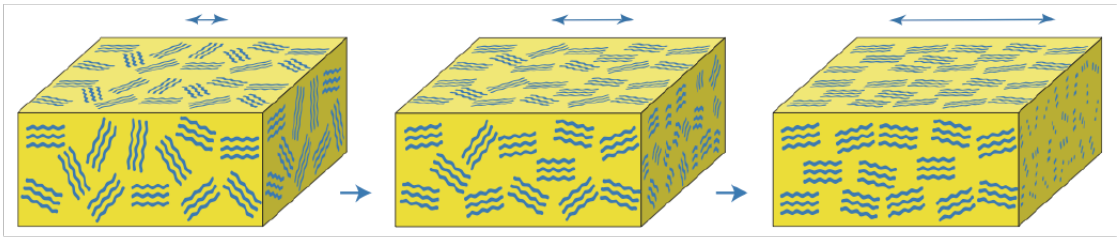

C

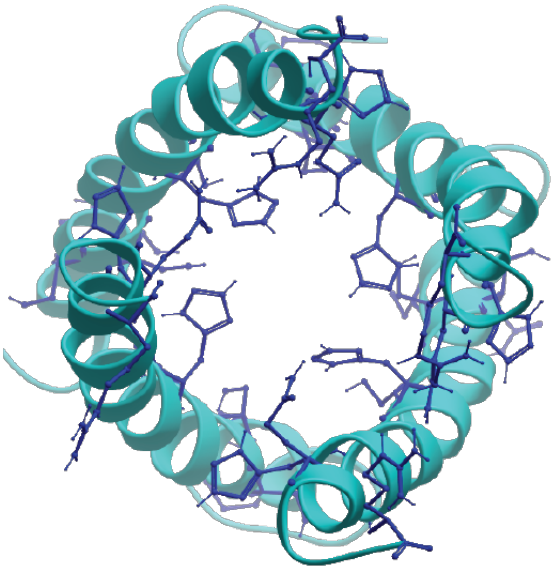

PDB ID: 2KIX

Figure 5.1 (a) structure of Nafion (b) alignment of channels (blue squiggly lines) within Nafion PEM as a result of uniaxial deformation (c) polar channel contained in proton channel BM2

References

1. Zhang KD, Tian J, Hanifi D, Zhang Y, Sue AC, Zhou TY, Zhang L, Zhao X, Liu Y, Li ZT (2013) Toward a single-layer two-dimensional honeycomb supramolecular organic framework in water. J Am Chem Soc 135 (47):17913-17918. doi:10.1021/ja4086935
2. Zaccai NR, Chi B, Thomson AR, Boyle AL, Bartlett GJ, Bruning M, Linden N, Sessions RB, Booth PJ, Brady RL, Woolfson DN (2011) A de novo peptide hexamer with a mutable channel. Nat Chem Biol 7 (12):935-941. doi:10.1038/nchembio.692
3. Zhu BY, Zhou NE, Kay CM, Hodges RS (1993) Packing and hydrophobicity effects on protein folding and stability: effects of beta-branched amino acids, valine and isoleucine, on the formation and stability of two-stranded alpha-helical coiled coils/leucine zippers. Protein Sci 2 (3):383-394. doi:10.1002/pro.5560020310
4. Pielak RM, Chou JJ (2011) Influenza M2 proton channels. Biochim Biophys Acta 1808 (2):522-529. doi:10.1016/j.bbamem.2010.04.015